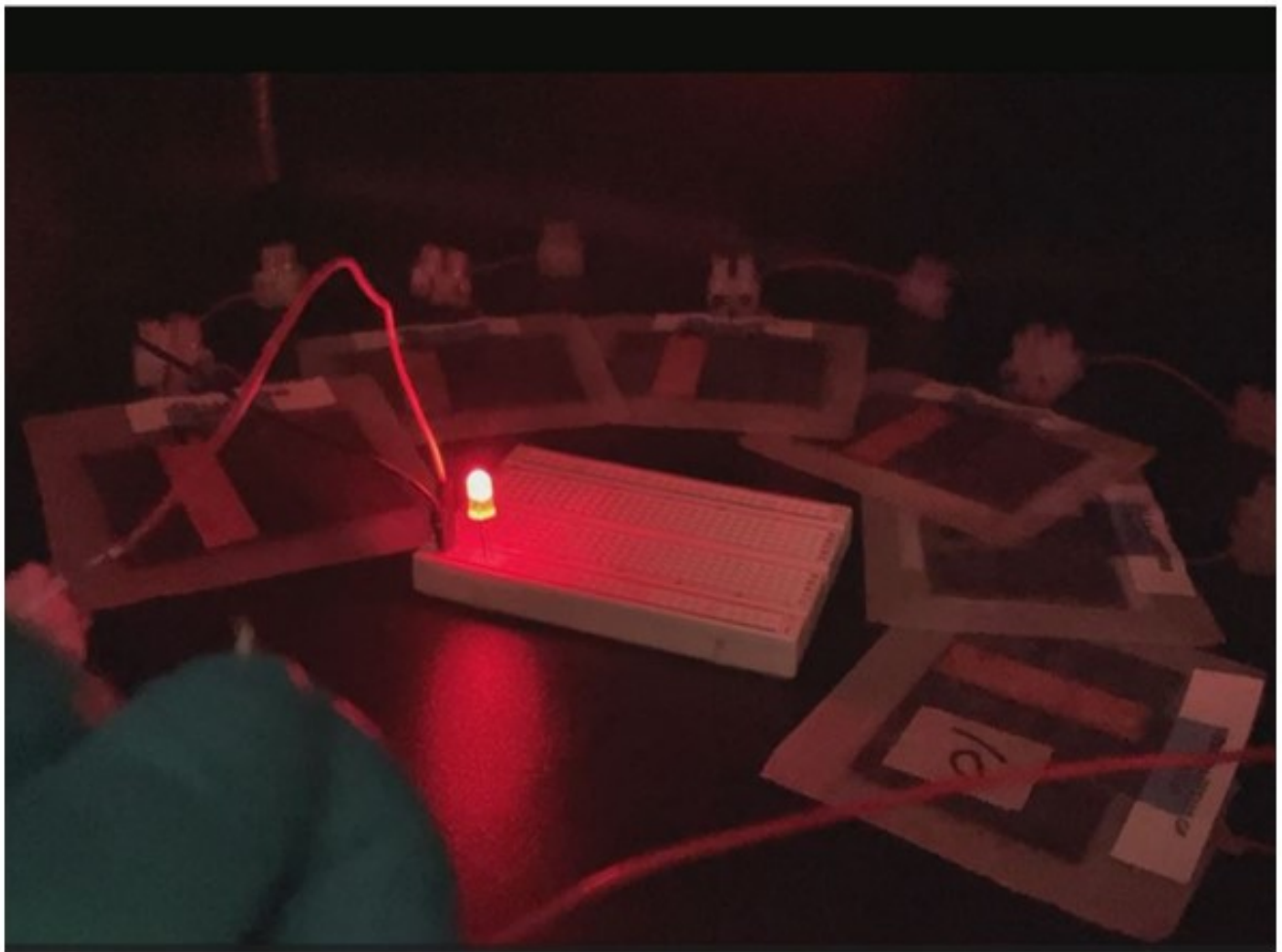


Structural Supercapacitor

A Proof of Concept and Performance Characterisation

Sian Ying Chen



Structural Supercapacitor

A Proof of Concept and Performance Characterisation

by

Sian Ying Chen

to obtain the degree of Master of Science
at the Delft University of Technology,
to be defended publicly on Wednesday June 28, 2023 at 13:00 PM.

Student number: 5200679
Thesis committee: Dr. K. (Kunal) Masania, TU Delft, Supervisor and Chair
Prof. C.A. (Clemens) Dransfeld, TU Delft, Examiner
Dr.ing. Saullo G. P. Castro, TU Delft, Examiner

This thesis is confidential and cannot be made public until December 28, 2023.

An electronic version of this thesis is available at <http://repository.tudelft.nl/>.

Contents

List of Figures	vi
List of Tables	xiv
Abstract	xvi
1 Introduction	1
1.1 The Goals and Conundrums of Electrified Transportation	1
1.1.1 Electrified Transportation Can Achieve Emission Goals	1
1.1.2 Sustainable Aviation Fuel Versus Aviation Technology Advancements	2
1.2 Structural Power Composites	2
1.2.1 Terminologies	2
1.2.2 Structural Power Composites Reduce Mass and Emissions	3
1.2.3 The Encapsulation Methods of Structural Power Composites	3
1.2.4 Develop Structural Supercapacitor for Structural Power Composite's Early Demonstration	4
1.3 Structural Supercapacitor Challenges	5
1.3.1 Research challenges	5
1.3.2 Application challenges	5
2 Literature Study	6
2.1 Categories of Multifunctional Energy Storage Composites	6
2.1.1 Embedded	7
2.1.2 Conformable	8
2.1.3 Structural Embedded	10
2.1.4 Structural Conformable	13
2.2 Electrodes	13
2.2.1 A porous electrode surface is desired for a high surface area	13
2.2.2 Carbon-Based Electrode Materials and Fabrication Methods	14

2.2.3	Surface Area and Scalability Comparison	19
2.3	Electrolytes	20
2.3.1	Terminologies and Categories	20
2.3.2	Ion transport mechanism	21
2.3.3	Solid Polymer Electrolyte	22
2.3.4	Dual Phase Polymer Electrolyte	23
2.3.5	Gel Polymer electrolyte	25
2.3.6	Electrolyte Salts and Ionic Liquids	25
2.4	Separator Selection for the Structural Supercapacitors	26
2.5	Challenges for the Current Collecting Terminals	26
2.6	Interconnection of the Structural Supercapacitors	27
2.7	Conform with Aerospace Regulations	28
2.8	Summary of Literature	30
2.9	Research Objective and Questions	31
3	Methodology and Materials	32
3.1	Structural Supercapacitor Design Concept	32
3.2	The Building Block Approach	33
3.3	Electrode	34
3.3.1	Materials and Equipment	34
3.3.2	Plain Weave Carbon Spread Tow Fabric	34
3.3.3	Carbon Slurry Deposition	35
3.3.4	Characterisation	37
3.4	Gel Polymer Electrolyte	39
3.4.1	Materials and Equipment	39
3.4.2	Polymer Electrolyte Solution	39
3.4.3	Gel Polymer Electrolyte Films	39
3.4.4	Characterisation	39
3.5	Structural Supercapacitor Cell Assembly	40
3.5.1	Batch One	41
3.5.2	Batch Two	42

3.5.3	Batch Three	45
3.6	Structural Supercapacitor Cell Characterisation	47
3.6.1	Electrochemical Performance	47
3.6.2	Full Cell Flexural Test	48
4	Results	49
4.1	Electrode	49
4.1.1	Heat Treatment Study of the Plain Weave Carbon Spread Tow Fabric	49
4.1.2	Dip Coated-Electrodes	50
4.1.3	Brush Application	51
4.1.4	Surface Area and Pore Analysis	54
4.2	Gel Polymer Electrolyte	57
4.2.1	FTIR Spectroscopy	58
4.2.2	Electrochemical Impedance Spectroscopy	59
4.3	Structural Supercapacitor Electrochemical Characterisation	61
4.3.1	Cyclic Voltammetry	61
4.3.2	Galvanostatic Charge-Discharge	64
4.3.3	The Ragone plot	67
4.3.4	Electrochemical Impedance Spectroscopy	68
4.4	The Demo	69
4.4.1	Self-Discharge Phenomena	70
4.4.2	Three Point Flexural Test	71
4.5	Multifunctionality Examination	73
5	Challenges	76
6	Conclusions	77
6.1	Answers to the Research Questions	77
6.1.1	The Experimental Approach	77
6.1.2	Electrode Materials and Fabrication Method	77
6.1.3	Gel Polymer Electrolyte Materials and Fabrication Method	78
6.1.4	Structural Supercapacitor Fabrication	78

6.1.5	Structural Supercapacitor Cell Performance	78
7	Bibliography	79
A	Literature Supplementary Information	91
B	Carbon Aerogel Reinforced Carbon Fabric	93
B.0.1	Materials and Equipment.	93
B.0.2	Method 1: Glass Plate Pressing	94
B.0.3	Method 2: Vacuum-Assisted Resin Transfer Moulding	95
B.0.4	Method 3: Glass Plate Pressing with Ethanol Solvent	96
B.0.5	Conclusions.	97
C	Gantt Chart	98
D	Measurements	100

List of Figures

1.1	Global transportation CO ₂ emissions by mode in selected years from 2000 to 2070 in the sustainable development scenario (in percentages for every sector). A re-plotted figure from the origin data [59].	1
1.2	The figure is replotted from the Waypoint 2050 document, which illustrates the means to achieve net-zero CO ₂ by 2050 [2]. The projected scenario presents rigorous new technology and sustainable aviation fuel development. By the end of 2050, the percentages of each sector's emission reduction contribution are (1) new technologies 34%, (2) operations and infrastructure 7%, (3) sustainable aviation fuels (SAF) 53%, and (4) Market-based measures (carbon offset and capture) 6%.	2
1.3	Structural Power Composite (SPC) case studies. (A) The cabin floor sandwich panel's face sheets as SPC [89]. (B) SPC is integrated into 50% of the airframe to power the electrified subsystems of the aircraft. [70]. (C) SPC applied to the CityAirbus eVTOL [60]. (D) SPC applied for the CubeSat structural frame [84].	3
1.4	Four different interfaces between the electrode and the encapsulator of the structural Power Composite (SPC). (A) Electrolyte matrix-fibre interface (B) Metal-fibre interface (C) Pouch bag-fibre interface (D) Fibre-fibre interface.	4
1.5	The performance of supercapacitors compared to typical lithium-ion batteries. [111]	4
1.6	Structural Power Composite concepts regarding proximity to humans and integration complexity. Red regions are the integrated structural power composites. (A) Fuselage floor sheet panels (B) Semi-truck trailers (C) Passenger car (D) Fixed-wing drone (E) Robotics (Boston Dynamics Spot) (F) Smart Glasses (Portable electronics) (G) Quad-drone (H) Satellite structure. CAD file sources: [3, 12, 44, 106, 126, 134, 135, 144]	5
2.1	The categories of structural power composites configuration. The highlighted red box is the fibre-fibre interface method which is demonstrated in this work. The highlighted green boxes are the encapsulation methods that resemble the direct embed approach that creates potential delamination and low compression strength.	6
2.2	Embedded approach of multifunctional composites. (A) LiPo batteries as the fixed wing for a drone [132]. (B) LiPo batteries embedded into the sandwich foam core to conduct flexural tests [41]. (C) LiPo batteries are embedded into the sandwich foam core (top) and laminate layer (bottom) to conduct vibration and acoustic tests [42]. (D) LiPo batteries are embedded into the sandwich foam core for tension, compression and flexural tests [116].	7
2.3	Mechanical tests of the LiPo battery embedded in sandwich core [116]. (A) Tensile test. (B) Three-point bending test (C) Compression test.	8
2.4	A woven flexible supercapacitor that uses fibre bundles as electrodes which are impregnated with a solid electrolyte [117].	8
2.5	3D-printed battery materials and procedures. [79]. (A) 3D-printed battery materials. (B) The popularity of 3D printing processes for cathode and anode based on the number of reviews.	9

2.6	(A) Direct ink writing of disposable paper supercapacitors on a curved surface. (B) Illustration of the supercapacitor printing process and layers. [1]	9
2.7	Different SPC configurations showing their constituents without the encapsulating encapsulator [85].	10
2.8	The assembly diagram of the four embedding interfaces of the structural embedded. The coloured legend indicates the SPC components (A) The processing steps of the electrolyte matrix-fibre interface. (B) The processing steps of the pouch bag-fibre interface. (C) The processing steps of the metal-fibre interface. (D) The processing steps of the fibre-fibre interface.	11
2.9	The demonstration of the four interfaces of the structural embedded method. (A) The electrolyte matrix-fibre interface demonstration [29, 127, 128]. (B) The pouch bag-fibre interface demonstration [146]. (C) The metal-fibre interface demonstration [114]. (D) The fibre-fibre interface demonstration [114].	11
2.10	PRINTCAP concept design [129].	13
2.11	The specific surface area and the single fibre tensile strength of different activation methods. [99]	14
2.12	(A) and (B): As-received fibre surface. (C) and (D): Heat-treated fibre surfaces. (E) and (F): KOH-activated carbon fibres (incipient wetness, burn-off of 6.8%). (G) and (H) KOH activated carbon fibres (impregnation, burn-off of 14.9%) [99]	14
2.13	(A) Brunauer-Emmett-Teller (BET) Specific surface area of different weight ratios of the coated activated carbon. (B) The different activated carbon loading affects the galvanostatic charge-discharge (GCD) test (left) and the Ragone plots (right). (C) Activated carbon-coated carbon fibre electrodes.	15
2.14	(A): SEM image of CNT sizing. (B): SEM image of CNT grafting. (C): BET surface and specific capacity comparison [51].	16
2.15	(A) CNT infiltration process illustration (B) The SEM images of different types of infiltrated single-walled carbon nanotubes (SWCNT) [113]. The specific surface area (SSA) values are provided for each type of SWCNT.	16
2.16	(A) and (B) are the images of fracture surfaces of carbon fibre which show unevenly distributed GNPs and aggregation [128] (C) Spray-coating GNP particles ($500 \text{ m}^2/\text{g}$ specific area) on carbon fibres. A BET-specific surface area of $2.29 \text{ m}^2/\text{g}$ is obtained [6]. (D) Spray-coating GNP particles ($750 \text{ m}^2/\text{g}$ specific area) on carbon fibres. A BET-specific surface area of $4.72 \text{ m}^2/\text{g}$ is obtained [6]. (E) The electrophoretic deposition (EPD) setup [54]. (F) The EPD of graphene nanoplatelets on spread tow fabrics using an applied voltage of 10V and a 3-minute deposition time [54]. (G) The EPD of graphene nanoplatelets on spread tow fabrics using an applied voltage of 20V and a 3-minute deposition time [54] A BET-specific surface area of $191 \text{ (m}^2/\text{g)}$ is reported.	17
2.17	The sol-gel, supercritical drying and carbonization process to obtain carbon aerogels [75].	18
2.18	SEM images of (A) As-received carbon fibre (CF) with surface crenulations. (B) Uniformly coated carbon aerogel (CAG) on CF surface. (C) CAG with interconnected pore structures filled between CF (D) Closer image of the CAG's porous structure [100].	18
2.19	SEM images. (A) and (D) Carbon aerogel (CAG) mixed with 5wt% GNP coated on carbon fibres (CF) [64]. (B) and (E) CAG mixed with 3wt% GNP750 (750 means the surface area in m^2/g) [6]. (C) and (F) CAG mixed with 1wt% MWCNT [6].	19
2.20	Brunauer-Emmett-Teller (BET) specific surface area comparison of the electrode materials.	20

2.21 (A) Different types of structural supercapacitor electrolytes. (B) Multifunctional performance of the electrolyte matrix [50].	21
2.22 The electrolyte salt affects the ionic conductivity and Young's modulus of the solid polymer electrolytes. (A) The ionic conductivity increases when the SN-LiTFSI ion content increases in the DGEBA resin. The three orange boxes show that ionic conductivity decreases when curing cycles increase [19]. (B) The inverse relation between the ionic conductivity and Young's modulus [19].	23
2.23 The inverse relation of the ionic conductivity and the modulus properties of the solid polymer electrolytes. (A) As the EMITFSI ionic liquid increases in the DGEBA resin, the ionic conductivity increases while Young's modulus decreases. (B) As the EMITFSI ionic liquid increases in the PEGDGE resin, the ionic conductivity increases while the compression modulus decreases [62].	24
2.24 A schematic diagram of a reaction-induced phase separation method [118].	24
2.25 A schematic diagram of a polymerisation-induced phase separation method by heat treatment [110].	24
2.26 SEM images showing the increase of the epoxy weight ratio reduces the pores in the gel polymer electrolytes, which contain the liquid electrolyte [145]. PVDF:LiTF 25:75 wt% with (a)(b) 0 wt% epoxy, (c)(d) 15 wt% epoxy, (e)(f) 30 wt% epoxy and (g)(h) 100 wt% epoxy.	25
2.27 Images of optical microscopy showing the increase of the areal density of glass fabric separators reduces the fabric pore openings, thus eliminating the short-circuiting issue. [62].	27
2.28 Structural supercapacitor (SSC) configurations [20]. The dark region is the electrodes shown to be connected to a positive or negative terminal. The light region is the separator. (A) Single SSC cell (B) Cells in series to increase the voltage window (C) Cells in parallel to increase the capacitance.	28
2.29 Structural supercapacitors embedded in C-beams to power a mockup aircraft door. [22, 78]	29
3.1 Structural supercapacitor 2D-concept. The gel polymer consists of cations and anions represented by dots. The polymer chains are depicted in black, with the degree of cross-linking indicated in green.	32
3.2 The BBA for creating a structural supercapacitor. At the full cell level, the 2D cell is coloured green to indicate the infusion of epoxy resin.	33
3.3 (A) TeXtreme® Spread Tow fabric 200gsm before heat treatment. (B) The SEM image of the PW-CSTF and its binder material. (C) A close view of the binder material.	34
3.4 The illustration of the carbon particle deposition using dip coating and brush application. (A) Carbon particles (B) Adding ethanol (C) Adding SPI carbon conductive paint. (D) Vortex mixing the slurry Icon sources: [37, 39, 39, 40, 45, 46]	35
3.5 Fabrication process of the graphene nanoplatelets-based slurry. (A) Graphene nanoplatelets (B) Adding ethanol (C) Adding SPI carbon conductive paint and sealed with Parafilm (D) 10 minutes vortex mixing of the slurry.	37
3.6 Three-electrode setup for the cyclic voltammetry measurement.	37

3.7	An illustration of the manufacturing process for the batch 3 structural supercapacitors (SSC). The upper block shows the step-by-step process for Batch 3, which uses a gel polymer electrolyte separator. The bottom block shows the SSC cross-section for each step. Icon source: [14, 56, 86, 125]	40
3.8	The illustration of the semi-cell lamination process and the VARTM vacuum system layup for the full-cells. (A) Batch 3 layup sequence. (B) Batch 1&2 layup sequence. The cold trap is only needed for the semi-cell assembly. The flow mesh is only needed for VARTM. Icon sources: [47], ChemSketch.	41
3.9	Batch one gel polymer electrolyte samples from LiTFSI 0wt% to 60wt%.	42
3.10	Batch 1 semi-cell assembly. (A) The copper tapes are attached to the heat-treated PW-CSTF. (B) Brush application of the b-GNP400 slurry. (C) Wetting the electrode surface with liquid polymer electrolyte. (D) Assembling semi-cell. (E) Vacuum bagging setup of the Semi-cell in an oven. (F) The assembled semi-cell.	43
3.11	(A) Liquid polymer electrolyte solutions of LiTFSI-10% to LiTFSI-60%. (B) Gel polymer films after vacuum drying.	44
3.12	Batch 2 semi-cell. (A) An assembled semi-cell. (B) Wires are attached to the copper tape of the semi-cell. (C) Vacuum pressing of the 12 semi-cells.	44
3.13	Batch 2 full cells. (A) Cells 1 to 6 and their 3D layup. (B) Cells 7 to 12 and their 3D layup. . . .	45
3.14	The 3D layup of the batch 3 cells. (A) Batch 3 cells 1 to 5 with a gel polymer electrolyte (GPE) separator. (B) Batch 3 cells 6 to 10 with GPE-impregnated glass fabrics as the separator. . . .	46
3.15	Full cells in batch three before and after VARTM.	46
3.16	(A) The full cell is sealed in a PE pouch bag. A resistor is connected between the terminals to dissipate residual currents during the test. (B) The flexural test setup.	48
4.1	(A) The time history of the PW-CSTF mass loss as a function of temperature. (B) The time history of the PW-CSTF mass loss rate of the PW-CSTF. (C) PW-CSTF mass and its mass loss rate as a function of temperature.	49
4.2	Plain weave carbon spread tow fabric and their SEM images before and after heat treatment at 330°C for 30 minutes.	50
4.3	Performance of the dip-coated electrodes. (A) The electrode-specific capacitance versus the electrode weight. (B) The slurry-specific capacitance versus the slurry weight. (C) Areal capacitance versus areal density. (D) CV curves of the highest electrode-specific capacitance for each slurry formula. The number 3 indicates the electrode is dipped 3 times. (E) Cyclic voltammetry (CV) of the PW-CSTF and the PW-CSTF electrodes deposited with carbon paint.	51
4.4	Performance of the brush application electrodes with the AC and GNP slurries. (A) Electrode-specific capacitance versus the electrode weight. (B) Slurry-specific capacitance versus the slurry weight. (C) Areal capacitance versus areal density. (D) CV curves of the highest electrode-specific capacitance for each GNP slurry formula. "1b" and "2b" means the number of brushes, and the numbers in the bracket are the numbered samples.	52
4.5	Performance of the brush application electrodes with the GNP-AC mixed slurry. (A) Electrode-specific capacitance versus the slurry weight. (B) Slurry-specific capacitance versus the slurry weight. (C) Areal capacitance versus the areal density. (D) CV curves of the highest electrode-specific capacitance for each slurry formula.	53

4.6	The comparison of the three categories of slurries. (A) Electrode-specific capacitance versus the electrode weight. (B) Slurry-specific capacitance versus the slurry weight. (C) Areal capacitance versus the areal density. (D) Surfaces of the GNP slurry samples.	54
4.7	The isotherms for the surface area determination and the pore size distribution of the carbon particles and their corresponding slurries. (A) Isotherms of the GNP and AC particles. (B) Isotherms of the b-GNP300 and b-AC300 slurries. (C) Cumulative pore volumes (D) The differential pore volumes, which implies the pore size distribution.	55
4.8	The scanning electron microscope images of the electrodes' surface and their carbon materials. (A) Activated charcoal (AC) particles. (B) Graphene nanoplatelets (GNP). (C) SPI carbon conductive paint coated PW-CSTF (D1) Electrode surface deposited by b-AC300 slurry. (D1) and (D2) are magnified images of (D1). (E1) Electrode surface deposited by b-GNP300 slurry. (E2) and (E3) are magnified images of (E1).	56
4.9	The Brunauer-Emmett-Teller (BET) specific surface area of the carbon-based electrodes. The b-GNP300/PW-CSTF electrode exhibited superior performance and was comparable to the PW-CSTF infused with carbon aerogel.	57
4.10	Liquid polymer electrolyte from LiTFSI-10 to LiTFSI-100.	57
4.11	The FTIR spectrum of the (A) Polymer electrolyte solution (B) Cured gel polymer electrolyte.	58
4.12	(A) The FTIR spectrum of the cured gel polymer electrolyte (GPE) from 0% to 100% of the PVDF-HFP wt% and the GPE materials. The bandwidths of the crystalline and the amorphous region are labelled. LiTFSI-0% to LiTFSI-50% are vacuum dried at 70°C for 24 hrs while concentrations LiTFSI-60% to LiTFSI-100% are dried for 72 hrs. (B) The thicknesses of the GPEs.	59
4.13	(A) The Nyquist plot of the gel polymer electrolyte (GPE) LiTFSI-0%. 4 sample measurements are plotted. (a) The high-frequency region of the Nyquist plot. (B) The Nyquist plot of the LiTFSI-0% to 50% GPE at high-frequency regions. Multiple samples are measured for each GPE concentration.	59
4.14	(A) The Nyquist plot of the gel polymer electrolyte (GPE) LiTFSI-60%, 80% and 100%. Multiple samples are measured for each GPE concentration. (a) The Nyquist plot shows the full frequency range from low to high. (B) Different LiTFSI concentrations influence the ionic conductivity and the GPE bulk resistance.	60
4.15	The cyclic voltammetry (CV) measurements for the semi-cells of batch 1 and batch 2. (A) Batch 1 semi-cell CV measurements of 9 and 11. (B) The CV curves of batch 2 semi-cells showed ohmic responses (forward and backward scan overlaps and having a straight line with a slope).	61
4.16	The cyclic voltammetry (CV) measurements. (A) Batch 2 semi-cells 10, 11 and 12. Each cell is scanned for 7 cycles from 0.1 V to 0.7 V with a 0.1 V increment. (B) The batch 2 semi-cells 10 to 12 and batch 3 semi-cells which has a gel polymer electrolyte separator. Batch 3 semi-cells have a higher thickness.	62
4.17	The cyclic voltammetry (CV) measurements. (A) Comparison of batch 3 cells 1 to 5 before and after epoxy infusion. (B) The full cells of the three different structural supercapacitor designs, in which all gel polymer electrolytes contain the same LiTFSI concentration (60 wt% of PVDF-HFP). "b2 full cell 12" and "b3 full cell 3" both contain a gel polymer electrolyte (GPE) as a separator. b2 full cell 12 has a GPE thickness of 145 μm , and b3 full cell 13 has a GPE thickness of 198 μm . "b3 full cell 8" contains two layers of GPE-impregnated glass fabric.	63

- 4.18 The impact of the epoxy infusion on coulombic efficiency (CE) and equivalent series resistance (ESR) before and after the infusion process. The GCD test is conducted using a 5 mV constant current on batch 2 cells and a 1 mA constant current for batch 3 cells. (A) The CE of batch 2 semi-cells and full-cells from 0.2 V to 0.7 V. (B) The CE of batch 3 semi-cells and full-cells using a gel polymer electrolyte (GPE) separator. (C) The CE of batch 3 semi-cells and full-cells using a GPE-impregnated glass fabric separator. (D) The relationship between the LiTFSI concentration and the ESR of the semi-cells and the full-cells. 64
- 4.19 The LiTFSI influence on the specific capacitance, energy and power normalised by the full-cell weight and the slurry deposition weight (active mass of the cell). The values are obtained by performing galvanostatic charge-discharge using a voltage window of 0.7 V and a constant current of 1 mA. (A1) Specific capacitance. (A2) Slurry-specific capacitance. (B1) Specific energy. (B2) Slurry-specific energy (C1) Specific power (C2) Slurry-specific power. 65
- 4.20 The image presents the change of the interface between the semi-cell and the glass fabric encapsulation when the LiTFSI concentration is increased in the gel polymer electrolyte. (A) to (E) are batch 3 cells 1 to 5. The whitened locations indicate the contact of the epoxy and the gel polymer electrolyte. As the LiTFSI concentration increases, the whitened area also increases, indicating that there is a reaction between the epoxy and the LiTFSI ions. 66
- 4.21 (A) The weight constituents of batch 2 full cells 10 to 12 and batch 3 full cells 1 to 10 are shown in percentage. 66
- 4.22 The semi-cell and full-cell weights of the batch 2 full cells 10 to 12 and batch 3 full cells 1 to 10. The right axis shows the weight increase percentage from the semi-cell to the full-cell. 67
- 4.23 The galvanostatic charge-discharge (GCD) is performed on the full cells using a constant current from 1 mA to 15 mA. The specific energy and the specific power are plotted as the Ragone plot. (A) The Ragone plot of the energy and power values normalised by the full cell weight. (B) The Ragone plot of the energy and power values normalised by the slurry weight. (C) The coulombic efficiency of batch 3 cells 1 to 5, which use the gel polymer electrolyte separators. 67
- 4.24 The electrochemical impedance spectroscopy (EIS) measurement of batch 3 full cells 1 to 5. (A) Nyquist plots of the batch-3 semi-cells and the full-cells. (B) The high-frequency region of the suppressed semi-circles of the Nyquist plots. (C) The fitted semi-circle of batch 3 full-cell 3 is used as an example to show the intercepts of the semi-circle with the real impedance axis. (D) The high-frequency region of the Nyquist plot indicates the different R_A and R_B of the semi-cell and the full-cell. 69
- 4.25 (A) The charge setup illustration for charging the cells individually. (B) The discharge setup illustration for powering the red LED. The connection points for the PicoScope to measure the voltage drop across the 6 cells in series (blue channel), and the connection points to measure the passing current, which is determined using the ohm's law with a 1-ohm resistor (12 120 ohm resistors in parallel). 70
- 4.26 The voltage and time history of the 6 cells powering a red LED. 70
- 4.27 The self-discharge phenomena are presented as the voltage drop over time. (A1) The self-discharge effect of batch 3 cells 1 to 5 using a gel polymer electrolyte (GPE). (A2) The time required for the voltage to decrease by half. (B1) The self-discharge effect of batch 3 cells 6 to 10 using a GPE-impregnated glass fabric. (B2) The time required for the voltage to decrease by half. 71
- 4.28 The stress-strain plots of batch 2 and batch 3 full cells. (A) Batch 2 full cells 1 to 6. (B) Batch 2 full cells 7 to 12. (C) Batch 3 full cells 1 to 5. (D) Batch 3 full cells 6 to 10. Batch 3 samples are tested up to a maximum deformation of 7 mm. 72

4.29	The two graphs presents the influence of the LiTFSI concentration and different batches on the flexural properties. (A) The relationship between the flexural chord modulus and LiTFSI concentration. (B) The relationship between the flexural strength and the LiTFSI concentration.	73
4.30	The fibre volume fraction of the glass fabric encapsulation.	73
4.31	The data presented is batch 3 cells 1 to 5, which uses a gel polymer electrolyte as the separator and is measured using a 1 mA constant current. The influence of LiTFSI concentration on (A) Specific capacitance and flexural strength, (B) Specific capacitance and flexural modulus, (C) Slurry-specific capacitance and flexural strength, (D) Slurry-specific capacitance and flexural modulus.	74
4.32	(A) The multifunctionality study of the flexural modulus versus the specific capacitance. (B) The multifunctionality study of the flexural strength versus the specific capacitance.	75
4.33	The structural supercapacitor multifunctionality comparison figures constructed by Greenhalgh et al. [50]. The number of each data point is the reference number in the review literature. The approximate SSC performance of this work is presented as the red cross. The graphs are plotted as the specific capacitance normalised with the active mass (slurry mass) versus (a) The tensile Young's modulus (GPa) and (b) The tensile strength (MPa).	75
A.1	Left: Parallel SSC design with interlaced current collectors pattern. Right: SSC design with the pattern of the locally coated material on carbon fabrics [91].	92
B.1	Structural supercapacitor concept reinforced by carbon aerogel (CAG). CAG image: [88]. The dots in the gel polymer represents cations and anions. The black-coloured chains in the gel polymer represent polymer chains with a degree of cross-linking labelled in green.	93
B.2	(A) Resorcinol-formaldehyde (RF) solution. (B) Heat-treated carbon non-crimp (NCF) fabrics (C) Soaking NCF in the RF solution. (D) Glass plate-pressed RF gel-coated NCF. (E) NCF before (left) and after (right) RF gel coating.	94
B.3	(A) Resorcinol-formaldehyde (RF) infusion trial 1, 300-millibar vacuum infusion. (B) Resorcinol-formaldehyde (RF) infusion trial 2, 800-millibar vacuum infusion. (C) Trial 2 VARTM of the cured vacuum setup. (D) The hydrophobic surface of the non-crimp fabric.	95
B.4	(A) Non-crimp fabric coated with resorcinol-formaldehyde (RF) gel. (B) SEM image of a single fibre coated with the RF gel (C) Carbonization of the sample under a nitrogen vented furnace at 600°C for 30 minutes. (D) Glass plate clamping method.	96
B.5	(A) Spread tow fabrics coated with carbon aerogel [7].	97
C.1	Production Gantt chart for batch one.	98
C.2	Production Gantt chart for batch two.	99
C.3	Production Gantt chart for batch three.	99
D.1	The weight ratios of the three different slurries based on varying concentrations of activated charcoal.	100
D.2	CV plots of the dip-coated samples. (A) CV curve of the Dip-AC-12 slurry.(B) CV curve of the Dip-AC-16 slurry. (C) CV curve of the Dip-AC-20 slurry. The numbers 1 to 3 indicate the number of dips. (D) Surfaces of the dipping samples.	102

D.3	CV plots of the electrode samples brush-coated with the GNP slurry. (A) CV curves of the b-GNP200 slurry. (B) CV curves of the b-GNP300 slurry. (C) CV curves of the b-GNP400 slurry. (D) CV curves of the b-GNP500 slurry.	103
D.4	CV plots of the electrode samples brush-coated with the AC slurry. (A) CV curves of the b-AC200 slurry. (B) CV curves of the b-AC300 slurry. (C) CV curves of the b-AC400 slurry. (D) CV curves of the b-AC500 slurry.	104
D.5	CV plots of the electrode samples brush-coated with the GNP-AC mixed slurry. (A) Specific capacitance normalised by the electrode weight (PW-CSTF and slurry). (B) Specific capacitance normalised by the slurry weight. (C) Areal capacitance is normalised by the surface area of the PW-CSTF. (D) CV curves of the highest electrode-specific capacitance for each slurry formula. The numbers 1&2 were brushed once, while 3&4 were brushed twice.	105
D.6	The FTIR spectrum and the corresponding functional groups at the transmittance peaks of the (A) PVDF-HFP [52, 80, 96, 124] (B) TEP [36, 83, 136] and (C) LiTFSI [77, 102, 103, 143].	106
D.7	The behaviour of the Nyquist plot of gel polymer electrolyte (GPE) LiTFSI-60% when the alternating potential V_{rms} is varied. The gel polymer electrolyte LiTFSI-60% is vacuum dried for 24 hours at 70°C. The electrochemical impedance spectroscopy was measured on the fifth day after the GPE was produced.	107
D.8	(A) Slurry deposition weight using the brush application method for batch 1 to batch 3. (B) Relationship between gel polymer electrolyte thickness and LiTFSI concentrations. Batch 1 and 2 used a 600 μm solution casting gap while batch3 used a 800 μm gap.	107
D.9	Stress strain plots of the mock-up samples. (A) With a PE film as the gel polymer electrolyte (GPE) mock-up, without a pouch bag. (B) With a PE film as the gel polymer electrolyte (GPE) mock-up, with a pouch bag. (C) Without a PE film as the GPE mock-up, without a pouch bag. (D) Without a PE film as the GPE mock-up, with a pouch bag.	111

List of Tables

3.1	Activated charcoal slurry formulation table for dip coating.	35
3.2	Formulations of activated charcoal and graphene nanoplatelets based slurries developed for brush application.	36
3.3	The formulation of activated charcoal and graphene nanoplatelets mixed slurries developed for brush application.	36
3.4	Batch 1 produces 12 cells with 6 different gel polymer electrolyte concentrations.	41
3.5	Slurry formula table for batch 1.	42
3.6	Batch 1 semi-cell dimensions.	42
3.7	Batch 2 structural supercapacitors cell code names.	43
3.8	Slurry formula table for batch 2.	44
3.9	Batch 2 cell dimensions.	45
3.10	Batch three supercapacitor cell code names.	46
3.11	Slurry formula table for batch 3.	46
3.12	Batch 3 cell dimensions.	47
3.13	Samples for the mock-up flexural testing. Five samples are used for each mock-up category .	48
4.1	BET-specific surface area and the sample mass.	55
4.2	The impedance values of the batch-3 full cells using the fitted semi-circles.	68
4.3	Mean values of flexural chord modulus of elasticity and flexural strength of the mock-up samples. The mean values are the average of five specimen measurements.	71
A.1	Brunauer-Emmett-Teller (BET) surface area of the electrodes.	91
D.1	Dip coating sample properties.	100
D.2	Brush application of the activated charcoal (AC) sample properties.	101
D.3	Brush application of the graphene nanoplatelets (GNP) sample properties.	101
D.4	Brush application of the mixed activated charcoal-graphene nanoplatelets sample properties. .	102
D.5	Brush application of the mixed activated charcoal-graphene nanoplatelets sample properties. .	103

D.6	Formulation table of the gel polymer electrolyte for batch 1.	104
D.7	Dimensions of the mock-up samples with no PE film as the mock-up gel polymer electrolyte. Each dimension of the samples is measured five times at different locations.	105
D.8	Dimensions of the mock-up samples with PE film as the mock-up gel polymer electrolyte. Each dimension of the samples is measured five times at different locations.	108
D.9	Batch 2 full cell dimensions for the three-point flexural test. Each dimension of the samples is measured five times at different locations.	108
D.10	Batch 3 full cell dimensions for the three-point flexural test. Each dimension of the samples is measured five times at different locations.	109
D.11	Mean values and standard deviation of the mock-up samples with no PE film as the gel polymer electrolyte mock-up.	109
D.12	Mean values and standard deviation of the mock-up samples with a PE film as the gel polymer electrolyte mock-up.*The sample's data is excluded from the mean and STD calculation.	110
D.13	The flexural chord modulus and the flexural strength of batch 2 and batch 3 full cells. Batch 3 cells are tested to a maximum of 7 mm deformation.	110

Abstract

A structural supercapacitor (SSC) is a composite material that bears mechanical loads and stores energy, and its encapsulation method of the device is vital for scale-up. Here we present an SSC with an encapsulation interface consisting of spread-tow fabric electrodes and glass fabric encapsulators infused with epoxy resin. Through surface functionalisation of fibres, a high surface area electrode of $231.43 \text{ m}^2/\text{g}$ was separated by a gel polymer electrolyte (GPE) separator and encapsulated in an epoxy polymer. To study the SSC's performance, different GPEs are produced by adding lithium bis(trifluoromethanesulfonyl)imide (LiTFSI) into poly(vinylidene fluoride-co-hexafluoropropylene) (PVDF-HFP). The LiTFSI concentration is varied from 0% to 100% based on the weight of PVDF-HFP. The highest energy storage performance occurred at LiTFSI 60 wt% in the PVDF-HFP, with a cell-specific capacitance of 25.72 mF/g , cell-specific energy of 2.08 mWh/kg and cell-specific power of 25.04 mW/kg . With a flexural modulus of 3.39 GPa and a flexural strength of 52.07 MPa , this further develops high-performance SSCs in the future.

Introduction

1.1. The Goals and Conundrums of Electrified Transportation

1.1.1. Electrified Transportation Can Achieve Emission Goals

A considerable decrease in carbon dioxide (CO₂) from the transportation sector will occur in the coming decades due to the global effort that commits to being climate-neutral by 2050. Passenger cars are currently the main contributor to CO₂ emissions shown in Figure 1.1. However, this sector is projected to decrease its emission level to zero in the next five decades due to its electrification [59]. For median and heavy-duty vehicles, they are expected to have two times more emissions than the aviation sector by 2050. In the aviation sector, the decrease rate of CO₂ is substantially slower. It will eventually become the highest emission contributor by 2060, which requires new advancements in technological solutions.

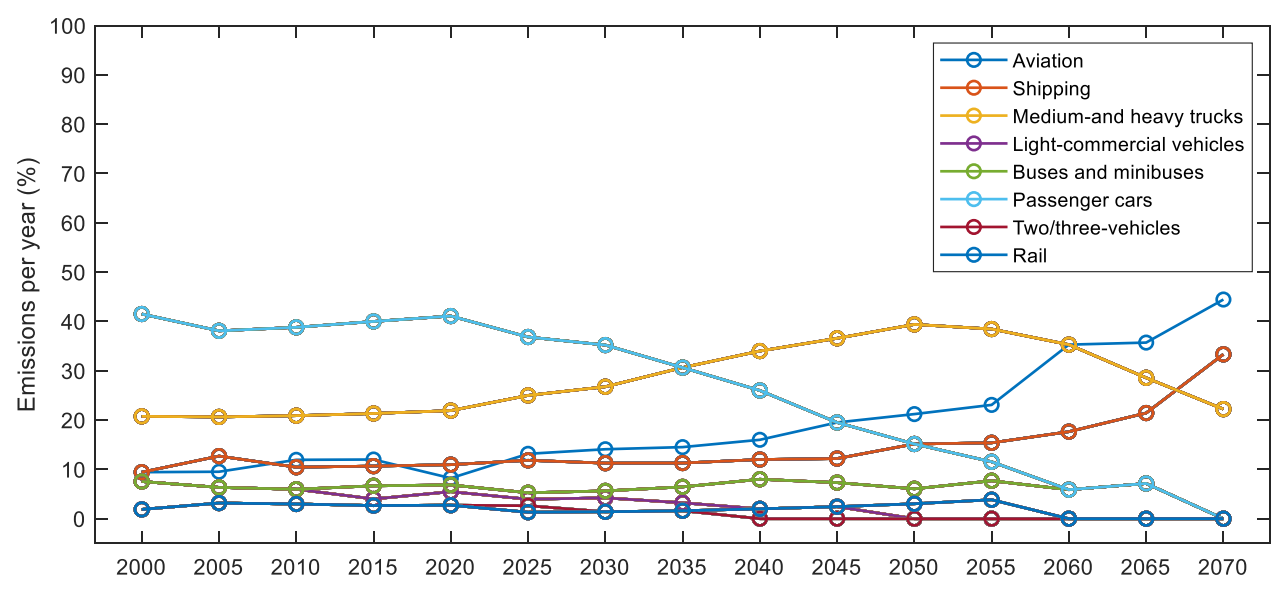


Figure 1.1: Global transportation CO₂ emissions by mode in selected years from 2000 to 2070 in the sustainable development scenario (in percentages for every sector). A re-plotted figure from the origin data [59].

1.1.2. Sustainable Aviation Fuel Versus Aviation Technology Advancements

In order for aviation to achieve net zero by 2050, four strategies are presented by the International Air Transport Association (IATA) shown in Figure 1.2: (1) Sustainable aviation fuel (SAF), (2) new technologies development, (3) market-based measures (carbon offset and capture), (4) operations and infrastructure [2]. The two main contributors to emission reduction are SAF and new technologies. SAF is projected to be the major contributor to obtaining net zero in the future despite there being aggressive technological advances in aviation. Despite successful tests of SAF on regional aircraft, sustainable aviation fuel (SAF) currently only contributes 0.1% to total jet fuel (0.05% in the EU) and has taken 15 years to reach this level [32, 58, 87]. The EU's targets of 65% SAF by 2050 will be challenging due to the high costs and energy-intensive infrastructures required for production [32].

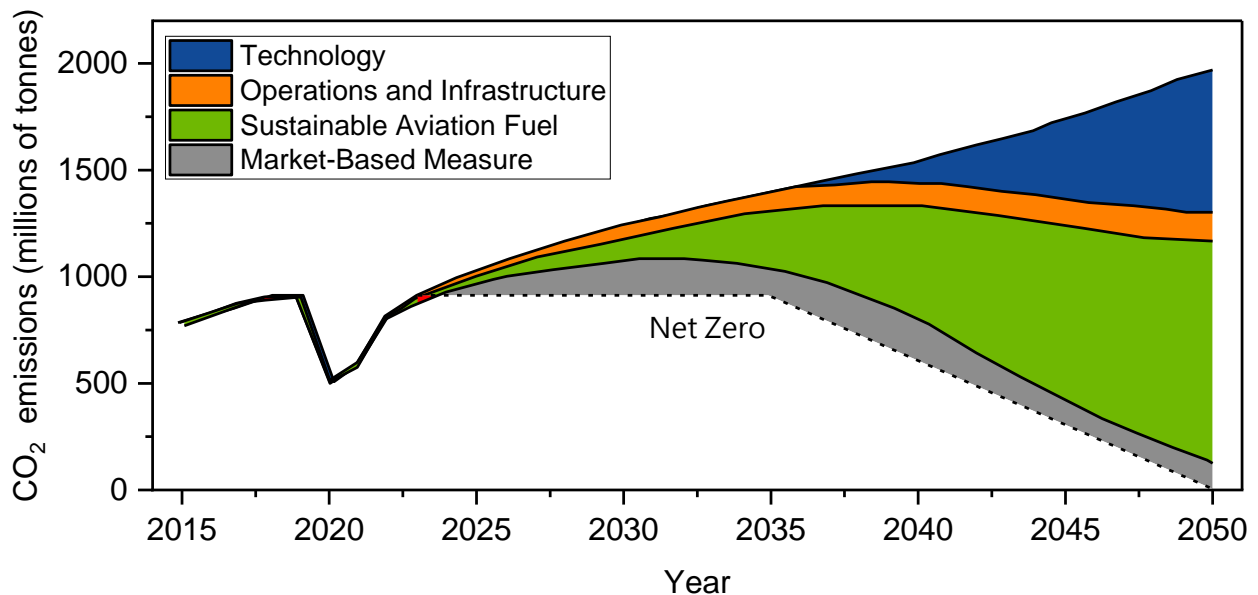


Figure 1.2: The figure is replotted from the Waypoint 2050 document, which illustrates the means to achieve net-zero CO₂ by 2050 [2]. The projected scenario presents rigorous new technology and sustainable aviation fuel development. By the end of 2050, the percentages of each sector's emission reduction contribution are (1) new technologies 34%, (2) operations and infrastructure 7%, (3) sustainable aviation fuels (SAF) 53%, and (4) Market-based measures (carbon offset and capture) 6%.

While SAF can only replace the current jet fuel to achieve a carbon-neutral target, developing new technologies such as hydrogen and electric aircraft can make planes emission-free. However, hydrogen fuel has low energy density, which requires pressurisation, while batteries are heavy. The battery weight needed per passenger for the same flight distance is 24 times greater than the weight of kerosene required per passenger, thus making long-haul electric flights unrealistic. Unlike liquid fuel mass that depletes over time, the battery mass remains the same and is regarded as "parasitic mass", which decreases the efficiency of the vehicle. While adding more batteries increases the range and power, the added mass will also stifle the vehicle's efficiency. To solve this issue, the development of structural power composites (SPC) can revolutionise the transportation sector by enabling all-electric, emission-free vehicles with improved range and power performance.

1.2. Structural Power Composites

1.2.1. Terminologies

A structural power composite is a fibre-reinforced polymer composite which stores energy to function as a power source. Structural power composites is a term that was introduced by Professor Leif E. Asp and Professor Emile S. Greenhalgh in 2014 and was later widely used and reported in this research realm [10].

Structural power composites are widely reported on storing energy using battery and supercapacitor mechanisms. Those energy storage methods have led to the use of specific terms of "structural battery" (SB) and "structural supercapacitor" (SSC) in the research community. The configuration of an SPC consists of six fundamentals: (1) positive electrode, (2) negative electrode, (3) separator, (4) current collecting terminals, (5) electrolyte matrix (6) encapsulator. Representative review papers for SB are referenced as [9, 11, 21, 69, 150, 154], and the review for SSC are referenced as [16, 25, 50, 148, 150, 154].

1.2.2. Structural Power Composites Reduce Mass and Emissions

Standalone battery mass can be reduced when structural power composites (SPC) are integrated into the structure, saving tremendous weight and volume to enable a higher range and payload. The case studies which show the advantages of structural power composites (SPC) are reported in [Figure 1.3](#). For medium-haul aircraft such as the A220-100 and the A320, structural power composites can be integrated as the cabin floor face sheets to power the flight entertainment system or to be integrated into the airframe to reduce emissions [70, 89]. A more ambitious approach to replace the entire airframe of a CityAirbus will result in a 25% overall weight reduction [60]. A demonstration has been performed using the CubeSat structural frames as the SPC, which reduced 30% of the battery mass.

Case Studies	SPC Energy Density Requirements	SPC Power Density Requirements	SPC Mechanical Properties	Improvements	Notes
(A) A220-100 Cabin Floor	>144 Wh/kg	>290 W/kg	E-modulus > 28 GPa Tensile/Compression > 219 MPa	Mass Savings: 261kg (2% max. Payload) CO2 reduction: 280 tonne/year NOx reduction: 1.2 tonne/year	- SPC used as the face sheets of the sandwich panels for the cabin floor to power the regional flight's entertainment system.
(B) A320 [MEA]	>100 Wh/kg	>55 W/kg	--	5.6% fuel efficiency	- 1500km mission - 50% SPC airframe
(C) CityAirbus eVTOL	>74 Wh/kg	>376 W/kg	E-modulus > 54 GPa Tensile/Compression > 203 MPa	25% Weight reduction	- Replacing all the eligible composite mass and batteries with structural power composites
(D) CubeSat	>35Wh/kg	--	E-modulus: 1.8 MPa Tensile Strength: 213 MPa	30% Battery weight reduction	- SPC used as the face sheets of the CubeSat structural frame.

Figure 1.3: Structural Power Composite (SPC) case studies. (A) The cabin floor sandwich panel's face sheets as SPC [89]. (B) SPC is integrated into 50% of the airframe to power the electrified subsystems of the aircraft. [70]. (C) SPC applied to the CityAirbus eVTOL [60]. (D) SPC applied for the CubeSat structural frame [84].

1.2.3. The Encapsulation Methods of Structural Power Composites

In order for structural power composites (SPC) to scale up and achieve their advantages in electrifying transportation, their encapsulation method is vital. SPCs are categorised in this report based on the encapsulation interfaces between the electrode and the encapsulator as (1) electrolyte matrix-fibre interface, (2) pouch bag-fibre interface, (3) metal fibre interface and (4) fibre-fibre interface. The four interfaces are shown in [Figure 1.4](#). Structural power composite (SPC) is one of the subsets of multifunctional composites. Multifunctional composites possess both the capability of energy storage and mechanical strength and can be classified as embedded, conformable and structural [67]. A detailed review of each category is presented in [section 2.1](#).

The electrolyte matrix-fibre encapsulation interface uses insulating fabrics to encapsulate the electrolyte matrix-impregnated structural power composite (SPC). The pouch bag-fibre encapsulation interface uses insulating fabrics to encapsulate the SPC sealed with pouch bags. The metal-fibre encapsulation interface uses insulating fabrics to encapsulate SPCs whose electrodes are metallic substrates instead of fabrics. However, none of the three interfaces mentioned above provides sufficient shear strength with the encapsulator to prevent delamination [50]. Therefore, a novel fibre-fibre interface is studied. The fibre-fibre encapsulation interface uses insulating fabrics to encapsulate fibrous electrodes to enhance interlaminar strength and efficient packaging through continuous structural resin impregnation between the fibrous electrode and the encapsulator interface. This approach allows for conventional composite manufacturing techniques for scale-up and eliminates delamination issues from different thermal expansions.

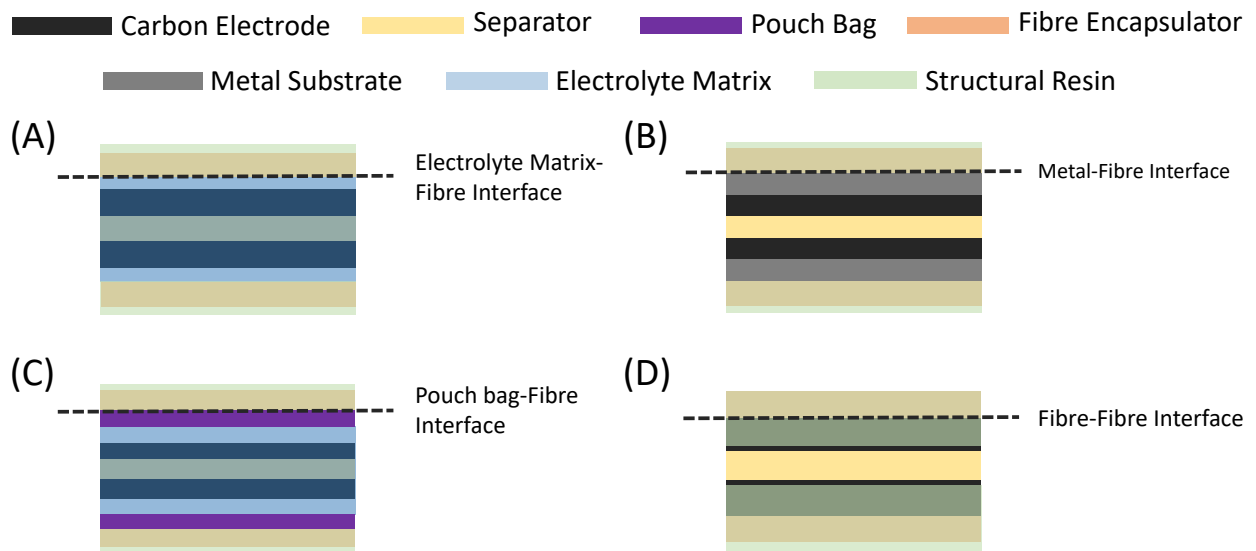


Figure 1.4: Four different interfaces between the electrode and the encapsulator of the structural Power Composite (SPC). (A) Electrolyte matrix-fibre interface (B) Metal-fibre interface (C) Pouch bag-fibre interface (D) Fibre-fibre interface.

1.2.4. Develop Structural Supercapacitor for Structural Power Composite's Early Demonstration

To assess the potential value and advantages of structural power composites (SPCs), it is essential to demonstrate their effectiveness in an appropriate application as soon as possible. While SPCs cannot be the sole energy provider in an electric system in the early stages, they can be integrated with other energy sources. Thus, research on SPC integration within electrical and structural systems is vital.

Structural supercapacitors (SSCs) based on electric double-layer capacitors (EDLCs) are highly suitable for scaling up and demonstrating the potential of SPCs [50, 148]. EDLC is a type of supercapacitor where charges are stored electrostatically on electrodes, a non-Faradic storage mechanism [111]. This physical reaction allows a long service life of durability for EDLCs. In addition, due to the lower volumetric change and less moisture sensitivity compared to batteries, this allows SSCs to increase their size and geometry complexity [50]. The comparison of a supercapacitor with a battery is shown in Figure 1.5 [111]. Despite the advantages of EDLCs, they have lower specific energy compared to batteries. However, their high specific power is well-suited for rapid charge-discharge applications.

Function	Supercapacitor	General lithium-ion battery
Charging time	10 s	Up to 60 min
Cycle life	1 million or 30,000 h	500 or higher
Cell voltage	2.3–2.75 V	3.6 V
Specific energy (Wh kg^{-1})	5 (Typical value)	120–240
Specific power (W kg^{-1})	Up to 10,000	1000–3000
Service life (industrial)	10–15 years	5–10 years
Charge temperature	–40 to 65°C	0–45°C

Figure 1.5: The performance of supercapacitors compared to typical lithium-ion batteries. [111]

1.3. Structural Supercapacitor Challenges

To promote sustainable transport, the design and manufacturing of structural power composites must prioritise scalability and structural supercapacitors based on electric double-layer capacitors are a promising option. The challenges in both research and application aspects as addressed.

1.3.1. Research challenges

There is a lack of research on efficient encapsulation methods with high interlaminar strength and simple manufacturing methods for scale-up [50]. Limitations for scale-up from the process aspect include the requirement of a glovebox for cell assembly and the chemical vapour deposition (CVD) and carbonization chambers for electrodes incorporating carbon aerogel and carbon nanotube materials [50, 51, 100]. The materials used for the structural supercapacitors should also be nonhazardous since the energy storage of structural supercapacitors (SSC) is no longer confined in a protective casing but as a structural element. When SSC fails as a structure, the energy storage chemicals exposed to the environment must be environmentally friendly.

1.3.2. Application challenges

Figure 1.6 shows all the potential applications for structural power composites (SPC) and the desired applications suitable for early demonstration. Red parts indicate transformed structural components in SPCs. Blue regions use the structural embedded method for simple geometries and large areas. Green regions use conformable 3D printing for complex geometries and smaller sizes. Yellow areas, ideal for demonstration, have simple geometries and low proximity to humans. The terms structural embedded and structural conformable SPCs shown in Figure 1.6 are elaborated in subsection 2.1.3 and subsection 2.1.4. It is crucial for early structural power composites (SPC) demonstrations to have a minimum proximity between humans so that a failure will not be harmful. A simple geometry, such as a flat surface, allows simple conventional composite manufacturing methods beneficial for scaling up. Truck trailers (B) and fixed-wing drones (D) are applications suitable for early demonstration. The structural supercapacitor (SSC) used as the truck trailer panels have the potential to capture the energy from regenerative braking to charge the battery and provide power for the trailer's lighting or refrigeration. The SSC integration of fixed-wing drones can be used for reducing the battery current peaks or for short power bursts during manoeuvres.

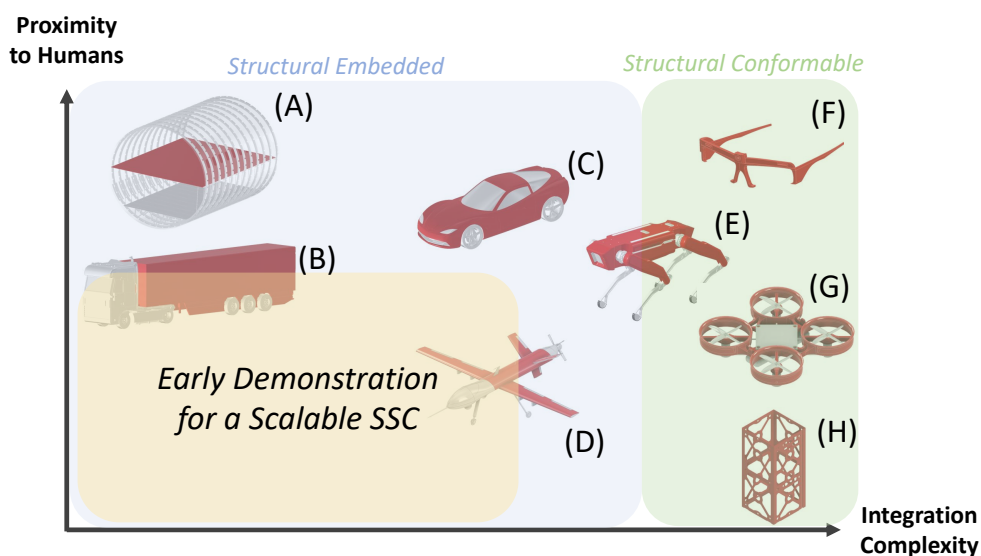


Figure 1.6: Structural Power Composite concepts regarding proximity to humans and integration complexity. Red regions are the integrated structural power composites. (A) Fuselage floor sheet panels (B) Semi-truck trailers (C) Passenger car (D) Fixed-wing drone (E) Robotics (Boston Dynamics Spot) (F) Smart Glasses (Portable electronics) (G) Quad-drone (H) Satellite structure. CAD file sources: [3, 12, 44, 106, 126, 134, 135, 144]

Literature Study

Multifunctional energy storage composites are classified in [section 2.1](#), and the state-of-the-art for each category is presented. The rest of the chapters present the electric double-layer capacitor-based structural supercapacitor's fundamentals: electrode, electrolyte, separator, current collectors and their assembly.

2.1. Categories of Multifunctional Energy Storage Composites

Multifunctional energy storage composites can be classified into three categories shown in [Figure 2.1](#): embedded, conformable and structural.

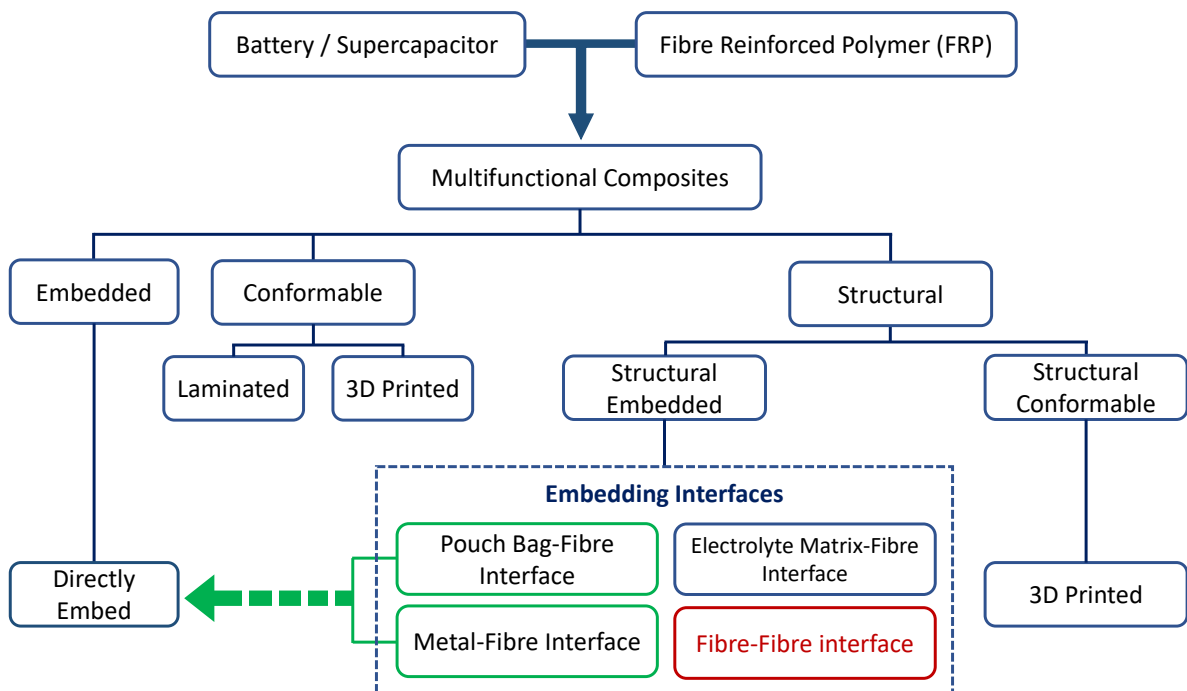


Figure 2.1: The categories of structural power composites configuration. The highlighted red box is the fibre-fibre interface method which is demonstrated in this work. The highlighted green boxes are the encapsulation methods that resemble the direct embed approach that creates potential delamination and low compression strength.

2.1.1. Embedded

The embedded approach means that the pristine battery cell with its insulation sheath included is directly embedded in a fibre-reinforced polymer composite laminate or embedded into a foam core of a sandwich structure. It is reported that the tensile and flexural properties of the structure have little change, and the battery performance showed little degradation. However, the compression strength and modulus dropped significantly [93]. Thomas et al. reported the use of a multifunctional structural LiPo (lithium-ion polymer) battery as the wing of the Wasp micro-air vehicle shown in Figure 2.2 (A) [132]. The structural battery accounts for 57% of the vehicle weight. Galos et al. embedded LiPo batteries into the sandwich foam core and into a fibre laminate to study its bending, acoustic and vibrational behaviours shown in Figure 2.2 (B, C) [41, 42]. Shalouf et al. embedded LiPo batteries as the core of sandwich structures with carbon fibre-reinforced polymer (CFRP) face sheets shown in Figure 2.2 (D) [116]. The tensile, compression and flexural behaviours are studied.

Galos et al. conducted three-point bending tests of LiPo battery-embedded sandwich panels [41]. It is observed that the cracking of the sandwich panel will occur at the core/battery interface due to the local stress concentration induced by the different stiffness of the battery and the foam core. The battery performance (internal resistance, charge/discharge and capacity) are reported to be unaltered during bending, foam core failure and battery deformation.

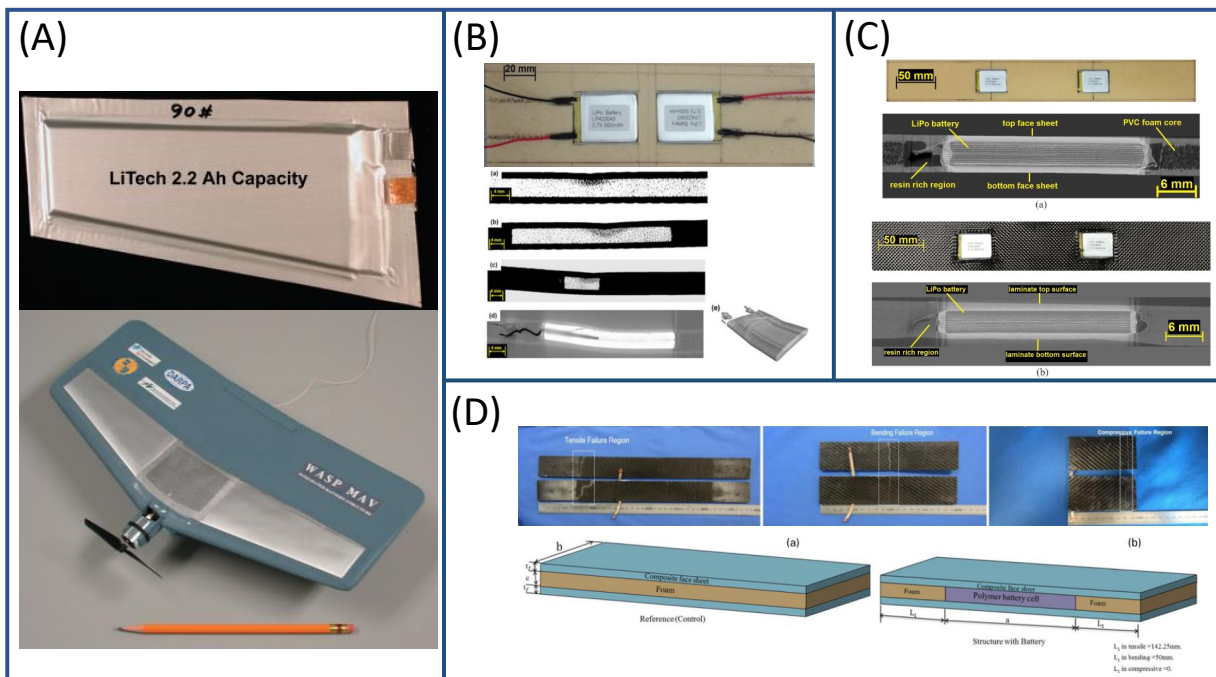


Figure 2.2: Embedded approach of multifunctional composites. (A) LiPo batteries as the fixed wing for a drone [132]. (B) LiPo batteries embedded into the sandwich foam core to conduct flexural tests [41]. (C) LiPo batteries are embedded into the sandwich foam core (top) and laminate layer (bottom) to conduct vibration and acoustic tests [42]. (D) LiPo batteries are embedded into the sandwich foam core for tension, compression and flexural tests [116].

Shalouf et al. reported the mechanical testing result shown in Figure 2.3 that the tensile and flexural strength of a sandwich panel with and without LiPo battery embedded remained the same, while the flexural modulus decreased [116]. The compression strength is reported to decrease to half compared to the full foam core sandwich due to the poor lateral stiffness that originated from the lack of mechanical connection in the battery layers. On the other hand, the battery capacity decreased for all tensile, compression and bending tests, while the bending test had the lowest decrease. Although embedding batteries in composite laminate and sandwich structure degrades compression properties, the system only provides volume savings but not mass savings. The discontinuity of material properties in the structure also creates issues such as poor lateral stiffness and interlaminar strength.

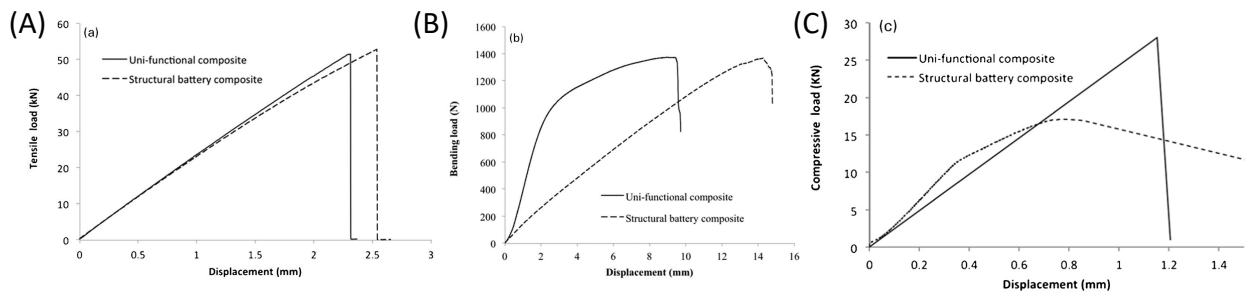


Figure 2.3: Mechanical tests of the LiPo battery embedded in sandwich core [116]. (A) Tensile test. (B) Three-point bending test (C) Compression test.

2.1.2. Conformable

Conformable means that the multifunctional composite is able to adapt its volume or shape for the desired surface and boundaries. However, this results in a low stiffness which cannot be used as structures. Conformable energy storage devices can be fabricated using lamination and 3D printing.

Laminated

Laminated flexible batteries and supercapacitors realise their flexibility with the use of flexible electrodes such as carbon film/fibres, paper, or other textiles [90, 141]. Those flexible electrodes are impregnated with gel or ionic electrolytes. Instead of laminating full sheets of electrodes and separators. Another approach is to laminate fibre bundles into a woven fabric with energy storage, flexibility and stability shown in Figure 2.4 [117]. These supercapacitor fibre bundle electrodes are activated to increase surface area and are impregnated with a solid electrolyte.

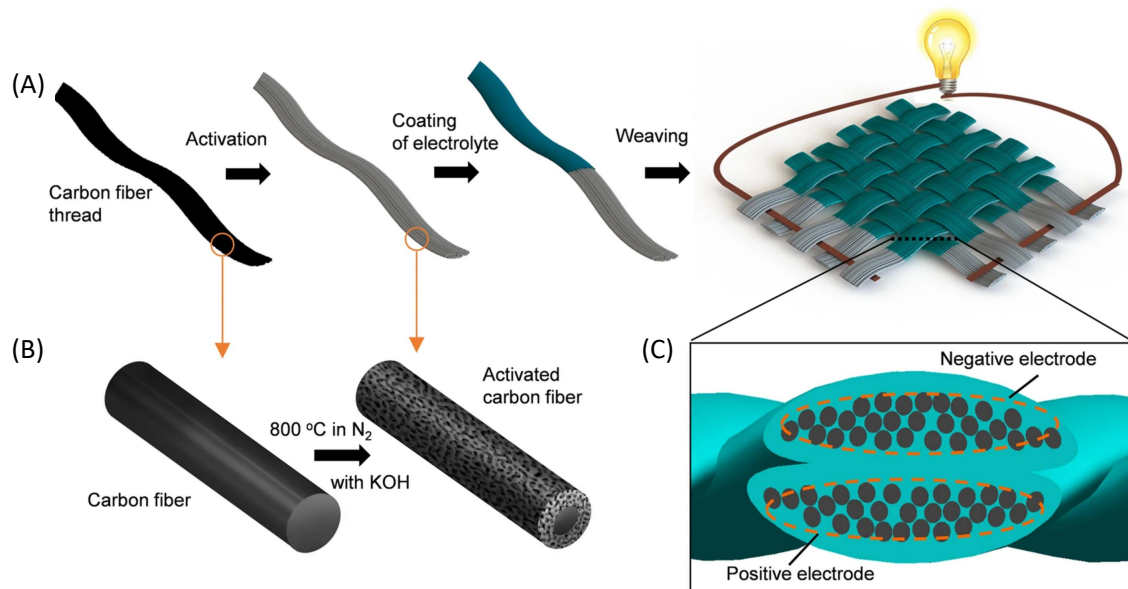


Figure 2.4: A woven flexible supercapacitor that uses fibre bundles as electrodes which are impregnated with a solid electrolyte [117].

3D-printed

3D-printed batteries/supercapacitor has the advantage of printing complex geometries and creating more surface area for more power and capacity. Battery modulus has been printed using direct ink writing (DIW), fused deposition modelling (FDM), ink-jet printing (IJP) and stereolithography (SLA) processes. Among these processes, DIW is the most popular process to print electrodes due to its capability of a wide range of printable materials, high resolution and multi-material printing [79]. The electrolyte is then filled between the electrodes using a sol-gel process. Figure 2.5 shows the common materials and the printing methods for batteries.

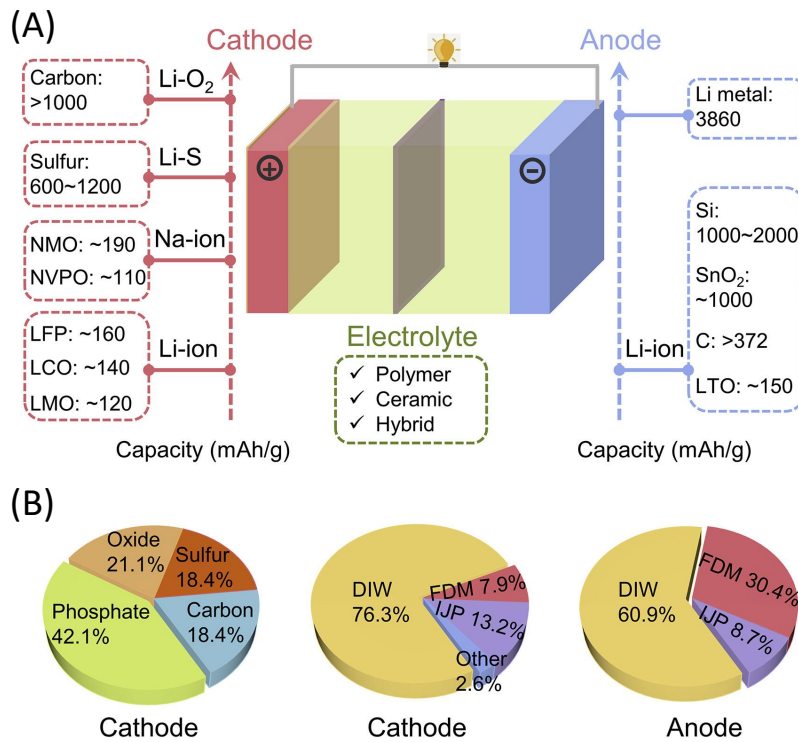


Figure 2.5: 3D-printed battery materials and procedures. [79]. (A) 3D-printed battery materials. (B) The popularity of 3D printing processes for cathode and anode based on the number of reviews.

Abey et al. printed degradable, nontoxic supercapacitors using direct ink writing (DIW) in a sandwich configuration shown in Figure 2.6 [1]. A gel polymer layer is printed between the electrodes as the electrolyte and the separator, which can withstand pressure up to 200 kPa (finger-pinching pressure). However, a long process of drying the solvent from the electrodes takes seven days to avoid cracks and delamination of the layers.

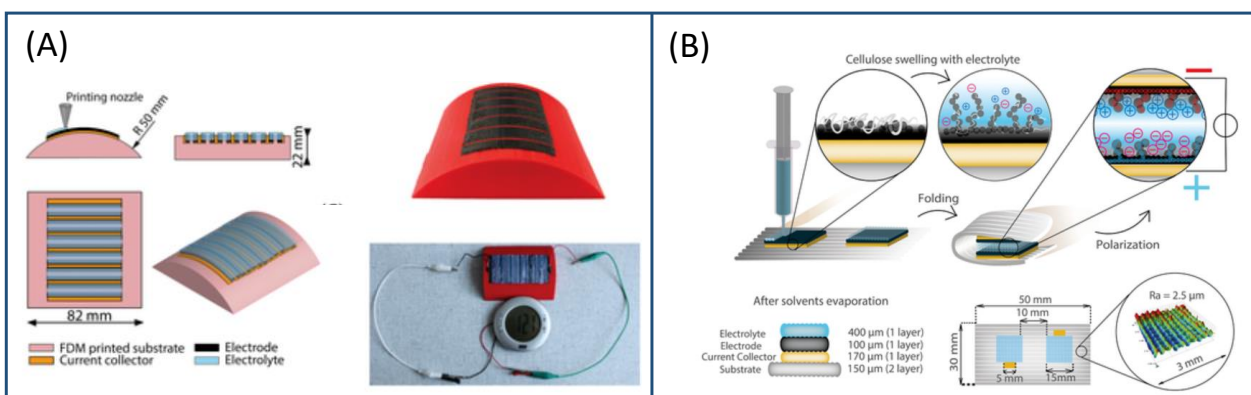


Figure 2.6: (A) Direct ink writing of disposable paper supercapacitors on a curved surface. (B) Illustration of the supercapacitor printing process and layers. [1]

2.1.3. Structural Embedded

Structural embedded is a terminology equivalent to structural power composite (SPC) that includes the study of structural batteries (SB) and structural supercapacitors (SSC). Structural embedded configurations showing its fundamentals are shown in Figure 2.7 [85]. However, the configurations shown do not include the encapsulator. At the final stage of assembly, the device has to be encapsulated with several electrical and chemical insulation fabric layers, which are infused with a structural resin which also provides mechanical strength. This assembly configuration is similar to the embedded; therefore, this category is named structural embedded.

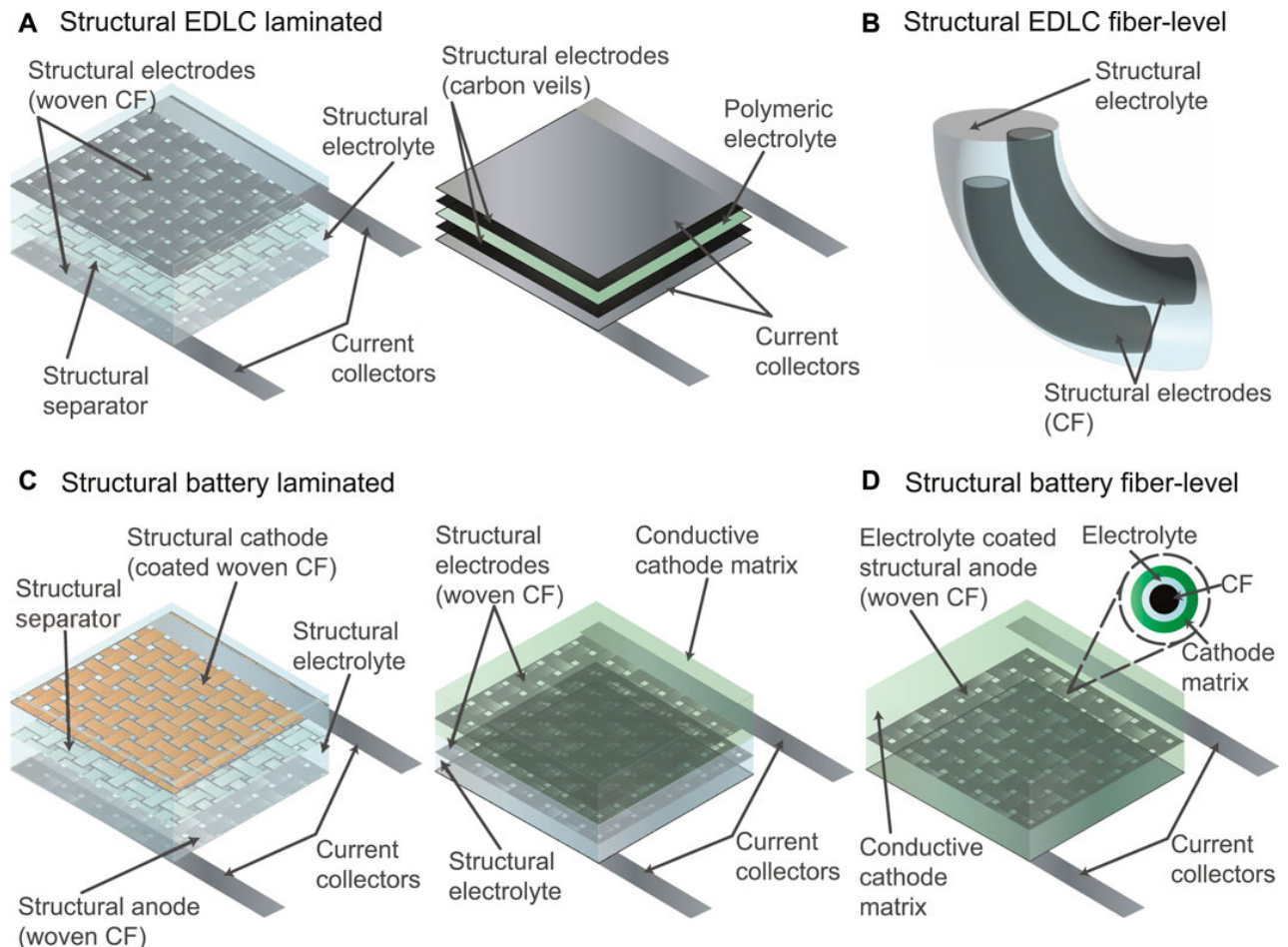


Figure 2.7: Different SPC configurations showing their constituents without the encapsulating encapsulator [85].

The structural embedded method can be further categorised depending on the interfaces between the energy storage device and the encapsulation layer as (A) electrolyte matrix-fibre interface, (B) pouch bag-fibre interface, (C) metal-fibre interface, (D) fibre-fibre interface. The assembly diagrams of (A) to (D) are shown in Figure 2.8. The demonstrations of (A) to (D) are shown in Figure 2.9.

Electrolyte Matrix-Fibre Interface

The electrolyte matrix-fibre interface is shown in Figure 2.8 (A). The fabric electrodes are grafted or deposited with carbon nanoparticles. An insulating layer such as glass or aramid fibre (A)-1 separates the electrodes. This dry laminate is then infused with an electrolyte matrix, a blend of a structural resin, plasticizer and ionic salt (A)-2. Recent representative works presented by Greenhalgh, Javaid, Ding, Pernice and Moyer et al. are shown in Figure 2.9 (A) [29, 49, 64, 66, 84, 94]. Most of the research stopped at step (A)-2 to focus

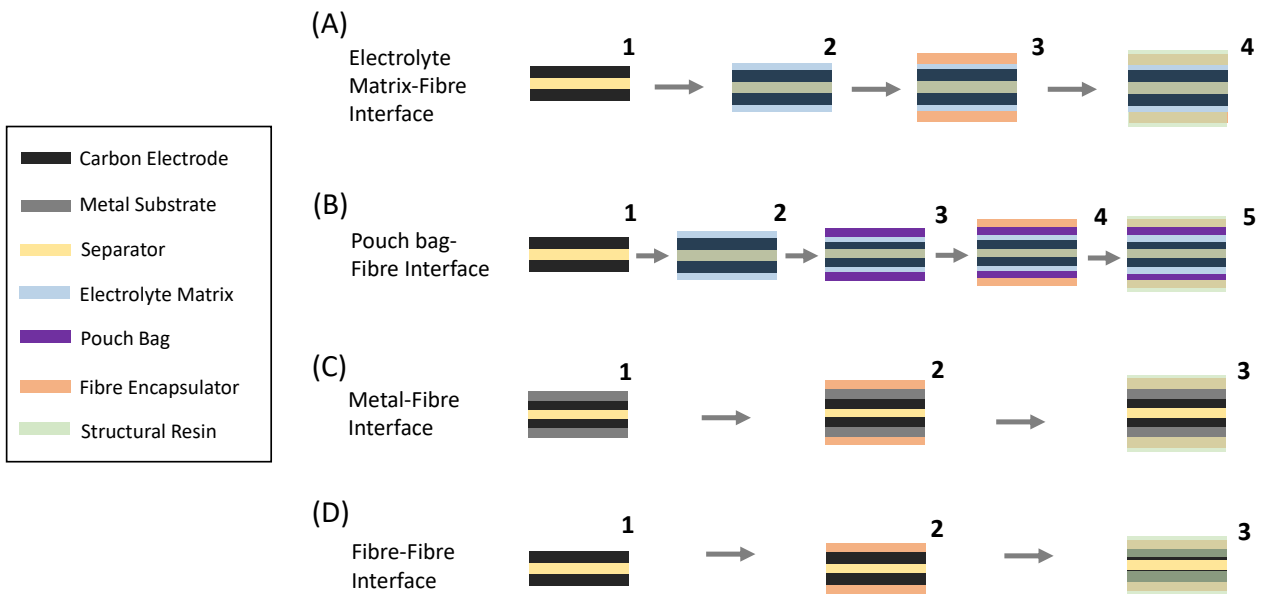


Figure 2.8: The assembly diagram of the four embedding interfaces of the structural embedded. The coloured legend indicates the SPC components (A) The processing steps of the electrolyte matrix-fibre interface. (B) The processing steps of the pouch bag-fibre interface. (C) The processing steps of the metal-fibre interface. (D) The processing steps of the fibre-fibre interface.

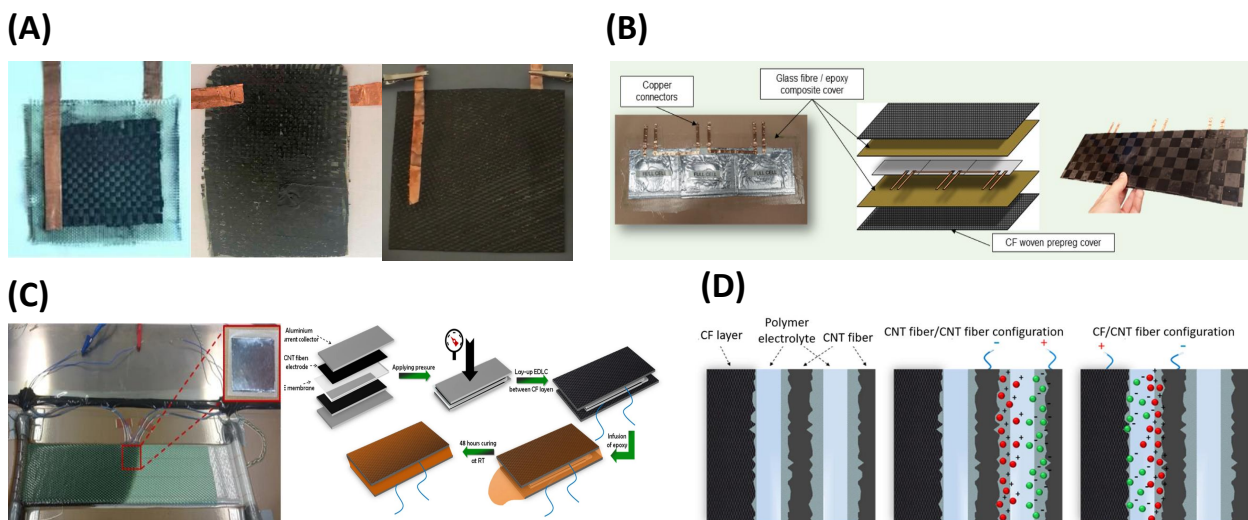


Figure 2.9: The demonstration of the four interfaces of the structural embedded method. (A) The electrolyte matrix-fibre interface demonstration [29, 127, 128]. (B) The pouch bag-fibre interface demonstration [146]. (C) The metal-fibre interface demonstration [114]. (D) The fibre-fibre interface demonstration [114].

on the electrode and electrolyte matrix development. However, the device needs to be further encapsulated since the electrolyte matrix can be contaminated. The electrolyte matrix can be insulated by layers of glass fabric impregnated with epoxy by steps (A)-3 to (A)-4, providing electrical insulation and mechanical strength. However, the encapsulator will decrease the specific properties of the reported structural power composite. Besides the increased weight, Greenhalgh et al. reported that the infused epoxy for encapsulation might leach out the ionic liquid in the electrolyte matrix, causing a significant drop in energy storage performance [50].

Pouch Bag-Fibre Interface

The pouch bag-fibre interface configuration in [Figure 2.8 \(B\)](#) seals the structural power composite (SPC) shown in (B)-2 in a pouch bag to prevent contamination of the ambient environment (B)-3. Afterwards, the pouch bag is laminated by fabrics in (B)-4 and infused with structural resin in (B)-5. Using a pouch bag for encapsulation increases the technology readiness level (TRL) since the reaction between the matrix electrolyte and the structural resin can be neglected. Examples of the SPC being sealed in a pouch are demonstrated by the research group of Asp and Greenhalgh shown in [Figure 2.9 \(B\)](#) [8, 15, 48, 98, 146]. However, sealing SPCs in a pouch bag creates poor interlaminar strength between the SPC-pouch bag interface and the pouch bag-encapsulator interface [50]. The results of the large panel testing might align with the directly embedded approach, in which compressive strength is decreased due to delamination [116]. Since the pouch bag-fibre interface is similar to the embedded method, this configuration also allows using liquid electrolytes. Dong et al. injected a liquid electrolyte into a PET membrane-wrapped battery configuration and embedded multiple pouch cells into carbon fibre prepregs [30]. The gaps between the pouch cells are stiffened with a carbon fibre stiffening beam to improve the bending and compression strength. A high specific energy of 90 Wh/kg is reported.

Metal-Fibre Interface

The metal fibre interface in [Figure 2.8 \(C\)](#) is a method that deposits electrode materials on metal substrates (C)-1. The metal substrates are the current collectors, which are thin (20µm used by Wang et al.[139]) and have little mechanical strength. The substrates are then separated by a gel polymer membrane which is both the electrolyte and separator. The sandwich is then encapsulated with epoxy-infused fabric layers (C)-2 (C)-3, resulting in a fibre metal laminate. The benefit of a metal fibre interface is that no infusion or wet layup of the electrolyte matrix is needed for the whole device. The electrolyte materials can be confined between the electrodes. Using a metal substrate may also increase the energy storage properties since the metal substrate is a current collector which is highly conductive and continuous. If carbon fabrics are used for encapsulation, an external short circuit might occur, which needs to be further insulated unless glass or aramid fabrics are used. Since the gel polymer electrolyte is a very soft material with low strength, it is reported to act as a delamination which can be strengthened by epoxy interlocking using grid interleaves [114]. The fibre-metal configuration has been demonstrated by Wang, Senokos, Lekakou et al. shown in [Figure 2.9 \(C\)](#) [74, 114, 115, 139].

Fibre-Fibre Interface

The fibre-fibre interface in [Figure 2.8 \(D\)](#) uses conductive fabric as electrodes. They are separated by a polymer electrolyte membrane or an insulating fabric as a separator (D)-1. The difference between the metal-fibre interface is that the fibre-fibre interface configuration replaces the metal substrates with fabric electrodes. The laminate is then encapsulated with additional fabric layers (D)-3 and infused with structural resin (D)-4. The benefit of this configuration is that the structural resin is continuous between the fabric electrodes and the encapsulating layers. Like the metal-fibre interface, the electrolyte can also be confined between the electrodes. As a result, interlaminar shear strength between the electrode and the electrolyte may be higher compared to the other three interfaces. The overall weight may also be the lowest due to efficient packaging. However, the structural resin impregnated in the fabric electrode may significantly decrease energy storage. Therefore, there is a need to design an SPC with a fibre-fibre interface to examine its encapsulation effect.

Senokos et al. have briefly demonstrated a fibre-fibre interface using a carbon fibre electrode and a carbon nanotube fibre electrode as a structural supercapacitor (SSC) shown in [Figure 2.9 \(D\)](#). The energy storage performance is reported to be lower than using two carbon nanotube fibre electrodes [114]. Pandey et al. produced a pseudocapacitor-based SSC having a fibre-fibre interface [91]. The electrodes coated with graphene and grown with metal oxides are further coated with polyacrylamide (PAM) gel electrolyte and is separated by a glass fabric layer. The device is then directly encapsulated with epoxy-impregnated carbon fabrics.

2.1.4. Structural Conformable

Structural conformable is a structural power composite that is manufactured using 3D printing. This emerging research project, PRINTCAP, has been initiated by the collaboration of Thales SA, Technische Universität Dresden (TUD), Hochschule für Technik Wirtschaft und Kultur Leipzig (HTWK Leipzig) and NAWA Technologies in 2022. The design is to achieve a sandwich configuration as shown in Figure 2.10 [129]. Carbon nanotube-deposited continuous carbon fibre as electrodes and separators are printed in layers. However, the encapsulation method of the 3D-printed structural power composites also needs to be considered for safety. A final insulating layer must also be printed around the final product.

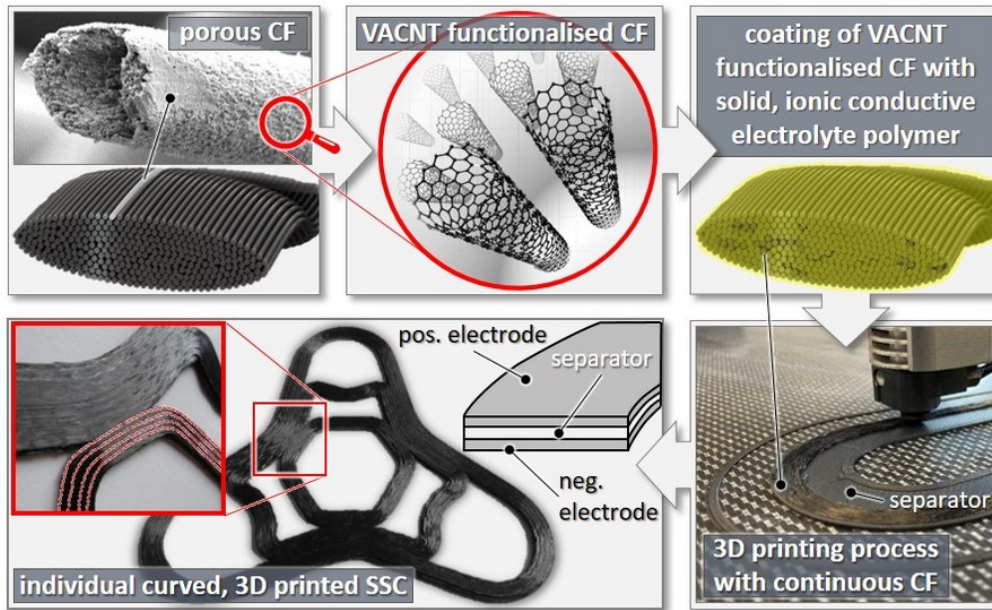


Figure 2.10: PRINTCAP concept design [129].

2.2. Electrodes

2.2.1. A porous electrode surface is desired for a high surface area

The performance of an electric double-layer capacitor (EDLC) electrode critically depends on its conductivity and porosity, which enable a high surface area when deposited onto conductive substrates. Capacitance (C) and energy storage (E) of a capacitor are governed by Equation 2.1 and Equation 2.2, respectively. These equations reveal that surface area A positively correlates with capacitance and energy storage. Here, ϵ_0 represents the dielectric constant of the free space (vacuum), which is approximately equivalent to $\epsilon = \epsilon_0 \cong 8.85 \times 10^{-12}$ F/m. In addition, ϵ_r denotes the relative dielectric constant of the material while v represents the applied voltage.

It is noteworthy, however, that the surface area A measured from the Brunauer-Emmett-Teller (BET) surface area analysis does not reflect the contact area of the electrode and the electrolyte. The surface morphology and wettability of the electrode also significantly influence the contact area, thereby influencing the overall performance of the EDLC electrode.

$$C = \frac{\epsilon A}{d} = \frac{\epsilon_0 \epsilon_r A}{d} \quad (2.1)$$

$$E = \frac{1}{2} C v^2 \quad (2.2)$$

2.2.2. Carbon-Based Electrode Materials and Fabrication Methods

Carbon fibres have been identified as a viable electrode material for supercapacitors due to their favourable mechanical and electrical conductivity properties. However, their low surface area ($0.21 \text{ m}^2/\text{g}$) poses challenges to their use in supercapacitors [99]. Various techniques have been proposed to enhance the electrochemically active surface area of carbon fibre electrodes while preserving or improving their mechanical properties.

Activation of Carbon Fibres

The term "activation" refers to physical or chemical processes that can remove pyrolysis products or burn off carbon to increase the specific carbon fibre area while maintaining its mechanical strength. To investigate this, Qian et al. examined various physical and chemical activation methods for plain weave carbon fabric shown in Figure 2.11 [99]. Physical activation using air and CO_2 caused a decrease in the fabric's tensile strength. However, using the incipient wetness method (KOH1 in Figure 2.11) led to a more than 100-fold increase in specific surface area with only a slight improvement in tensile stress. The incipient wetness process soaks the samples of various KOH concentrations for three hours, followed by drying and activation under pure nitrogen at 800°C for 30 minutes. The authors attributed this improvement to the removal of surface defects on the fibre through low and uniform burn-off. These findings suggest that the incipient wetness method may be a promising approach for carbon fibre activation in various applications. The SEM images of activated fibre surfaces are shown in Figure 2.12.

	Specific surface area (m^2/g)	Tensile strength (MPa)
As-received	0.21	3300 ± 200
HNO_3	0.50	3100 ± 260
Air	0.60	1900 ± 220
CO_2	1.10	2400 ± 250
KOH1	23.3	3600 ± 160
KOH2	0.90	2600 ± 320

Figure 2.11: The specific surface area and the single fibre tensile strength of different activation methods. [99]

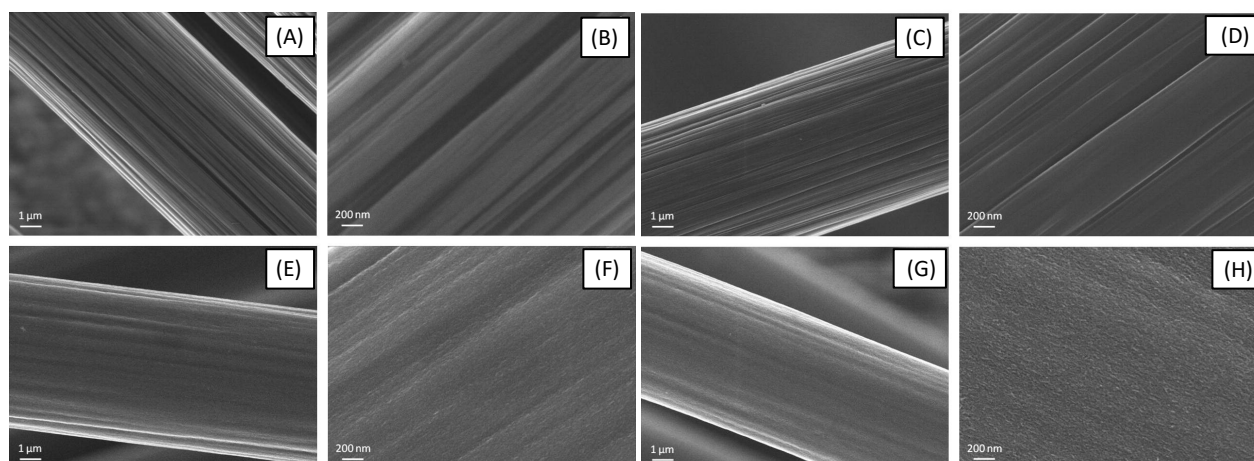


Figure 2.12: (A) and (B): As-received fibre surface. (C) and (D): Heat-treated fibre surfaces. (E) and (F): KOH-activated carbon fibres (incipient wetness, burn-off of 6.8%). (G) and (H) KOH activated carbon fibres (impregnation, burn-off of 14.9%) [99]

Activated Carbon

Activated carbon is a preferred material for supercapacitor electrodes due to its high specific surface area (1000-2000 m^2/g), low cost and chemical stability [112][29]. In a study by Ding et al., a viscous slurry paste composed of activated carbon, carbon black, and polytetrafluoroethylene (PTFE) was prepared and applied onto carbon fabrics with varying weight ratios [29]. As the activated carbon weight percentage increases, the specific surface area increases, with the highest value of $162.77 m^2/g$ reported. Figure 2.13 (A) illustrates the specific surface area of activated carbon at varying weight ratios, and Figure 2.13 (B) shows the galvanostatic charge-discharge (GCD) test and Ragone plots that were affected by the different activated carbon loadings. Activated carbon-coated carbon fibre electrodes are also depicted in Figure 2.13 (C). To fabricate structural supercapacitors with a metal-fibre interface, depositing activated carbon-based slurry paste on metal current collectors is performed by Wang et al. [139].

(A)

electrode	desized WCF	desized WCF/AC4	desized WCF/AC9	desized WCF/AC11	desized WCF/AC13	desized WCF/AC15
SSA (m^2/g)	12.74	22.73	99.93	132.12	149.32	162.77

(B)

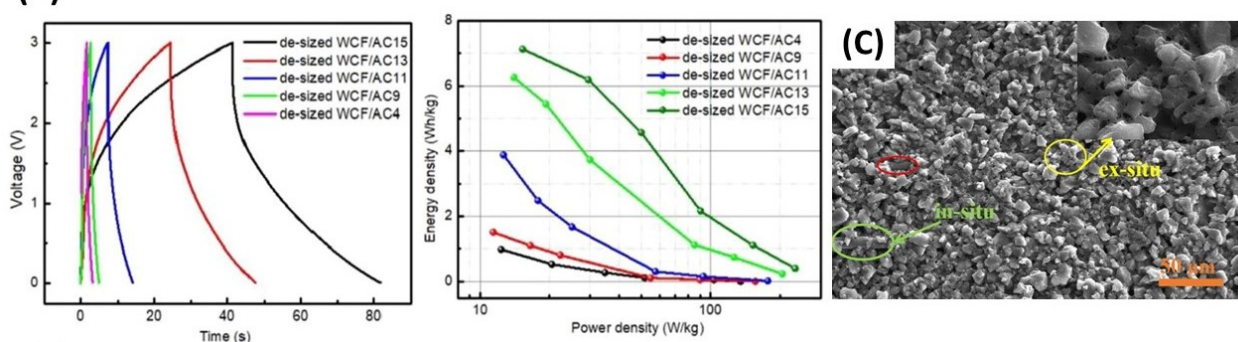


Figure 2.13: (A) Brunauer-Emmett-Teller (BET) Specific surface area of different weight ratios of the coated activated carbon. (B) The different activated carbon loading affects the galvanostatic charge-discharge (GCD) test (left) and the Ragone plots (right). (C) Activated carbon-coated carbon fibre electrodes.

Carbon Nanotubes

Various techniques have been employed to attach CNTs to carbon fabrics to increase their surface area, including sizing, grafting, and infiltration. In the sizing method, CNTs are dispersed into a surfactant solution, and the carbon fabric is immersed in the solution before undergoing pyrolysis. Alternatively, grafting involves growing CNTs on a catalyst-treated fabric via chemical vapour deposition (CVD). Lastly, the infiltration approach uses a vacuum source to impregnate carbon fabrics with a solution of negatively charged carbon nanotubides. These various methods have shown promise for improving the specific surface area of electrode materials in supercapacitors.

Qian et al. compared the specific surface area and electrode-specific capacitance of carbon nanotube (CNT)-sized and CNT-grafted carbon fibres [51]. Figure 2.14 shows the scanning electron microscope (SEM) images of sized and grafted carbon fibres. Also, their specific surface area and capacitance. Results showed that both techniques increased specific surface area and capacitance compared to as-received carbon fabrics and KOH activation. Senokos et al. introduced four types of single-walled carbon nanotubes (SWCNT) on the spread tow carbon fabrics using vacuum infiltration [113]. The process is shown in Figure 2.15 (A), and the scanning electron microscope images of different types of SWCNT are shown in Figure 2.15 (B). The highest specific surface area (SSA) shown in Figure 2.15 is $196 m^2/g$ from Supergrowth SWCNT. The SWCNT (Tuball) infiltrated spread tow carbon fabrics showed little change of tensile strength and modulus, while there is an overall improvement in in-plane shear properties of different kinds of SWCNT.

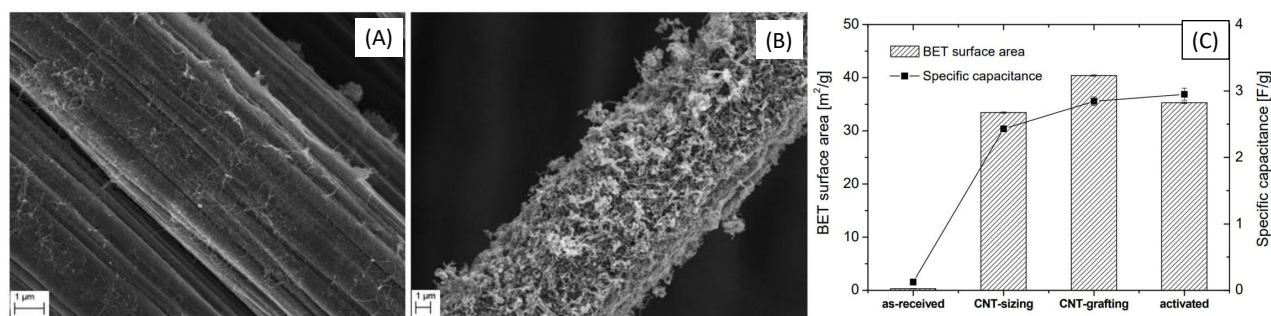


Figure 2.14: (A): SEM image of CNT sizing. (B): SEM image of CNT grafting. (C): BET surface and specific capacity comparison [51].

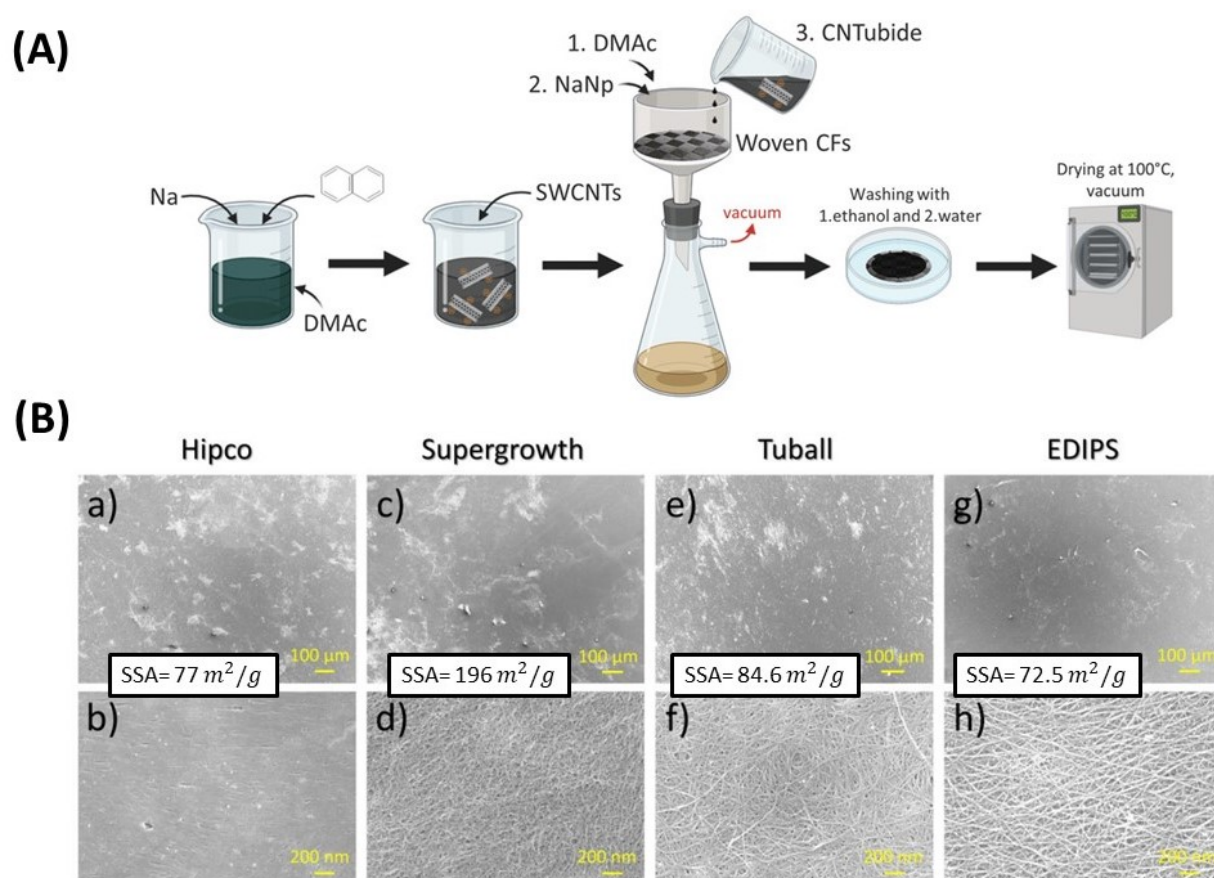


Figure 2.15: (A) CNT infiltration process illustration (B) The SEM images of different types of infiltrated single-walled carbon nanotubes (SWCNT) [113]. The specific surface area (SSA) values are provided for each type of SWCNT.

Carbon nanotubes (CNTs) can be used to produce a metal-fibre interface-based structural supercapacitor by depositing them on metal substrates. Senokos et al. grew CNTs on aluminium substrates using a floating catalyst chemical vapour deposition method [114]. The high contact area between the CNTs and the aluminium collector leads to a high energy density (37 mWh/kg) and power density (30 W/kg).

Graphene Nanoplatelets

Graphene nanoplatelets (GNPs) are nanoscale platelet-like particles made of graphene, a two-dimensional material consisting of a single layer of carbon atoms arranged in a hexagonal lattice. Its high surface area is beneficial for high-energy storage. The methods to deposit GNPs are spraying, brushing and electrophoretic deposition (EPD).

Xoan et al. employed a spray-coating method to increase the surface area of woven carbon fibres (WCF) using graphene nanoplatelets (GNPs) [128]. However, using a surfactant while preparing the GNP solution, without adding a binder, resulted in poor attachment of GNPs to the fabric after matrix infusion. This caused a dragging effect, as depicted in Figure 2.16 (A) and (B), which led to the reaggregation of GNPs and the formation of GNP-rich areas. This resulted in reduced interfacial adhesion and low mechanical properties. Artigas-Arnaudas et al. also spray-coated a GNP solution on carbon fibre fabrics which contains a polyvinylidene fluoride (PVDF) binder shown in Figure 2.16 (C) and (D) [6]. A Brunauer-Emmett-Teller surface area of $4.72 \text{ (m}^2/\text{g)}$ is reported.

Apart from spraying, brushing Graphene nanoplatelets (GNPs) paste onto fabric is a quick and low-cost way. Javaid et al. produced a GNP ink mixed with the uncured polymer electrolyte, brushed onto the carbon fibre fabrics as electrodes [66]. Those electrodes are used to sandwich a filter paper separator and then infused with polymer electrolyte to form a structural supercapacitor cell.

Hubert and Pandey et al. have demonstrated electrophoretic deposition (EPD) to produce high surface area carbon fibre electrodes [54, 91]. The EPD process involves the deposition of GNP under an electric field shown in Figure 2.16 (E) [54]. GNPs are charged negatively due to oxygen-containing functional groups on their surface. A GNP suspension is prepared in an aqueous base solvent. Carbon fibre spread tows are then continuously immersed in the suspension. A direct current (DC) electric field is applied between the carbon fibre spread tow and the graphite paper counter electrode. The electric field draws negatively charged GNPs to the positively charged carbon fibres, resulting in their deposition on the carbon fibre surface. Deposition time and the applied voltage are studied, and it is reported that a three-minute EPD at 30 volts can obtain a surface area of $193 \text{ (m}^2/\text{g)}$.

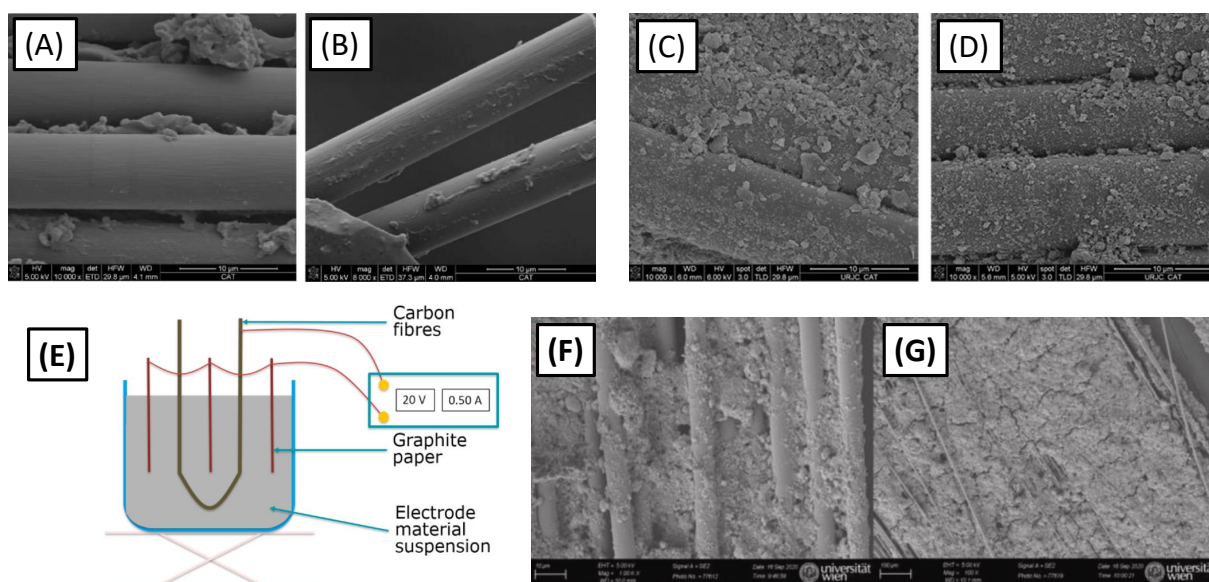


Figure 2.16: (A) and (B) are the images of fracture surfaces of carbon fibre which show unevenly distributed GNPs and aggregation [128] (C) Spray-coating GNP particles ($500 \text{ m}^2/\text{g}$ specific area) on carbon fibres. A BET-specific surface area of $2.29 \text{ m}^2/\text{g}$ is obtained [6]. (D) Spray-coating GNP particles ($750 \text{ m}^2/\text{g}$ specific area) on carbon fibres. A BET-specific surface area of $4.72 \text{ m}^2/\text{g}$ is obtained [6]. (E) The electrophoretic deposition (EPD) setup [54]. (F) The EPD of graphene nanoplatelets on spread tow fabrics using an applied voltage of 10V and a 3-minute deposition time [54]. (G) The EPD of graphene nanoplatelets on spread tow fabrics using an applied voltage of 20V and a 3-minute deposition time [54] A BET-specific surface area of $191 \text{ (m}^2/\text{g)}$ is reported.

Reduced Graphene Oxide

Reduced graphene oxide (rGO) is a derivative of graphene synthesised from graphene oxide (GO). Ogata et al. [22] developed an all-graphene oxide supercapacitor device with rGO as the electrode and GO as the separator, achieving a layup of rGO/GO/rGO. Given its desirable ionic conductivity and insulating properties, GO can be simultaneously used as a separator and a solid electrolyte. Despite rGO's suitability as an electrode material for supercapacitors due to its high surface area and electrical conductivity, it has not been used to develop structural supercapacitors.

Carbon Aerogel

Carbon aerogel (CAG) is a unique material that comprises a 3D network of interconnected nanometer-sized carbon particles that form a highly porous structure with a diameter ranging from 7 to 10 nm [75]. It is a widely-reported electrode material for supercapacitors and structural supercapacitors. Resorcinol and formaldehyde are the most commonly used precursors for synthesising CAG for structural supercapacitors. The CAG synthesis process involves three key stages: (1) sol-gel, where the precursors are mixed together with a catalyst to form a gel, (2) drying, where the solvent is removed to create a solid aerogel; and (3) carbonization, where the aerogel is heated to a high temperature in an inert atmosphere to produce a carbon aerogel with the desired porosity and conductivity. A diagram of the three processes is shown in Figure 2.17.

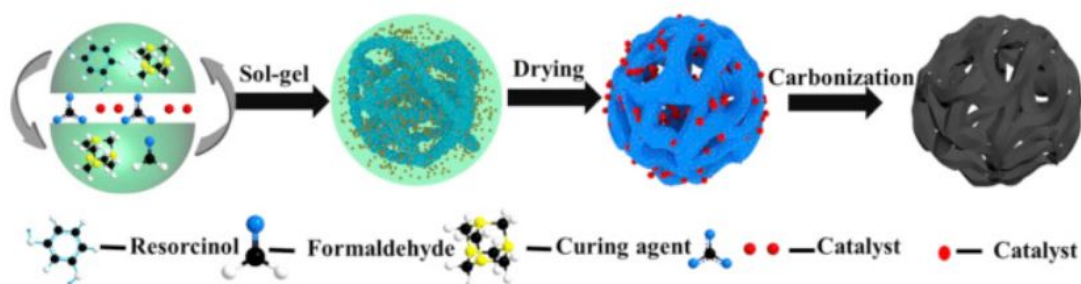


Figure 2.17: The sol-gel, supercritical drying and carbonization process to obtain carbon aerogels [75].

Qian et al. coated carbon aerogel (CAG) on carbon fibres to increase the surface area of electrodes by the pressing and infusion methods [100]. For the pressing method, the carbon fibre fabrics were soaked in the resorcinol-formaldehyde (RF) solution and then pressed between two glass plates. Resin infusion under Flexible Tooling (RIFT) impregnates the RF solution mixture into the fabric. The impregnated fabrics are dried at different temperatures and then pyrolyzed in a furnace at 800°C for 30 min under N_2 . The CAG-coated fibres are shown in Figure 2.18. A Brunauer–Emmett–Teller (BET) surface area of 163.1 (m^2/g) and 118 (m^2/g) are obtained for the pressing and infusion methods, respectively. Artigas-Arnaudas et al. also used the pressing method to obtain a BET surface area of 54.61 (m^2/g) [6].

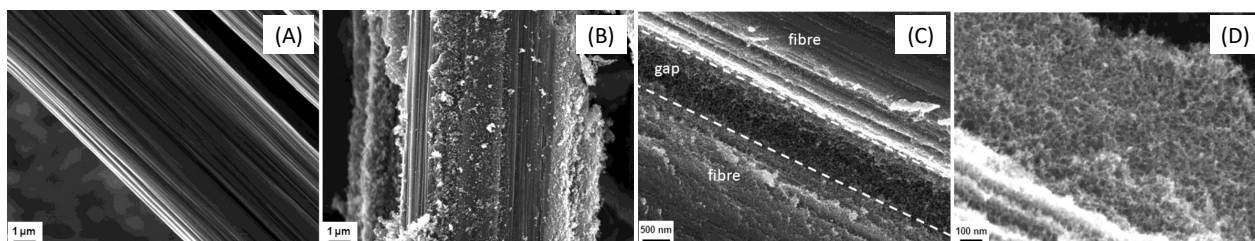


Figure 2.18: SEM images of (A) As-received carbon fibre (CF) with surface crenulations. (B) Uniformly coated carbon aerogel (CAG) on CF surface. (C) CAG with interconnected pore structures filled between CF (D) Closer image of the CAG's porous structure [100].

Carbon aerogel (CAG) can also be mixed with graphene nanoplatelets (GNP) and carbon nanotubes (CNT) to enhance its surface area further. Artigas-Arnaudas et al. dispersed 1 wt% multi-walled carbon nanotubes in resorcinol-formaldehyde (RF) solution, graphene nanoplatelets 3 wt% in RF solution, and produced carbon aerogel mixed with GNP and CNT shown in Figure 2.19 (C to F). [6]. Carbon fabric is then soaked into the solution, dried and carbonised to produce carbon aerogel mixed with CNT and GNP. It is reported that the specific area and the electrode-specific capacitance increased with the GNP and CNT additives compared to the standalone CAG. However, the fibre strength decreased with the introduction of the CAG due to the oxidation effect during the pyrolysis process at high temperatures. Javid et al. used the same soaking approach but a higher 5wt% GNP in the RF solution shown in Figure 2.19 (A) and (B), which obtained a high surface area of $223 \text{ m}^2/\text{g}$ [64].

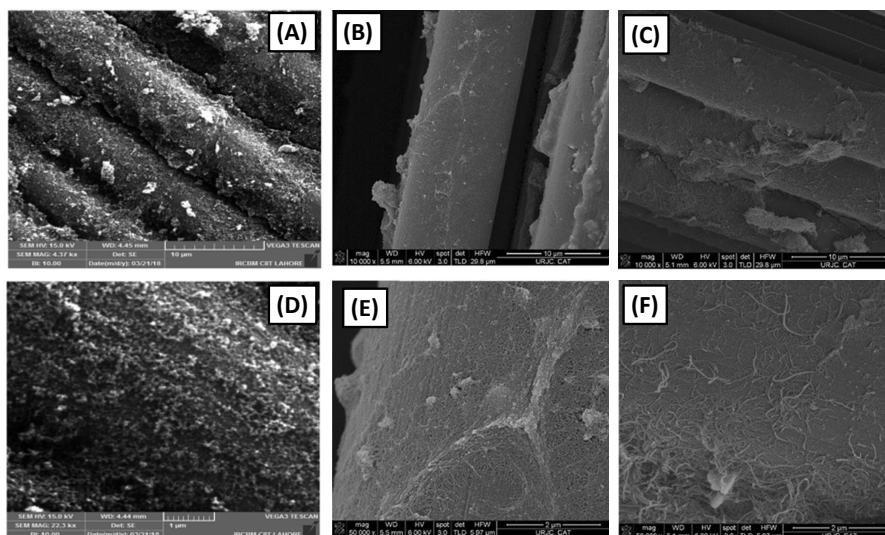


Figure 2.19: SEM images. (A) and (D) Carbon aerogel (CAG) mixed with 5wt% GNP coated on carbon fibres (CF) [64]. (B) and (E) CAG mixed with 3wt% GNP750 (750 means the surface area in m^2/g) [6]. (C) and (F) CAG mixed with 1wt% MWCNT [6].

2.2.3. Surface Area and Scalability Comparison

The surface area is proven by experimental work, which correlates with the capacitance and electrochemical series resistance [6, 64]. Therefore, a high surface area is a crucial electrode characteristic for structural supercapacitors (SSC). Figure 2.20 shows the full list of the electric double-layer capacitor (EDLC)-based SSC electrodes' specific surface area, and its supplementary list is shown in Table A.1. The materials are characterised by carbon nanoparticles, mixed carbon nanoparticles and metallic nanowires. Metallic nanowires are a category in which the metal nanowires are grown onto carbon fibres, making the SSC a hybrid or pseudocapacitor that is out of this project's scope. The mixed carbon nanoparticles category means that more than one kind of carbon-based nanomaterial is used to form the electrode. Metallic nanowires and carbon aerogel (CAG) have shown to be promising candidates for providing high surface area and good mechanical properties for structural supercapacitors (SSC) [50].

Regarding scalability in size, methods such as an autoclave growing metal nanowires and chemical vapour deposition (CVD) of carbon nanotubes are limited by the chamber size, in which centimetre-size samples are produced. Larger will be costly to maintain and operate. The process temperature should also be lower than the carbon fibre degradation temperature to maintain its material strength from surface oxidation. High processing temperatures, such as CVD and the pyrolysis of the solid resorcinol-formaldehyde polymer, require a high temperature that potentially damages the carbon fibres. Regarding safety, carbon aerogel (CAG) production involves toxic and fatal resorcinol and formaldehyde materials, creating a dangerous work environment when a scale-up infusion is conducted. Electrophoretic Deposition, spraying coating and nanoparticle infiltration are suitable processing methods for achieving a high surface area electrode.

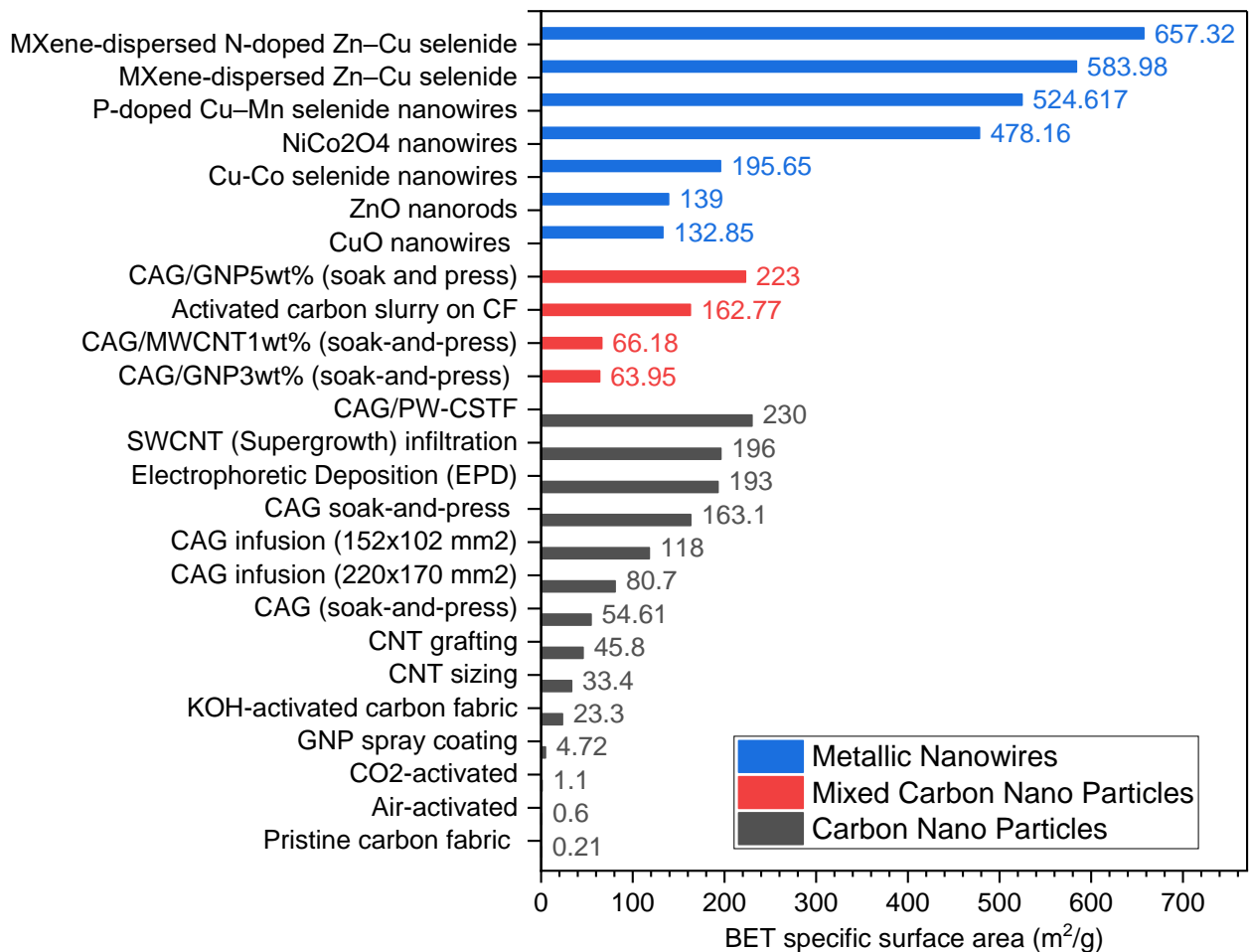


Figure 2.20: Brunauer-Emmett-Teller (BET) specific surface area comparison of the electrode materials.

2.3. Electrolytes

2.3.1. Terminologies and Categories

The electrolyte types used in structural supercapacitors (SSC) can be classified into homogeneous and heterogeneous, shown in Figure 2.21 (A). Homogeneous includes solid and gel electrolytes, while heterogeneous means the electrolyte system has a solid and liquid phase. The heterogeneous electrolyte is also used interchangeably as a dual-phase or bi-continuous electrolyte [50, 110].

Figure 2.21 (B) shows the multifunctionality of the electrolyte matrix (SE). The red dot is the ideally defined multifunctional point of Young's modulus 1 GPa and ionic conductivity of 1 mS/cm by Greenhalgh et al. [50][62]. Solid electrolytes are formed by directly mixing salts in polymer matrices. Dual-phase electrolytes consist of a solid phase which carries the mechanical stress, and a liquid or a gel phase responsible for the ion transport. The gel polymer electrolyte consists of a polymer host swollen by a liquid electrolyte medium. The difference between a gel electrolyte and a dual-phase electrolyte is the liquid and solid phases are immiscible and separated by an interfacial region. Solid and dual-phase electrolytes are reportedly used for the electrolyte matrix-fibre interface and the pouch bag-fibre interface through impregnation [8, 64, 94, 98]. The gel electrolyte is reportedly produced as a film to serve as an electrolyte matrix and separator used for the metal fibre interface and fibre-fibre interface [74, 114, 115].

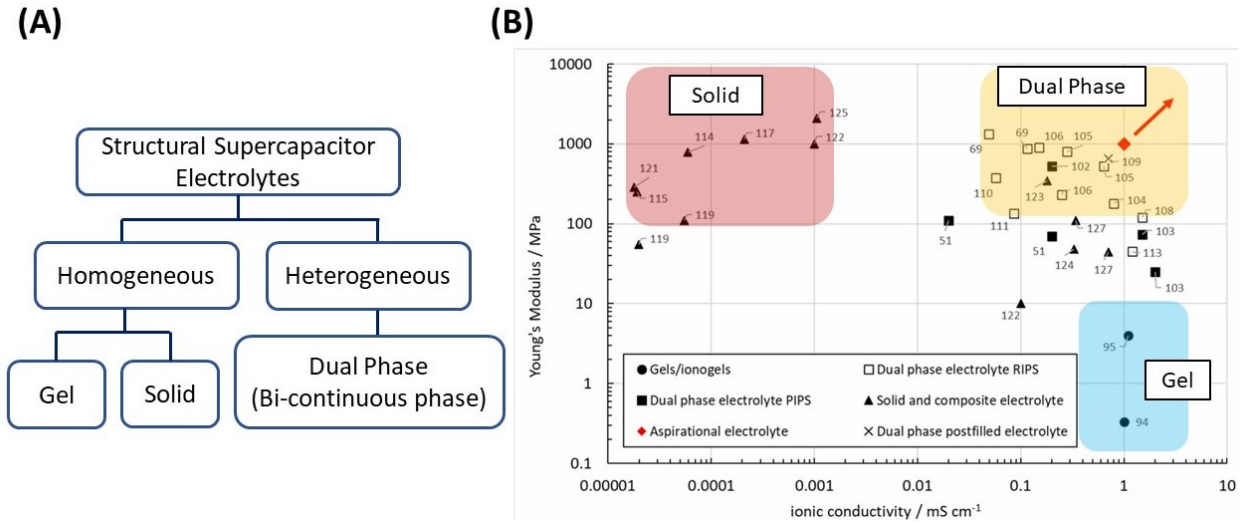


Figure 2.21: (A) Different types of structural supercapacitor electrolytes. (B) Multifunctional performance of the electrolyte matrix [50].

2.3.2. Ion transport mechanism

The ionic conductivity, σ in a polymer electrolyte can be described by the Kohlrausch summation (Equation 2.3) and the Nernst–Einstein relationship (Equation 2.4) [76, 104, 109, 151]. Where n_i is the charge concentration, q_i is the number of charges, u_i is the mobility, k_B is the Boltzmann's constant, T is the Kelvin temperature, and D is the diffusion coefficient.

$$\sigma = \sum n_i q_i \mu_i \quad (2.3)$$

$$\sigma = (n_i q^2 k_B T) D \quad (2.4)$$

The ionic conductivity in the structural supercapacitor's (SSC) electrolyte matrix (SE) is affected by the ion transport mechanism, which includes (1) Diffusion, (2) Segment motion, and (3) Ion hopping [151]. These mechanisms are driven by the applied electric field during the charge and discharge of the SSC.

Diffusion

The diffusion mechanism occurs when ions transport through a liquid medium. Diffusion occurs in liquid and gel electrolytes but is not apparent in solid electrolytes. The behaviour of ionic diffusion under an electrostatic response is described by the Nernst-Planck equation [73]:

$$f_j = -D_j \nabla n_j - D_j \left(\frac{z_j e n_j}{kT} \nabla \phi \right) + n_j v \quad (2.5)$$

In Equation 2.5, f_j , D_j and n_j are the flux (rate of mass transport), diffusion coefficient and ion number density (concentration), respectively. The first term is Fick's law, which considers the ions' concentration gradient. The second term presents the electrostatic ions response due to the electric field, and the third term is the convection flow of the fluid.

Segment Motion

Segment motion refers to the movement mechanism of the local repeating units in solid polymer chains containing charged or polar groups. Segment motion is caused by the thermal fluctuation of the charged or polar groups, which has a higher effect when the operating temperature is above T_g [109, 151]. The amorphous regions in the solid polymer also have a higher segment motion of local polymer chains [151].

Ion Hopping

While segment motion describes the polymer motion, the ions hopping describes the movement of the ions dissolved in the polymer. Ions in a solid polymer are able to hop from one point defect or vacancy to another and form ion-dipole bonds with the polar groups of a polymer chain. Ion hopping reaction can be described by the Arrhenius model in Equation 2.6 [151]:

$$\sigma = \sigma_0 \exp\left(\frac{-E_a}{kT}\right) \quad (2.6)$$

σ is the rate of a chemical reaction which is the ionic conductivity. σ_0, E_a , and k refer to the pre-exponential factor, activation energy, and Boltzmann constant. Activation energy is inversely proportional to the ionic conductivity and represents the barrier to ion transport, while the temperature increases the ionic conductivity exponentially.

While Equation 2.6 describes the ion hopping for the glassy solid polymer, the temperature-dependent ionic conductivity of the gel and solid polymer electrolytes whose temperature operates above its T_g can be described with the Vogel-Tamman-Fulcher (VTF) equation Equation 2.7 [76, 104, 151]. B is the pseudo-activation energy which is expressed as E_a/k .

$$\sigma = \sigma_0 T^{\frac{1}{2}} \exp\left(-\frac{B}{T - T_0}\right) \quad (2.7)$$

2.3.3. Solid Polymer Electrolyte

Solid polymer electrolytes structural supercapacitors (SSC) involve dissolving electrolyte salt into a structural resin, such as bisphenol A diglycidyl ether (DGEBA), poly(ethylene glycol) diacrylate (PEGDGE) or other epoxy types [62, 63, 139].

Choi et al. produced a solid polymer electrolyte by mixing an electrolyte consisting of succinonitrile (SN) and lithium bis(trifluoromethanesulfonyl)imide (LiTFSI) and then mixed with DGEBA [19]. The SN is a plasticiser which forms a solvation layer around the LiTFSI cations Li^+ , which increases the ionic conductivity. When the SN-LiTFSI amount increases in the DGEBA resin, the measured relaxation and segment motion increase, leading to an increase in ionic conductivity [19].

Inverse Relation of Mechanical Integrity and Ionic Conductivity

However, the increase in ionic conductivity also decreased the polymer's strength and Young's modulus. An increase of 30 wt% to 70 wt% of SN-LiTFSI in DGEBA led to a drop of Young's modulus from 1 GPa to 10 MPa while the conductivity increased from $10^{-9}(S/cm)$ to $10^{-4}(S/cm)$ shown in Figure 2.22. This is due to the increased segment motion that allows the polymer chains to move more freely. Ion transfer in solid electrolytes favours amorphous polymer structures, while crosslinks and crystalline structures hinder it [76, 151]. Amorphous structures are able to provide a higher segment motion compared to crosslink and crystalline polymers. This is due to the polymer chain motion being restricted for crosslinks, and the structure is closely packed for crystalline polymers.

Addition of Inorganic Fillers

Adding inorganic inert fillers such as SiO_2 , TiO_2 , and Al_2O_3 , or active fast conductors such as LATP and LLZTO can increase ionic conductivity by decreasing polymer crystallinity and enhancing chain segment motion [140, 145, 148]. Javaid added a 7.5 wt% of mesoporous silica particles in a DGEBA-PEGDGE-EMITFSI electrolyte and reported a 65% increase in ionic conductivity, 87.5% increase in Compression modulus and an 83.5% increase in compression strength [62].

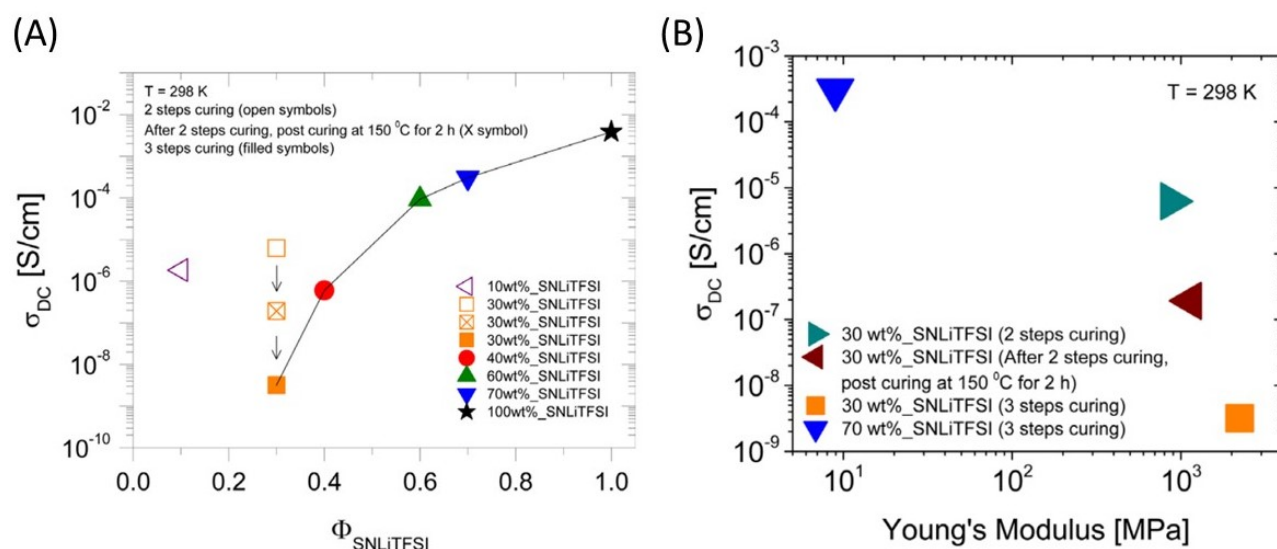


Figure 2.22: The electrolyte salt affects the ionic conductivity and Young's modulus of the solid polymer electrolytes. (A) The ionic conductivity increases when the SN-LiTFSI ion content increases in the DGEBA resin. The three orange boxes show that ionic conductivity decreases when curing cycles increase [19]. (B) The inverse relation between the ionic conductivity and Young's modulus [19].

2.3.4. Dual Phase Polymer Electrolyte

Dual-phase, or bi-continuous polymer electrolyte, is a polymer electrolyte containing a solid and a liquid phase, and the two phases have a distinct boundary. The solid phase is a structural resin that provides mechanical integrity, while the liquid or gel phase consists of ionic liquid or dissolved salts [50, 142]. Three different methods used to produce a dual-phase polymer electrolyte are (1) reaction-induced phase separation (RIPS), (2) polymerisation-induced phase separation (PIPS), and (3) Liquid electrolyte post-filling [50].

Reaction-induced phase separation (RIPS) is a method to create microstructures in a polymer filled with liquid electrolytes based on the insolubility of the liquid electrolyte and the structural resin. A dual-phase polymer electrolyte is created with RIPS by Wendong et al. [142]. A bisphenol A diglycidyl ether (DGEBA) resin is mixed with an isophorone diamine (iPDA) curing agent and different EMIMTFSI wt% to form a homogeneous solution. Once the highly crosslinked solid polymer phase has been formed by the DGEBA and the iPDA, the EMIMTFSI ionic liquid will be separated from the cured polymer and create microstructures [142]. An inverse relation between Young's modulus and ionic conductivity is shown in Figure 2.23 (A). Javaid also reported a reverse relation between the increased ionic conductivity and the decreased compressive strength of a PEGDGE¹-EMIMTFSI² dual-phase polymer electrolyte shown in Figure 2.23 (B) [62]. A schematic image of a RIPS method is shown in Figure 2.24 [118].

Polymerisation-induced phase separation (PIPS) is a method in which a dual-phase polymer is produced based on polymerization from ultraviolet (UV) or heat treatment [57, 110]. The crosslinking reaction in the reaction-induced phase separation (RIPS) is also a type of polymerisation but the difference is that the phase separation is based on the insoluble materials. To obtain a dual-phase polymer based on PIPS, a liquid electrolyte of lithium trifluoromethanesulfonate (LiTFS) dissolved into a DMMP³ and ethylene carbonate (EC) solvent (50%-50%). The liquid electrolyte of 39 wt% is then mixed with a monomer (bisphenol A ethoxylate dimethacrylate) and an AIBN⁴ thermal initiator by Schneider et al. [110]. The polymer solution is then heated to decompose AIBN to form long-chain molecules from monomers shown in Figure 2.25.

¹Poly(ethylene glycol) diglycidyl ether

²1-Ethyl-3-methylimidazolium bis(trifluoromethylsulfonyl)imide

³Dimethyl methylphosphonate

⁴2,2'-azobis(2-methylpropionitrile)

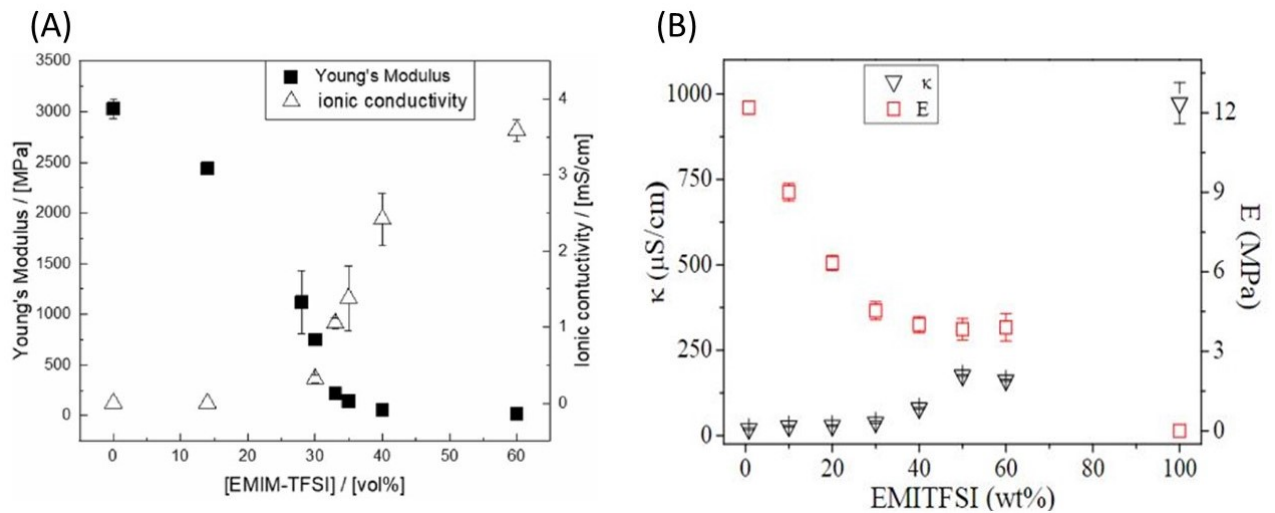


Figure 2.23: The inverse relation of the ionic conductivity and the modulus properties of the solid polymer electrolytes. (A) As the EMITFSI ionic liquid increases in the DGEBA resin, the ionic conductivity increases while Young's modulus decreases. (B) As the EMITFSI ionic liquid increases in the PEGDGE resin, the ionic conductivity increases while the compression modulus decreases [62].



Figure 2.24: A schematic diagram of a reaction-induced phase separation method [118].

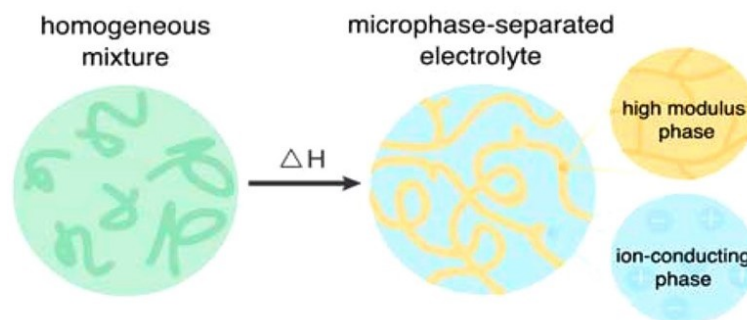


Figure 2.25: A schematic diagram of a polymerisation-induced phase separation method by heat treatment [110].

The post-filled method is to soak a porous membrane into a liquid electrolyte. The electrolyte-soaked membrane is also used as a separator [97]. The porous membrane can be fabricated using the non-solvent phase inversion or vapour-induced phase separation method [13, 97, 108]. Pu et al. soaked a porous PVDF-HFP⁵ membrane into a $LiPF_6$ -based liquid electrolyte and achieved an ionic conductivity of 1.2 (mS/cm) [97]. The literature shows that the post-filled method is not commonly used to produce electrolyte matrix for structural supercapacitors [50, 148], which may be due to the complex production steps.

⁵Poly(vinylidene fluoride-co-hexafluoropropylene)

2.3.5. Gel Polymer electrolyte

Gel polymer electrolytes (GPEs) increase the low ionic conductivity of solid polymer electrolytes (SPEs) having ionic conductivity from $10^{-5} - 10^{-2} (mS/cm)$ to over $1 (mS/cm)$ [76, 151]. This is achieved by incorporating a plasticizer or solvent into a polymer matrix, resulting in a gel-like electrolyte that can support high ion loadings [76]. GPEs combine the diffusivity properties of liquid electrolytes with the chemical and mechanical stability of polymer chains [151].

A gel polymer electrolyte (GPE) reinforced by epoxy is produced by Wang et al. [139]. Polyvinylidene fluoride (PVDF), lithium triflate (LiTf), tetrahydrofuran (THF), and epoxy are blended with different weight ratios to prepare different gel polymers that emphasise mechanical integrity or ionic conductivity shown in Figure 2.26. An electrolyte with an ionic conductivity of 24.8 mS/cm is achieved, significantly above the set goal of 1 mS/cm. This is due to the high intake of LiTf, which has a 63.75 wt% of the GPE.

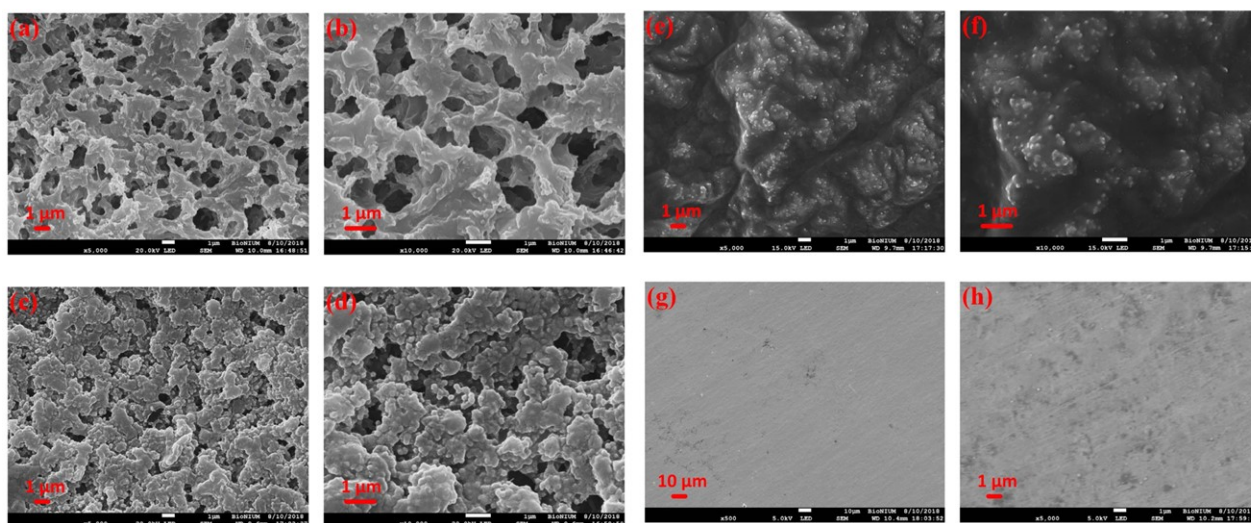


Figure 2.26: SEM images showing the increase of the epoxy weight ratio reduces the pores in the gel polymer electrolytes, which contain the liquid electrolyte [145]. PVDF:LiTf 25:75 wt% with (a)(b) 0 wt% epoxy, (c)(d) 15 wt% epoxy, (e)(f) 30 wt% epoxy and (g)(h) 100 wt% epoxy.

Although gel polymer electrolytes (GPE) can achieve desirable ionic conductivity for electrolyte matrix, it is a soft material which may be penetrated during the vacuum infusion of the encapsulating structural resin under a high vacuum. The limitation results in using a small pressure which decreases the fibre volume fraction [114]. The gel electrolyte's mechanical strength can be increased by introducing a higher degree of crosslinking with a structural resin such as epoxy [139].

2.3.6. Electrolyte Salts and Ionic Liquids

In order to provide a high ion intake for the electrolyte matrix to achieve high ionic conductivity, an electrolyte salt with high ion mobility, dissociation constant, and solubility needs to be selected [76]. Lithium salts shown in Equation 2.8, Equation 2.9, and Equation 2.10 are ranked by their mobility, dissociation and solubility in nonaqueous solvents based on mixed alkyl carbonates [76, 147].

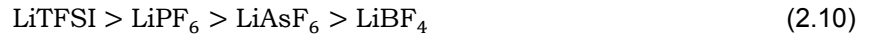
Ion mobility:



Dissociation constant:



Solubility:



LiTFSI is shown to have a high dissociation constant and solubility, which can produce a high content of lithium ions to enhance ionic conductivity. However, apart from the performance, the safety and limitation of electrolyte salts with the environment also need to be considered [62]. *LiClO₄* is an oxidiser that can intensify the fire, and *LiPF₆* hydrolyses at 70 °C which is not stable at elevated temperatures. *TBAPF₆* has the benefit of operating stably at ambient moisture, which can be exposed to open air. However, it has poor ionic conductivity. *LiTFSI* is a liquid at room temperature; however, it crystallises in a moist environment, degrading ionic conductivity.

Ionic liquids are room-temperature molten salts with a high viscosity [148]. Ionic liquids such as *EMIMBF₄* and *EMIMTFSI* used for the electrolytes of the structural supercapacitors has the benefit of being non-flammable while still having oral toxicity [50, 120, 121]. Since lithium-based electrolytes are toxic, corrosive and harmful to the environment, the ionic liquid is considered the next generation of "green solvents" [38, 138].

2.4. Separator Selection for the Structural Supercapacitors

Structural supercapacitors (SSCs) require separators exhibiting ionic conductivity and electrical insulation to prevent short circuits and facilitate electron mobility. Materials with a porous and low tortuosity pore structure are preferred to achieve high ionic conductivity [50]. Thin (micrometre scale) separators are necessary for high capacity and low equivalent series resistance (ESR) while chemically stable with the electrolyte [152]. Insulative fabrics such as glass and aramid fibre and non-fabric separators such as filter paper, polypropylene (PP), and polyethersulfone (PES) are commonly used as SSC separators [50]. In addition, using gel polymer electrolytes, which serve as the electrolyte matrix and separator, yields higher energy storage [145].

Javid compared different separator materials for structural supercapacitors (SSC) by using filter paper, glass fabrics and polypropylene (PP) membrane [62]. Filter paper showed the highest shear modulus and no delamination due to its good adhesion with the matrix, but it had the lowest capacity density, which may be due to its pores being blocked by the structural resin part of the electrolyte matrix [50, 62, 63]. The polypropylene (PP) membrane had the highest capacitance density since it had the smallest thickness among the three materials. However, the PP separator had the lowest shear properties and delamination effect. This also supports that a pouch bag-fibre interface for the encapsulation method will cause delamination. Glass fabrics had shear and electrical properties between the PP membrane and filter paper. Therefore, it is commonly selected as the separator material for SSCs [62, 119, 149].

Using fabric materials with low area densities as separators will cause short circuits since large pores openings allow the contact of the electrodes. Figure 2.27 shows that by using ACG1, ACG2 and Tissa 1 do not show discharge capacity due to short circuits, while Tissa 2 and Tissa 3 show charge-discharge capacitance [62]. Therefore, selecting appropriate glass fabrics that do not contain large holes while being thin and have a low area density is crucial. When multiple low-area density fabrics are used for the separator to obtain a balanced layup, the fabric can be laid up with a shift to avoid open holes and resin pockets [62, 130].

2.5. Challenges for the Current Collecting Terminals

Good current collector characteristics are having good contact with the electrode active materials, high electrical conductivity, and remaining stable during charge-discharge [152]. The interface between current collectors and active materials creates internal resistance, which affects power losses [137]. Increasing the contact area and modifying the collector surface can reduce charge transfer resistance [152]. The resistivity of the current collector is lowered by Portet et al. by lowering the resistivity of the current collector by a two-step procedure in which an aluminium foil current collector is etched and dip coated with a carbonaceous powder [95].

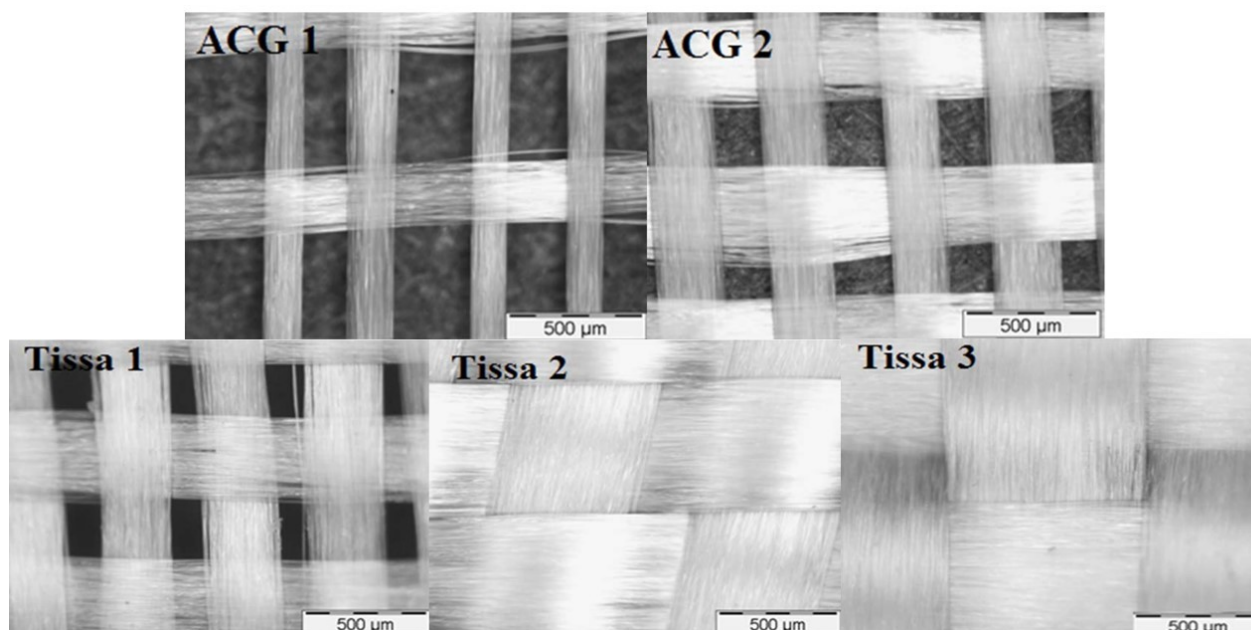


Figure 2.27: Images of optical microscopy showing the increase of the areal density of glass fabric separators reduces the fabric pore openings, thus eliminating the short-circuiting issue. [62].

For the SSC current collectors, copper tapes as current collectors attached to the electrodes is the most convenient method [29, 100]. Copper wires as current collectors are interlaced into the carbon fabrics by Javaid et al. [65]. To improve the current collector-electrode interface, binding agents (PTFE, Nafion, PVdF, or PVB) can be mixed with conductive carbon additives that can be brushed on the current collector as conductive adhesives [152]. However, the binder materials may cause the resistivity to increase.

Carbon fibre can also act as both an electrode and a current collector. However, carbon fibres have higher resistivity compared to copper and aluminium, which can induce a potential drop that leads to energy and power loss [54]. Some research papers state that they used carbon fabric as current collectors and electrodes [92] [84]. However, they define CF as the current collectors of coated electrode materials, not the terminal that connects with an external power source. Copper or aluminium tapes must still be attached. Screen printing can also produce current collectors with various patterns. Johannisson et al. compared screen-printed silver conductive ink on unidirectional spread tow fibres with copper current collectors, which screen-printed showed a lower capacitance [68].

2.6. Interconnection of the Structural Supercapacitors

A structural supercapacitor (SSC) single cell, consisting of only two electrodes and a separator, has limited energy storage in the material aspect. While SSC can expand in two-dimensional to increase its energy storage, it can also be connected in parallel or in series and form SSC packs and modules as conventional supercapacitors.

The structural supercapacitors (SSC) connected in series and in parallel are shown in Figure 2.28 [20]. For a set of stacking cells, attaching current collectors at the top and bottom surfaces as in Figure 2.28 (B) puts the cells in series, decreasing the capacitance while increasing the voltage window. Interlacing the current collectors as Figure 2.28 (C) at each electrode puts the cells in parallel to increase the capacitance. The SSC electrical properties can be tailored by increasing the thickness of the SSC laminate through parallel and series connections.

A schematic concept design of a multilayer assembly in which two structural supercapacitor (SSC) cells are connected in series is shown in Figure A.1 [91]. The electrode materials are coated in a grid pattern, in which the grid gaps are impregnated with epoxy resin to increase its mechanical interlocking through the thickness. This interlocking design is similar to the perforated interleaves SSC design by Senokos et al., except Pandey et al. uses a glass fabric separator pressed by two gel electrolyte-coated electrodes, while Senokos et al. use gel electrolytes as the separator [91, 114]. The grid pattern is valuable for scaling up SSC since it can produce laminates with both safe-life and fail-safe designs.

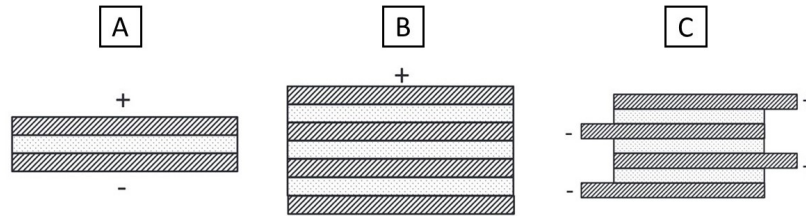


Figure 2.28: Structural supercapacitor (SSC) configurations [20]. The dark region is the electrodes shown to be connected to a positive or negative terminal. The light region is the separator. (A) Single SSC cell (B) Cells in series to increase the voltage window (C) Cells in parallel to increase the capacitance.

2.7. Conform with Aerospace Regulations

Structural power composites' (SPCs) concepts are often reported to be implemented on aircraft, which need to adhere to the European Aviation Safety Agency's (EASA) regulations [34] [35]. Structural supercapacitors (SSC) have been embedded in a composite C-beam structure to demonstrate the opening of an aircraft door during an emergency as shown in Figure 2.29 [22, 78]. The regulations for having supercapacitors on large aeroplanes are presented, but their regulations can also be used as design guidelines for automobiles and electronic devices.

EASA proposed a special condition for airworthiness supercapacitors on large aeroplanes in addition to the regulations from CS25 (CS25.601, CS 25.1529, CS 25.1309 and CS 25.863). The regulations are rewritten in short and categorised into design, installation, operation, failure and maintenance.

Design

1. Preclude thermal runaway (self-sustaining, uncontrolled rise in temperature or pressure).
2. Minimise the probability of ignition at areas where flammable liquids and vapour might escape.
3. Possible ignition sources, electrical faults, equipment overheating, and protective device malfunctioning need to be shown as analysis or tests.

Installation

1. Installation must have provisions to prevent any hazardous effect on the structure or essential systems that the maximum amount of heat may cause from short circuits.
2. The charging rate of the supercapacitors must be controlled automatically to prevent overheating and overcharging.
3. Temperature sensing and over-temperature warning system should be provided with a means for automatically disconnecting the supercapacitor from its charging source when over-heated.
4. Means to prevent insufficient charging of the Supercapacitor.

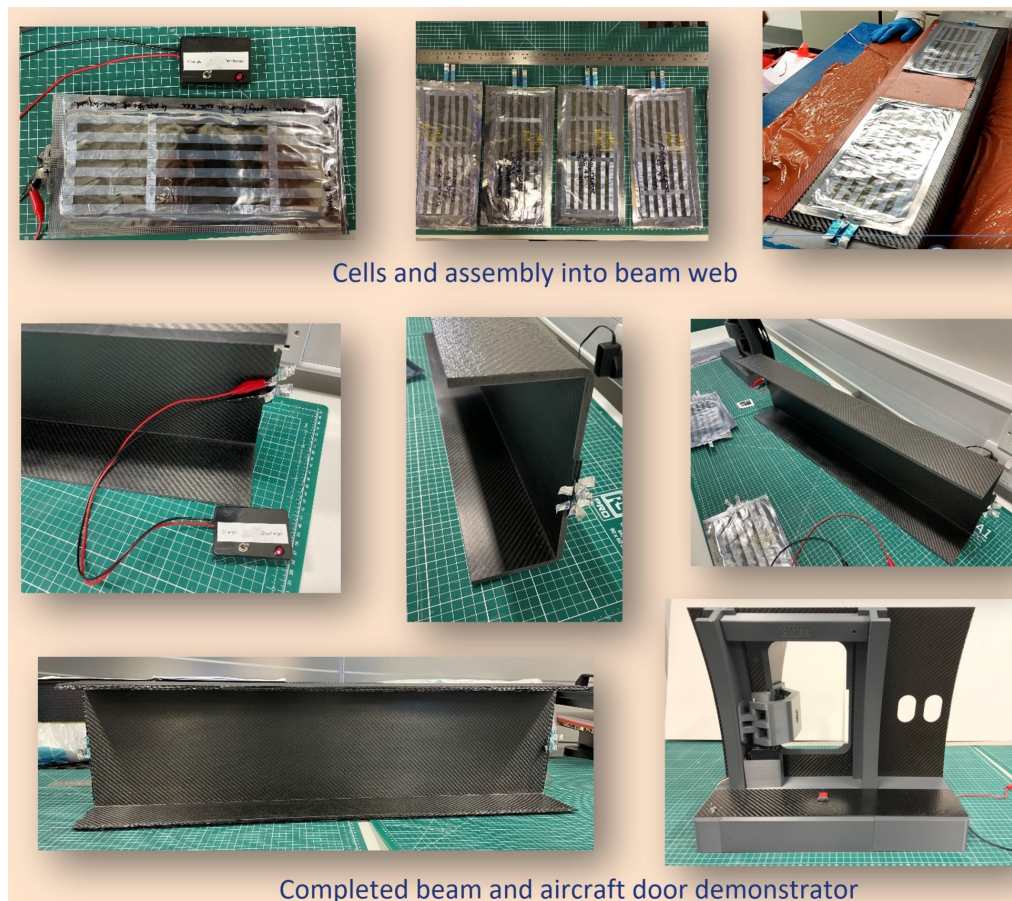


Figure 2.29: Structural supercapacitors embedded in C-beams to power a mockup aircraft door. [22, 78]

Operation

1. No explosive or toxic gasses in normal operation.
2. Escaped corrosive fluids or gasses may not damage the surrounding structure or adjacent systems.
3. When the supercapacitor's function is required for the safe operation of the aeroplane, a warning feature must be provided when the capacity has fallen below acceptable levels.

Failure

1. Means available for controlling or extinguishing a fire.
2. Any catastrophic failure condition is improbable and does not result from a single failure.
3. Hazardous or major failure condition is extremely remote

Maintenance

1. Measure supercapacitors' performance at appropriate intervals to ensure they function safely during their operation on the aeroplane.

The challenge for structural supercapacitors (SSC) is to conform to the supercapacitor regulations while adding structural failure as supercapacitor failure. The design guidelines are presented as follows:

1. A structural health monitoring system must be implemented in the structure in addition to the detection of short circuits, temperature and capacity. In the case of damage detection, the SSC should be disconnected from the charging source, and the energy stored in the SSC must be discharged to the zero-volt potential difference.
2. Active materials for energy storage may not be flammable, toxic or corrosive. Solid and gel electrolytes should be used and not liquid electrolytes.
3. Design an encapsulator using fire-retardant materials capable of venting out vapour generated from the electrolyte in case of an overheating.
4. SSC failures should be remote, meaning far away from humans.

The requirements for structural supercapacitors (SSC) mentioned above challenge the current proposed applications for structural power composites (SPC). Widely proposed applications, such as aircraft and passenger electric cars, may not be ideal applications for SSCs when implementing aerospace regulations as design guidelines.

2.8. Summary of Literature

Structural supercapacitors (SSC) should be designed and manufactured with a scalable approach. There is a knowledge gap in which the fibre-fibre encapsulation method is not well-understood. The effect of the epoxy infusion within the fibre-fibre encapsulation interface needs to be studied. The moisture ingress during the SSC manufacturing is less of an issue since SSC can be dried after assembly [50]. A manufacturing process should be designed to eliminate the need for glove boxes and dry rooms while minimising their material exposure to the environment.

The electrode materials for SSC involve depositing conductive materials with high surface areas on their fabric or metal-based current collectors. Spraying, solution casting, and paint brushing are scalable methods that require a binder. Infiltration and electrophoretic deposition (EPD) are also scalable methods that produce high surface areas. The graphene nanoplatelets (GNP) and carbon aerogel (CA) combination has the highest surface area of $223 \text{ m}^2/\text{g}$. Although good SSC performance can be achieved using chemical vapour deposition (CVD) and carbonization of resorcinol-formaldehyde polymer into carbon aerogel (CA), they have limitations, such as damaging the strength of the fabric electrodes and using lethal and toxic materials [4, 122, 123].

Gel polymer electrolytes (GPE) sandwiched by two fabric electrodes is the potential SSC scale-up method. The dual-phase electrolyte matrix, which contains lithium salts or ionic liquids, is often infused in fabric electrodes using vacuum-assisted resin transfer moulding (VARTM). While these materials work well for small-scale applications, they are expensive and not economically feasible for large-scale infusion projects. GPEs can be a cost-effective solution for fabricated metre-scale SSC panels using a roll-to-roll process. Although GPEs don't have as high mechanical strength as dual-phase electrolytes, applying a grid pattern of GPE enables a through-thickness structural resin interlocking that enhances bending strength [91, 114].

2.9. Research Objective and Questions

This project aims to study the lack of research on the structural supercapacitor (SSC) encapsulation method with a fibre-fibre interface and tackle the challenges in [section 1.3](#). The research objective is stated as follows:

Research Objective

Fabricate a structural supercapacitor proof of concept having a fibre-fibre encapsulation interface and examine its electrochemical and mechanical properties.

The main research question is formulated from the research objective as the following:

Main Research Question

How does the ion concentration of the gel polymer electrolyte, the encapsulation using epoxy infusion, and the optimisation of a high surface area electrode influence the electrochemical and flexural properties of the structural supercapacitor with a fibre-fibre encapsulation interface?

The main research question leads to the subquestions of the structural supercapacitor's (SSC) fundamentals and manufacturing methods:

1. What is the experimental approach to studying the structural supercapacitor's (SSC) performance?
2. What are the electrode materials and their fabrication method?
 - (a) What is the material combination of the carbon electrode?
 - (b) What is the deposition method of electrode materials on the carbon fabric?
 - (c) What is the selection criterion for an optimal electrode material?
 - (d) How does the carbon material deposition weight influence the electrode performance?
 - (e) What is the selected optimal electrode's surface morphology and surface area?
 - (f) What are the advantages of this electrode material and fabrication process for scaling up?
3. What are the gel polymer electrolyte (GPE) materials and their fabrication method?
 - (a) How do the LiTFSI concentrations in the GPE affect the physical properties and the ionic conductivity?
 - (b) What are the advantages of this electrolyte material and fabrication process for scaling up?
4. What is the fabrication method for an SSC cell?
 - (a) What is the layup configuration for the SSC cell?
 - (b) What are the assembly steps of the SSC cell?
 - (c) Why is this assembly process beneficial for a scale-up demonstration?
5. What is the performance of an SSC cell?
 - (a) How does the epoxy-infused encapsulation layer affect the final cell's performance?
 - (b) What is the electrical performance of the SSC cell?
 - (c) What is the mechanical performance of the SSC cell?
 - (d) What is the multifunctionality of an SSC cell?

Methodology and Materials

3.1. Structural Supercapacitor Design Concept

The structural supercapacitor (SSC) design is presented in [Figure 3.1](#). The design uses plain weave carbon spread tow fabric (PW-CSTF) as electrodes. The electrodes are then deposited with porous carbon particles such as graphene nanoplatelets or activated carbon. A gel polymer is used as both the electrolyte and the separator. Copper tapes are used as current collecting terminals, which are attached to the PW-CSTF. The laminate is then encapsulated by glass fabrics and infused with structural resin. An alternative approach derived from this concept is shown in [Appendix B](#). The design included a carbon aerogel (CAG) scaffold in the carbon fabric, explained in [Figure B.1](#). This approach was not implemented due to the unavailability of a pyrolysis chamber and the inability to process the carbon fibres after heat treatment.

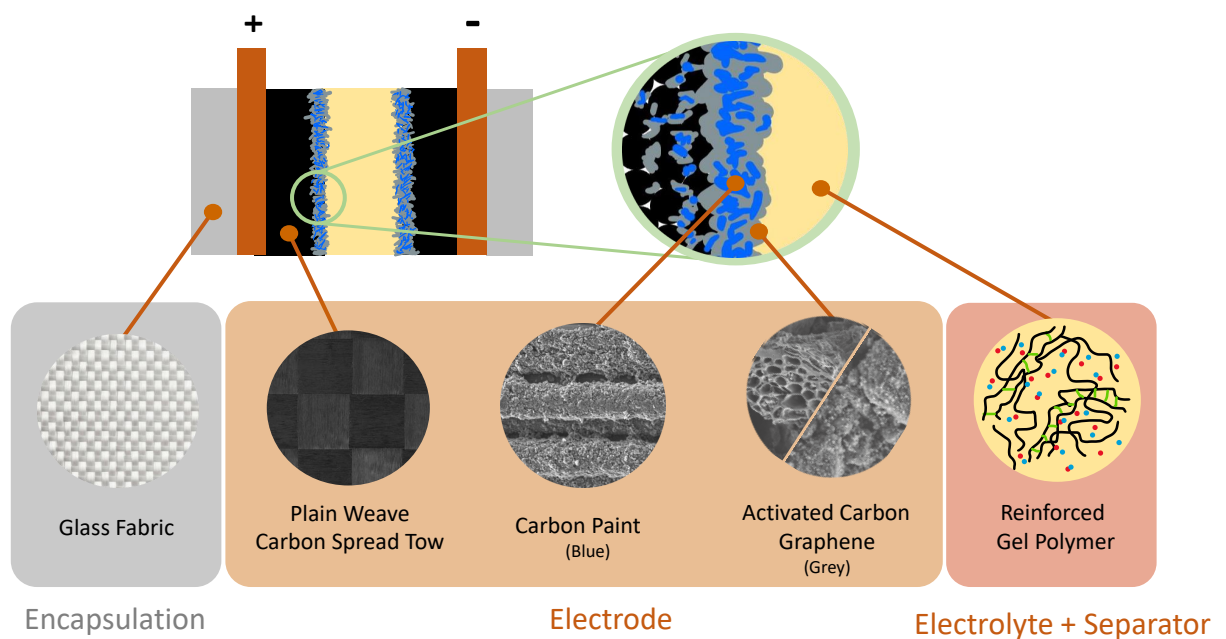


Figure 3.1: Structural supercapacitor 2D-concept. The gel polymer consists of cations and anions represented by dots. The polymer chains are depicted in black, with the degree of cross-linking indicated in green.

This design offers several advantages. Firstly, the fabric electrode and the glass fabric encapsulation interface are impregnated with a continuous epoxy material which provides a better interfacial property compared to the other embedding interfaces. Secondly, implementing a gel polymer electrolyte (GPE) as the separator eliminates the need for glass fabric separators which reduces weight. Thirdly, the GPE can prioritise ionic conductivity over mechanical integrity as it is only confined between the electrodes. The design resembles a sandwich structure in which the gel electrolyte core is sandwiched by two electrode face sheets infused with structural resin. The soft gel polymer electrolyte (GPE) presents a challenge as it may cause a short circuit in case of penetration. Further mechanical integrity enhancement may be required. The structural resin infusion may also infiltrate the interface between the electrode and gel polymer electrolyte, hindering the electric double-layer formation.

3.2. The Building Block Approach

The building block approach (BBA) is a method for optimising a complex system by breaking it down into smaller components that are optimised individually and then assembled into a larger system. It has been successfully demonstrated in optimising aerospace structures through test-validated simulations [18, 31, 53].

The methodology for investigating the structural supercapacitor (SSC) concept design is presented using the building block approach (BBA) in Figure 3.2. BBA presents the SSC concept design from its material constituents and different stages of cell manufacturing. The initial steps are to characterise the electrode and gel polymer electrolyte materials, followed by assembling them into a semi-cell without impregnating epoxy resin. Finally, the epoxy infusion is conducted to create a full cell at the top level of the BBA.

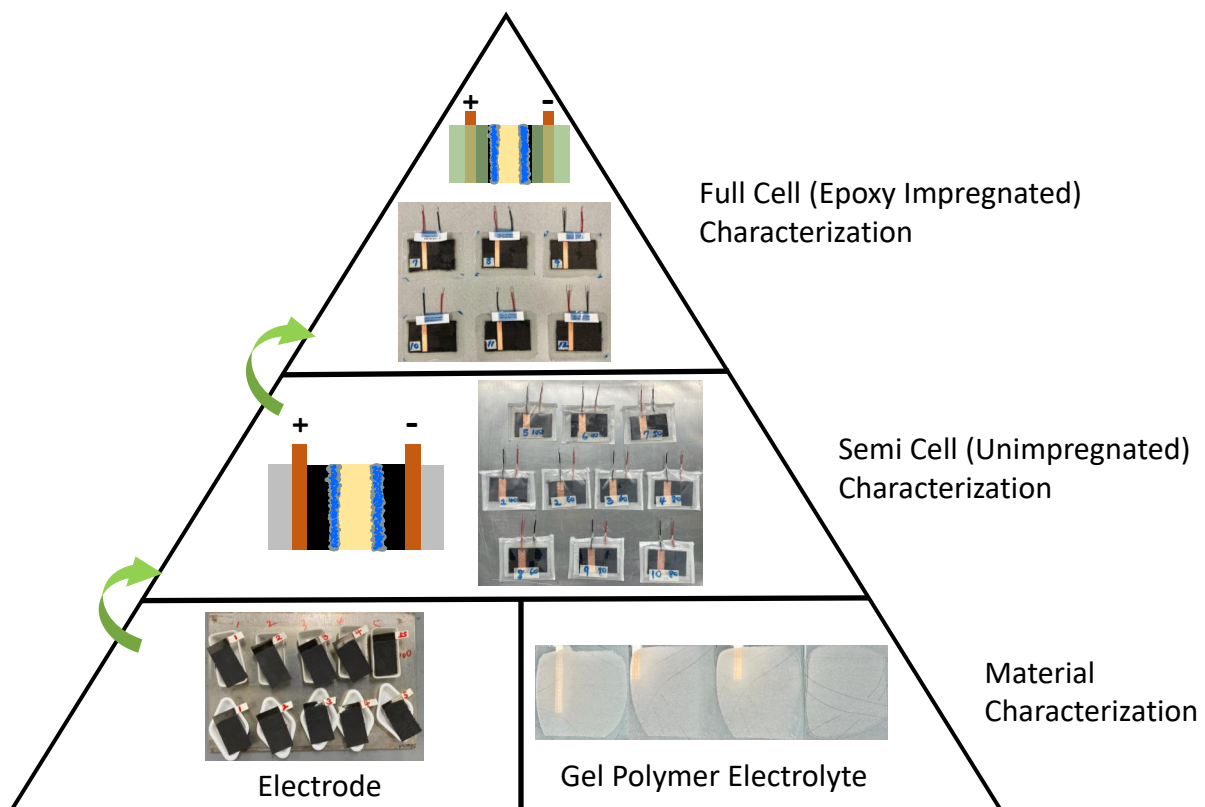


Figure 3.2: The BBA for creating a structural supercapacitor. At the full cell level, the 2D cell is coloured green to indicate the infusion of epoxy resin.

3.3. Electrode

3.3.1. Materials and Equipment

The electrode material utilised in this study was provided by TeXtreme® Spread Tow fabric 1025 (plain weave, 200 gsm, epoxy compatible). Activated charcoal (242276) and graphene nanoplatelets (900407) were purchased from Sigma-Aldrich. Ethanol absolute (83813.360) was purchased from VWR International, and the carbon conductive paint was purchased from SPI Supplies. To connect the current collecting terminal to the external measurement device, a double-sided 3M copper tape with a width of 6mm is utilised.

The equipment to fabricate the electrodes includes a magnetic stirrer (IKA RET basic) and a VWR VV3 vortex mixer. A Nabertherm muffle furnace valve (maximum temperature 1300°C) with inner dimensions of 230x240x170 (width-depth-height in mm) is used for carbon fabric heat treatment. Haver EML Digital Plus is used for sieving carbon particles.

3.3.2. Plain Weave Carbon Spread Tow Fabric

Plain weave carbon spread tow fabric (PW-CSTF) has a smooth surface which has the advantage of reducing short circuits due to fewer ridges or bumps from its crests [50, 131]. In addition, PW-CSTF is made up of many thin, closely spaced carbon tows, which are spread out to create a wider weave pattern. The result is a fabric with a higher fibre content, which increases mechanical properties and electrical percolation [7, 50, 131].

The plain weave carbon spread tow fabric (PW-CSTF) includes binders and sizing on its materials shown in [Figure 3.3](#), which require partial removal by heat treatment in a nitrogen-vented furnace before the deposition of carbon slurry. Partial removal improves electrical percolation while maintaining the fabric's processability.

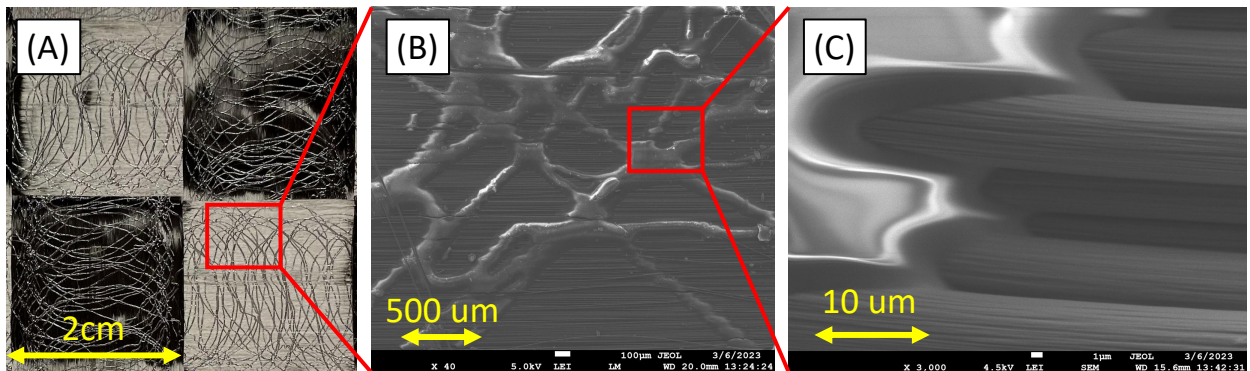


Figure 3.3: (A) TeXtreme® Spread Tow fabric 200gsm before heat treatment. (B) The SEM image of the PW-CSTF and its binder material. (C) A close view of the binder material.

3.3.3. Carbon Slurry Deposition

Activated charcoal (AC, equivalent to activated carbon) and graphene nanoplatelets (GNP) were selected as electrode materials due to their high surface area. The particle size of the AC is reduced from 150 μm to below 65 μm since a smaller particle size is critical for forming compact connection electrodes [43]. SPI carbon conductive paint is used as a binder to produce slurries. Dip coating and brush application are used to deposit the carbon slurry on the fabric substrate. The schematic of the slurry deposition is shown in [Figure 3.4](#).

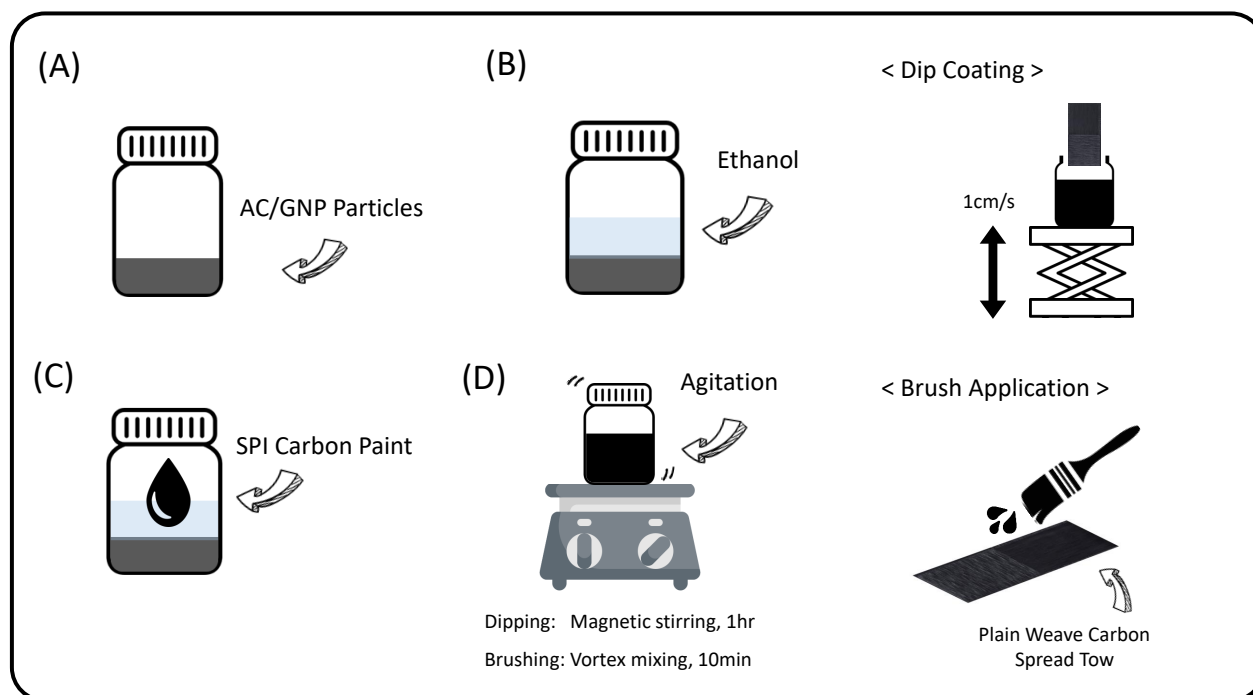


Figure 3.4: The illustration of the carbon particle deposition using dip coating and brush application. (A) Carbon particles (B) Adding ethanol (C) Adding SPI carbon conductive paint. (D) Vortex mixing the slurry
Icon sources: [37, 39, 39, 40, 45, 46]

Dip Coating

Dip coating is applied to achieve a controlled slurry loading on the fabric electrodes. Heat-treated plain weave carbon spread tow fabric (PW-CSTF) is dip-coated in an activated charcoal (AC)-based slurry. Three different slurry formulations are shown in [Table 3.1](#). The mass percentage of each constituent is shown in [Figure D.1](#).

Code Name	g		
	Ethanol	Activated Charcoal (AC)	SPI carbon conductive paint (20 wt% of the AC)
Dip-AC-12	78.9	12	2.4
Dip-AC-16	78.9	16	3.2
Dip-AC-20	78.9	20	4

Table 3.1: Activated charcoal slurry formulation table for dip coating.

The dipping samples are 2-by-4 cm plain weave carbon spread tow fabric (PW-CSTF), with copper tape affixed to the 2 cm edge. Both sides of the PW-CSTF are first brushed with SPI carbon conductive paint. The slurry is prepared by mixing activated charcoal (AC), ethanol and SPI carbon conductive paint with a magnetic stirrer at 1000 rpm for 1 hour.

A 3-second dip coating is performed by raising and lowering the lifting automatic platform with a speed of 1 cm/s. The slurry is not agitated during dipping but is continuously stirred at 1000 rpm at other times. After the dip-coating process, the samples are dried at room temperature in a fumehood until a stable sample weight is achieved. For each slurry concentration (Dip-AC-12, Dip-AC-16, Dip-AC-20), three samples are dipped. Three samples are dipped for each slurry concentration (Dip-AC-12, Dip-AC-16, Dip-AC-20), and each of the three samples is dipped from one to three times. A total of nine fabric electrodes were produced, and their area and weight properties are shown in [Table D.1](#).

Brush Application

The brush application method is employed subsequent to the dip coating study with the aim of improving slurry deposition. Activated charcoal (AC) and graphene nanoplatelets (GNP) are utilised to produce slurries. Their formulations are shown in [Table 3.2](#). An AC and GNP hybrid slurry is also produced, which formulation is shown in [Table 3.3](#).

Code Name	AC	Ethanol	SPI Carbon Conductive Paint	mg				
				Code Name	GNP	Ethanol	SPI carbon conductive paint	AC/GNP plus Paint wt%
b-AC200	200	1000	1000	b-GNP200	200	1000	1000	54.5
b-AC300	300	1000	1000	b-GNP300	300	1000	1000	56.5
b-AC400	400	1000	1000	b-GNP400	400	1000	1000	58.3
b-AC500	500	1000	1000	b-GNP500	500	1000	1000	60

Table 3.2: Formulations of activated charcoal and graphene nanoplatelets based slurries developed for brush application.

Code Name	mg			
	AC	GNP	Ethanol	SPI Carbon Conductive Paint
b-AC80-GNP320	80	320	1000	1000
b-AC160-GNP240	160	240	1000	1000
b-AC240-GNP160	240	160	1000	1000
b-AC320-GNP80	320	80	1000	1000

Table 3.3: The formulation of activated charcoal and graphene nanoplatelets mixed slurries developed for brush application.

The slurry preparation for brush application is shown in [Figure 3.5](#). Activated charcoal (AC) and/or graphene nanoplatelets (GNP) are mixed with ethanol and SPI carbon conductive paint by vortex mixing for ten minutes. The slurry is then brushed onto 2-by-4 cm PW-CSTF on one surface. Afterwards, the samples are air-dried at room temperature in a fumehood until a stable sample weight is recorded.

For the activated carbon (AC) slurry, a total of 20 samples were prepared. Five samples were dipped for each slurry concentration (b-AC200 to b-AC500 in [Table 3.2](#)), and each of the five samples was dipped from one to five times. For the graphene nanoplatelets (GNP)-based slurry, a maximum of two brushes are applied. 16 samples are prepared for the four different GNP slurries (b-GNP200 to b-GNP500 in [Table 3.2](#)). Four samples were prepared for each slurry concentration, two being brushed once and the other two being brushed twice.



Figure 3.5: Fabrication process of the graphene nanoplatelets-based slurry. (A) Graphene nanoplatelets (B) Adding ethanol (C) Adding SPI carbon conductive paint and sealed with Parafilm (D) 10 minutes vortex mixing of the slurry.

3.3.4. Characterisation

Thermogravimetric Analysis

Thermogravimetric analysis (TGA) was conducted using a Perkin Elmer TGA 4000 to monitor the mass loss of a plain weave carbon spread tow fabric (PW-CSTF) under a prescribed heating profile. The heating profile consisted of an initial temperature of 30°C, a heating rate of 20°C/min, and a maximum temperature of 800°C for 2 hours. The heating was conducted in a nitrogen-purged atmosphere.

Cyclic Voltammetry

The cyclic voltammetry test is performed to measure the capacitance of the electrodes in a 1M (mol/L) sodium sulfate (Na_2SO_4) aqueous electrolyte. The Metrohm Autolab is used to perform the electrochemical measurements of the electrodes. A three-electrode setup shown in Figure 3.6 is used for electrode characterisation [153]. For each electrode sample, five cycles of CV analysis are performed with a voltage window from 0 V to 0.5 V.

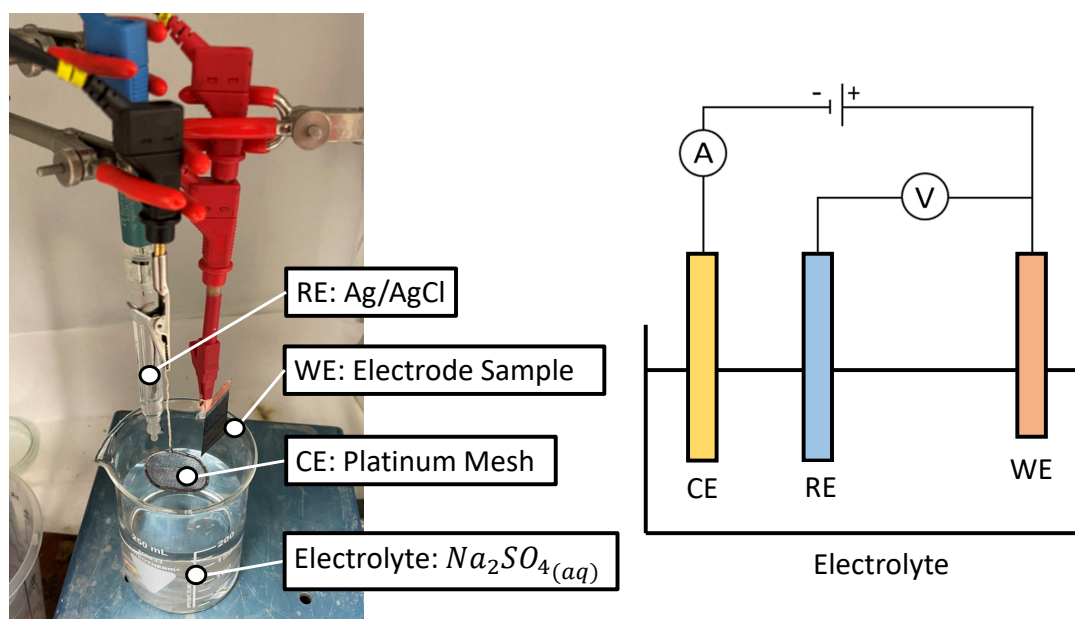


Figure 3.6: Three-electrode setup for the cyclic voltammetry measurement.

Equation 3.1 is used to calculate the total capacitance C_T [153]. ΔQ is the total charge and ΔV is the defined voltage range. ν is the scan rate and V_0 is the voltage range from 0 to 0.5V. The current response i is integrated with respect to the time history to obtain the charge. The defined voltage range to determine capacitance is the forward plus the backward scan $2V_0$, two times the voltage range.

$$C_T = \frac{\Delta Q}{\Delta V} = \frac{\int_0^{2V_0/\nu} |i| dt}{2V_0} \quad (3.1)$$

Three performance indexes are used to compare the samples: electrode-specific capacitance (F/g) (Carbon fabric plus slurry), slurry-specific capacitance (F/g) and areal capacitance (F/m^2). The selection criterion of the slurry formula is to select the highest values while also ensuring a good surface condition.

Gas Absorption Analysis

The NOVAtouch gas absorption analyser from Quantachrome Instruments is used to measure the Brunauer-Emmett-Teller (BET) surface area and the pore size distribution. Activated charcoal (AC) and graphene nanoplatelets (GNP) particles, as well as their slurries "b-AC300" and "b-GNP300" brushed on the plain weave carbon spread tow fabric (PW-CSTF), are characterised.

The electrodes coated with slurry are cut into small pieces and inserted into glass sample cells for measurements. Vacuum degassing is first performed to remove unwanted vapours. Activated charcoal (AC) and graphene nanoplatelets (GNP) particles are assigned to a heating profile of 250°C for 20 hours. As for the slurry-coated plain weave carbon spread tow fabric (PW-CSTF), the heating profile is set as 60°C for 40 hours since the maximum service for the SPI carbon conductive paint is 65°C.

After degassing, the sample cells are inserted with 9mm glass filler rods and dipped into a liquid nitrogen bath to perform gas absorption analysis. Brunauer-Emmett-Teller (BET) method is used to determine the surface face area by using Equation 3.2 [61, 101]. The instrument obtains the amount of gas adsorbed W and the P/P_0 term. The specific area can then be determined using the intercepts from the fitted linear curve.

$$\frac{1}{W \left(\left(\frac{P_0}{P} \right) - 1 \right)} = \frac{1}{W_m C} + \frac{C - 1}{(W_m C)} \left(\frac{P}{P_0} \right) \quad (3.2)$$

Surface Morphology

The water drop test is performed with a KSV CAM 200 Optical Contact Angle Goniometer to examine the wettability of the electrode surface with distilled water. The surface morphology is examined using a JEOL Scanning Electron Microscope.

3.4. Gel Polymer Electrolyte

3.4.1. Materials and Equipment

The materials for gel polymer electrolytes purchased from Sigma-Aldrich include poly(vinylidene fluoride-co-hexafluoropropylene) (PVDF-HFP 427187) as the co-polymer that incorporates the liquid medium. Triethyl phosphate (TEP 8.21141) as the solvent and the bis(trifluoromethane)sulfonimide lithium (LiTFSI, 15224-50G-F) as the electrolyte salt.

The equipment for fabricating gel polymer films includes a film applicator (Sheen Instruments 1117/200mm), and the speed is controlled by the Erichsen Film Applicator (Model 509MC-I). The liquid polymer electrolytes are casted on glass plates provided by Riboglas Glashandel B.V. The vacuum drying of the gel polymer electrolytes is performed in the Thermoscientific Vacutherm vacuum oven (40x30x30 cm, maximum 400°C), which is vacuumed by a VACUUBRAND MD 4 NT Diaphragm pump.

3.4.2. Polymer Electrolyte Solution

Ten liquid polymer electrolytes with varying LiTFSI concentrations from 0 wt% to 100 wt% of the PVDF-HFP are produced using the formulation table in [Table D.6](#). The code names in the table are used in this report for electrolytes. For every solution, 9 grams of TEP and 2 grams of PVDF-HFP pellets are added into a glass vial and mixed with a magnetic stirrer at 550 rpm, 70°C for four hours until it fully dissolves into a homogeneous solution. Afterwards, the polymer solution is added with different amounts of LiTFSI and with an addition of 1 gram TEP. The glass vials are sealed with Parafilm, and the solution is mixed for 16 hours at 65°C, 250 rpm. Finally, the mixed liquid polymer solutions are degassed in a vacuum desiccator at full vacuum for 30 minutes.

3.4.3. Gel Polymer Electrolyte Films

To produce gel polymer electrolytes (GPE), the liquid polymer electrolyte solutions are poured onto glass plates, and solution casting is performed using a 600 µm film applicator gap. The casted polymer electrolyte solutions are then vacuum dried at 70°C. Two batches of GPE are made, which have different drying periods. The first batch of the GPE LiTFSI-0% to LiTFSI-60% is vacuum dried at 70 °C for 24 hrs, while the second batch of GPE LiTFSI-60% to LiTFSI-100% is dried for 72 hrs. Volatiles vented from the oven are collected with a cold trap before reaching the vacuum pump.

3.4.4. Characterisation

The Fourier transform infrared (FTIR) was performed to study the functional groups in the liquid and cured electrolytes. Electrochemical impedance spectroscopy (EIS) is performed to determine the bulk resistance R_b of the gel polymer electrolyte (GPE). The ionic conductivity σ can then be calculated using [Equation 3.3](#) in which t is the thickness of the GPE, and A is the area of the GPE in contact with the 9 mm diameter brass electrodes.

$$\sigma = \frac{t}{R_b A} \quad (3.3)$$

For GPE LiTFSI-0% to 60%, a frequency range of 0.5 Hz to 10 MHz with an alternating voltage of 5 mV_{rms} is applied. For GPE LiTFSI-60%, 80% and 100%, a frequency range of 0.1 Hz to 1 MHz is applied with an alternating voltage of 500 mV_{rms} . EIS is measured using the Novocontrol Impedance Analyser.

3.5. Structural Supercapacitor Cell Assembly

Three batches of structural supercapacitor (SSC) cells, namely batch one to batch three, are produced. Batch one served as the first trial for the SSC concept. Afterwards, subsequent improvements are implemented for batch 2, followed by final improvements for batch 3. The assembly process is illustrated in Figure 3.7. The vacuum setups for the semi-cell assembly and the full-cell epoxy infusion are presented in Figure 3.8.

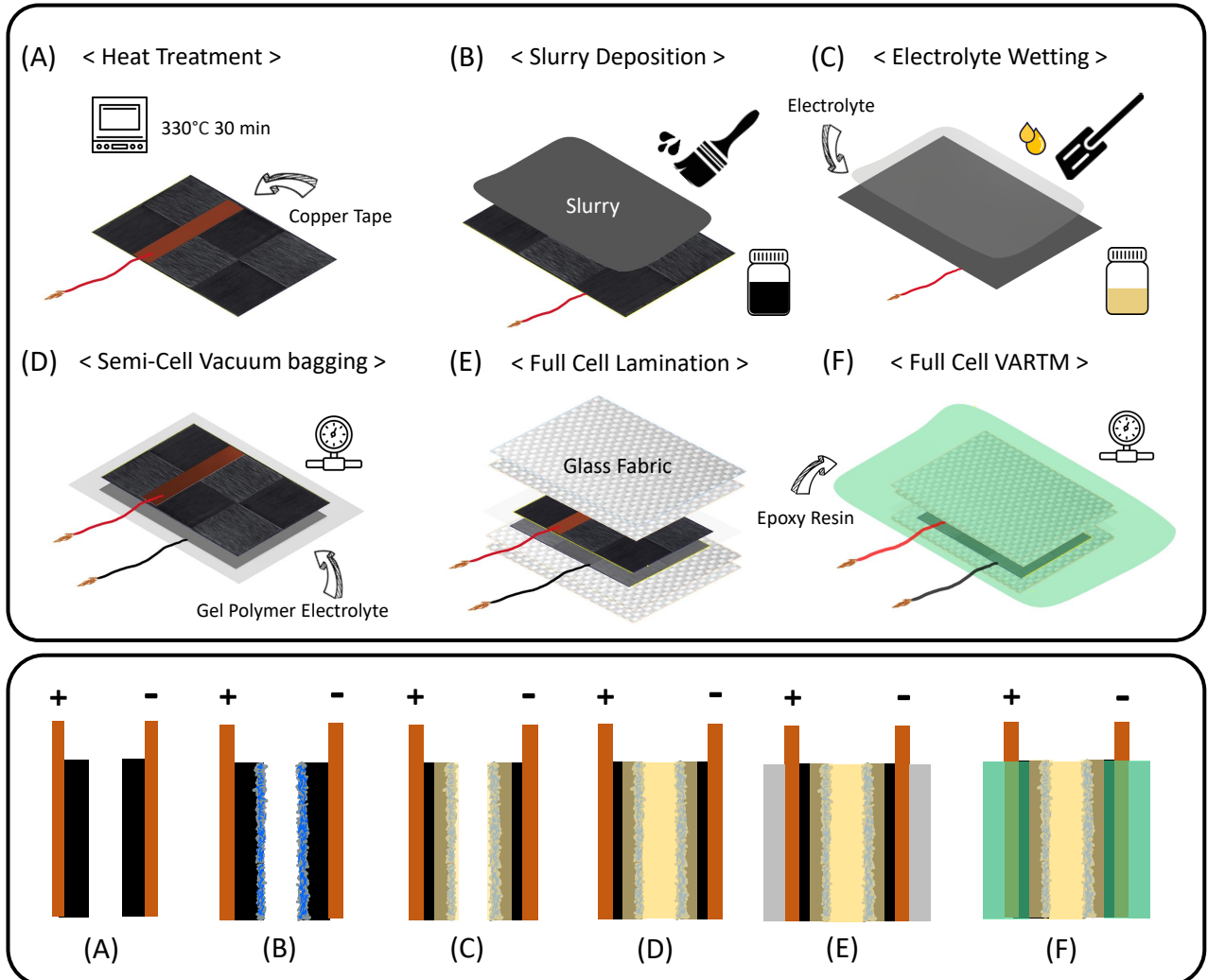


Figure 3.7: An illustration of the manufacturing process for the batch 3 structural supercapacitors (SSC). The upper block shows the step-by-step process for Batch 3, which uses a gel polymer electrolyte separator. The bottom block shows the SSC cross-section for each step. Icon source: [14, 56, 86, 125]

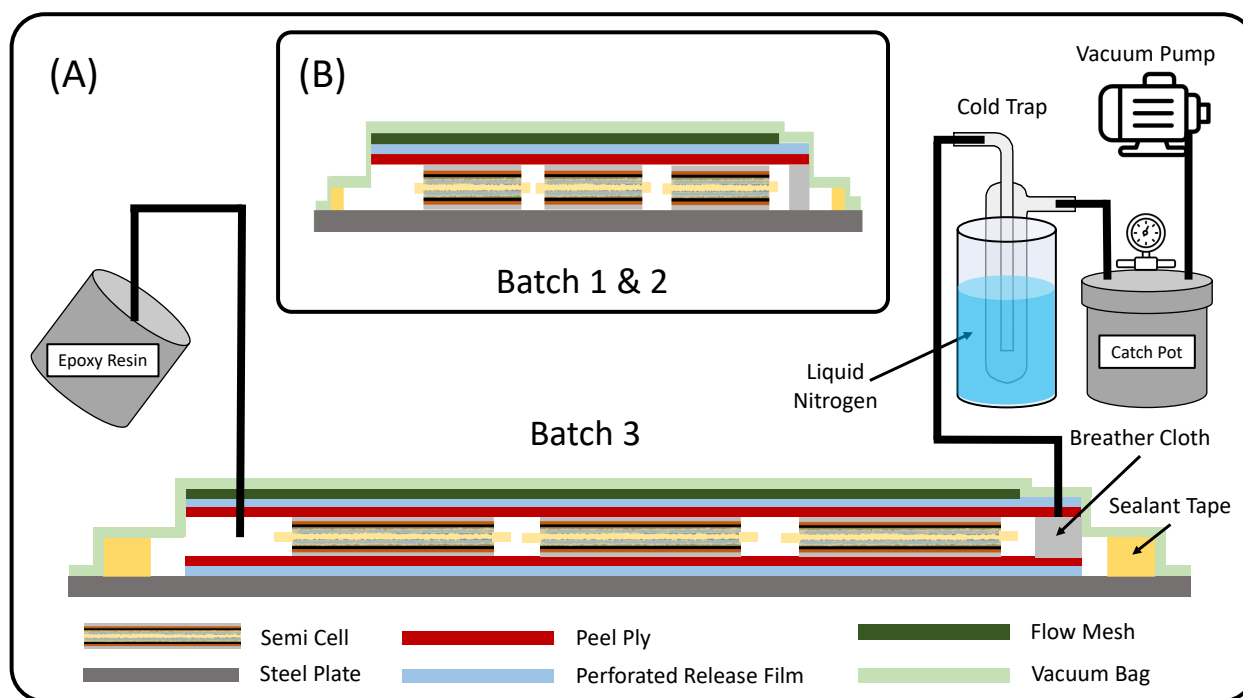


Figure 3.8: The illustration of the semi-cell lamination process and the VARTM vacuum system layup for the full-cells. (A) Batch 3 layup sequence. (B) Batch 1&2 layup sequence. The cold trap is only needed for the semi-cell assembly. The flow mesh is only needed for VARTM. Icon sources: [47], ChemSketch.

3.5.1. Batch One

Batch one represents the first attempt to assemble the characterised electrode and gel polymer electrolyte into a semi-cell. In this batch, twelve cells are produced using the "b-GNP400" slurry as the electrode material. Seven gel polymer electrolytes (GPE) of LiTFSI-0% to LiTFSI-60% are produced. The code names of the cells are shown in Table 3.4. The Gantt chart for batch 3 production is shown in Figure C.1.

Cell Code	Gel Polymer Electrolyte TEP/PVDF-HFP	Carbon Slurry
Cell 1	LiTFSI-10%	b-GNP400
Cell 2		
Cell 3		
Cell 4		
Cell 5		
Cell 6		
Cell 7	LiTFSI-20%	
Cell 8		
Cell 9		
Cell 10		
Cell 11		
Cell 12		

Table 3.4: Batch 1 produces 12 cells with 6 different gel polymer electrolyte concentrations.

The slurry "b-GNP400" in Table 3.2 is used for batch one. The amount of slurry required for 24 substrates (60mm-by-40mm) is shown in Table 3.5. Before the brush application, the copper tape is attached to the 40 mm side of the PW-CSTF. The b-GNP400 slurry is applied on the same electrode surface to which the copper tape is attached. This design attempted to reduce the internal resistance since placing the copper tape on the other surface would generate higher internal resistance due to the epoxy infusion.

Code name	g		
	GNP	Ethanol	SPI carbon conductive paint
b-GNP400	4.8	12	12

Table 3.5: Slurry formula table for batch 1.

Solution casting is performed using a 600 μm film applicator blade gap at a casting speed of 15 mm/min. The casted polymer electrolyte solutions are vacuum dried for 24 hours at 70°C to produce gel polymer electrolyte films shown in Figure 3.9.

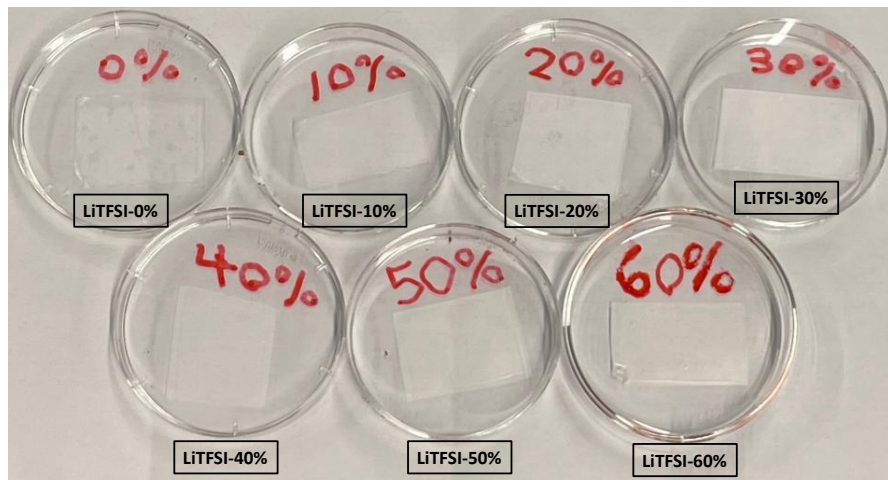


Figure 3.9: Batch one gel polymer electrolyte samples from LiTFSI 0wt% to 60wt%.

Twelve semi-cells are assembled by applying a 25 mbar vacuum for 30 minutes and a 200 mbar vacuum for 24 hours at 70°C. The assembled semi-cells are then wrapped with Parafilms for semi-cell characterisation. The semi-cell assembly process is shown in Figure 3.10, and their dimensions are shown in Table 3.6.

Components	Dimensions (mm*mm)
Plain weave carbon spread tow fabric	60*40
Gel polymer electrolyte	65*45

Table 3.6: Batch 1 semi-cell dimensions.

3.5.2. Batch Two

Batch two improves the design of batch one by relocating the copper tape to the outer surface of the plain weave carbon spread tow fabric (PW-CSTF). Twelve structural supercapacitor (SSC) cells are fabricated. 6 cells are deposited with b-AC300 slurry, and 6 cells are deposited with b-GNP300 slurry. The code names for batch two cells are shown in Table 3.7, and the Gantt chart of batch 2 is shown in Figure C.2. Slurries "b-AC300" and "b-GNP300" in Table 3.2 are used as the electrode material. Six gel polymer electrolytes (GPE) of LiTFSI-10% to LiTFSI-60% are produced.

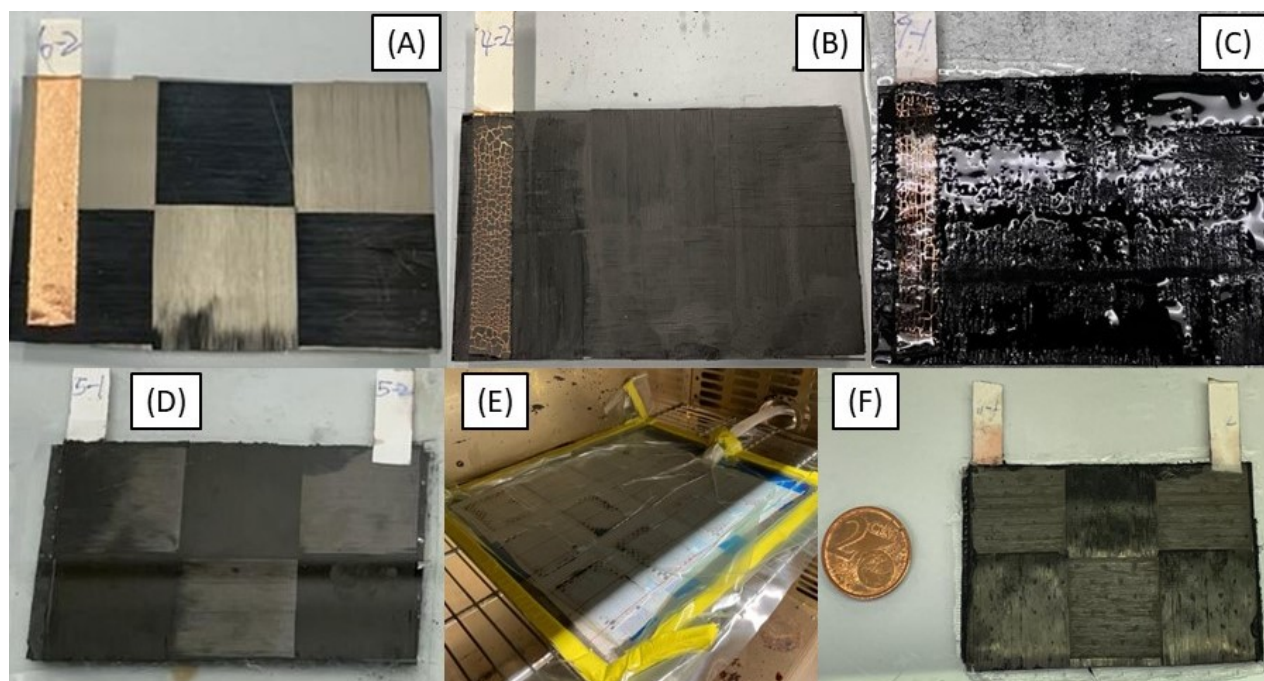


Figure 3.10: Batch 1 semi-cell assembly. (A) The copper tapes are attached to the heat-treated PW-CSTF. (B) Brush application of the b-GNP400 slurry. (C) Wetting the electrode surface with liquid polymer electrolyte. (D) Assembling semi-cell. (E) Vacuum bagging setup of the Semi-cell in an oven. (F) The assembled semi-cell.

Cell Code	Carbon Slurry	Gel Polymer Electrolyte TEP/PVDF-HFP	Encapsulation
Cell 1	b-AC300	LiTFSI-10%	PW-CSTF x 2 Glass Fabric x 2
Cell 2		LiTFSI-20%	
Cell 3		LiTFSI-30%	
Cell 4		LiTFSI-40%	
Cell 5		LiTFSI-50%	
Cell 6		LiTFSI-60%	
Cell 7	b-GNP300	LiTFSI-10%	Glass Fabric x 4
Cell 8		LiTFSI-20%	
Cell 9		LiTFSI-30%	
Cell 10		LiTFSI-40%	
Cell 11		LiTFSI-50%	
Cell 12		LiTFSI-60%	

Table 3.7: Batch 2 structural supercapacitors cell code names.

The liquid polymer electrolytes are casted with a 15 mm/min speed using a 600 μm gap and are vacuum dried at 70°C for 24hrs. The polymer electrolytes in their casted liquid state and after drying are shown in [Figure 3.11](#). The slurry required for 24 substrates is shown in [Table 3.8](#). After the slurry deposition, the copper tape is attached to the other electrode surface. 12 semi-cells are then laminated and vacuum bagged with an 850 mbar vacuum at 70°C for 24 hours. The wires are then attached to the copper tape current collectors. An example of a semi-cell can be seen in [Figure 3.12](#).

The full cells of cells 1 to 6 are fabricated by encapsulating the semi-cells using two layers of glass fabric and two layers of plain weave carbon spread tow fabric (PW-CSTF). The full cells 7 to 12 are encapsulated

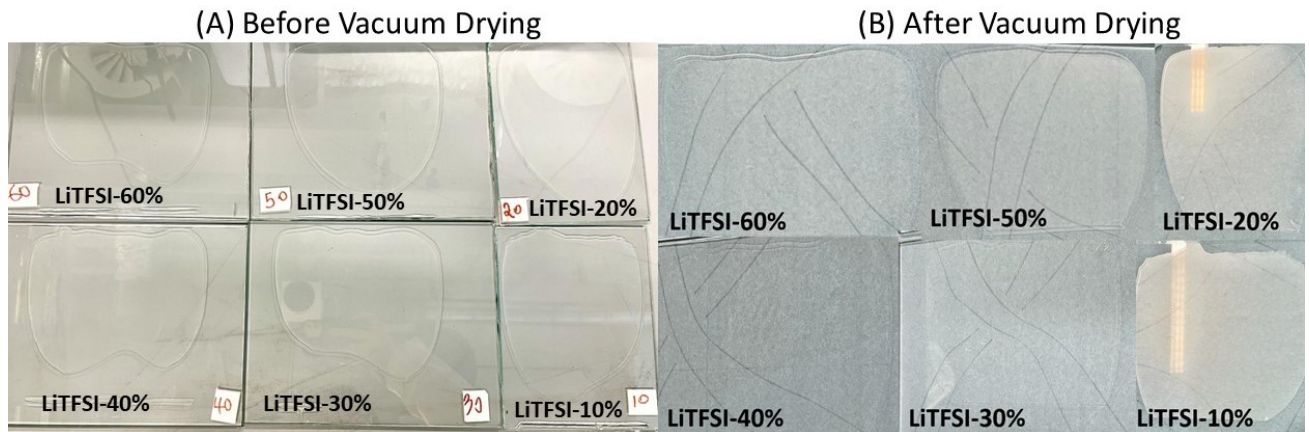


Figure 3.11: (A) Liquid polymer electrolyte solutions of LiTFSI-10% to LiTFSI-60%. (B) Gel polymer films after vacuum drying.

Code name	AC/GNP	g	
		Ethanol	SPI carbon conductive pain
b-GNP300	1.8	6	6
b-AC300	1.8	6	6

Table 3.8: Slurry formula table for batch 2.

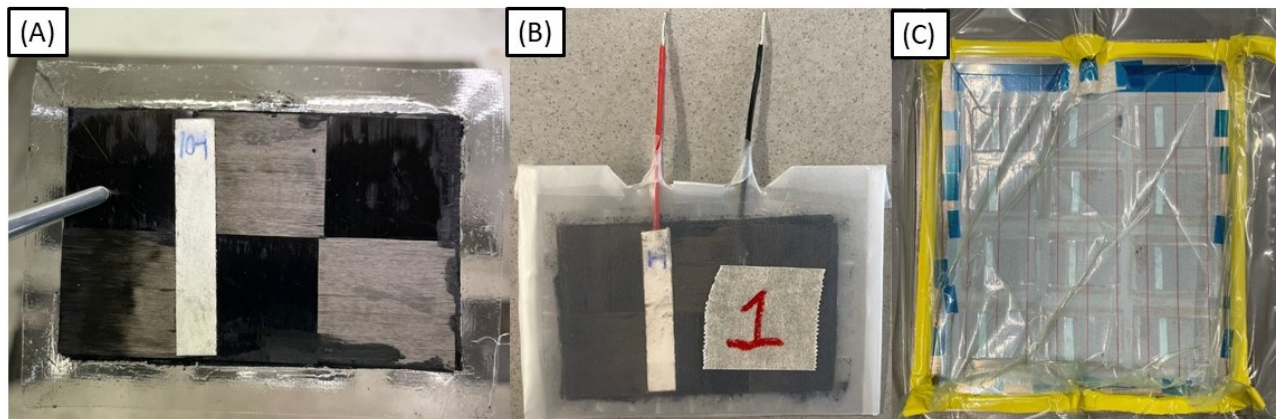


Figure 3.12: Batch 2 semi-cell. (A) An assembled semi-cell. (B) Wires are attached to the copper tape of the semi-cell. (C) Vacuum pressing of the 12 semi-cells.

by four layers of glass fabric. The VARTM (vacuum-assisted resin transfer moulding) is performed for epoxy infusion. The VARTM for cells 1 to 6 was infused using a 55 mbar vacuum and cured at a 250 mbar vacuum. The VARTM for cells 7 to 12 was infused using an 850 mbar vacuum. The full cells from cell 1 to cell 12 are shown in [Figure 3.13](#). The layup dimensions of batch 2 are shown in [Table 3.9](#).

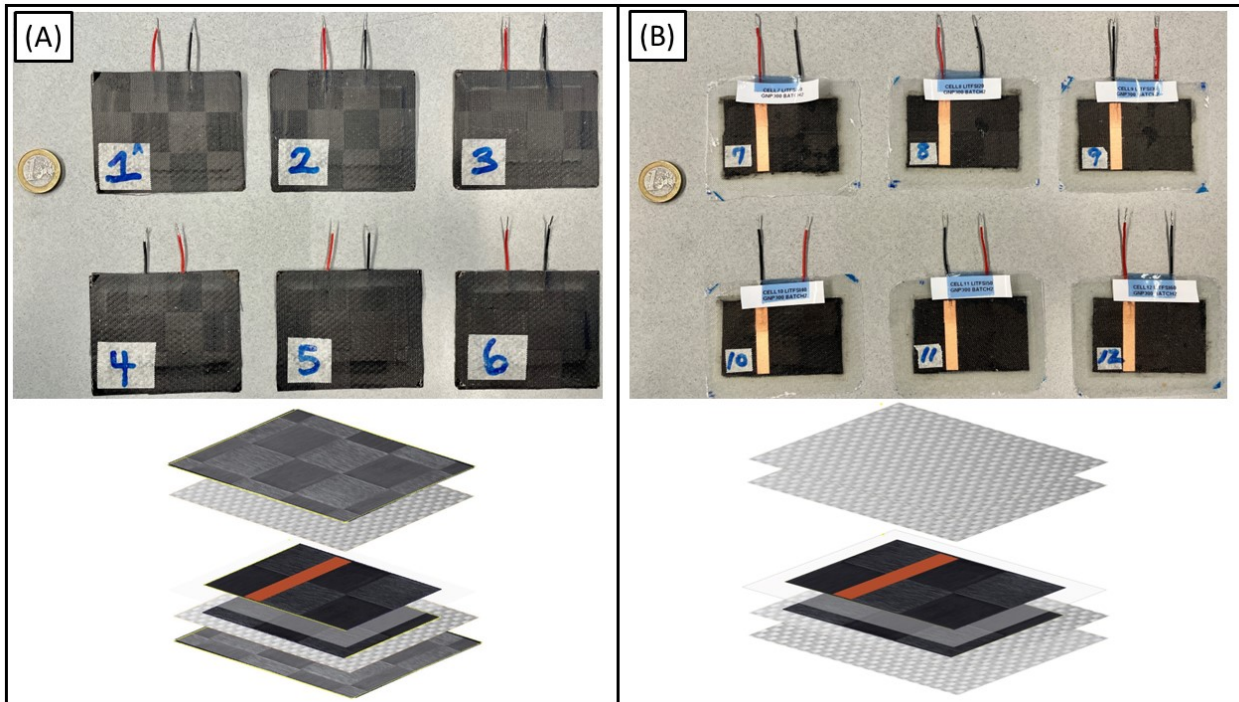


Figure 3.13: Batch 2 full cells. (A) Cells 1 to 6 and their 3D layout. (B) Cells 7 to 12 and their 3D layout.

Components	Dimensions (mm*mm)
Plain weave carbon spread tow fabric	60*40
Gel polymer electrolyte	65*45
Glass fabric insulation	80*65
Plain weave carbon spread tow fabric	80*65

Table 3.9: Batch 2 cell dimensions.

3.5.3. Batch Three

In batch 3, ten full cells are produced using "b-GNP300" slurry as the electrode material. The code names of the cells are shown in Table 3.10. The Gantt chart for batch 3 production is shown in Figure C.3.

Copper tape and the wires are attached to the plain weave carbon spread tow fabric (PW-CSTF) after the heat treatment. The width of the copper tape was increased from 6 mm (batch 1 and 2) to 12 mm. Afterwards, the b-GNP300 slurry shown in Table 3.11 was deposited onto 20 substrate surfaces. The film applicator gap was increased from 600 μm to 800 μm for solution-casting gel polymer electrolytes. Cells 1 to 5 employ a gel polymer electrolyte (GPE) separator shown in Figure 3.14 (A), while cells 6 to 10 employ two GPE-impregnated glass fabrics as the separator shown in Figure 3.14 (B). The GPE-impregnated glass fabrics are then sandwiched between two electrodes, and the outer surface of the semi-cells is wetted with the same liquid gel electrolyte. The semi-cells are assembled by vacuum pressing with an 850 mbar vacuum at 70°C for 24 hours, and the full-cell is fabricated using VARTM at an 850 mbar vacuum for epoxy infusion and curing. The full cells before and after epoxy resin infusion are shown in Figure 3.15. The layout dimensions of batch 3 are shown in Table 3.12.

Cell Code	Carbon Slurry	Separator	Gel Polymer Electrolyte TEP/PVDF-HFP
Cell 1	b-GNP300	Gel Polymer Electrolyte	LiTFSI-40%
Cell 2			LiTFSI-50%
Cell 3			LiTFSI-60%
Cell 4			LiTFSI-80%
Cell 5			LiTFSI-100%
Cell 6	b-GNP300	Gel Polymer Electrolyte Impregnated Glass Fabric	LiTFSI-40%
Cell 7			LiTFSI-50%
Cell 8			LiTFSI-60%
Cell 9			LiTFSI-80%
Cell 10			LiTFSI-100%

Table 3.10: Batch three supercapacitor cell code names.

Code name	g		
	GNP	Ethanol	SPI carbon conductive paint
b-GNP300	3	10	10

Table 3.11: Slurry formula table for batch 3.

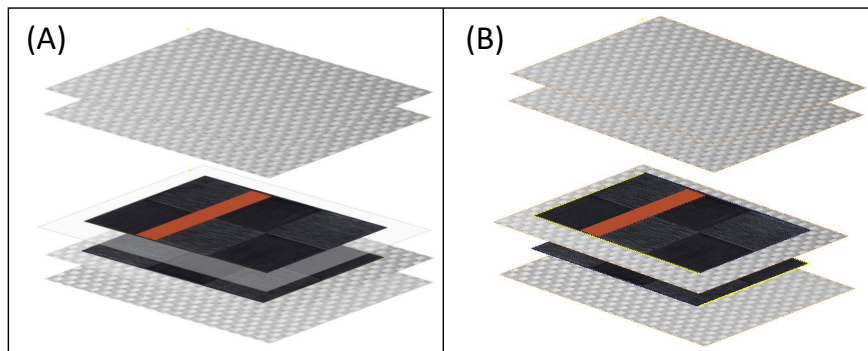


Figure 3.14: The 3D layup of the batch 3 cells. (A) Batch 3 cells 1 to 5 with a gel polymer electrolyte (GPE) separator. (B) Batch 3 cells 6 to 10 with GPE-impregnated glass fabrics as the separator.

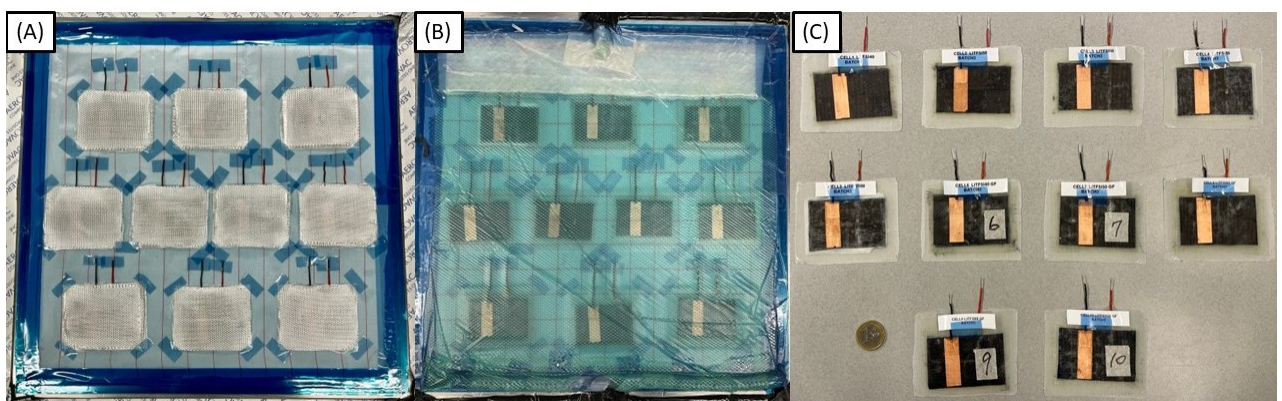


Figure 3.15: Full cells in batch three before and after VARTM.

Components	Dimensions (mm*mm)
Plain weave carbon spread tow fabric	60*40
Gel polymer electrolyte	65*45
Gel polymer electrolyte-impregnated glass fabric separator	70*50
Glass fabric insulation	80*70

Table 3.12: Batch 3 cell dimensions.

3.6. Structural Supercapacitor Cell Characterisation

3.6.1. Electrochemical Performance

The Metrohm Autolab is used for electrochemical performance. Cyclic voltammetry (CV) is first conducted on the semi-cells to evaluate their electrical double-layer behaviour and to determine their voltage window to prevent overcharging. A voltage window study from 0 V to 0.1 V is scanned with a 2 mV/s scan rate. The voltage window is then incrementally increased for 0.1 V until a spike is observed on the CV curve.

Galvanostatic charge-discharge (GCD) measurements are performed on both the full-cells and the semi-cells to determine the coulombic efficiency (CE), equivalent series resistance (R_{ES}), discharge-specific capacitance, discharge-specific energy, and discharge-specific power. The relation between the energy storage and the voltage window is studied using a 5 mA constant current applied for batch 2 cells 10 to 12, and a 1 mA constant current is applied for batch 3 cells 1 to 10. Once the maximum voltage window is determined, current values from 1 mA to 15 mA are applied to the cells using a fixed voltage window to study the current influence on the cell performance.

The coulombic efficiency (CE) is determined using Equation 3.4, in which Q is the amount of charge, I is the applied constant current, and t is the charge and discharge time.

$$CE = \frac{Q_{\text{discharge}}}{Q_{\text{charge}}} = \frac{It_{\text{discharge}}}{It_{\text{charge}}} \quad (3.4)$$

The equivalent series resistance (R_{ES}) of the cell is determined using the initial voltage drop during the GCD discharge curve. R_{ES} can be determined using Equation 3.5, in which ΔV is the voltage drop and I is the applied constant current.

$$R_{ES} = \frac{\Delta V}{I} \quad (3.5)$$

The discharge capacitance $C_{\text{discharge}}$ is determined by Equation 3.6 [153].

$$C_{\text{discharge}} = \frac{I\Delta t}{\Delta V} \quad (3.6)$$

The discharge energy $E_{\text{discharge}}$ (Joules) is determined by Equation 3.7, which is the integral of voltage over time [81, 153]. The discharge power $P_{\text{discharge}}$ (Wh) is determined by dividing the discharge energy by the discharge time shown in Equation 3.8. $E_{\text{discharge}}$ is divided by 3600 to convert Joules to Watt-hour.

$$E_g = \int_0^{t_d} IV dt \quad (3.7)$$

$$P_{\text{discharge}} = \frac{E_g}{3600 t_{\text{discharge}}} \quad (3.8)$$

Electrochemical impedance spectroscopy (EIS) is performed in which a frequency is applied from 0.1 Hz to 1 mega Hz using an alternating current potential of 10 mV_{RMS} . The behaviour at the high-frequency region is fitted with a semi-circle.

3.6.2. Full Cell Flexural Test

The three-point flexural test is performed on batch 2 and batch 3 full cells. To comply with safety measures, the full cells are required to be sealed with polyethylene (PE) foils during the test shown in Figure 3.16. To examine the effect of the PE foil on the flexural test data, mock-up samples without electrode and electrolyte materials are fabricated and tested in sealed PE foils prior to the full cell tests. PE pouch bags are used for containing the material and volatiles from the full cell failure, and the mock-up test samples are to prove that there is no puncture of the PE bag when the sample fails. An 850 vacuum is applied to fabricate the mock-up samples using VARTM. The flexural stress σ and strain ε are determined using Equation 3.9 and Equation 3.10 from the ASTM D7264 standard.

$$\sigma = \frac{3PL}{2bh^2} \quad (3.9)$$

$$\varepsilon = \frac{8\delta h}{L^2} \quad (3.10)$$

P is the applied load, L is the support span, b is the specimen width and h is the specimen thickness. The dimensions for each mock-up sample are shown in Table D.7 to Table D.8. The flexural modulus of elasticity E_f^{chord} is determined using the chord modulus method in Equation 3.11, in which the strain range from 0.001 to 0.003 is used.

$$E_f^{\text{chord}} = \frac{\Delta\sigma}{\Delta\varepsilon} \quad (3.11)$$

Mock-up samples are made with the layup of two 6cm-by-4cm plain weave carbon spread tow fabrics (PW-CSTF) sandwiched by four layers of 8 cm by 7 cm glass fabrics, having the same fabric layup and dimensions as the batch 3 full cells. The mock-up samples are categorised into different study groups shown in Table 3.13. The different study groups are used to investigate the effect of the PE films and PE protection bags on flexural properties.

Group code	PE Film	PE Pouch Bag	Number of Samples
with-film-and-bag	v	v	5
with-film-no-bag	v	x	5
no-film-with-bag	x	v	5
no-film-no-bag	x	x	5

Table 3.13: Samples for the mock-up flexural testing. Five samples are used for each mock-up category

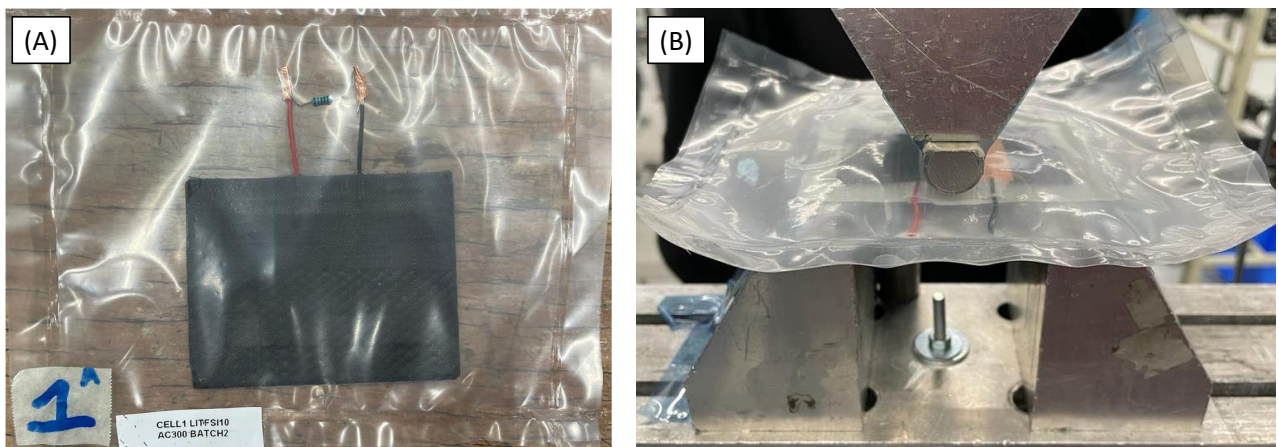


Figure 3.16: (A) The full cell is sealed in a PE pouch bag. A resistor is connected between the terminals to dissipate residual currents during the test. (B) The flexural test setup.

Results

4.1. Electrode

4.1.1. Heat Treatment Study of the Plain Weave Carbon Spread Tow Fabric

In order to partially remove the binders on the plain weave carbon spread tow fabric (PW-CSTF), the thermogravimetric analysis (TGA) is performed to search for the suitable temperature. Figure 4.1 (A) shows a plain weave carbon spread tow fabric (PW-CSTF) mass reduction affected by the programmed temperature. The degradation of the binder and sizing materials attributed to a weight loss of 9%.

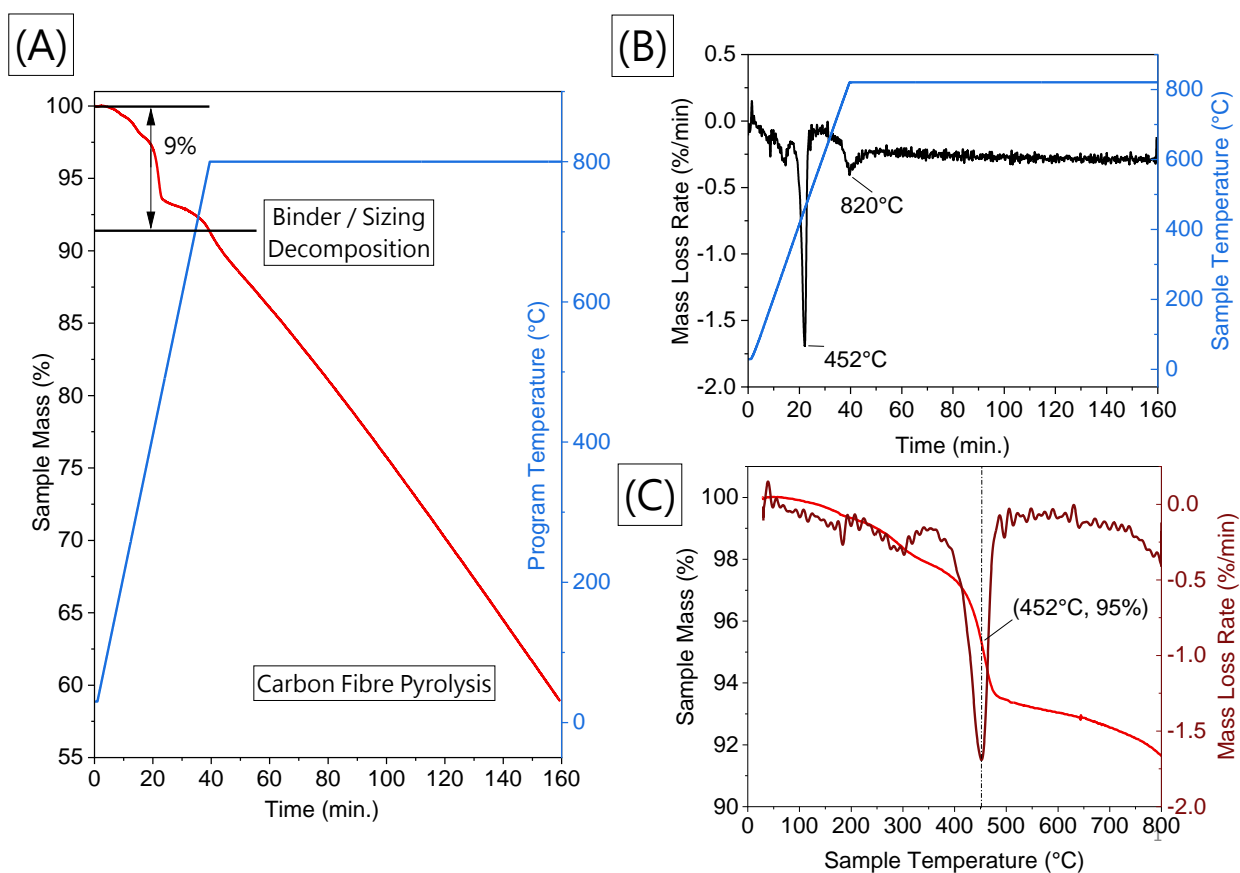


Figure 4.1: (A) The time history of the PW-CSTF mass loss as a function of temperature. (B) The time history of the PW-CSTF mass loss rate of the PW-CSTF. (C) PW-CSTF mass and its mass loss rate as a function of temperature.

After the programmed temperature reaches 800°C, a steady weight loss from the decomposition of PW-CSTF due to pyrolysis is observed. The derivative thermogravimetry (DTG) shown in Figure 4.1 (B) identified the highest mass loss rate from the degradation of the binder and the sizing at 452°C. To find the corresponding sample mass percentage at 452°C, the sample mass percentage and the DTG are plotted according to the temperature history shown in Figure 4.1 (C). The sample mass percentage at 452°C is 95%, indicating a mass loss of 5%.

Thermogravimetric analysis (TGA) indicated that the heat treatment at 452°C will result in a rapid binder decline. Thus, a lower temperature is searched by an experimental approach by performing heat treatments using 40mm-by-60mm PW-CSTF samples in a furnace vented with nitrogen. The heat treatment is performed for 30 minutes using various temperatures starting from 450°C. Temperatures at 450°C and 400°C showed weave separation upon handling. At 350°C, weave separation occurred when the fabric was slightly bent. Eventually, the heat treatment at 330°C showed that the fabric could be bent without weave separation while the binder patterns were no longer visible. The comparison of the PW-CSTF surfaces before and after the 330°C 30-minute heat treatment is shown in Figure 4.2.

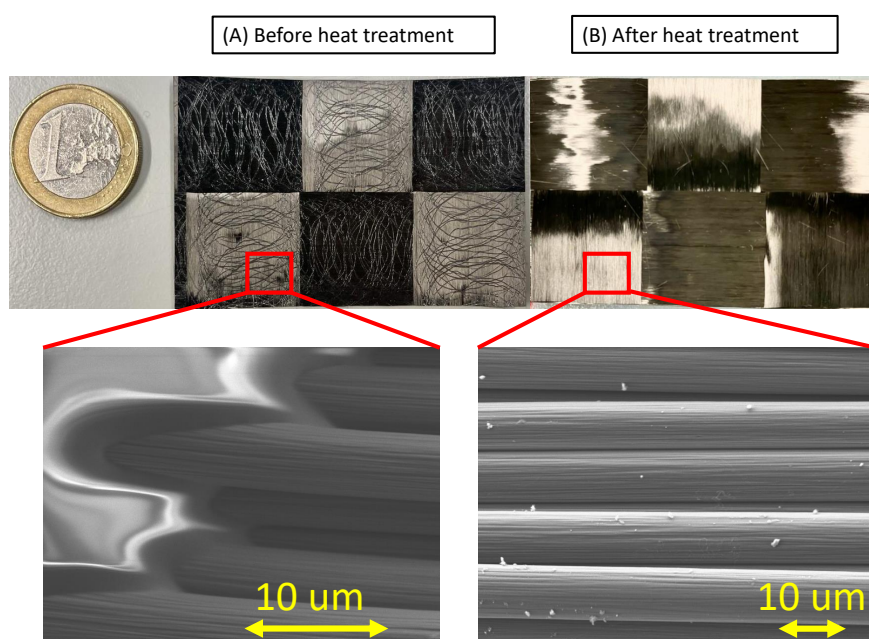


Figure 4.2: Plain weave carbon spread tow fabric and their SEM images before and after heat treatment at 330°C for 30 minutes.

4.1.2. Dip Coated-Electrodes

In Figure 4.3 (A), electrode-specific capacitance $C_{sp,E}$ and the electrode weight showed a positive correlation. However, a negative correlation is shown in Figure 4.3 (B) between the slurry-specific capacitance $C_{sp,S}$ and the slurry weight. The findings suggest that increasing the concentration of the activated charcoal (AC) in the slurry can increase the total capacitance; however, the increase rate decreases since there is a finite electrode surface contact with the electrolyte. The slurry-specific capacitance provides useful information on the electrode's surface properties, such as wettability with the electrolyte and the contact surface area.

The samples among each slurry formula that has the highest electrode-specific capacitance are compared in Figure 4.3 (D). The CV curves show blunt edges and slanted behaviours, which indicates the resistance of the slurry, PW-CSTF and its interface with the copper tape. In (E), the heat-treated plain weave carbon spread tow fabric (PW-CSTF) and its deposition of the carbon paint showed negligible capacitance. This implies that the active material that stores charge is the slurry material.

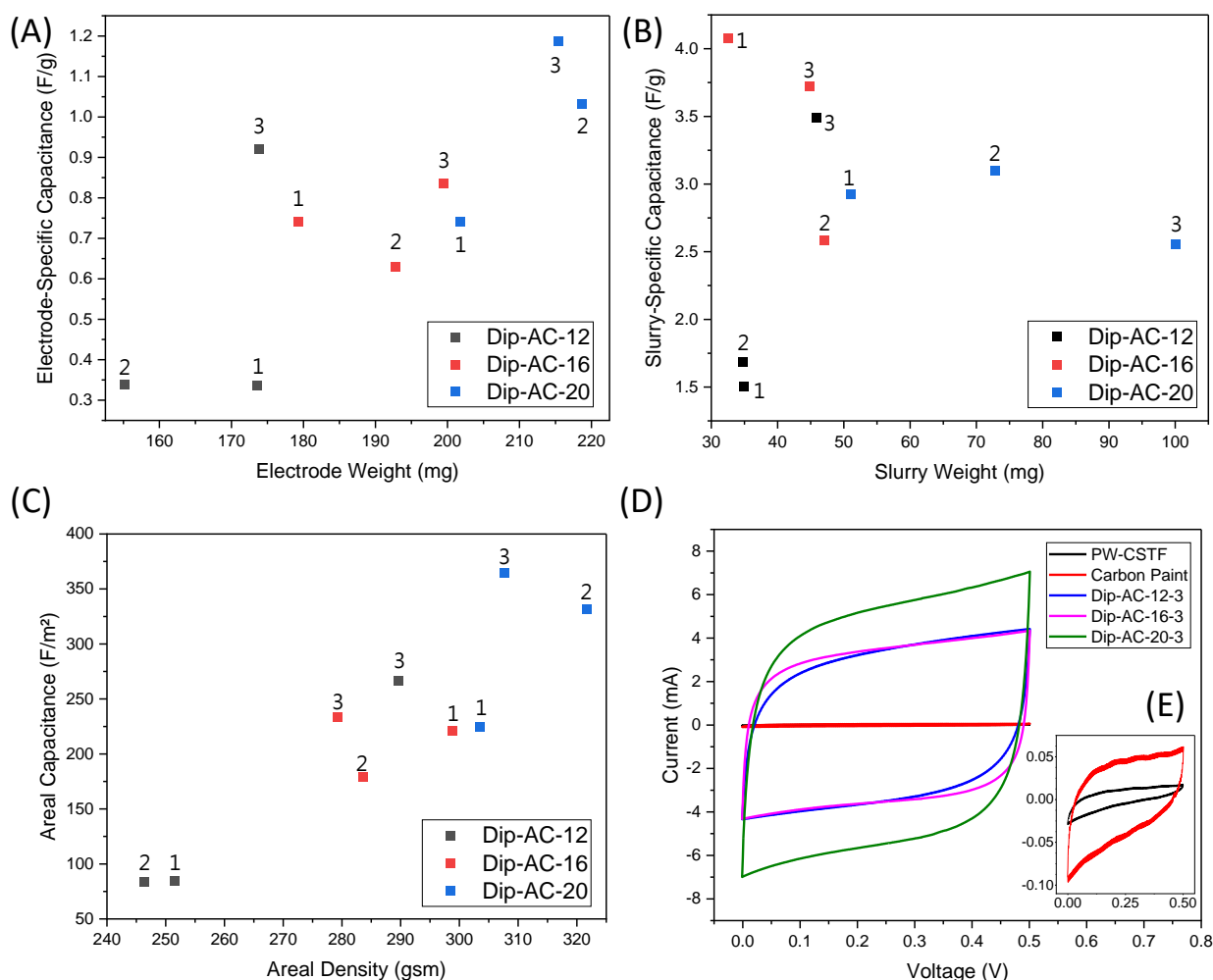


Figure 4.3: Performance of the dip-coated electrodes. (A) The electrode-specific capacitance versus the electrode weight. (B) The slurry-specific capacitance versus the slurry weight. (C) Areal capacitance versus areal density. (D) CV curves of the highest electrode-specific capacitance for each slurry formula. The number 3 indicates the electrode is dipped 3 times. (E) Cyclic voltammetry (CV) of the PW-CSTF and the PW-CSTF electrodes deposited with carbon paint.

The cyclic voltammetry (CV) measurements of all the electrodes in Figure D.2 showed a rectangular shape indicating an electric double-layer capacitor (EDLC) behaviour [81]. The slanted shapes of the CV curves indicate non-homogeneous electrode surfaces, which may be caused by slurry agglomeration shown in Figure D.2 (D) during the withdrawal from dip coating. The agglomeration showed poor attachment to the fabrics.

4.1.3. Brush Application

The brush application of the GNP-based slurry on the fabric electrodes showed a superior performance behaviour than the AC-based slurry in Figure 4.4 (A) and (C). The GNP slurry demonstrated a positive correlation between both the electrode-specific capacitance and areal capacitance versus the increased slurry weight. In contrast, the AC slurry showed a negative correlation. Figure 4.4 (B) indicates that the GNP slurry has a higher slurry-specific capacitance than the AC slurry. Although GNP slurry has a higher specific capacitance, surface cracks are observed at high GNP concentrations. The highest GNP slurry concentration, "b-GNP500", generates large surface cracks that can be taped off easily. Slurries "b-GNP400" and "b-GNP300" also showed surface cracks when two brushes were applied.

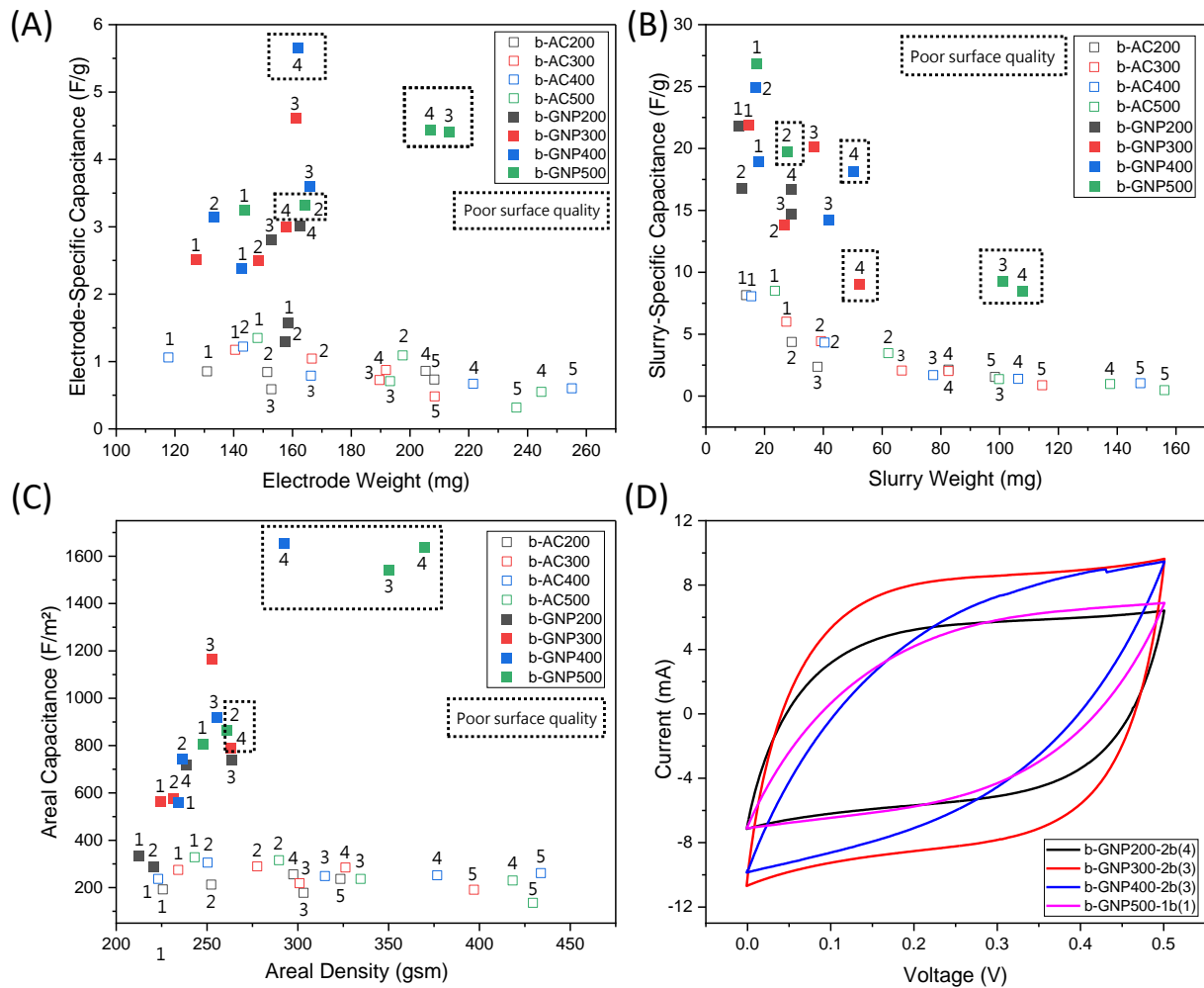


Figure 4.4: Performance of the brush application electrodes with the AC and GNP slurries. (A) Electrode-specific capacitance versus the electrode weight. (B) Slurry-specific capacitance versus the slurry weight. (C) Areal capacitance versus areal density. (D) CV curves of the highest electrode-specific capacitance for each GNP slurry formula. "1b" and "2b" means the number of brushes, and the numbers in the bracket are the numbered samples.

In Figure 4.4 (D), slurries "b-GNP400" and "b-GNP500" showed blunt and slanted CV shapes due to their surface crack defects and a thicker slurry deposition. The GNP slurry CV curves in Figure D.3 showed that for the same slurry deposition, both blunt and rectangular shapes exist. This implies that the slurry mixture and the slurry intake on the brush were not homogeneous. Nevertheless, "b-GNP200", "b-GNP300", and "b-GNP400" all showed that a rectangular CV curve could be obtained, while "b-GNP500" had only narrow CV shapes, which indicates high electrode resistance due to surface cracks.

The CV curves of the activated carbon (AC)-based slurry shown in Figure D.4 (A) to (C) did not show any correlation between the number of brushes with the total capacitance, while in (D) the "b-AC500" slurry showed a decrease in total capacitance when the brush number increases.

Due to the good performance of the b-GNP400 slurry, a mixed slurry with carbon particles, ethanol and SPI carbon paint of a weight ratio of 2:5:5 is produced. The carbon particle has different ratios of AC and GNP. Figure 4.5 showed that the increase of GNP wt% increased the performance; however, all slurry formulas showed a poor quality surface within the samples. Figure D.5 showed an increase in the blunt shape and the slanted slope when a second brush was applied, which is similar to the GNP slurry.

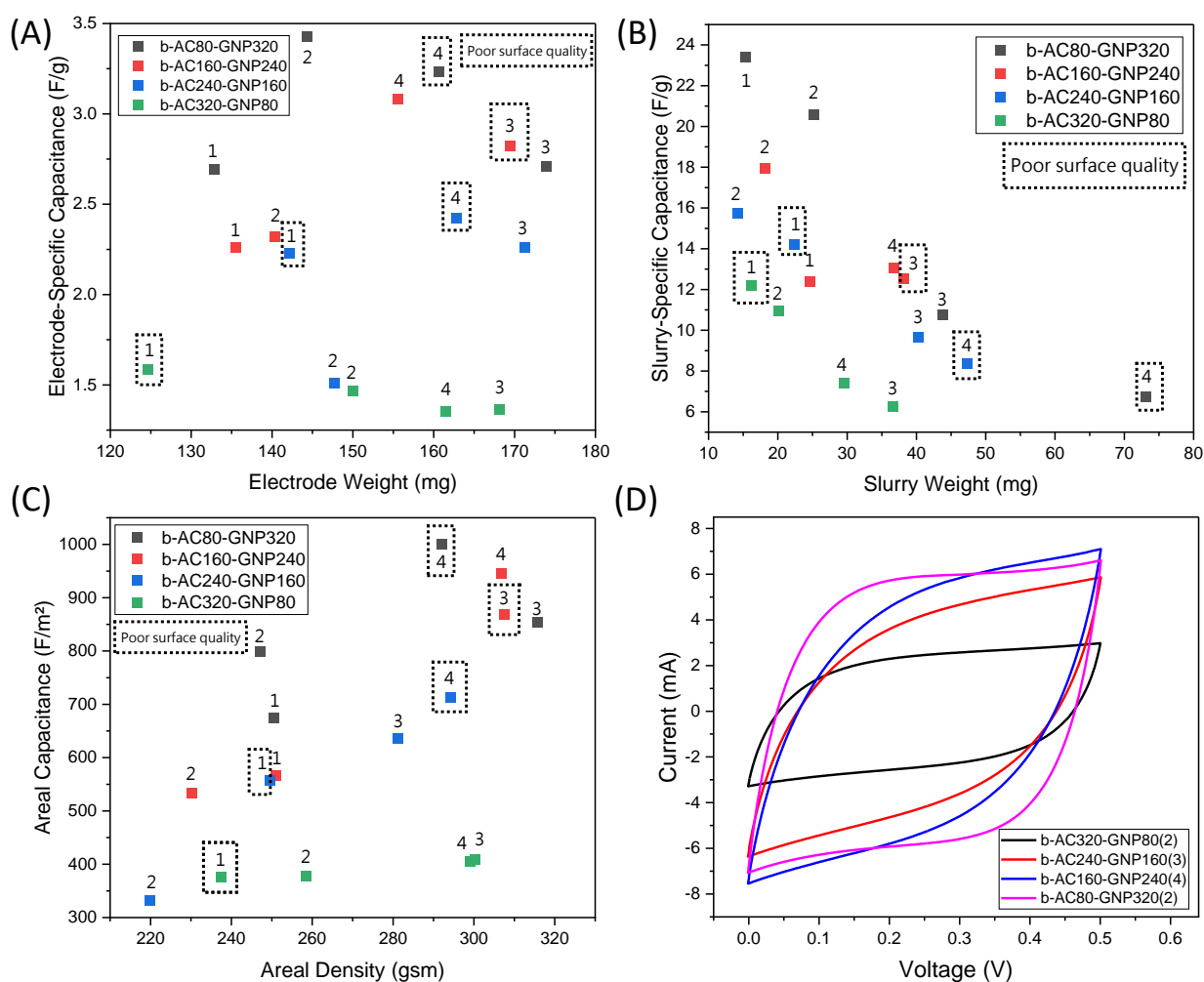


Figure 4.5: Performance of the brush application electrodes with the GNP-AC mixed slurry. (A) Electrode-specific capacitance versus the slurry weight. (B) Slurry-specific capacitance versus the slurry weight. (C) Areal capacitance versus the areal density. (D) CV curves of the highest electrode-specific capacitance for each slurry formula.

A comparison between the three slurry categories is illustrated in Figure 4.6. The results show that the GNP slurry exhibited the highest specific and areal capacitance, with the "b-GNP300" and "b-GNP400" slurries performing the best. These two slurries will be applied to cell fabrication. However, this comparison is based on a sodium sulfate (Na_2SO_4) aqueous electrolyte solution, and the result might change if a different electrolyte or a different electrolyte concentration is used.

To conclude, the highest performance electrode is the b-GNP300 slurry with two-time brushing, having an electrode-specific capacitance of $4.61 F/g$ and an areal capacitance of $1164.3 F/m^2$. When considering the slurry-specific capacitance, "b-GNP500" has the highest value of $26.88 F/g$. The obtained result is used as a selection criterion for the best electrode slurry used for cell production. Those values characterised in a liquid electrolyte using distilled water may be underestimated since the electrode's surface for the activated charcoal and graphene nanoplatelets are both hydrophobic. The contact angle of a water droplet on the electrode coated with a single brush layer of b-GNP300 and b-AC300 slurry has similar values at 110° shown in Table D.5, indicating hydrophobic surfaces [72].

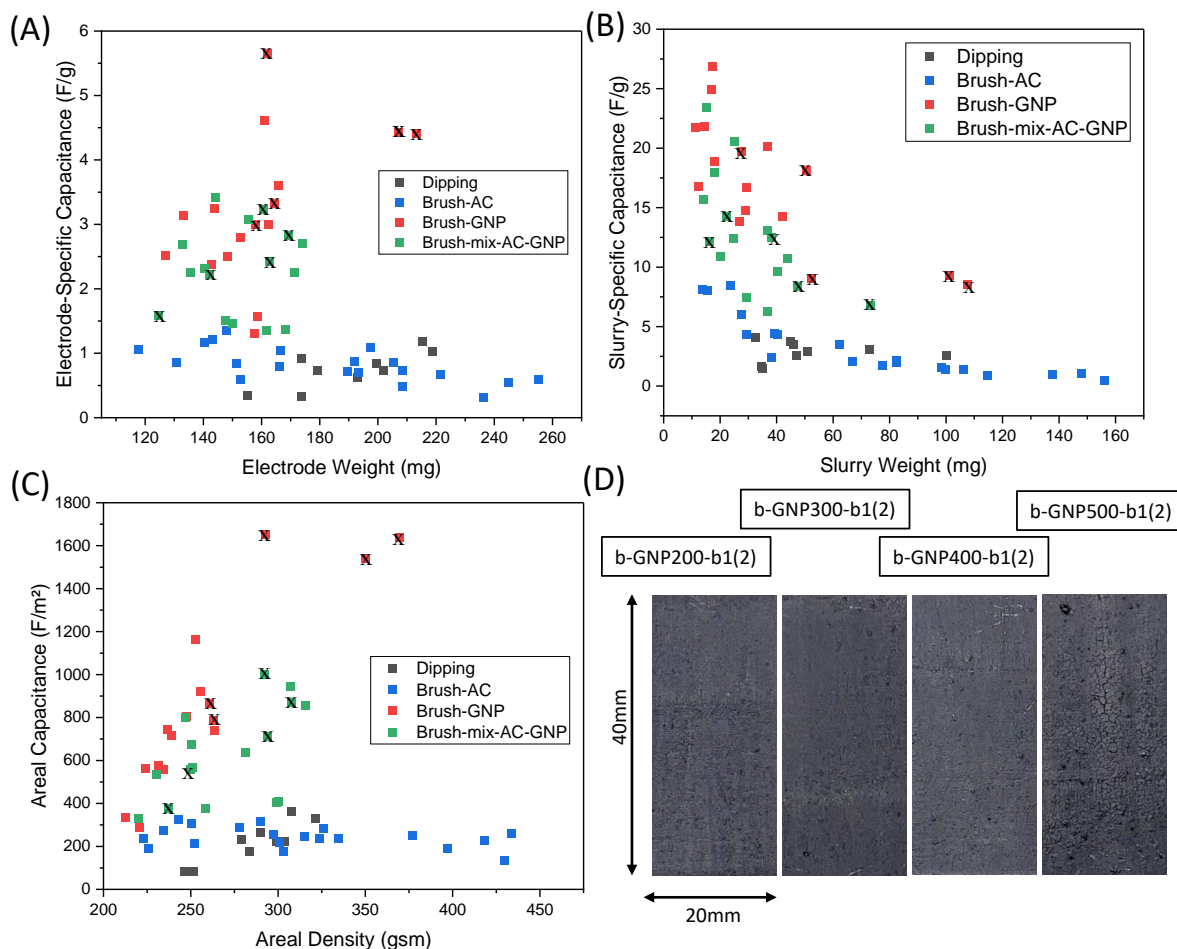


Figure 4.6: The comparison of the three categories of slurries. (A) Electrode-specific capacitance versus the electrode weight. (B) Slurry-specific capacitance versus the slurry weight. (C) Areal capacitance versus the areal density. (D) Surfaces of the GNP slurry samples.

4.1.4. Surface Area and Pore Analysis

The isotherms of the activated charcoal (AC) and graphene nanoplatelets (GNP) particles are shown in Figure 4.7 (A), and the isotherms of the plain weave carbon spread tow fabrics (PW-CSTF) deposited with b-AC300 and b-GNP300 slurries are shown in Figure 4.7 (B). Three distinct stages and hysteresis at the high relative pressure can be observed. This is categorised in IUPAC as H3 or H4 hysteresis loops, depending on the volume adsorbed at low relative pressures [61].

The first stage showed a steep increase in the adsorbed pore volumes at low relative pressures. This is contributed by the adsorbate's monolayer coverage on the micropores and the small mesopores, as well as the condensation due to micropore filling. The first stage measures the volume of micropores in the material in which the activated charcoal (AC) has a higher volume of micropores than graphene nanoplatelets (GNP) shown in Figure 4.7 (D).

The second stage of the type 2 isotherm is a linear region where multilayer adsorption begins, and mesopore adsorption continues. The monolayers on the pores are formed in the first stage, which is used to determine the BET surface area shown in Table 4.1. After the linear region, the volume adsorbed starts to increase at the third stage, which is dominated by macropore and mesopore filling, as well as pore condensation. During desorption, the condensed adsorbate remains trapped in the smaller pores when the condensed adsorbate in the larger pores has already started to vaporize, leading to a hysteresis effect [101, 133].

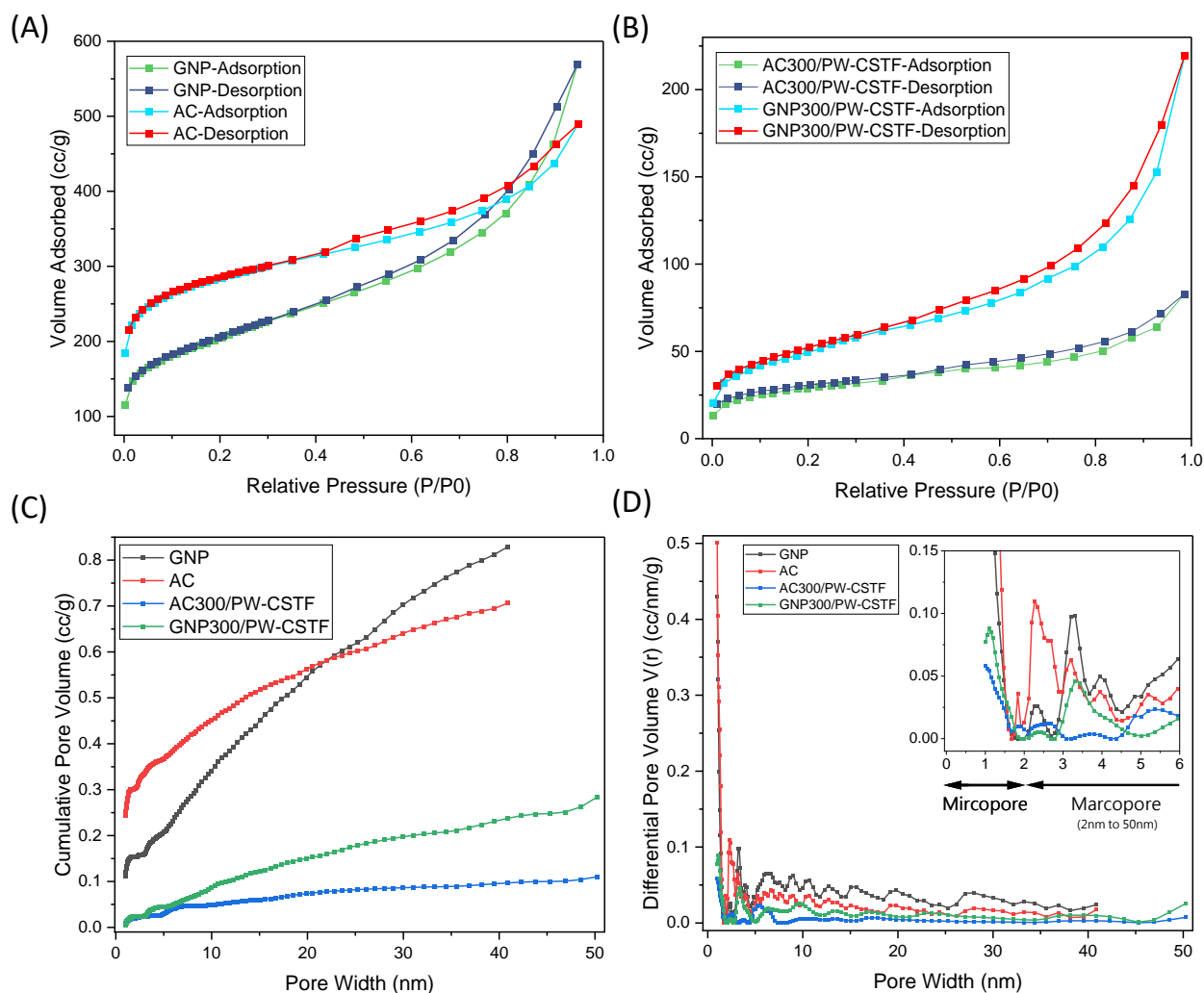


Figure 4.7: The isotherms for the surface area determination and the pore size distribution of the carbon particles and their corresponding slurries. (A) Isotherms of the GNP and AC particles. (B) Isotherms of the b-GNP300 and b-AC300 slurries. (C) Cumulative pore volumes (D) The differential pore volumes, which implies the pore size distribution.

Measurements	AC	GNP	PW-CSTF/b-AC300	PW-CSTF/b-GNP300
BET Specific Surface Area (m^2/g)	1034.13	610.17	100.23	231.43
Degassed Sample Weight (mg)	35	47	230.6	213.1

Table 4.1: BET-specific surface area and the sample mass.

According to Figure 4.7 (C) and (D), after the slurries are deposited onto the plain weave carbon spread tow fabrics (PW-CSTF), micropore volume significantly decreased due to the carbon paint that fills up the pores and covers their material surfaces. The high surface area of activated charcoal is decreased 10 times when deposited on the PW-CSTF, as shown in Table 4.1. The mesopore volume and the BET-specific surface area of the b-GNP300 slurry are two times greater than that b-AC300 slurry since mesopores are favourable for ion storage [62]. The higher mesopore volume is reflected in the specific capacitance shown in Figure 4.6.

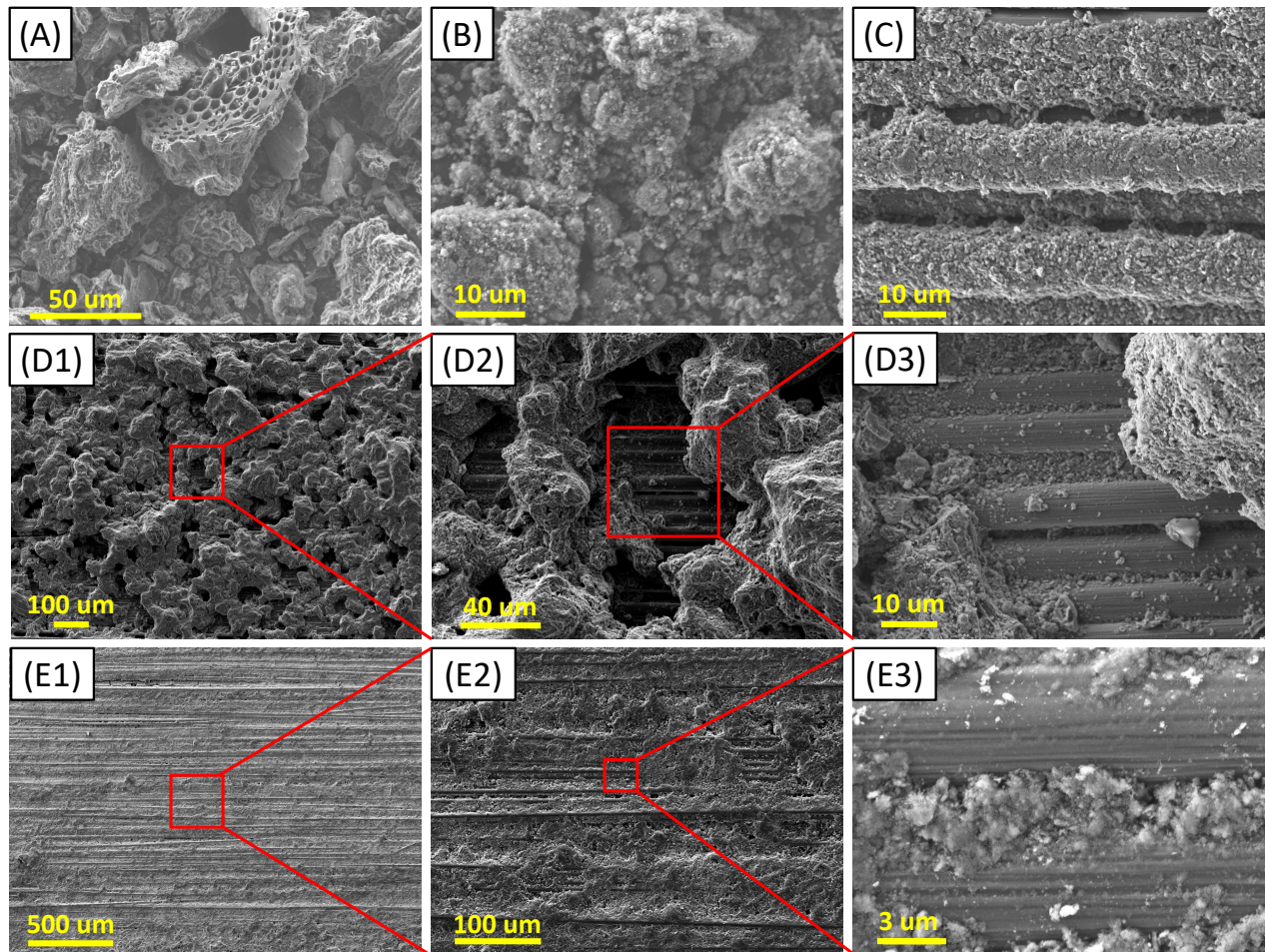


Figure 4.8: The scanning electron microscope images of the electrodes' surface and their carbon materials. (A) Activated charcoal (AC) particles. (B) Graphene nanoplatelets (GNP). (C) SPI carbon conductive paint coated PW-CSTF (D1) Electrode surface deposited by b-AC300 slurry. (D1) and (D2) are magnified images of (D1). (E1) Electrode surface deposited by b-GNP300 slurry. (E2) and (E3) are magnified images of (E1).

The scanning electron microscope (SEM) images for the b-GNP300 and b-AC300 are shown in [Figure 4.8](#). The AC-300 slurry is shown to create a thick layer of porous slurry deposition on the plain weave carbon spread tow fabric while the GNP-300 slurry creates a thin layer of slurry which is able to fill between the fibre gaps to increase conductive pathways.

To conclude, the graphene nanoplatelets (GNP)-based slurry outperforms the activated charcoal (AC)-based slurry in terms of capacitance can be substantiated by the BET surface area and pore size distribution. However, the hydrophobic surfaces of the electrode surface during the CV test may underestimate capacitance values. The plain weave carbon spread tow fabric (PW-CSTF) deposited with b-GNP300 slurry showed the highest BET-specific surface area of $231.43 \text{ m}^2/\text{g}$ among the reported carbon electrodes from the literature shown in [Figure 4.9](#).

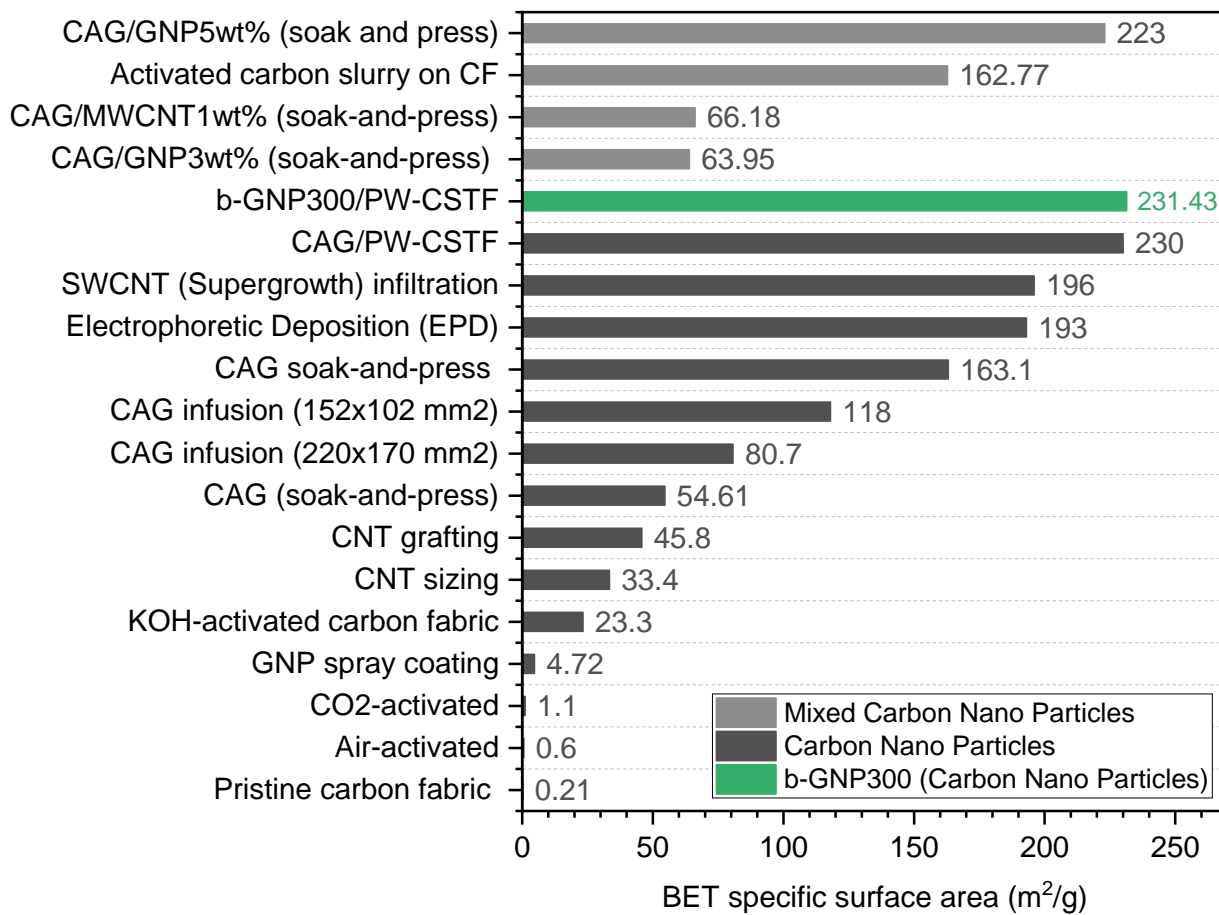


Figure 4.9: The Brunauer-Emmett-Teller (BET) specific surface area of the carbon-based electrodes. The b-GNP300/PW-CSTF electrode exhibited superior performance and was comparable to the PW-CSTF infused with carbon aerogel.

4.2. Gel Polymer Electrolyte

The liquid polymer electrolytes from LiTFSI-0% to LiTFSI-100% are shown in Figure 4.10. As the LiTFSI concentration increases to 40% PVDF-HFP wt%, the solution starts to turn yellow. The maximum LiTFSI limit for which solution casting is still feasible is the LiTFSI-100% polymer solution which LiTFSI has equal weights to PVDF-HFP.

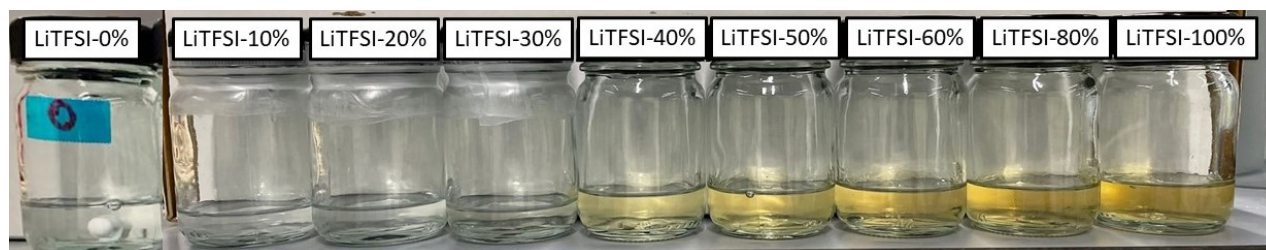


Figure 4.10: Liquid polymer electrolyte from LiTFSI-10 to LiTFSI-100.

4.2.1. FTIR Spectroscopy

The Fourier transform infrared (FTIR) spectrum is first measured for the gel polymer electrolyte materials. The wavenumber versus transmittance of the LiTFSI, PVDF-HFP and TEP are presented in Figure D.6. The LiTFSI spectrum in Figure D.6 (C) shows the hydrophilic property of the LiTFSI salt.

The FTIR spectra of the polymer electrolyte solution containing LiTFSI 0% to 100 % wt% of PVDF-HFP are shown in Figure 4.11 (A). The indicator for the LiTFSI function groups in the solution can be shown in 1 (571, CF_3) and 5 (1140, $C-SO_2-N$). The TEP function group in the solution is shown at 2 (797, $P-O$) 3 (966, $O-P-O$) 4 (1019, $P-O$) 6 (1261, $P-O$) 8 (2984, $C-H$). The transmittance of those bandwidths decreases when the LiTFSI concentration increases. In contrast, the PVDF-HFP function group 7 (1400, CF_2 and CF_3) in the solution decreases. This indicates that when more LiTFSI ions are incorporated into the polymer, the coulombic interaction between the TEP and the Li^+ increases [33].

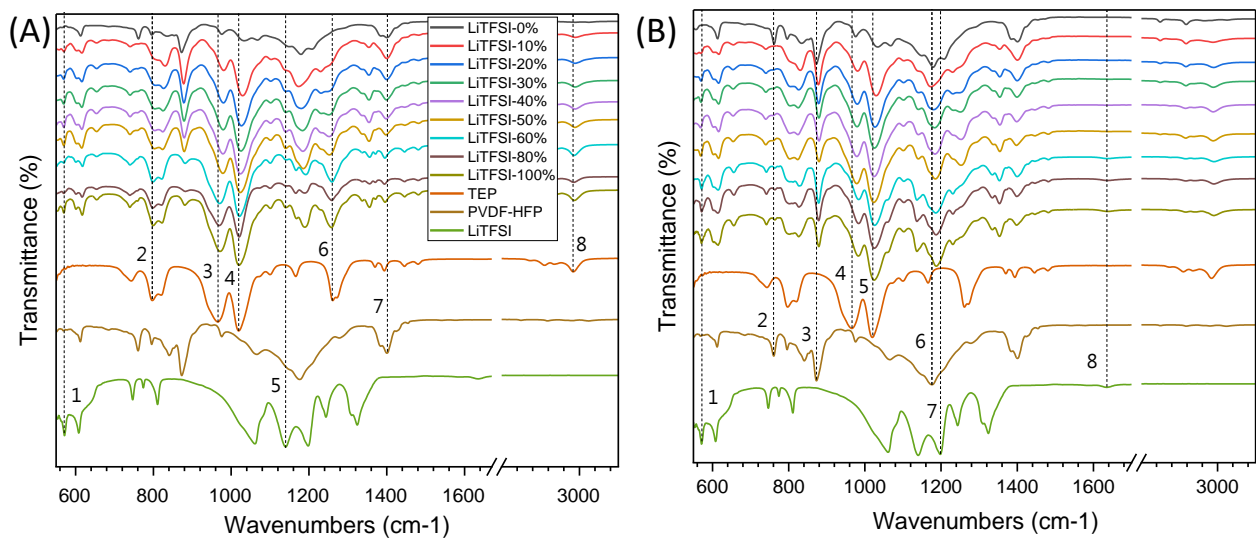


Figure 4.11: The FTIR spectrum of the (A) Polymer electrolyte solution (B) Cured gel polymer electrolyte.

After solution casting and film drying, the FTIR spectra of the gel polymer electrolytes (GPE) are shown in Figure 4.11 (B). The spectra showed contributions of TEP function groups in the GPE, which confirms that there is a liquid medium in the GPE after drying, which contains LiTFSI. The increase of the LiTFSI function groups can be shown in 1 (571, CF_3). When the LiTFSI concentration increases, more TEP solvent is contained in the gel to provide ion capacity shown in 4 (966, $O-P-O$) and 5 (1019, $P-O$). The increased LiTFSI concentration interacted with the PVDF-HFP function group 6 (1176, CF_2 and CF_3), causing a shift to 7 (1198, CF_3). After drying, the hydrophilic property in the gel shown in 8 (1635, $H-O-H$) becomes more significant.

The shifts in the amorphous and crystalline bandwidths of the PVDF-HFP at Figure 4.11 (B) 2 (761) and 3 (873) are studied using Figure 4.12 (A). When LiTFSI is included, the bands that represent the PVDF-HFP crystalline region (PVDF-) at 612, 761 and 796 cm^{-1} shifted to higher frequencies at 615, 764 and 802 cm^{-1} respectively. Transmittance intensity decreases for the shift from 612 and 796 cm^{-1} does not mean that crystallinity increases but rather with the overlapping of LiTFSI function groups. To examine the crystallinity decrease without the LiTFSI band overlapping, the shift of the 761 and 841 both showed a decrease in crystallinity. The amorphous region at the 873 cm^{-1} showed an increase of transmittance, indicating the LiTFSI reaction with the amorphous -HFP region of the PVDF-HFP. From the FTIR spectrum study, the LiTFSI inclusion in the PVDF-HFP decreases crystallinity and increases the swelling of the PVDF-HFP polymer by containing more solvents which led to an increase in gel polymer thickness shown in Figure 4.12 (B).

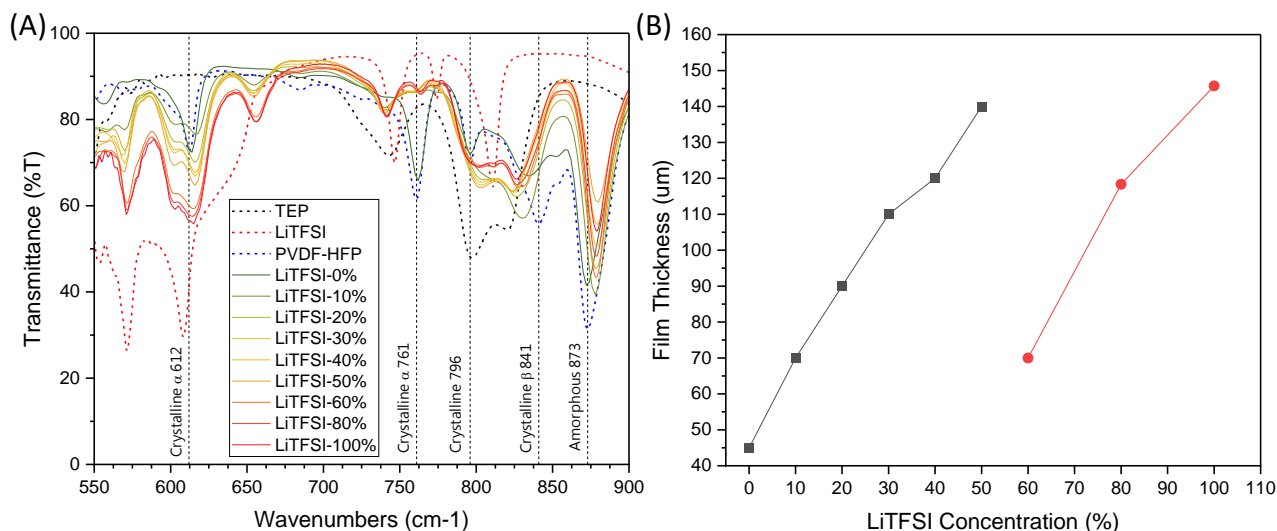


Figure 4.12: (A) The FTIR spectrum of the cured gel polymer electrolyte (GPE) from 0% to 100% of the PVDF-HFP wt% and the GPE materials. The bandwidths of the crystalline and the amorphous region are labelled. LiTFSI-0% to LiTFSI-50% are vacuum dried at 70ircC for 24 hrs while concentrations LiTFSI-60% to LiTFSI-100% are dried for 72 hrs. (B) The thicknesses of the GPEs.

4.2.2. Electrochemical Impedance Spectroscopy

The electrochemical impedance spectroscopy (EIS) of the gel polymer electrolytes (GPE) is presented as the Nyquist plot. The Nyquist plot of the gel polymer electrolyte (GPE) LiTFSI-0% is shown in Figure 4.13 (A).

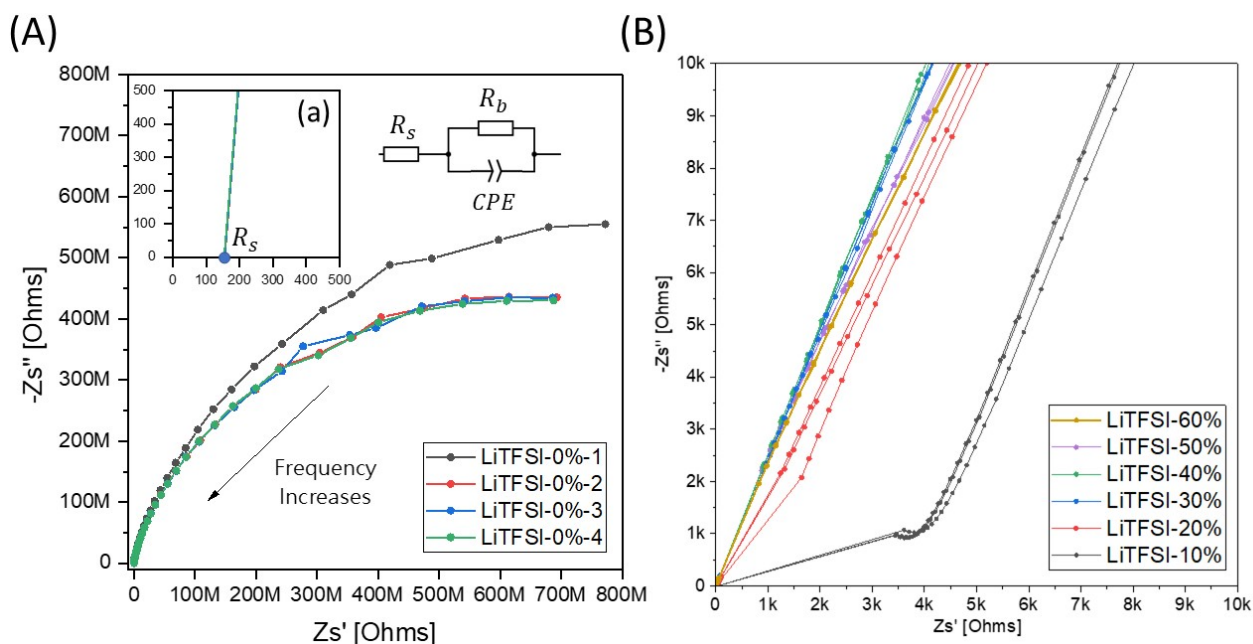


Figure 4.13: (A) The Nyquist plot of the gel polymer electrolyte (GPE) LiTFSI-0%. 4 sample measurements are plotted. (a) The high-frequency region of the Nyquist plot. (B) The Nyquist plot of the LiTFSI-0% to 50% GPE at high-frequency regions. Multiple samples are measured for each GPE concentration.

Figure 4.13 (A) showed a portion of the suppressed semi-circle which can be fitted using a resistance R_b and a constant phase element (CPE) (a virtual element that represents a non-ideal capacitance element in real systems). R_b is the bulk resistance of the GPE and R_s in Figure 4.13 (a), which is one of the intercepts of the semi-circle on the real axis, indicates the electrode resistance and the contact resistance at the interfaces. The value R_b is the other semi-circle intercept which, when deducting R_s represents the GPE bulk resistance.

The R_b for GPE LiTFSI-0% projects to be in the scale of giga-ohms, indicating no ionic conductivity due to the absent LiTFSI ions. However, there is still capacitance behaviour from the PVDF-HFP.

The EIS measurements of the gel polymer electrolyte (GPE) containing LiTFSI are shown in Figure 4.13 (B). The EIS measurement is conducted five days after the gel is produced. The Nyquist plots exhibit discontinuities at high frequencies, which are suspected to be attributed to the presence of brass electrodes. Brass electrodes are non-blocking electrodes which may exert additional capacitive behaviour and faradic behaviours with the GPE. This result in additional impedance and makes it difficult to distinguish the impedance contribution from the GPE.

In order to obtain an approximation of the bulk electrolyte resistance, the brass electrode-related impedance and the interface impedance are included in the GPE impedance. Hence, the bulk electrolyte resistance (R_b) is defined to be the corresponding real axis value at the endpoint of the high-frequency region of the slope before discontinuity occurs. For the Nyquist plots of GPE LiTFSI-10%, which have a transition of the slope to a semi-circle, R_b is defined to be the lowest point at the transition. The validity of this method is proved in Figure D.7 by varying the potential V_{rms} to show that the point before discontinuity occurs has close values on the real axis. In addition, only the low-frequency slope will change. This method is introduced by Mathis et al. [81].

The Nyquist plots of the gel polymer electrolytes (GPE) LiTFSI-60%, 80% and 100% are presented in Figure 4.14 (A). At the high-frequency region, suppressed semi-circles appear. It is difficult to distinguish whether the semi-circle is contributed by the GPE or the charge transfer at brass electrodes. However, based on the literature that uses blocking electrodes to measure GPE impedance, the semi-circle and the tilted slope should be continuously connected [5, 71]. Some GPE LiTFSI-80% Nyquist plots showed only a tilted line intersecting

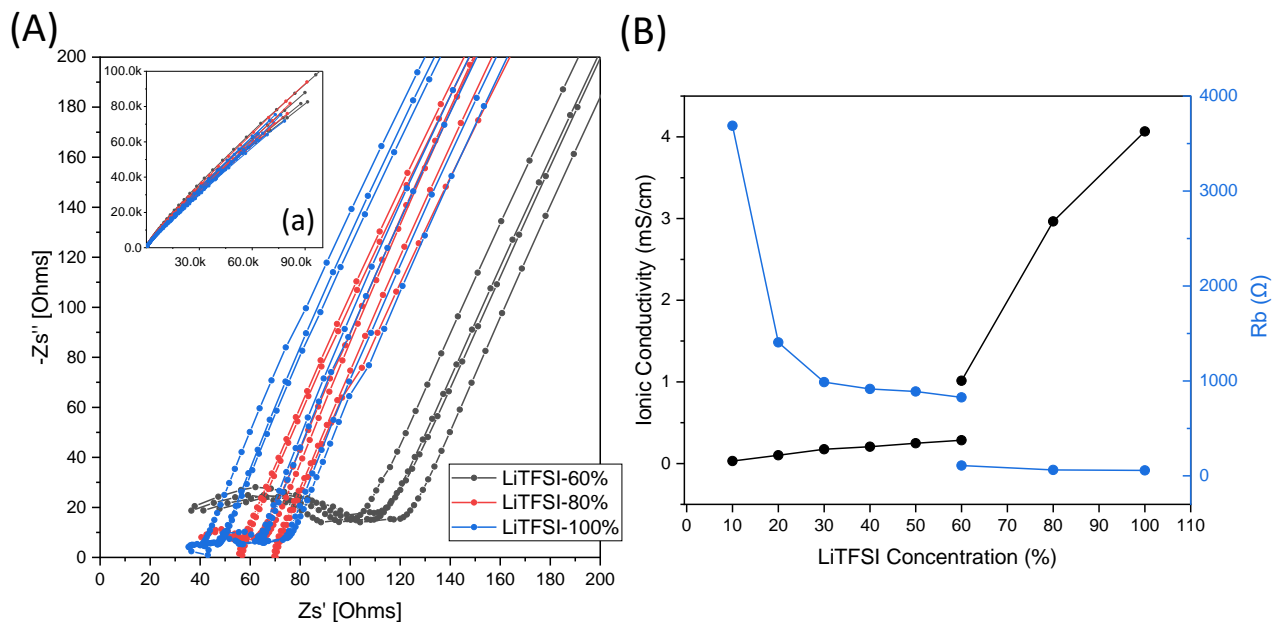


Figure 4.14: (A) The Nyquist plot of the gel polymer electrolyte (GPE) LiTFSI-60%, 80% and 100%. Multiple samples are measured for each GPE concentration. (a) The Nyquist plot shows the full frequency range from low to high. (B) Different LiTFSI concentrations influence the ionic conductivity and the GPE bulk resistance.

at the real axis. This indicates a constant phase element (CPE) in series with a resistance contributed by the bulk electrolyte and the electrodes. In Figure 4.14 (a), a 45 degrees slope in the low-frequency region is observed, indicating a diffusion-dominant behaviour whose impedance can be explained using the Warburg impedance.

The estimated bulk gel polymer electrolyte (GPE) impedance R_b and the ionic conductivity σ are shown in Figure 4.14 (B). An ionic conductivity above 1 mS/cm is obtained for GPE LiTFSI-60% to LiTFSI-100%. When considering the same drying profile and measuring conditions, both GPE LiTFSI-0% to LiTFSI-60% and GPE LiTFSI-60% to LiTFSI-100% both showed an increased ionic conductivity and decreased bulk GPE resistance. However, GPE LiTFSI-60% to LiTFSI-100% has a significantly higher ionic conductivity. A three-times ionic conductivity difference is observed for the two GPE LiTFSI-60%. The main reason is that GPE LiTFSI-0% to LiTFSI-60% are measured after the fifth day of the GPE production, while GPE LiTFSI-60% to LiTFSI-100% are measured on the same day as the GPE is produced. It is suspected that the LiTFSI-TEP liquid electrolyte might be phasing out from the PVDF-HFP, or it is affected by the moisture.

4.3. Structural Supercapacitor Electrochemical Characterisation

4.3.1. Cyclic Voltammetry

Cyclic voltammetry (CV) with a 2 mV/s scan rate was first performed on the semi-cells of each batch. In Batch 1, an undesirable short-circuit effect was observed in the semi-cells. This effect occurred when the semi-cells, which had copper tapes attached to the same surface as the slurry, were subjected to a high vacuum pressure of 200 mbars. This is shown in Figure 4.15 (A), in which an asymmetric current response of a high positive current indicates that the copper tapes may have penetrated the gel polymer electrolyte and caused a short circuit which resulted in an ohmic behaviour. The graphene nanoplatelets-based slurry (b-GNP400) is still capable of accumulating ions from charge transfer, thus showing a slanted rectangular shape indicating its capacitive behaviour. Only two semi-cells which contain high LiTFSI concentration were measured since the results were not satisfactory.

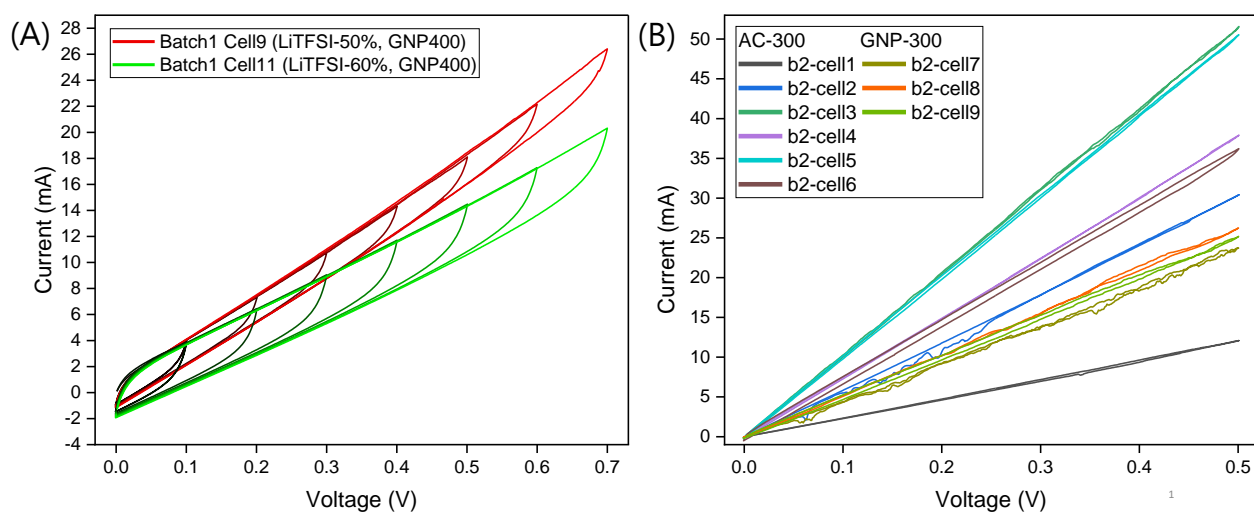


Figure 4.15: The cyclic voltammetry (CV) measurements for the semi-cells of batch 1 and batch 2. (A) Batch 1 semi-cell CV measurements of 9 and 11. (B) The CV curves of batch 2 semi-cells showed ohmic responses (forward and backward scan overlaps and having a straight line with a slope).

From the lesson learned from batch 1, the semi-cells of batch 2 were fabricated by attaching the copper tapes at the outer surface of the plain-weave carbon fibre spread tow. The vacuum used to assemble the semi-cells is reduced to 850 mbar. The cyclic voltammetry (CV) measurements of batch 2 cells 1 to 6 are shown in Figure 4.15 (B). The activated charcoal (AC)-based slurry (b-AC300) showed a CV plot with ohmic behaviours from the forward and backward scan overlapping. Rectangular shapes in the CV plots are absent, which indicates there is no charge storage capability. Despite the pore size analysis of the b-AC300 slurry showing the existence of mesopores and good wettability with triethyl phosphate, the occurrence of short circuits is suspected to be caused by the sharp edges of the AC particles, which have penetrated the gel polymer electrolyte.

In contrast to Batch 1, where capacitive behaviour was still observed due to the short circuit region being limited at the copper tape, Batch 2 exhibits no capacitive behaviour since the AC slurry is spread uniformly across the entire surface, resulting in a complete short circuit between the two electrodes. Batch 2 cells 1 to 6 provided information that the gel polymer electrolyte cannot separate the AC-coated electrodes.

For batch 2 cells 7 to 12, GNP300 slurry is used instead of GNP400 slurry since b-GNP400 showed cracked surfaces when deposited on the plain-weave carbon spread tow fabric (PW-CSTF). In Figure 4.15 (B), batch 2 cells 7,8 and 9 showed no capacitive response until the LiTFSI wt% of the PVDF-HFP reached 40% at cell 10 shown in Figure 4.16 (A). Batch 2 cells 7 to 10 provided information that LiTFSI 40 wt% of the PVDF-HFP is the minimum threshold for a semi-cell to obtain capacitive behaviour. This threshold can be observed from the colour gradient of the polymer electrolyte solution shown in Figure 4.10 when the polymer solution starts to turn yellow at LiTFSI-40%.

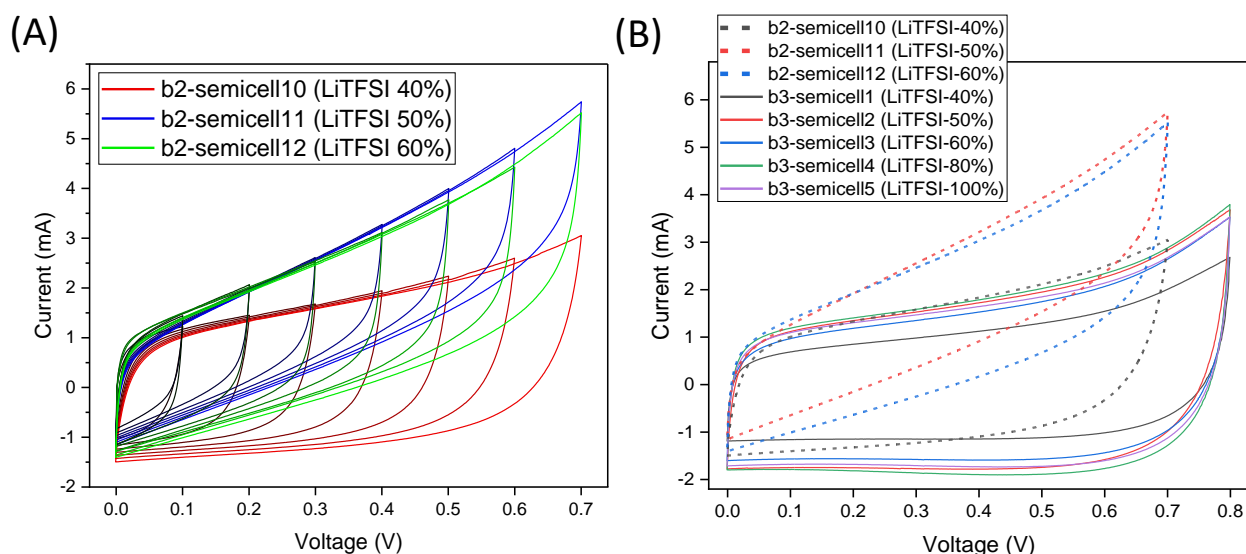


Figure 4.16: The cyclic voltammety (CV) measurements. (A) Batch 2 semi-cells 10, 11 and 12. Each cell is scanned for 7 cycles from 0.1 V to 0.7 V with a 0.1 V increment. (B) The batch 2 semi-cells 10 to 12 and batch 3 semi-cells which has a gel polymer electrolyte separator. Batch 3 semi-cells have a higher thickness.

In Figure 4.16 (A), asymmetric cyclic voltammety (CV) having slanted rectangular shapes occur at higher LiTFSI concentration (LiTFSI 50% and 60%) while the lower LiTFSI-40% has less effect. This implies that the high concentration of LiTFSI had a detrimental effect on the mechanical integrity of the gel polymer electrolyte, leading to short circuits during semi-cell assembly under an 850 mbar vacuum. Although factors such as imbalanced ion adsorption and desorption during forward and backward scans, electrode degradation, and uneven slurry application can contribute to the slanted shape observed in the results, these effects proved to be less pronounced in the case of b2-semicell10 (LiTFSI-40%). This suggests that short circuits remain an influence. Therefore, two methods to improve short circuits are executed: (1) Increasing the film applicator blade gap for solution casting gel polymer electrolyte from 600 μm to 800 μm . (2) Adding two layers of plain weave glass fabric impregnated with gel polymer electrolyte.

In Figure 4.16 (B), the CV plots of batch 3 cells 1 to 5, which used thicker gel polymer electrolytes (GPE), showed no slanted shapes. This proved that the slanted shape is indeed a result of short circuits caused by the presence of thinner GPEs. From Figure 4.16 (B), the maximum voltage window for the semi-cell is set as 0.7 V. As the applied voltage window approaches 0.7 V, a spike appears, indicating parasitic side reactions and electrolyte degradation that subsequently reduce the coulombic efficiency. [81, 149, 153].

The effect of epoxy infusion on the cyclic voltammetry (CV) measurements for batch 3 cells 1 to 5 are shown in [Figure 4.17](#) (A). A reduction in charge transfer and the parasitic side reaction peaks at higher voltage windows are observed. This observation suggests that the role of epoxy infusion involves more than just filling the vacant spaces and voids within the semi-cell. There are interactions between the epoxy and the gel polymer electrolyte (GPE) which resulted in capacity loss.

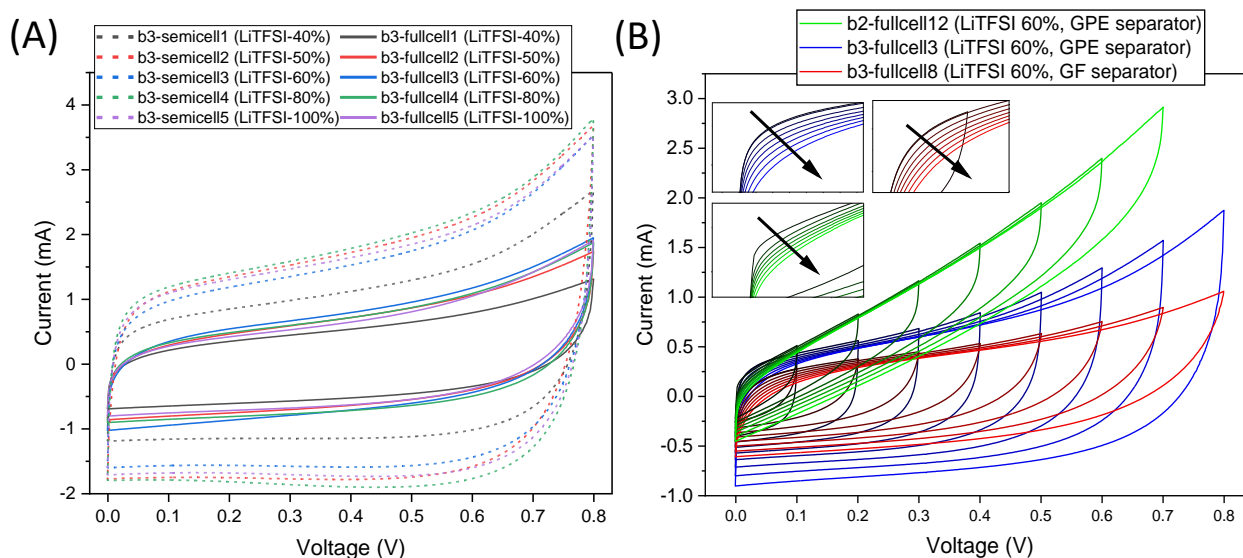


Figure 4.17: The cyclic voltammetry (CV) measurements. (A) Comparison of batch 3 cells 1 to 5 before and after epoxy infusion. (B) The full cells of the three different structural supercapacitor designs, in which all gel polymer electrolytes contain the same LiTFSI concentration (60 wt% of PVDF-HFP). "b2 full cell 12" and "b3 full cell 3" both contain a gel polymer electrolyte (GPE) as a separator. b2 full cell 12 has a GPE thickness of 145 μm , and b3 full cell 13 has a GPE thickness of 198 μm . "b3 full cell 8" contains two layers of GPE-impregnated glass fabric.

The comparative analysis of the two improvements to alleviate short circuits in batch 3 is shown in [Figure 4.17](#) (B). The thickening of the gel polymer electrolyte (GPE) and the use of GPE-impregnated glass fabrics as separators eliminated the slanted shape caused by short circuits. Nonetheless, the implementation of glass fabric as separators impeded ionic mobility, leading to a decrease in capacitance (as observed by a smaller area under the cyclic voltammetry plot) and an increase in equivalent series resistance (manifested by blunter edges). The three boxes located at the top left corner in [Figure 4.17](#) (B) indicate that following each cyclic voltammetry (CV) scan, a delayed current response was observed in the subsequent scan. This phenomenon may be caused by a potential delay in ion diffusion or capacitor relaxation.

The slurry weight (the sum of the two electrodes) for each cell and the gel polymer electrolyte (GPE) thicknesses used for each batch are shown in [Figure D.8](#). The hand brush application showed large slurry weight variations, which may affect the study of the LiTFSI concentration-dependent electrochemical performance. The GPE showed an increase in thickness when the LiTFSI concentration increases, which conforms which the findings from FTIR characterisation.

4.3.2. Galvanostatic Charge-Discharge

Galvanostatic charge-discharge measurements of the semi-cells and the full-cells are shown in Figure 4.18. Batch 2 cells 10 to 12 in Figure 4.18 (A) have a decreasing CE when the voltage window increases, which is due to the short circuit effect that dissipates the charged energy. Batch 3 cells 1 to 5 shown in Figure 4.18 (B), which use a gel polymer electrolyte (GPE), has the highest coulombic efficiency (CE) at high LiTFSI concentrations compared with (A) and (C). Batch 3 cells 1 to 5 also have the lowest equivalent series resistance (ESR) shown in Figure 4.18 (D). Batch 3 cells 6 to 10 in Figure 4.18 (C), which uses GPE-impregnated glass fabric, showed low CE compared to GPE separators due to the high ESR shown in Figure 4.18 (D) which is contributed by the glass fabric separator.

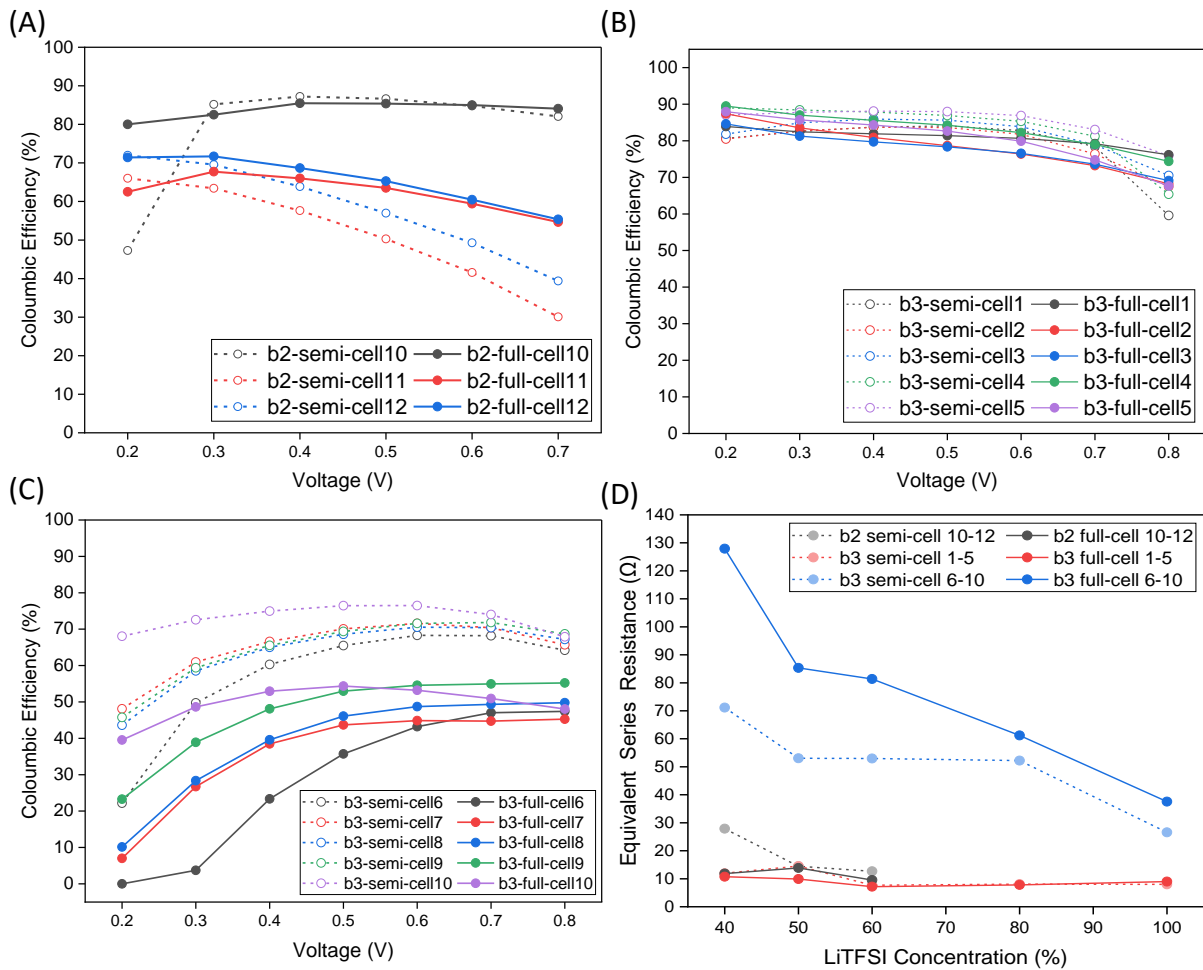


Figure 4.18: The impact of the epoxy infusion on coulombic efficiency (CE) and equivalent series resistance (ESR) before and after the infusion process. The GCD test is conducted using a 5 mV constant current on batch 2 cells and a 1 mA constant current for batch 3 cells. (A) The CE of batch 2 semi-cells and full-cells from 0.2 V to 0.7 V. (B) The CE of batch 3 semi-cells and full-cells using a gel polymer electrolyte (GPE) separator. (C) The CE of batch 3 semi-cells and full-cells using a GPE-impregnated glass fabric separator. (D) The relationship between the LiTFSI concentration and the ESR of the semi-cells and the full-cells.

The specific capacitance, energy and power are normalised using the cell weights and the slurry weights presented in Figure 4.19. The performance, normalised by the cell weight, depicted in Figure 4.19 (A1), (B1), and (C1), indicates that the decrease in performance from the semi-cell to the full cell is not solely attributed to weight normalisation. The decline is also influenced by the effect of epoxy infusion. For instance, the weight of batch 3 cells 1 to 5 increased 2.7 to 3.5 times from the semi-cell to the full cell. However, a significant decline of 7 to 9 times in cell-specific capacitance and cell-specific energy was observed. This indicates that the epoxy can be blended with the LiTFSI ions in the gel polymer electrolyte shown in Figure 4.20, thus reducing ionic conductivity. Another reason may be that the epoxy is able to impregnate the dry space around the fibres, which decreases conductive paths.

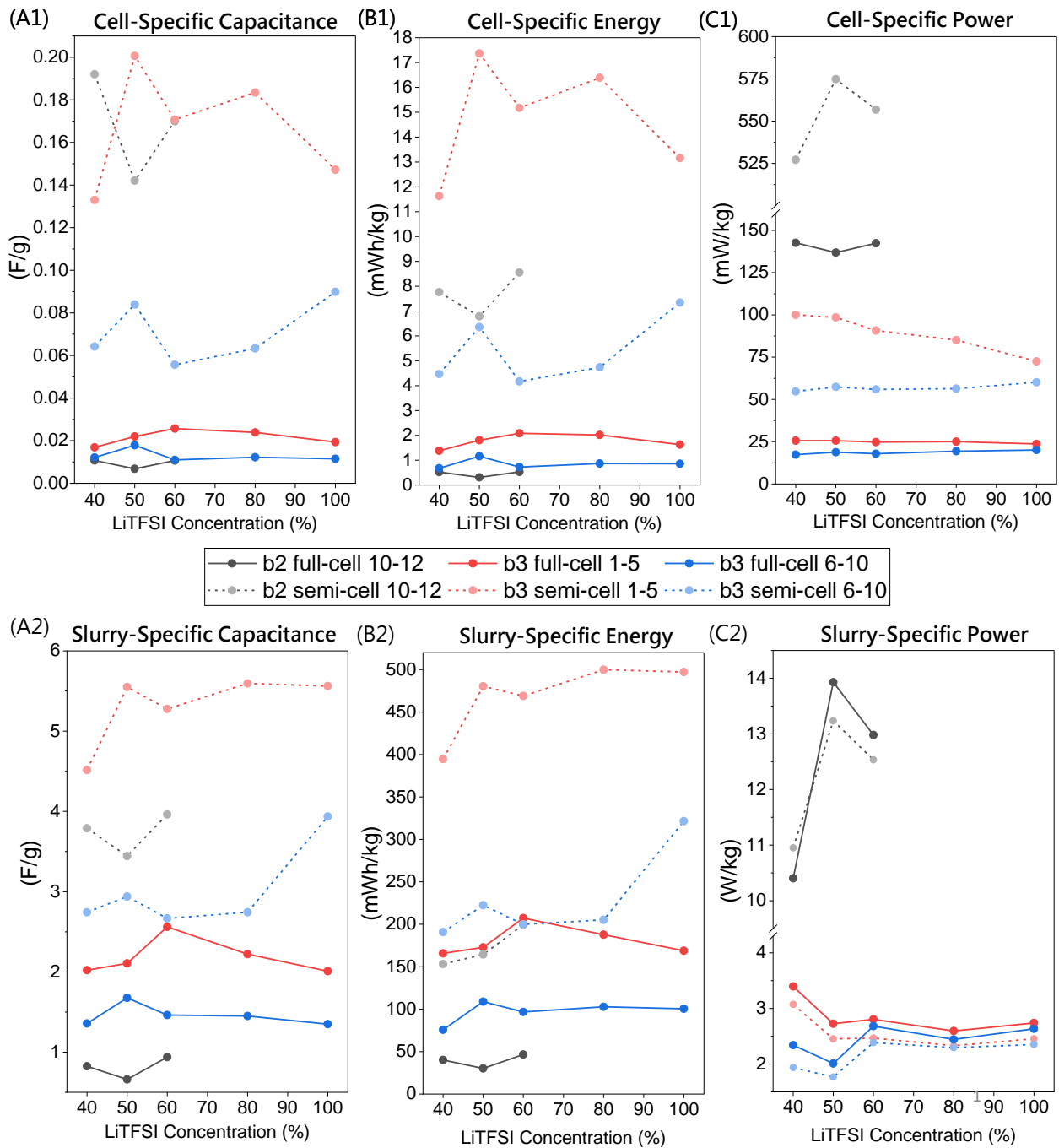


Figure 4.19: The LiTFSI influence on the specific capacitance, energy and power normalised by the full-cell weight and the slurry deposition weight (active mass of the cell). The values are obtained by performing galvanostatic charge-discharge using a voltage window of 0.7 V and a constant current of 1 mA. (A1) Specific capacitance. (A2) Slurry-specific capacitance. (B1) Specific energy. (B2) Slurry-specific energy (C1) Specific power (C2) Slurry-specific power.

The performance degradation due to the epoxy infusion can be examined independently by normalising the performance values with the unchanged slurry weight shown in Figure 4.19 (A2), (B2) and (C2). The slurry-specific capacitance and energy decreased 2 to 3 times after epoxy infusion for batch 3 cells 1 to 5. A desired outcome which indicates a successful encapsulation is that the cell-specific performance decreases the same percentage as the increased weight from semi-cell to full-cell, meaning the slurry is unaffected by the epoxy.



Figure 4.20: The image presents the change of the interface between the semi-cell and the glass fabric encapsulation when the LiTFSI concentration is increased in the gel polymer electrolyte. (A) to (E) are batch 3 cells 1 to 5. The whitened locations indicate the contact of the epoxy and the gel polymer electrolyte. As the LiTFSI concentration increases, the whitened area also increases, indicating that there is a reaction between the epoxy and the LiTFSI ions.

The "b3-full-cell3", which uses a gel polymer electrolyte separator LiTFSI-60wt%, showed the highest cell-specific capacitance of 25.72 mF/g , cell-specific energy of 2.08 mWh/kg and cell-specific power of 25.04 mW/kg . The respective slurry-specific values are 2.56 F/g , 207.24 mWh/kg and 2.47 W/kg . The respective areal performance is 12.54 mF/cm^2 , $0.7 \mu\text{Wh/cm}^2$ and 0.012 mW/cm^2 . The performance starts to decrease when the LiTFSI concentration increases further than LiTFSI-60wt%.

Figure 4.21 shows the percentage mass of the constituents in the full cells. A large weight percentage is contributed to the encapsulation materials while the current collecting materials (PW-CSTF and copper tape) contain 10% to 12%. The slurry weight, which is the active mass that contributes to the adsorption and desorption of the ions, only contains 1% of the mass. The semi-cell's weight increased from 275% to 400% to the full cell shown in Figure 4.22. An improvement in the mechanical integrity of the gel polymer electrolyte enables the use of a higher vacuum pressure to reduce the epoxy weight percentage.

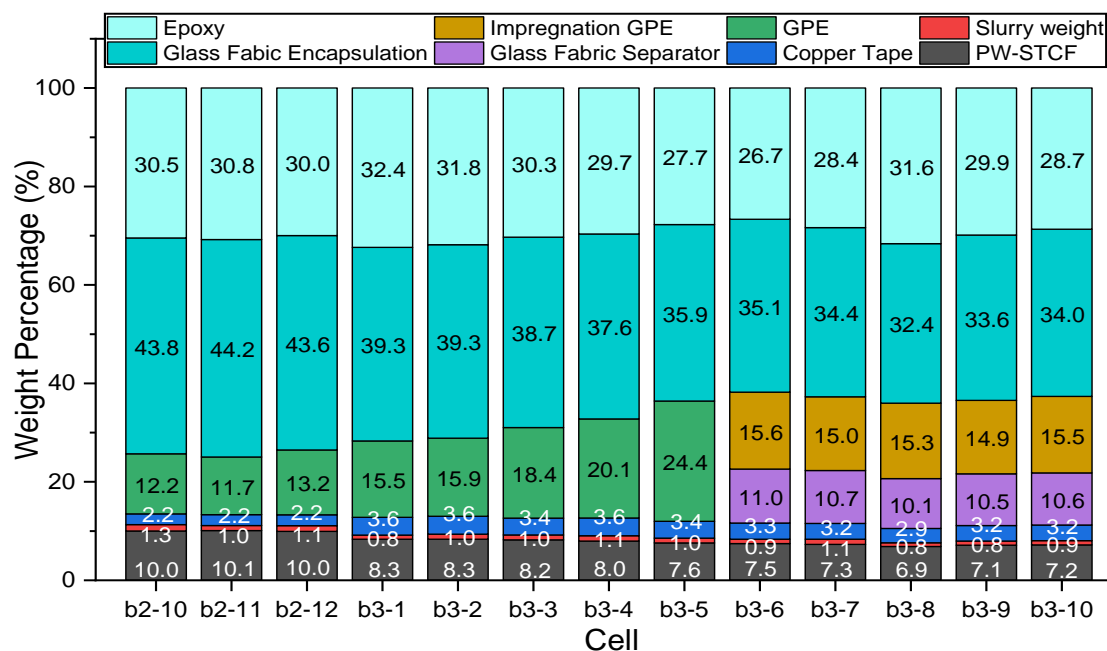


Figure 4.21: (A) The weight constituents of batch 2 full cells 10 to 12 and batch 3 full cells 1 to 10 are shown in percentage.

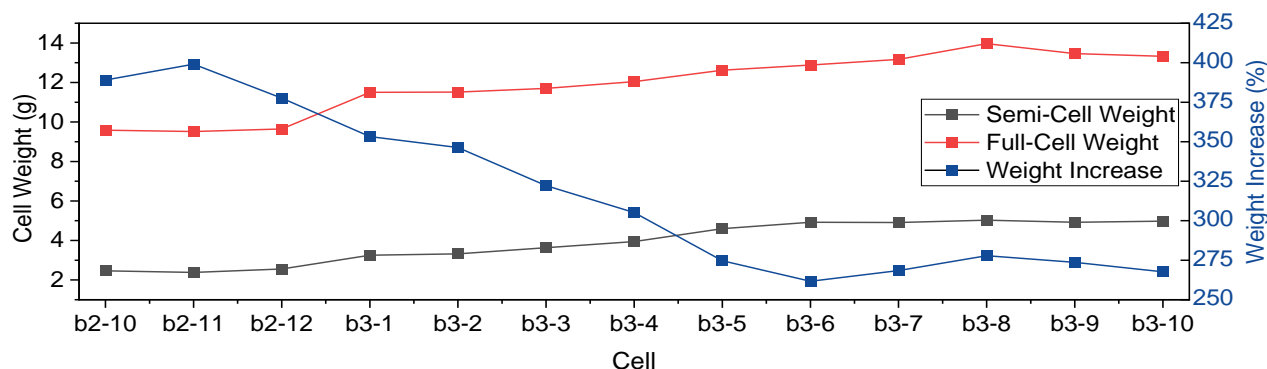


Figure 4.22: The semi-cell and full-cell weights of the batch 2 full cells 10 to 12 and batch 3 full cells 1 to 10. The right axis shows the weight increase percentage from the semi-cell to the full-cell.

4.3.3. The Ragone plot

The galvanostatic charge-discharge (GCD) measurement with a voltage window of 0 V to 0.7 V is continued by increasing the constant current from 1 mA to 15 mA with a 1 mA increment to study the energy storage and power relationship. The result is plotted as a Ragone plot which is normalised by the full cell weight and the slurry shown in Figure 4.23 (A) and (B). The Ragone plot is a useful tool to visualise the power and energy storage behaviour in order to select a suitable operating system and make comparisons with other devices.

The Ragone plot showed that the specific energy decreases and the specific power increases when the applied current increases due to the equivalent series resistance (ESR) of the cell. The slopes are more vertical in batch cells 1 to 5 that use gel polymer electrolyte (GPE) separators, indicating a desired lower ESR. In Figure 4.23 (C), the coulombic efficiencies of the batch 3 gel polymer electrolytes also increased up to 98% when the current increased due to the reduced polarisation and the improved charge transfer effects.

An unusual behaviour of a sharp decrease in specific energy for all cells is observed when the constant current rises from 1 mA to 2 mA, which is indicated using arrows in Figure 4.23. The effect is due to an increased equivalent series resistance (ESR) from 1 mA application to 2 mA. After increasing from 2 mA, the ESR becomes constant. This ESR rise could be attributed to the increased electrolyte polarisation from 1 mA to 2 mA, restricting the ion movements. After 2 mA, the polarisation is stabilised and resulted in a constant ESR.

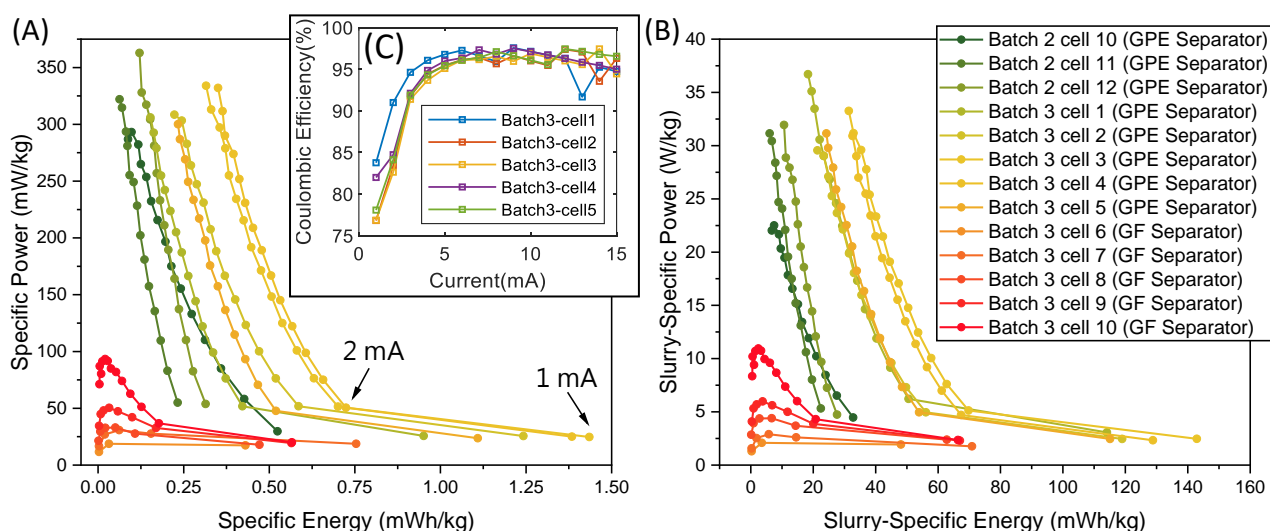


Figure 4.23: The galvanostatic charge-discharge (GCD) is performed on the full cells using a constant current from 1 mA to 15 mA. The specific energy and the specific power are plotted as the Ragone plot. (A) The Ragone plot of the energy and power values normalised by the full cell weight. (B) The Ragone plot of the energy and power values normalised by the slurry weight. (C) The coulombic efficiency of batch 3 cells 1 to 5, which use the gel polymer electrolyte separators.

4.3.4. Electrochemical Impedance Spectroscopy

The Nyquist plots of batch 3 cells 1 to 5, which use the gel polymer electrolytes (GPE) separators, are presented in Figure 4.24 (A). The Nyquist plots of the cells showed tilted lines at the low-frequency region and suppressed semi-circles at the high-frequency region. This continuous Nyquist plot proves that the reason for a discontinuous plot measured during the GPE characterisation shown in Figure 4.13 and Figure 4.14 is due to the effect from brass electrodes. The use of carbon materials as blocking electrodes provides a continuous Nyquist plot.

The semi-circle is fitted using the Metrohm Autolab curve fitting software shown in Figure 4.24 (B). Mei et al. extracted the resistance values of the electrode, bulk electrolyte and diffuse layer resistance from the Nyquist plot using simulation support with experimental methods [82]. Their interpretation of the resistance is applied in this report.

In Figure 4.24 (C), the impedance value at point R_A indicates the electrode resistance, the resistance between the electrode and its interface with the copper current collector. As this value changes, the whole curve shifts along the real impedance axis without changing its shape [82]. The distance between R_A and R_B is the impedance value R_{AB} that represents the bulk resistance of the gel polymer electrolyte. A higher ion concentration leads to a lower R_{AB} , and conversely [82]. R_B is the sum of R_A and R_{AB} , which is the internal resistance (or equivalent series resistance). Beyond R_B a slope is observed, which represents the diffuse layer resistance and the Warburg impedance R_C .

The fitted R_A , R_{AB} , R_B and the centre coordinates are shown in Table 4.2. The discrepancy of R_A is due to the brush application method. The value of R_{AB} indicates that the value decreases as LiTFSI concentration increases, which conforms with the findings of Mei et al. [82]. The equivalent series resistance (ESR) for cells is shown to be at 2.54 to 3.87 Ω , which is significantly lower compared to the ESR measured by the galvanostatic charge-discharge (GCD) using the voltage drop during discharge shown in Figure 4.18 (D).

In this study, the diffuse layer resistance and the Warburg impedance are suspected to affect the voltage response in the GCD measurements, which results in a higher ESR. Mei et al. [82] presented numerical models which are supported by experiments showing that the ESR determined from the GCD voltage drop is equivalent to the R_B from the Nyquist plot, and the diffuse layer resistance does not contribute to the voltage drop. However, Charoen-amornkitt et al. stated that diffuse layer resistance should be included in the internal resistance for porous electrodes with rough surfaces [17].

Cell	Ω				ESR (GCD Voltage Drop)
	R_A	R_{AB}	R_B	Centre (Z' , $-Z''$)	
b3-cell1 (LiTFSI 40%)	3.27	0.60	3.87	(3.57, -0.18)	11.96
b3-cell2 (LiTFSI 50%)	3.02	0.62	3.64	(3.33, -0.19)	14.53
b3-cell3 (LiTFSI 60%)	2.18	0.36	2.54	(2.36, -0.08)	7.69
b3-cell4 (LiTFSI 80%)	2.63	0.24	2.87	(2.75, -0.04)	8.09
b3-cell5 (LiTFSI 100%)	3.06	0.29	3.35	(3.2, -0.07)	7.99

Table 4.2: The impedance values of the batch-3 full cells using the fitted semi-circles.

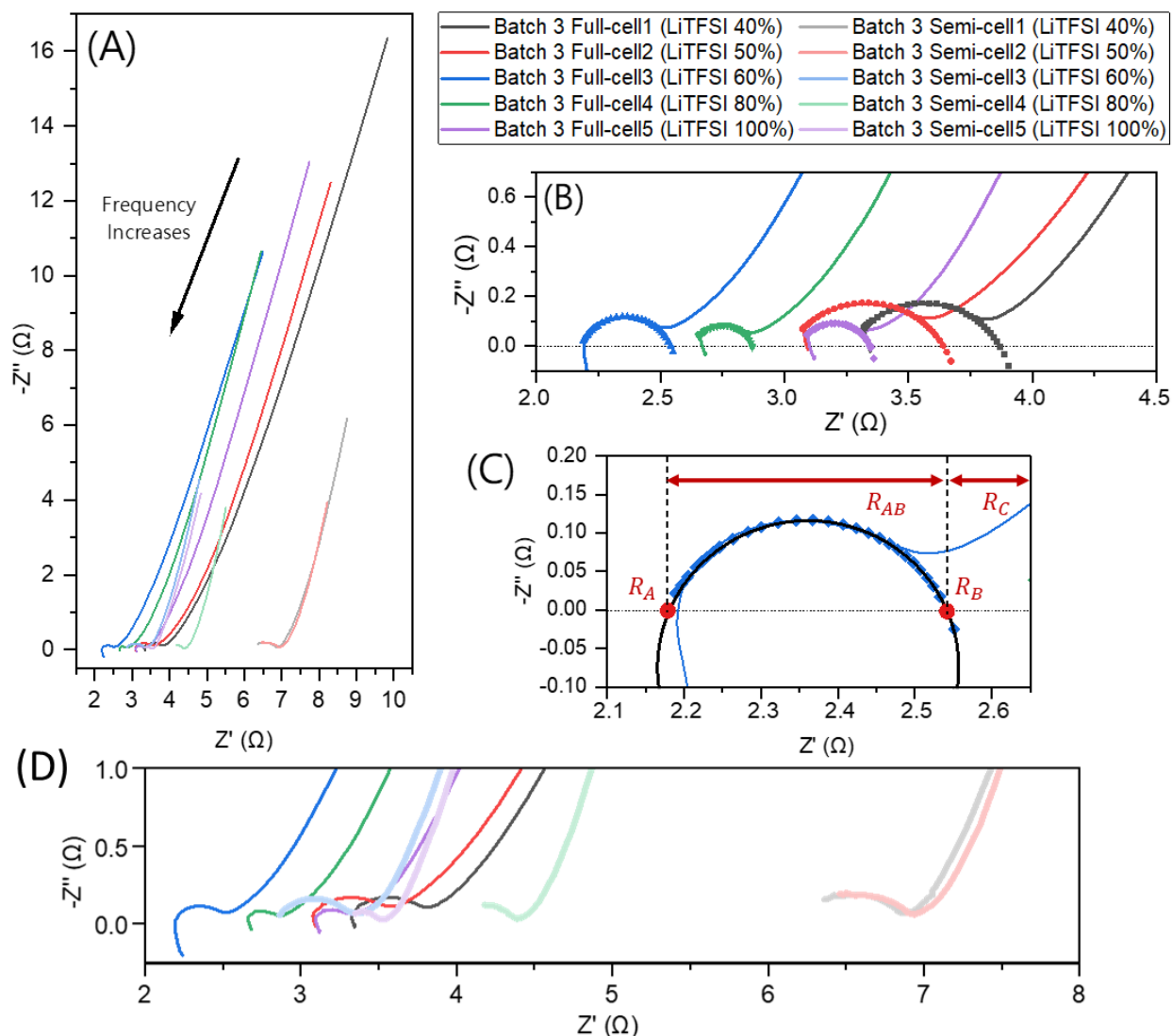


Figure 4.24: The electrochemical impedance spectroscopy (EIS) measurement of batch 3 full cells 1 to 5. (A) Nyquist plots of the batch-3 semi-cells and the full-cells. (B) The high-frequency region of the suppressed semi-circles of the Nyquist plots. (C) The fitted semi-circle of batch 3 full-cell 3 is used as an example to show the intercepts of the semi-circle with the real impedance axis. (D) The high-frequency region of the Nyquist plot indicates the different R_A and R_B of the semi-cell and the full-cell.

4.4. The Demo

The demo is performed by connecting the full cells in series to power a red LED. The red LED has a forward voltage of 1.8-2.0 V and a forward current of 20 mA. Batch 3 cells 3, 4, and 5 were each charged up to 0.7 volts and connected in series. However, the red LED did not light up due to the insufficient voltage. The voltages measured with a multi-meter for cells 3, 4, and 5 after two minutes of charging are 0.31 V, 0.35 V and 0.33 V, respectively, indicating a self-discharge issue. To achieve the desired voltage, batch 3, cells 1 to 5, and cell 10 (6 cells in total) are charged to 0.7 V individually and connected in series. A total voltage of 2.71 volts is measured before discharging.

The demo setup is illustrated in Figure 4.25. The cells are charged individually using a 1.4 V power supply in series with a 140-ohm resistor shown in Figure 4.25 (A). During discharge shown in Figure 4.25 (B), the 6 charged cells are then connected in series with a red LED and a 1-ohm resistor. The PicoScope is used to measure the voltage drop across the cells and the voltage across the 1-ohm resistor (twelve 120-ohm resistors in parallel) to obtain the passing current. The discharge voltage history of the 6 cells in series is shown in Figure 4.26. The LED dims out after 8 minutes and 20 seconds, and the discharge energy is 0.08 Joules.

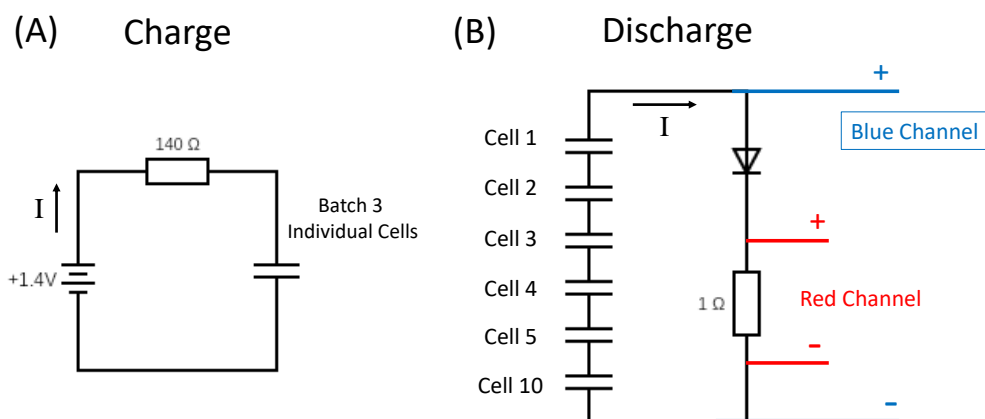


Figure 4.25: (A) The charge setup illustration for charging the cells individually. (B) The discharge setup illustration for powering the red LED. The connection points for the PicoScope to measure the voltage drop across the 6 cells in series (blue channel), and the connection points to measure the passing current, which is determined using the ohm's law with a 1-ohm resistor (12 120 ohm resistors in parallel).

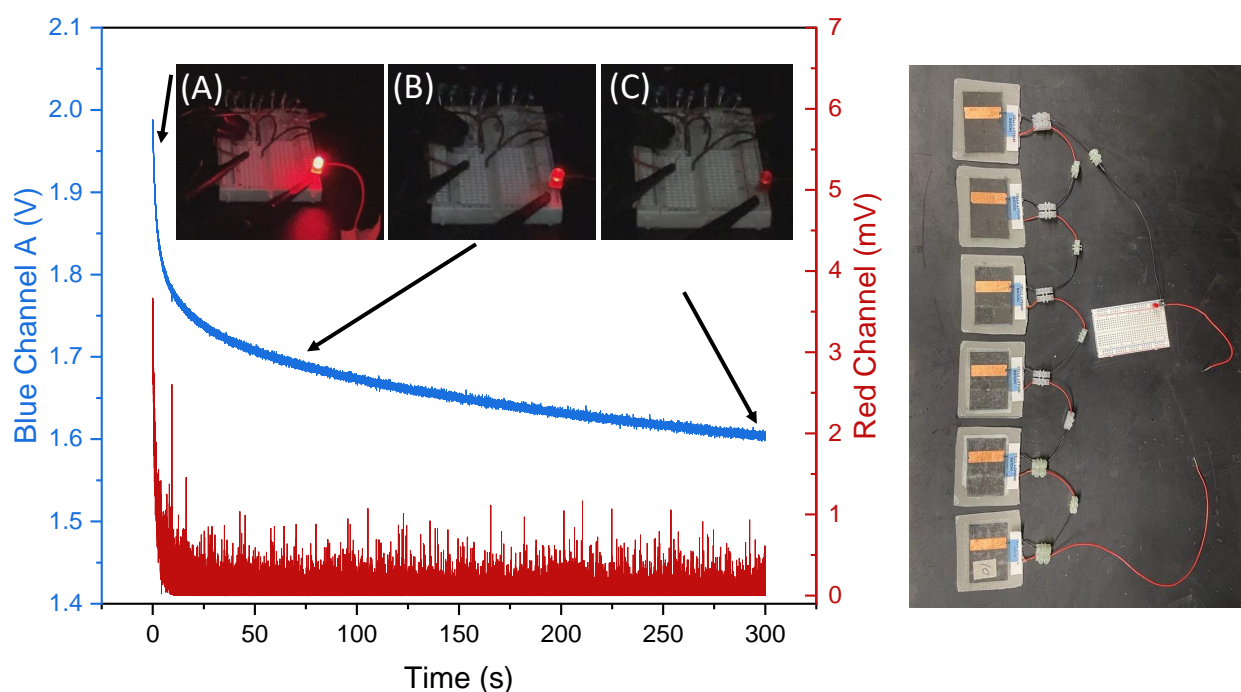


Figure 4.26: The voltage and time history of the 6 cells powering a red LED.

4.4.1. Self-Discharge Phenomena

The demo test showed that cells which charged up to 0.7 V would quickly drop to a steady voltage, indicating self-discharge. The self-discharge test is conducted by charging batch-3 cells up to 0.7 V with a 10 mA constant current and then setting the current to 0 to represent an open circuit. The voltage response is then measured with respect to the time shown in Figure 4.27 (A1) and (B1). In Figure 4.27 (A2) which a gel polymer electrolyte (GPE) separator is used, the time for the voltage to be halved increased when the LiTFSI concentration increased. Whereas in Figure 4.27 (B2), in which GPE-impregnated glass fabrics are used as the separator, the time for the voltage to be halved is more consistent between 1.5 to 2 minutes.

The self-discharge phenomena may arise from the moisture ingress into the gel polymer electrolyte during solution casting and assembly. Or the introduction of impurities in the casted polymer solution when drying in the vacuum oven. Moreover, degradation of the electrolyte/separator occurred during the search for the maximum voltage window for the cells.

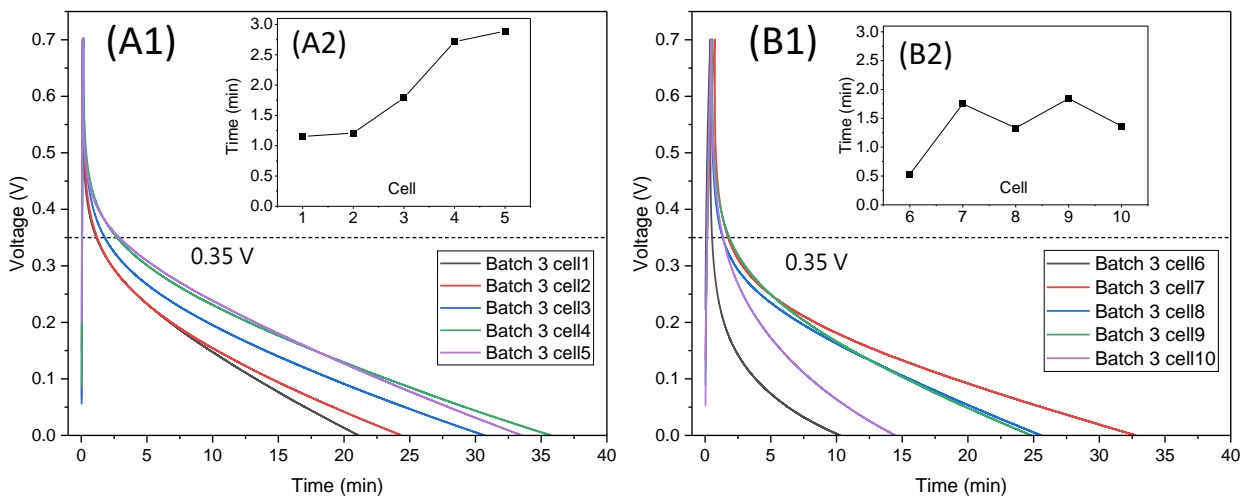


Figure 4.27: The self-discharge phenomena are presented as the voltage drop over time. (A1) The self-discharge effect of batch 3 cells 1 to 5 using a gel polymer electrolyte (GPE). (A2) The time required for the voltage to decrease by half. (B1) The self-discharge effect of batch 3 cells 6 to 10 using a GPE-impregnated glass fabric. (B2) The time required for the voltage to decrease by half.

4.4.2. Three Point Flexural Test

The mean values and the standard deviations (STD) for the flexural chord modulus of elasticity and flexural strength of the mock-up samples are shown in Table 4.3. Individual measurement values for each specimen are shown in Table D.11 and Table D.12. The stress-strain plots for each mock sample are shown in Figure D.9.

Sample Groups	Flexural Chord Modulus (GPa) Mean (STD)	Flexural Strength (MPa) Mean (STD)
no-film-no-bag	11.29 (0.85)	295.28 (26.49)
no-film-with-bag	12.21 (1.1)	270.78 (27.96)
with-film-no-bag	11.89 (0.5)	168.14 (6.21)
with-film-with-bag	12.02 (0.42)	161.67 (9.29)

Table 4.3: Mean values of flexural chord modulus of elasticity and flexural strength of the mock-up samples. The mean values are the average of five specimen measurements.

When a PE film is added to the mock-up specimen without using a pouch bag, a 5.3% increase in flexural modulus and a 43% decrease in flexural strength are recorded. Other the other hand, when a PE film is added in the mock-up sample using a pouch bag, a 1.5% decrease in flexural modulus and a 40% decrease in flexural strength is reported. The findings imply that incorporating a polymer film at the mid-layer in the structural supercapacitor reduces flexural strength while having little effect on the flexural modulus.

When no PE films are added in the mock-up samples, adding a pouch bag resulted in an 8% increase in flexural modulus and an 8.3% decrease in flexural strength. On the other hand, when PE films are present in the mock-up samples, the addition of a pouch bag results in a 1.1% increase in flexural modulus and a 3.8% decrease in flexural strength. These results suggest that adding the pouch bag can overestimate the flexural modulus and underestimate the flexural strength.

The stress-strain plots of batch-2 and batch-3 full cells are shown in Figure 4.28, and their flexural modulus and flexural strength values are shown in Table D.13. To preserve batch 3 full cells from full cell failure, a maximum mid-span deformation limit of 7 mm is set. The influence of the LiTFSI electrolyte salt content on the flexural modulus and the flexural strength of the cells are shown in Figure 4.29. The fibre volume fractions of the cells are shown in Figure 4.30.

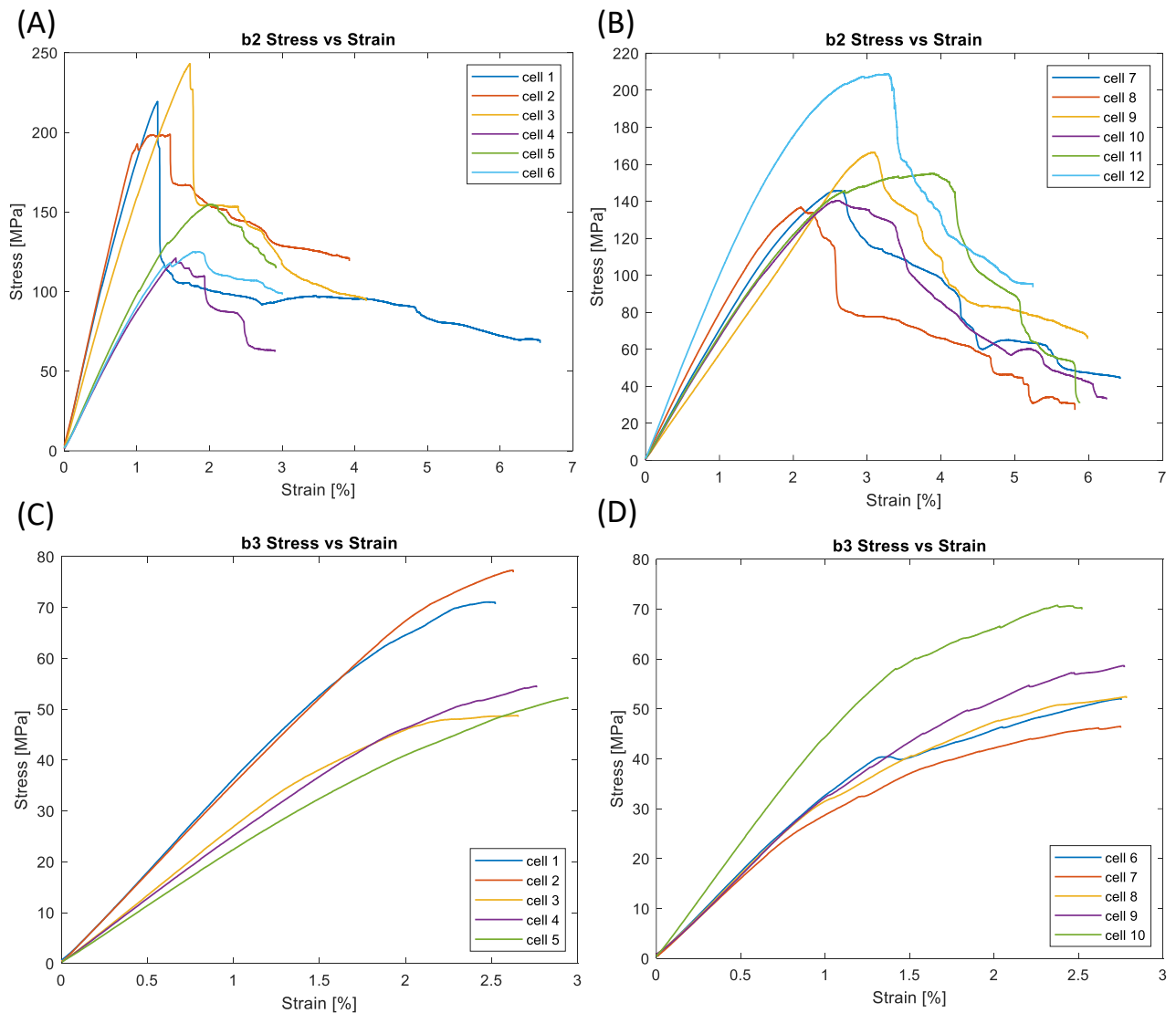


Figure 4.28: The stress-strain plots of batch 2 and batch 3 full cells. (A) Batch 2 full cells 1 to 6. (B) Batch 2 full cells 7 to 12. (C) Batch 3 full cells 1 to 5. (D) Batch 3 full cells 6 to 10. Batch 3 samples are tested up to a maximum deformation of 7 mm.

In Figure 4.29, batch-2 cell 1 to cell 6, which uses a 55 mbar vacuum for epoxy infusion and a 250 mbar vacuum for epoxy curing, is reported to have the highest flexural modulus and strength. The high values are also contributed by having the highest fibre volume fraction and the use of plain weave carbon fibre spread tow as the outermost encapsulation instead of glass fabrics. When the LiTFSI concentration increases from 10% to 60% in batch-2 samples, the flexural modulus decreases by approximately 50%, and the flexural strength decreases by 43%. Batch-2 cells 7 to 12, in which the vacuum pressure is decreased to 850 mbar for infusion and curing, showed a decrease in flexural properties compared to batch 2 cells 1 to 6. The reason may be due to the low fibre volume content and the use of all glass fabric encapsulation layers.

Regarding batch-3 cells, flexural modulus and strength are further decreased. Since the infusion and curing pressure are identical to batch 2 cells 7 to 12, the observed decrease may be attributed to the increased thickness of gel polymer electrolytes and the wider copper tapes that are prone to delamination. For batch-3 cells 1 to 5, which use gel polymer electrolytes as separators, an increase in LiTFSI concentration leads to a decrease in the flexural modulus and strength. However, in batch-3 cells 6 to 10, which uses two layers of glass fabric as separators, an increase in LiTFSI concentration results in an improvement of flexural modulus and strength.

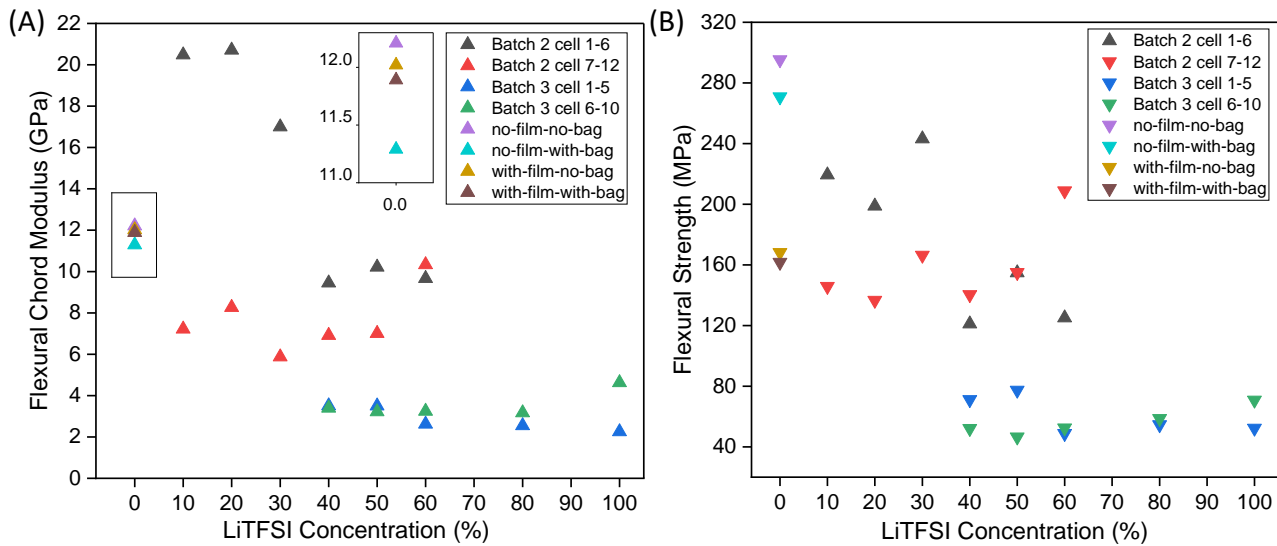


Figure 4.29: The two graphs presents the influence of the LiTFSI concentration and different batches on the flexural properties. (A) The relationship between the flexural chord modulus and LiTFSI concentration. (B) The relationship between the flexural strength and the LiTFSI concentration.

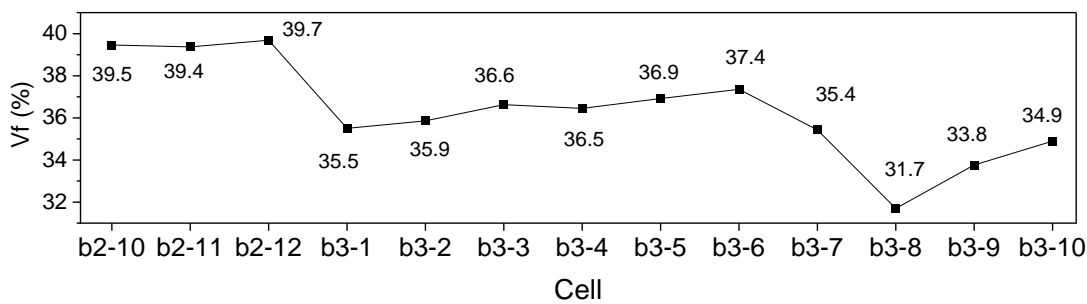


Figure 4.30: The fibre volume fraction of the glass fabric encapsulation.

4.5. Multifunctionality Examination

The influence of the LiTFSI concentration on the specific capacitance and the flexural properties are presented in Figure 4.31. When the LiTFSI concentration increased from 50% to 60% of the weight ratio of the PVDF-HFP, there was a significant drop in the flexural properties and an increase in the capacitance. Below LiTFSI 50% concentration, the capacitance increases and also do the flexural properties to a small extent. Above LiTFSI 60%, both the flexural properties and the specific capacitance drop. This is due to the high ion concentration of the gel polymer electrolyte (GPE) that hinders ionic mobility, while the increased GPE thickness causes a weaker interface between the two electrodes.

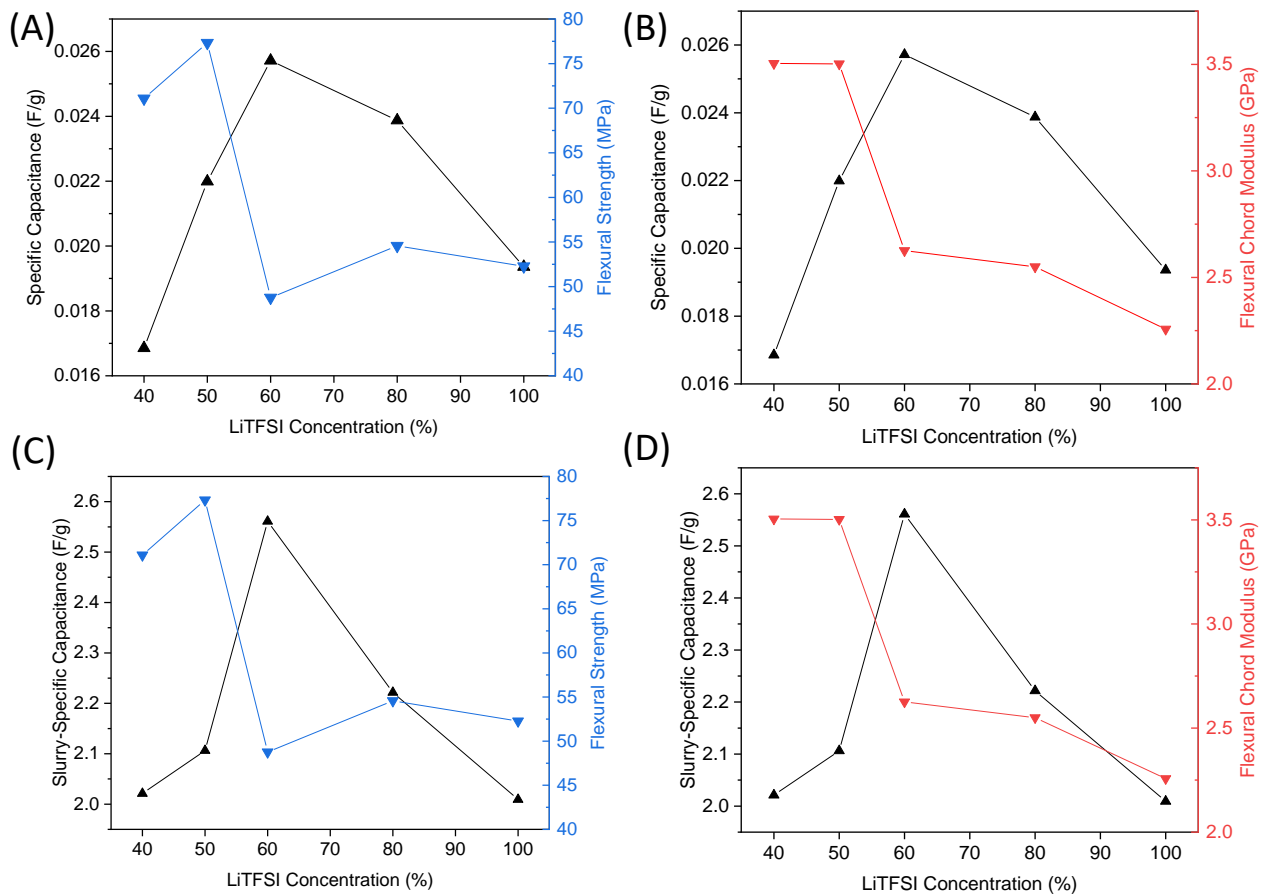


Figure 4.31: The data presented is batch 3 cells 1 to 5, which uses a gel polymer electrolyte as the separator and is measured using a 1 mA constant current. The influence of LiTFSI concentration on (A) Specific capacitance and flexural strength, (B) Specific capacitance and flexural modulus, (C) Slurry-specific capacitance and flexural strength, (D) Slurry-specific capacitance and flexural modulus.

Comparative multifunctionality of the structural supercapacitor (SSC) specific capacitance (normalised with the cell device) and the flexural properties is presented in Figure 4.32. The batch 2 and batch 3 cells are compared with the structural supercapacitors reported by Hudak et al., Reece et al., and Xu et al., that performed flexural tests [55, 105, 149]. The batch 3 SSCs from this work showed multifunctionality by having the points appear on the diagonal line of the chart instead of having an imbalance of flexural properties and capacitance. The SSC in this work also showed superior flexural strength. However, directly comparing the values with other literature values is inaccurate since each SSC uses different materials, laminate layout and electrochemical characterisation methods.

Hudak et al. applied 4 layers of 120 gsm carbon fabric and 2 layers of 120 gsm glass fabric as separators [55]. Although the reported specific capacitance is 0.125 F/g, the value is characterised by a Swagelok-type cell. On the other hand, the flexural properties are measured using a different 1-by-6-inch sample without measuring its electrochemical performance affected by scaling up. The multifunctionality characterisation should have both the flexural and electrochemical properties measured on the same sample cell.

The structural supercapacitor (SSC) produced by Reece et al. is an example of a pouch bag-fibre encapsulation. The SSC consists of a 250 gsm cellulose paper separator and a 120 gsm activated carbon plain-woven fabric infused with an epoxy/ $TEABF_4$ resin and encapsulated with a polymer laminated aluminium foil bag. The capacitance value 0.094 F/g measured with the EIS method is significantly different from the GCD measurement value 0.0046 F/g, which uses a low current density (0.0625 mA/cm^2).

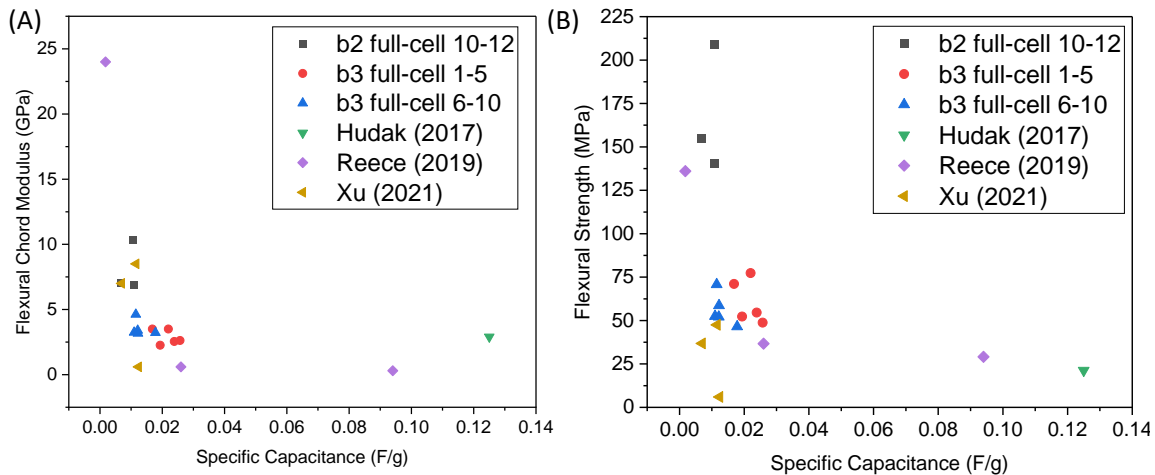
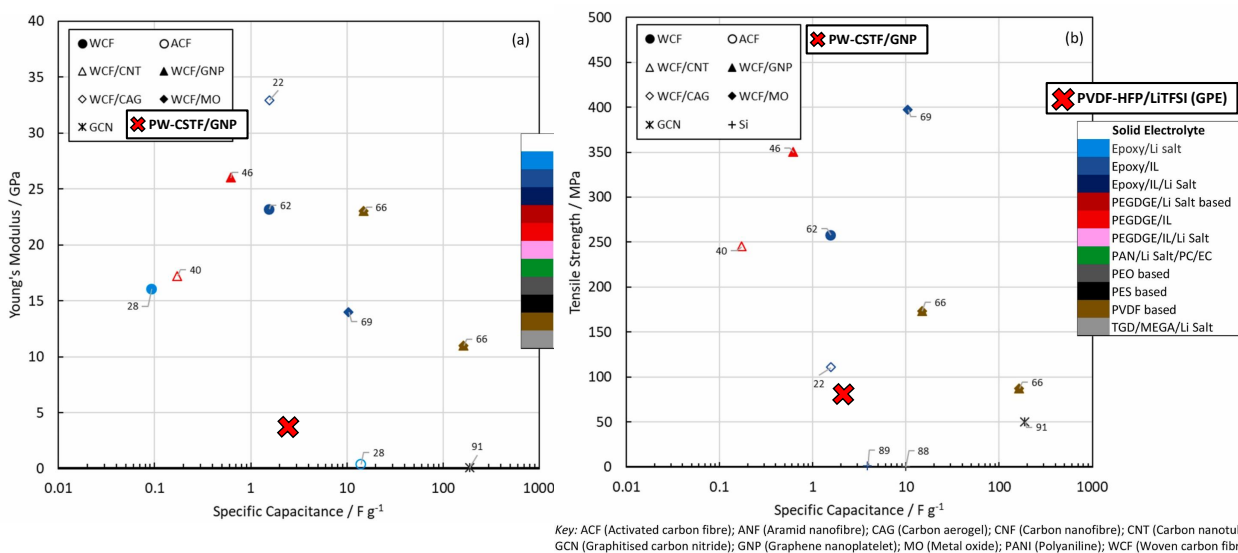


Figure 4.32: (A) The multifunctionality study of the flexural modulus versus the specific capacitance. (B) The multifunctionality study of the flexural strength versus the specific capacitance.

Xu et al. applied two layers of unidirectional discontinuous fibre and glass fabric separators with varying thicknesses to fabricate the structural supercapacitor (SSC). The use of the thin glass fibre separator showed a higher flexural stiffness than thick separators [149]. Senokos et al. also performed flexural testing on a metal-fibre encapsulation interface in which the SSC sample is laminated with 8 layers of 370 gsm carbon satin fabric [114]. High flexural properties of 60 GPa and 153 MPa are obtained. Specific capacitance, energy and power are 88 mF/g, 37.5 mWh/kg, and 30 W/kg, respectively. However, the specific values are only normalised using the SSC sample weight instead of the full composite laminate.

Since there is no standard for testing and fabricating the structural supercapacitors, it is obvious that the flexural properties can be improved by adding more layers of high-areal-density fabrics, and the electrical performance can be measured using a smaller sample size and a low current. Despite the discrepancies in measurement methods, directly comparing the performance with other materials systems still provide valuable insights for improvement. A rough comparison is shown in Figure 4.33 that uses the flexural properties of this work as the tensile modulus and tensile strength.



Key: ACF (Activated carbon fibre); ANF (Aramid nanofibre); CAG (Carbon aerogel); CNF (Carbon nanofibre); CNT (Carbon nanotube); GCN (Graphitised carbon nitride); GNP (Graphene nanoplatelet); MO (Metal oxide); PANI (Polyaniline); WCF (Woven carbon fibre).

Figure 4.33: The structural supercapacitor multifunctionality comparison figures constructed by Greenhalgh et al. [50]. The number of each data point is the reference number in the review literature. The approximate SSC performance of this work is presented as the red cross. The graphs are plotted as the specific capacitance normalised with the active mass (slurry mass) versus (a) The tensile Young's modulus (GPa) and (b) The tensile strength (MPa).

5

Challenges

The challenges encountered during the fabrication and characterisation of each building block of the structural supercapacitors (SSC) are addressed.

For the fabrication of the electrodes, the carbon slurry is deposited onto the plain weave carbon spread tow fabric (PW-CSTF) by brush application. Brushing the slurry manually creates inconsistent electrochemical behaviour measured by the cyclic voltammetry (CV). On the other hand, consistent CV plots are produced from the dip coating, which uses an automatic lifting platform. This suggests that the deposition process should be automated rather than performed manually to ensure better control and precision. Despite the dipping process having better control of deposition, the uneven fabric surface creates slurry agglomerates. Therefore, the deposition process utilises an automatic spraying process is recommended.

The gel polymer electrolyte (GPE) characterisation using electrochemical impedance spectroscopy (EIS) is observed to be unstable. Although part of the reason entails the use of brass electrodes, the other reason might be that the GPE system of LiTFSI-TEP liquid in the PVDF-HFP is not stable even though there are dipole-dipole bonds between the polymer and the liquid medium. The GPE, which is wrapped in Parafilm, encountered a three times ionic conductivity loss after 5 days. A turbidity test should be conducted to examine whether the LiTFSI forms salts over time. If the GPE system presented in this work is inherently unstable, then additives should be added, or a change of material is needed. If the system is stable, environmental conditions such as oxygen, moisture and light might be the cause of instability.

As for cell production, the applied vacuum pressure is the most crucial factor. In this work, an 850 millibar vacuum and a 198 μm gel polymer electrolyte separator thickness produced the best electrochemical performance. However, the low vacuum also produced a low fibre volume fraction that deteriorated the mechanical performance. The reason for applying a low vacuum is to avoid the penetration of the gel polymer electrolyte separator that creates a short circuit. In this work, despite using two layers of glass fabrics as separators, conductivity between the two electrode terminals is still measured using a multimeter. Therefore, in order to use GPE as the separator to achieve good electrolyte performance, additives need to be added to increase its mechanical integrity.

The undesired electrochemical behaviours of the cell include low coulombic efficiency (CE) and self-discharging. The CE for EDLCs should exceed 99% within a suitable voltage window [81]. However, the measured CE for cells 1 to 5 in batch 3 ranges from 70% to 90%. The reason is attributed to short circuits and gel polymer electrolyte (GPE) degradation, as mentioned earlier. Once the stability of the GPE is improved, it is expected that the voltage window of the cell will increase, resulting in higher energy storage. After epoxy infusion, the cell-specific energy dropped 9 times. A desired outcome which indicates a successful encapsulation is that the cell-specific performance decreases the same percentage as the increased weight from semi-cell to full-cell.

6

Conclusions

A structural supercapacitor (SSC) is demonstrated using glass fabrics to directly encapsulate the plain weave carbon spread tow fabric (PW-CSTF) electrodes with a gel polymer electrolyte separator. A fibre-fibre encapsulation interface is achieved. The SSC showed both energy storage and mechanical properties. The findings and contributions of this work are addressed to answer the research questions.

6.1. Answers to the Research Questions

6.1.1. The Experimental Approach

The building block approach (BBA) is applied to the research, which has provided a clear road map to characterise and interpret the structure supercapacitor's behaviour. The standalone materials for the electrode and electrolyte are first characterised, and then their mixture of carbon slurry and gel polymer electrolyte. Finally, the semi-cell assembly and the full-cell after epoxy infusion.

6.1.2. Electrode Materials and Fabrication Method

The GNP-300 slurry, which consists of graphene nanoplatelets (GNP), ethanol and carbon conductive paint, is deposited in the plain weave carbon spread tow (PW-CSTF) fabric using the brush application. GNP-300 slurry is selected based on its high surface area of $231.43 \text{ m}^2/\text{g}$ and high mesopore volumes properties compared to the activated charcoal (AC) slurry. In addition, GNP-300 slurry can also be deposited on the PW-CSTF without generating a cracked surface. Those desired properties are reflected on the cyclic voltammetry measurements of the electrode in a sodium sulfate solution, in which a 21.87 F/g slurry-specific capacitance is achieved. The relationship of the electrode performance versus the slurry deposition mass showed that the GNP-based slurry showed an increase in electrode-specific capacitance when its deposition mass increased. In contrast, the AC-based slurry showed a decrease in electrode-specific capacitance. Directly depositing slurry materials onto plain weave carbon spread tow (PW-CSTF) has the advantage of producing high surface area electrodes through an efficient manufacturing technique beneficial for scaling up.

6.1.3. Gel Polymer Electrolyte Materials and Fabrication Method

A gel polymer electrolyte (GPE) is produced in which the LiTFSI concentration is varied from 0% to 100% wt% of PVDF-HFP. When the LiTFSI concentration increases, the GPE thickness, viscosity and ionic conductivity increase. In contrast, the crystallinity of the GPE decreases, which implies a decrease in mechanical performance. Ionic conductivity of 1 mS/cm, 3 mS/cm and 4 mS/cm are achieved when the LiTFSI is 60%, 80% and 100% wt% of PVDF-HFP. However, GPE degradation is observed in which the ionic conductivity decreased 3 times after five days. Using GPE as separators offers the advantage of producing a separate film that can be directly sandwiched between the electrodes, eliminating the electrolyte infusion process.

6.1.4. Structural Supercapacitor Fabrication

This work proposed an efficient fabrication method for structural supercapacitors, which is suitable for large-scale production since the electrode and the gel polymer electrolyte separators can be stacked up layer-by-layer as in the conventional composite manufacturing process. Furthermore, the same vacuum bagging setup for the semi-cell can be further used for epoxy infusion, thus preventing the semi-cell from moisture and oxygen.

6.1.5. Structural Supercapacitor Cell Performance

The highest performance in terms of electrochemical performance for a full cell is reported to have a cell-specific capacitance of 25.72 mF/g, cell-specific energy of 2.08 mWh/kg and cell-specific power of 25.04 mW/kg. When normalised with the active material, the respective slurry-specific values are 2.56 F/g, 207.24 mWh/kg and 2.47 W/kg. The flexural modulus of the cell is 3.39 GPa, while the flexural strength is 52.07 MPa. After the epoxy infusion of the semi-cell, the cell-specific capacitance and energy decreased 7 to 9 times, while the slurry-specific capacitance and energy decreased 2 to 3 times. The reaction between the epoxy and the TEP-LiTFSI electrolyte is observed. The multi-functionality of this structural supercapacitor design exhibited a threshold at a LiTFSI concentration of 60% of PVDF-HFP. Beyond this threshold, an increase in LiTFSI concentration resulted in improved electrochemical performance but a decrease in flexural properties.

Bibliography

- [1] Aeby, X., Poulin, A., Siqueira, G., Hausmann, M.K., Nyström, G., 2021. Fully 3d printed and disposable paper supercapacitors. *Advanced Materials* 33, 2101328. URL: <https://onlinelibrary.wiley.com/doi/abs/10.1002/adma.202101328>, doi:<https://doi.org/10.1002/adma.202101328>, arXiv:<https://onlinelibrary.wiley.com/doi/pdf/10.1002/adma.202101328>.
- [2] Air-Transport-Action-Group(ATAG), . Waypoint 2050, an air transport action group project URL: https://aviationbenefits.org/media/167417/w2050_v2021_27sept_full.pdf.
- [3] An-Engineer, . An unmanned aerial vehicle (uav). fixed wing uav. İnsansız hava aracı (İha) URL: <https://grabcad.com/library/an-unmanned-aerial-vehicle-uav-fixed-wing-uav-insansiz-hava-araci-iha-1>.
- [4] Anthony, D.B., Qian, H., Clancy, A., Bismarck, A., Greenhalgh, E., Shaffer, M., 2017. Applying a potential difference to minimise damage to carbon fibres during carbon nanotube grafting by chemical vapour deposition. *Nanotechnology* 28. doi:[10.1088/1361-6528/aa783f](https://doi.org/10.1088/1361-6528/aa783f).
- [5] Arof, A.K., Amirudin, S., Yusof, S., Noor, I., 2013. A method based on impedance spectroscopy to determine transport properties of polymer electrolytes. *Physical chemistry chemical physics : PCCP* 16. doi:[10.1039/c3cp53830c](https://doi.org/10.1039/c3cp53830c).
- [6] Artigas, J., Muñoz, B., Sánchez, M., de Prado, J., Utrilla, M., Ureña, A., 2022. Surface modifications of carbon fiber electrodes for structural supercapacitors. *Applied Composite Materials* 29. doi:[10.1007/s10443-021-09998-5](https://doi.org/10.1007/s10443-021-09998-5).
- [7] Asfaw, H.D., Anthony Kucernak, and Emile S. Greenhalgh, a.M.S.S., 2023. Electrochemical performance of supercapacitor electrodes based on carbon aerogel-reinforced spread tow carbon fiber fabrics. *Composites Science and Technology* 238, 110042. URL: <https://www.sciencedirect.com/science/article/pii/S0266353823001355>, doi:<https://doi.org/10.1016/j.compsitech.2023.110042>.
- [8] Asp, L., Bouton, K., Carlstedt, D., Duan, S., Harnden, R., Johannisson, W., Johansen, M., Johansson, M., Lindbergh, G., Liu, F., Peuvot, K., Schneider, L.M., Xu, J., Zenkert, D., 2021a. A structural battery and its multifunctional performance. *Advanced Energy and Sustainability Research* 2. doi:[10.1002/aesr.202000093](https://doi.org/10.1002/aesr.202000093).
- [9] Asp, L.E., Bouton, K., Carlstedt, D., Duan, S., Harnden, R., Johannisson, W., Johansen, M., Johansson, M.K.G., Lindbergh, G., Liu, F., Peuvot, K., Schneider, L.M., Xu, J., Zenkert, D., 2021b. A structural battery and its multifunctional performance. *Advanced Energy and Sustainability Research* 2, 2000093. URL: <https://onlinelibrary.wiley.com/doi/abs/10.1002/aesr.202000093>, doi:<https://doi.org/10.1002/aesr.202000093>, arXiv:<https://onlinelibrary.wiley.com/doi/pdf/10.1002/aesr.202000093>.

- [10] Asp, L.E., Greenhalgh, E.S., 2014. Structural power composites. *Composites Science and Technology* 101, 41–61. URL: <https://www.sciencedirect.com/science/article/pii/S0266353814002218>, doi:<https://doi.org/10.1016/j.compscitech.2014.06.020>.
- [11] Asp, L.E., Johansson, M., Lindbergh, G., Xu, J., Zenkert, D., 2019. Structural battery composites: a review. *Functional Composites and Structures* 1, 042001. URL: <https://dx.doi.org/10.1088/2631-6331/ab5571>, doi:[10.1088/2631-6331/ab5571](https://doi.org/10.1088/2631-6331/ab5571).
- [12] Bhalekar, A., . Semi-trailer with truck URL: <https://grabcad.com/library/semi-trailer-with-truck-1>.
- [13] Bui, V.T., Nguyen, V.T., Nguyen, N.A., Umapathi, R., Larina, L.L., Kim, J.H., Kim, H.S., Choi, H.S., 2021. Multilayered pvdf-hfp porous separator via phase separation and selective solvent etching for high voltage lithium-ion batteries. *Membranes* 11. URL: <https://www.mdpi.com/2077-0375/11/1/41>, doi:[10.3390/membranes11010041](https://doi.org/10.3390/membranes11010041).
- [14] Candy-Design, . Pressure gauge free icon URL: https://www.flaticon.com/free-icon/pressure-gauge_10485856?term=valve+meter&page=1&position=1&origin=search&related_id=10485856.
- [15] Carlstedt, D., Rittweger, F., Runesson, K., Navarro-Suarez, A., Xu, J., Duan, S., Larsson, F., Riem-schneider, K., Asp, L., 2022. Experimental and computational characterization of carbon fibre based structural battery electrode laminae. *Composites Science and Technology* 220, 109283. doi:[10.1016/j.compscitech.2022.109283](https://doi.org/10.1016/j.compscitech.2022.109283).
- [16] Chan, K.Y., Jia, B., Lin, H., Hameed, N., Lee, J.H., Lau, K.T., 2018. A critical review on multifunctional composites as structural capacitors for energy storage. *Composite Structures* 188, 126–142. URL: <https://www.sciencedirect.com/science/article/pii/S0263822317321840>, doi:<https://doi.org/10.1016/j.compstruct.2017.12.072>.
- [17] Charoen-amornkitt, P., Suzuki, T., Tsushima, S., 2020. Effects of voltage-dependence of the constant phase element and ohmic parameters in the modeling and simulation of cyclic voltammograms. *Journal of The Electrochemical Society* 167, 166506. doi:[10.1149/1945-7111/abbe5d](https://doi.org/10.1149/1945-7111/abbe5d).
- [18] Chen, S.Y., van de Waerdt, W., Castro, S.G., 2023. Design for bird strike crashworthiness using a building block approach applied to the flying-v aircraft. *Heliyon* , e14723 URL: <https://www.sciencedirect.com/science/article/pii/S2405844023019308>, doi:<https://doi.org/10.1016/j.heliyon.2023.e14723>.
- [19] Choi, U.H., Jung, B., 2018. Ion conduction, dielectric and mechanical properties of epoxy-based solid polymer electrolytes containing succinonitrile. *Macromolecular Research* 26. doi:[10.1007/s13233-018-6061-9](https://doi.org/10.1007/s13233-018-6061-9).
- [20] Chung, D., 2018. Development, design and applications of structural capacitors. *Applied Energy* 231, 89–101. URL: <https://www.sciencedirect.com/science/article/pii/S0306261918314454>, doi:<https://doi.org/10.1016/j.apenergy.2018.09.132>.
- [21] Danzi, F., Salgado, R.M., Oliveira, J.E., Arteiro, A., Camanho, P.P., Braga, M.H., 2021. Structural batteries: A review. *Molecules* 26. URL: <https://www.mdpi.com/1420-3049/26/8/2203>, doi:[10.3390/molecules26082203](https://doi.org/10.3390/molecules26082203).
- [22] D.B. Anthony, S. Greenhalgh Emile, T.K.A.K.P.L.S.N.G.Q.S.R.E.S.M.S., Valkova, M., 2022. 20th european conference on composite materials, lausanne, switzerland .
- [23] Deka, B.K., Hazarika, A., Kim, J., Kim, N., Jeong, H.E., Park, Y.B., Park, H.W., 2019. Bimetallic copper cobalt selenide nanowire-anchored woven carbon fiber-based structural supercapacitors. *Chemical Engineering Journal* 355, 551–559. URL: <https://www.sciencedirect.com/science/article/pii/S1385894718316462>, doi:<https://doi.org/10.1016/j.cej.2018.08.172>.

- [24] Deka, B.K., Hazarika, A., Kim, J., Park, Y.B., Park, H.W., 2016. Multifunctional cuo nanowire embodied structural supercapacitor based on woven carbon fiber/ionic liquid-polyester resin. *Composites Part A: Applied Science and Manufacturing* 87, 256 – 262. URL: <https://www.scopus.com/inward/record.uri?eid=2-s2.0-84967214627&doi:10.1016/j.compositesa.2016.05.007>, cited by: 85.
- [25] Deka, B.K., Hazarika, A., Kim, J., Park, Y.B., Park, H.W., 2017a. Recent development and challenges of multifunctional structural supercapacitors for automotive industries. *International Journal of Energy Research* 41, 1397–1411. URL: <https://onlinelibrary.wiley.com/doi/abs/10.1002/er.3707>, doi:<https://doi.org/10.1002/er.3707>, arXiv:<https://onlinelibrary.wiley.com/doi/pdf/10.1002/er.3707>.
- [26] Deka, B.K., Hazarika, A., Kwak, M.J., Kim, D.C., Jaiswal, A.P., Lee, H.G., Seo, J., Jeong, C., Jang, J.H., Park, Y.B., Park, H.W., 2021. Triboelectric nanogenerator-integrated structural supercapacitor with in situ mxene-dispersed n-doped zn–cu selenide nanostructured woven carbon fiber for energy harvesting and storage. *Energy Storage Materials* 43, 402–410. URL: <https://www.sciencedirect.com/science/article/pii/S2405829721004542>, doi:<https://doi.org/10.1016/j.ensm.2021.09.027>.
- [27] Deka, B.K., Hazarika, A., Kwon, O., Kim, D., Park, Y.B., Park, H.W., 2017b. Multifunctional enhancement of woven carbon fiber/zno nanotube-based structural supercapacitor and polyester resin-domain solid-polymer electrolytes. *Chemical Engineering Journal* 325, 672–680. URL: <https://www.sciencedirect.com/science/article/pii/S1385894717308434>, doi:<https://doi.org/10.1016/j.cej.2017.05.093>.
- [28] Deka, B.K., Hazarika, A., Lee, S., Kim, D.Y., Park, Y.B., Park, H.W., 2020. Triboelectric-nanogenerator-integrated structural supercapacitor based on highly active p-doped branched cu–mn selenide nanowires for efficient energy harvesting and storage. *Nano Energy* 73, 104754. URL: <https://www.sciencedirect.com/science/article/pii/S2211285520303116>, doi:<https://doi.org/10.1016/j.nanoen.2020.104754>.
- [29] Ding, Y., Qi, G., Cui, Q., Yang, J., Zhang, B., Du, S., 2022. High-performance multifunctional structural supercapacitors based on in situ and ex situ activated-carbon-coated carbon fiber electrodes. *Energy & Fuels* 36, 2171–2178. URL: <https://doi.org/10.1021/acs.energyfuels.1c03966>, doi:10.1021/acs.energyfuels.1c03966, arXiv:<https://doi.org/10.1021/acs.energyfuels.1c03966>.
- [30] Dong, G.H., Mao, Y.Q., Guo, F.L., Li, Y.Q., Huang, P., Fu, S.Y., 2023. Structural battery composites with remarkable energy storage capabilities via system structural design. *Composite Structures* 306, 116615. URL: <https://www.sciencedirect.com/science/article/pii/S0263822322013472>, doi:<https://doi.org/10.1016/j.compstruct.2022.116615>.
- [31] Doubrava, R., Oberthor, M., Bělský, P., Cabrnoch, B., 2022. Application of bird-strike verified analysis for the design of fast helicopter composite cowling. *International Journal of Structural Integrity* 13, 649–658. doi:10.1108/IJSI-10-2021-0113.
- [32] EASA, . European aviation environmental report URL: https://www.easa.europa.eu/eco/eae_r/topics/sustainable-aviation-fuels#:~:text=Currently%20certified%20SAF%20are%20subject,of%20100%25%20SAF%20by%202030.
- [33] van Ekeren, W., Albuquerque, M., Ek, G., Mogensen, R., Brant, W., Costa, L., Brandell, D., Younesi, R., 2023. A comparative analysis of hydrofluoroethers as diluents on solvation structure and electrochemical performance in non-flammable electrolyte. *Journal of Materials Chemistry A* 11. doi:10.1039/D2TA08404J.
- [34] European-Union-Aviation-Safety-Agency-(EASA), 2007. Proposed special condition on installation of supercapacitors applicable to large aeroplanes category issue 1 .

- [35] European-Union-Aviation-Safety-Agency-(EASA), 2020. Certification specifications and acceptable means of compliance for large aeroplanes cs-25 Amendment 26.
- [36] Fales, B., Fujamade, N., Oomens, J., Rodgers, M., 2011. Infrared multiple photon dissociation action spectroscopy and theoretical studies of triethyl phosphate complexes: Effects of protonation and sodium cationization on structure. *Journal of the American Society for Mass Spectrometry* 22, 1862–71. doi:10.1007/s13361-011-0208-7.
- [37] Flaticon, K., . Stirrer free icon URL: https://www.flaticon.com/free-icon/stirrer_3032483?term=stirrer&page=1&position=11&origin=search&related_id=3032483.
- [38] Flieger, J., Flieger, M., 2020. Ionic liquids toxicity—benefits and threats. *International Journal of Molecular Sciences* 21. URL: <https://www.mdpi.com/1422-0067/21/17/6267>, doi:10.3390/ijms21176267.
- [39] Freepik, a. Paintbrush garage tool free icon URL: https://www.flaticon.com/free-icon/paintbrush-garage-tool_47547?term=paint+brush&page=3&position=85&origin=search&related_id=47547.
- [40] Freepik, b. Water drop free icon URL: https://www.flaticon.com/free-icon/water-drop_62805?term=drop&page=2&position=6&origin=search&related_id=62805.
- [41] Galos, J., Best, A., Mouritz, A., 2020. Multifunctional sandwich composites containing embedded lithium-ion polymer batteries under bending loads. *Materials Design* 185, 108228. URL: <https://www.sciencedirect.com/science/article/pii/S0264127519306665>, doi:<https://doi.org/10.1016/j.matdes.2019.108228>.
- [42] Galos, J., Khatibi, A.A., Mouritz, A.P., 2019. Vibration and acoustic properties of composites with embedded lithium-ion polymer batteries. *Composite Structures* 220, 677–686. URL: <https://www.sciencedirect.com/science/article/pii/S0263822319305173>, doi:<https://doi.org/10.1016/j.compstruct.2019.04.013>.
- [43] Ge, Z., He, Z.J., 2015. An effective dipping method for coating activated carbon catalyst on the cathode electrodes of microbial fuel cells. *RSC Adv.* 5. doi:10.1039/C5RA05543A.
- [44] Ghosh, N., . Cubesat URL: <https://grabcad.com/library/cubesat-66>.
- [45] Good-Ware, a. Glass-bottle URL: https://www.flaticon.com/free-icon/jar_1060489?term=glass+bottle&page=1&position=26&origin=search&related_id=1060489.
- [46] Good-Ware, b. Scissor lift free icon URL: https://www.flaticon.com/free-icon/scissor-lift_4344177?term=lifting+platform&page=1&position=6&origin=search&related_id=4344177.
- [47] Good-Ware, c. Water pump free icon URL: https://www.flaticon.com/free-icon/water-pump_4018882?term=pump&page=1&position=21&origin=search&related_id=4018882.
- [48] Greenhalgh, E., 2012. Structural power composites for hybrid vehicles (storage). ECCM 2012 - Composites at Venice, Proceedings of the 15th European Conference on Composite Materials .
- [49] Greenhalgh, E., Ankersen, J., Asp, L., Bismarck, A., Fontana, Q., Houille, M., Kalinka, G., Kucernak, A., Mistry, M., Nguyễn, S., Qian, H., Shaffer, M., Shirshova, N., Steinke, J., Wienrich, M., 2015. Mechanical, electrical and microstructural characterisation of multifunctional structural power composites. *Journal of Composite Materials* 49, 1823–1834. doi:10.1177/0021998314554125.
- [50] Greenhalgh, E.S., Nguyen, S., Valkova, M., Shirshova, N., Shaffer, M.S., Kucernak, A., 2023. A critical review of structural supercapacitors and outlook on future research challenges. *Composites Science and Technology* 235, 109968. URL: <https://www.sciencedirect.com/science/article/pii/S0266353823000611>, doi:<https://doi.org/10.1016/j.compscitech.2023.109968>.

- [51] H. Qian, H.L.Diao, M.H.J.A.N.S.E.G.M.S.A.B., 2012. Carbon fibre modifications for composite structural power devices. EUROPEAN CONFERENCE ON COMPOSITE MATERIALS URL: <http://www.escm.eu.org/eccm15/data/assets/1884.pdf>.
- [52] He, Z., Cao, Q., Jing, B., Wang, X., Deng, Y., 2017. Gel electrolytes based on poly(vinylidene fluoride-co-hexafluoropropylene)/thermoplastic polyurethane/poly(methyl methacrylate) with in situ sio₂ for polymer lithium batteries. RSC Adv. 7, 3240–3248. URL: <http://dx.doi.org/10.1039/C6RA25062A>, doi:10.1039/C6RA25062A.
- [53] Heimbs, S., Wagner, T., Meister, H., Brand, C., Calomfirescu, M., 2018. Bird strike on aircraft radome: Dynamic characterisation of quartz fibre composite sandwich for accurate, predictive impact simulations. EPJ Web of Conferences 183, 01007. doi:10.1051/epjconf/201818301007.
- [54] Hubert, O., Todorovic, N., Bismarck, A., 2022. Towards separator-free structural composite supercapacitors. Composites Science and Technology 217, 109126. URL: <https://www.sciencedirect.com/science/article/pii/S0266353821004826>, doi:<https://doi.org/10.1016/j.compscitech.2021.109126>.
- [55] Hudak, N.S., Schlichting, A.D., Eisenbeiser, K., 2017. Structural supercapacitors with enhanced performance using carbon nanotubes and polyaniline. Journal of The Electrochemical Society 164, A691. URL: <https://dx.doi.org/10.1149/2.0721704jes>, doi:10.1149/2.0721704jes.
- [56] iconixar, . Oven free icon URL: https://www.flaticon.com/free-icon/oven_1941808?term=oven&page=1&position=2&origin=search&related_id=1941808.
- [57] Ihrner, N., Johannisson, W., Sieland, F., Zenkert, D., Johansson, M., 2017. Structural lithium ion battery electrolytes via reaction induced phase-separation. Journal of Materials Chemistry A 5. doi:10.1039/C7TA04684G.
- [58] International-Energy-Agency(IEA), . Realizing the potential of sustainable aviation fuel URL: <https://airlines.iata.org/analysis/realizing-the-potential-of-sustainable-aviation-fuel>.
- [59] International-Energy-Agency(IEA), 2022. Global co₂ emissions in transport by mode in the sustainable development scenario, 2000-2070, iea, paris URL: <https://www.iea.org/data-and-statistics/charts/global-co2-emissions-in-transport-by-mode-in-the-sustainable-development-scenario-2000-2070>.
- [60] Ishfaq, A., Nguyen, S.N., Greenhalgh, E.S., Shaffer, M.S., Kucernak, A.R., Asp, L.E., Zenkert, D., Linde, P., 2023. Multifunctional design, feasibility and requirements for structural power composites in future electric air taxis. Journal of Composite Materials 57, 817–828. URL: <https://doi.org/10.1177/00219983221132621>, doi:10.1177/00219983221132621, arXiv:<https://doi.org/10.1177/00219983221132621>.
- [61] ISO, . Iso 9277:2022 determination of the specific surface area of solids by gas adsorption — bet method URL: <https://www.iso.org/standard/71014.html>.
- [62] Javaid, A., 2011. Structural polymer composites for energy storage devices, phd thesis , 161–172 URL: <https://spiral.imperial.ac.uk/bitstream/10044/1/9464/1/Javaid-A-2012-PhD-Thesis.pdf>.
- [63] Javaid, A., Ho, K., Bismarck, A., Steinke, J., Shaffer, M., Greenhalgh, E., 2016. Carbon fibre-reinforced poly(ethylene glycol) diglycidylether based multifunctional structural supercapacitor composites for electrical energy storage applications. Journal of Composite Materials 50, 2155–2163. URL: <https://doi.org/10.1177/0021998315602324>, doi:10.1177/0021998315602324, arXiv:<https://doi.org/10.1177/0021998315602324>.
- [64] Javaid, A., Irfan, M., 2018a. Multifunctional structural supercapacitors based on graphene nanoplatelets/carbon aerogel composite coated carbon fiber electrodes. Materials Research Expr Graphene aerogel modified ess 6, 016310. URL: <https://dx.doi.org/10.1088/2053-1591/aae862>, doi:10.1088/2053-1591/aae862.

- [65] Javaid, A., Irfan, M., 2018b. Multifunctional structural supercapacitors based on graphene nanoplatelet-carbon aerogel composite coated carbon fiber electrodes. *Materials Research Express* 6. doi:10.1088/2053-1591/aae862.
- [66] Javaid, A., Zafrullah, M.B., ul Haq Khan, F., Bhatti, G.M., 2019. Improving the multifunctionality of structural supercapacitors by interleaving graphene nanoplatelets between carbon fibers and solid polymer electrolyte. *Journal of Composite Materials* 53, 1401–1409. URL: <https://doi.org/10.1177/0021998318802622>, doi:10.1177/0021998318802622, arXiv:<https://doi.org/10.1177/0021998318802622>.
- [67] J.F. Snyder, D.J.O'Brien, E.W., 2015. Handbook of Solid State Batteries, Chapter 19. 2nd ed., WORLD SCIENTIFIC. URL: <https://www.worldscientific.com/doi/abs/10.1142/9487>, doi:10.1142/9487, arXiv:<https://www.worldscientific.com/doi/pdf/10.1142/9487>.
- [68] Johannisson, W., Carlstedt, D., Nasiri, A., Buggisch, C., Linde, P., Zenkert, D., Asp, L.E., Lindbergh, G., Fiedler, B., 2021. A screen-printing method for manufacturing of current collectors for structural batteries. *Multifunctional Materials* 4, 035002. URL: <https://doi.org/10.1088/2399-7532/ac2046>, doi:10.1088/2399-7532/ac2046.
- [69] Kalnaus, S., Asp, L.E., Li, J., Veith, G.M., Nanda, J., Daniel, C., Chen, X.C., Westover, A., Dudney, N.J., 2021. Multifunctional approaches for safe structural batteries. *Journal of Energy Storage* 40, 102747. URL: <https://www.sciencedirect.com/science/article/pii/S2352152X2100476X>, doi:<https://doi.org/10.1016/j.est.2021.102747>.
- [70] Karadotcheva, E., Nguyen, S.N., Greenhalgh, E.S., Shaffer, M.S.P., Kucernak, A.R.J., Linde, P., 2021. Structural power performance targets for future electric aircraft. *Energies* 14. URL: <https://www.mdpi.com/1996-1073/14/19/6006>, doi:10.3390/en14196006.
- [71] K.P., R., Subramanian, S., S, K., Hema, M., Chinnappanadar, S., D, V.P., 2014. Characterization of composite proton conducting polymer electrolyte based on poly(vinyl alcohol) 2, 28–33.
- [72] Law, K.Y., 2014. Definitions for hydrophilicity, hydrophobicity, and superhydrophobicity: Getting the basics right. *The Journal of Physical Chemistry Letters* 5, 686–688. URL: <https://doi.org/10.1021/jz402762h>, doi:10.1021/jz402762h, arXiv:<https://doi.org/10.1021/jz402762h>. pMID: 26270837.
- [73] Lee, E., 2019. Chapter 1 - electrophoresis of a single rigid particle, in: Lee, E. (Ed.), *Theory of Electrophoresis and Diffusiophoresis of Highly Charged Colloidal Particles*. Elsevier. volume 26 of *Interface Science and Technology*, pp. 3–45. URL: <https://www.sciencedirect.com/science/article/pii/B9780081008652000011>, doi:<https://doi.org/10.1016/B978-0-08-100865-2.0001-1>.
- [74] Lekakou, C., Moudam, O., Markoulidis, F., Andrews, T., Watts, J., Reed, G., 2011. Carbon-based fibrous edlc capacitors and supercapacitors. *Journal of Nanotechnology* 2011. doi:10.1155/2011/409382.
- [75] Li, F., Xie, L., Sun, G., Kong, Q., Su, F., Cao, Y., Wei, J., Ahmad, A., Guo, X., Chen, C.M., 2019. Resorcinol-formaldehyde based carbon aerogel: Preparation, structure and applications in energy storage devices. *Microporous and Mesoporous Materials* 279, 293–315. URL: <https://www.sciencedirect.com/science/article/pii/S1387181118306267>, doi:<https://doi.org/10.1016/j.micromeso.2018.12.007>.
- [76] Li, Z., Fu, J., Zhou, X., Gui, S., Wei, L., Yang, H., Li, H., Guo, X., 2023. Ionic conduction in polymer-based solid electrolytes. *Advanced Science* 10, 2201718. URL: <https://onlinelibrary.wiley.com/doi/abs/10.1002/advs.202201718>, doi:<https://doi.org/10.1002/advs.202201718>, arXiv:<https://onlinelibrary.wiley.com/doi/pdf/10.1002/advs.202201718>.
- [77] Liew, C.W., Kam, W., Lim, J., T subramaniam, R., 2013. Electrical, structural, and thermal studies of antimony trioxide-doped poly(acrylic acid)-based composite polymer electrolytes. *Ionics* 20. doi:10.1007/s11581-013-1012-0.

- [78] London, I.C., . Structural supercapacitors, scale-up, assembly and demonstration URL: <https://www.imperial.ac.uk/structural-power-composites/structural-supercapacitors/scale-up-assembly-and-demonstration/>.
- [79] Lyu, Z., Lim, G.J., Koh, J.J., Li, Y., Ma, Y., Ding, J., Wang, J., Hu, Z., Wang, J., Chen, W., Chen, Y., 2021. Design and manufacture of 3d-printed batteries. *Joule* 5, 89–114. URL: <https://www.sciencedirect.com/science/article/pii/S2542435120305183>, doi:<https://doi.org/10.1016/j.joule.2020.11.010>.
- [80] Mahendrakar, S., Anna, M., M., J., 2015. Structural, morphological and fir of pvdf-hfp and lithium tetrafluoroborate salt as polymer electrolyte membrane in lithium ion batteries 8, 319–328.
- [81] Mathis, T.S., Kurra, N., Wang, X., Pinto, D., Simon, P., Gogotsi, Y., 2019. Energy storage data reporting in perspective—guidelines for interpreting the performance of electrochemical energy storage systems. *Advanced Energy Materials* 9, 1902007. URL: <https://onlinelibrary.wiley.com/doi/abs/10.1002/aenm.201902007>, doi:<https://doi.org/10.1002/aenm.201902007>, arXiv:<https://onlinelibrary.wiley.com/doi/pdf/10.1002/aenm.201902007>.
- [82] Mei, B.A., Munteshari, O., Lau, J., Dunn, B., Pilon, L., 2018. Physical interpretations of nyquist plots for edlc electrodes and devices. *The Journal of Physical Chemistry C* 122, 194–206. URL: <https://doi.org/10.1021/acs.jpcc.7b10582>, doi:[10.1021/acs.jpcc.7b10582](https://doi.org/10.1021/acs.jpcc.7b10582), arXiv:<https://doi.org/10.1021/acs.jpcc.7b10582>.
- [83] Militzer, C., Buchsbaum, J., Dzhagan, V., Zahn, D.R.T., Wulff, H., Helm, C.A., Goedel, W.A., 2018. Atomic layer deposition of titanium phosphate from titanium tetrachloride and triethyl phosphate onto carbon fibers. *Advanced Materials Interfaces* 5, 1800423. URL: <https://onlinelibrary.wiley.com/doi/abs/10.1002/admi.201800423>, doi:<https://doi.org/10.1002/admi.201800423>, arXiv:<https://onlinelibrary.wiley.com/doi/pdf/10.1002/admi.201800423>.
- [84] Moyer, K., Meng, C., Marshall, B., Assal, O., Eaves, J., Perez, D., Karkkainen, R., Roberson, L., Pint, C.L., 2020. Carbon fiber reinforced structural lithium-ion battery composite: Multifunctional power integration for cubesats. *Energy Storage Materials* 24, 676–681. URL: <https://www.sciencedirect.com/science/article/pii/S240582971930916X>, doi:<https://doi.org/10.1016/j.ensm.2019.08.003>.
- [85] Navarro-Suarez, A., Shaffer, M., 2022. Designing structural electrochemical energy storage systems: A perspective on the role of device chemistry. *Frontiers in Chemistry* 9. doi:[10.3389/fchem.2021.810781](https://doi.org/10.3389/fchem.2021.810781).
- [86] Nendra-Wahyu, . Droplets free icon URL: https://www.flaticon.com/free-icon/droplets_6352746?term=drop&page=3&position=90&origin=search&related_id=6352746.
- [87] Neste-Corporation, . First flight in history with 100aviation fuel on a regional commercial aircraft URL: https://www.neste.com/releases-and-news/renewable-solutions/first-flight-history-100-sustainable-aviation-fuel-regional-commercial-aircraft?utm_campaign=clicks_communications_press_releases_corporate_neste_neste_press_release_grouped---fin_swe_nl_ger_usca_b2b_new_customers_sustainably-minded-decision-makers-sus_2022_q2&utm_source=twitter&utm_medium=social_organic&utm_content=saf_100_percent_first_flight_pr.
- [88] Nguyen, S., Anthony, D.B., Qian, H., Yue, C., Singh, A., Bismarck, A., Shaffer, M.S., Greenhalgh, E.S., 2019. Mechanical and physical performance of carbon aerogel reinforced carbon fibre hierarchical composites. *Composites Science and Technology* 182, 107720. URL: <https://www.sciencedirect.com/science/article/pii/S0266353819307596>, doi:<https://doi.org/10.1016/j.compscitech.2019.107720>.
- [89] Nguyen, S.N., Millereux, A., Pouyat, A., Greenhalgh, E.S., Shaffer, M.S.P., Kucernak, A.R.J., Linde, P., 2021. Conceptual multifunctional design, feasibility and requirements for structural power in aircraft cabins. *Journal of Aircraft* 58, 677–687. URL: <https://doi.org/10.2514/1.C036205>, doi:[10.2514/1.C036205](https://doi.org/10.2514/1.C036205), arXiv:<https://doi.org/10.2514/1.C036205>.

- [90] Palchoudhury, S., Ramasamy, K., Gupta, R.K., Gupta, A., 2019. Flexible supercapacitors: A materials perspective. *Frontiers in Materials* 5. URL: <https://www.frontiersin.org/articles/10.3389/fmats.2018.00083>, doi:10.3389/fmats.2018.00083.
- [91] Pandey, D., Sambath Kumar, K., Henderson, L., Suarez, G., Vega, P., Salvador, H., Roberson, L., Thomas, J., 2022. Energized composites for electric vehicles: A dual function energy-storing supercapacitor-based carbon fiber composite for the body panels (small 9/2022). *Small* 18. doi:10.1002/sml.202270040.
- [92] Park, H.W., Jang, M.S., Choi, J.S., Pyo, J., Kim, C.G., 2021. Characteristics of woven carbon fabric current collector electrodes for structural battery. *Composite Structures* 256, 112999. URL: <https://www.sciencedirect.com/science/article/pii/S0263822320329251>, doi:<https://doi.org/10.1016/j.compstruct.2020.112999>.
- [93] Pattarakunnan, K., Galos, J., Mouritz, A., 2019. A review of energy storage composite structures with embedded lithium-ion batteries.
- [94] Pernice, M.F., Qi, G., Senokos, E., Anthony, D.B., Nguyen, S., Valkova, M., Greenhalgh, E.S., Shaffer, M.S.P., Kucernak, A.R.J., 2022. Mechanical, electrochemical and multifunctional performance of a cfrp/carbon aerogel structural supercapacitor and its corresponding monofunctional equivalents. *Multifunctional Materials* 5, 025002. URL: <https://dx.doi.org/10.1088/2399-7532/ac65c8>, doi:10.1088/2399-7532/ac65c8.
- [95] Portet, C., Taberna, P., Simon, P., Laberty-Robert, C., 2004. Modification of al current collector surface by sol-gel deposit for carbon-carbon supercapacitor applications. *Electrochimica Acta* 49, 905-912. URL: <https://www.sciencedirect.com/science/article/pii/S0013468603007928>, doi:<https://doi.org/10.1016/j.electacta.2003.09.043>.
- [96] Priya, W.L.M., Suthanthiraraj, S.A., . Electrochemical and ftir studies of pvdf-hfp/(cf3so3)2zn/fe2o3 composite polymer electrolytes .
- [97] Pu, W., He, X., Wang, L., Jiang, C., Wan, C., 2006. Preparation of pvdf-hfp microporous membrane for li-ion batteries by phase inversion. *Journal of Membrane Science* 272, 11-14. URL: <https://www.sciencedirect.com/science/article/pii/S0376738805009300>, doi:<https://doi.org/10.1016/j.memsci.2005.12.038>.
- [98] Qi, G., Nguyen, S., Anthony, D.B., Kucernak, A., Shaffer, M., Greenhalgh, E., 2021. The influence of fabrication parameters on the electrochemical performance of multifunctional structural supercapacitors. *Multifunctional Materials* 4. doi:10.1088/2399-7532/ac1ea6.
- [99] Qian, H., Diao, H., Shirshova, N., Greenhalgh, E.S., Steinke, J.G., Shaffer, M.S., Bismarck, A., 2013a. Activation of structural carbon fibres for potential applications in multifunctional structural supercapacitors. *Journal of Colloid and Interface Science* 395, 241-248. URL: <https://www.sciencedirect.com/science/article/pii/S0021979712013902>, doi:<https://doi.org/10.1016/j.jcis.2012.12.015>.
- [100] Qian, H., Kucernak, A.R., Greenhalgh, E.S., Bismarck, A., Shaffer, M.S.P., 2013b. Multifunctional structural supercapacitor composites based on carbon aerogel modified high performance carbon fiber fabric. *ACS Applied Materials & Interfaces* 5, 6113-6122. URL: <https://doi.org/10.1021/am400947j>, doi:10.1021/am400947j, arXiv:<https://doi.org/10.1021/am400947j>. pMID: 23668320.
- [101] Quantachrome-Instrument, . Novatouch manual URL: https://www.quantachrome.com/gassorption/novatouch_series.html.
- [102] Ramesh, S., Liew, C.W., 2013. Dielectric and ftir studies on blending of [xpmma-(1-x)pvc] with litfsi. *Measurement* 46, 1650-1656. URL: <https://www.sciencedirect.com/science/article/pii/S0263224113000067>, doi:<https://doi.org/10.1016/j.measurement.2013.01.003>.

- [103] Ramesh, S., Ng, H., 2011. An investigation on pan-pvc-litfsi based polymer electrolytes system. *Solid State Ionics* 192, 2–5. URL: <https://www.sciencedirect.com/science/article/pii/S0167273810002894>, doi:<https://doi.org/10.1016/j.ssi.2010.05.045>. proceedings of the 17th International Conference on Solid State Ionics.
- [104] Ratner, M., Johansson, P., Shriver, D., 2000. Polymer electrolytes: Ionic transport mechanisms and relaxation coupling. *MRS Bulletin* 25. doi:[10.1557/mrs2000.16](https://doi.org/10.1557/mrs2000.16).
- [105] Reece, R., Lekakou, C., Smith, P., 2018. A structural supercapacitor based on activated carbon fabric and a solid electrolyte. *Materials Science and Technology* 35, pp 368 – 375.
- [106] Robbins, J., . C7 corvette URL: <https://grabcad.com/library/c7-corvette>.
- [107] Roh, H.D., Deka, B.K., Park, H.W., Park, Y.B., 2021. Multifunctional composite as a structural supercapacitor and self-sensing sensor using nico2o4 nanowires and ionic liquid. *Composites Science and Technology* 213, 108833. URL: <https://www.sciencedirect.com/science/article/pii/S0266353821001895>, doi:<https://doi.org/10.1016/j.compscitech.2021.108833>.
- [108] Sakakibara, K., Kagata, H., Ishizuka, N., Sato, T., Tsujii, Y., 2017. Fabrication of surface skinless membranes of epoxy resin-based mesoporous monoliths toward advanced separators for lithium ion batteries. *J. Mater. Chem. A* 5. doi:[10.1039/C6TA09005B](https://doi.org/10.1039/C6TA09005B).
- [109] Samui, A., Sivaraman, P., 2010. 11 - solid polymer electrolytes for supercapacitors, in: Sequeira, C., Santos, D. (Eds.), *Polymer Electrolytes*. Woodhead Publishing. Woodhead Publishing Series in Electronic and Optical Materials, pp. 431–470. URL: <https://www.sciencedirect.com/science/article/pii/B978184569772350011X>, doi:<https://doi.org/10.1533/9781845699772.2.431>.
- [110] Schneider, L.M., Ihrner, N., Zenkert, D., Johansson, M., 2019. Bicontinuous electrolytes via thermally initiated polymerization for structural lithium ion batteries. *ACS Applied Energy Materials* 2, 4362–4369. URL: <https://doi.org/10.1021/acsaem.9b00563>, doi:[10.1021/acsaem.9b00563](https://doi.org/10.1021/acsaem.9b00563), arXiv:<https://doi.org/10.1021/acsaem.9b00563>.
- [111] Scibioh, M.A., Viswanathan, B., 2020a. Chapter 2 - fundamentals and energy storage mechanisms—overview, in: Scibioh, M.A., Viswanathan, B. (Eds.), *Materials for Supercapacitor Applications*. Elsevier, pp. 15–33. URL: <https://www.sciencedirect.com/science/article/pii/B9780128198582000020>, doi:<https://doi.org/10.1016/B978-0-12-819858-2.00002-0>.
- [112] Scibioh, M.A., Viswanathan, B., 2020b. Chapter 3 - electrode materials for supercapacitors, in: Scibioh, M.A., Viswanathan, B. (Eds.), *Materials for Supercapacitor Applications*. Elsevier, pp. 35–204. URL: <https://www.sciencedirect.com/science/article/pii/B9780128198582000032>, doi:<https://doi.org/10.1016/B978-0-12-819858-2.00003-2>.
- [113] Senokos, E., Anthony, D.B., Rubio, N., Ribadeneyra, M.C., Greenhalgh, E.S., Shaffer, M.S.P., . Robust single-walled carbon nanotube-infiltrated carbon fiber electrodes for structural supercapacitors: from reductive dissolution to high performance devices. *Advanced Functional Materials* n/a, 2212697. URL: <https://onlinelibrary.wiley.com/doi/abs/10.1002/adfm.202212697>, doi:<https://doi.org/10.1002/adfm.202212697>, arXiv:<https://onlinelibrary.wiley.com/doi/pdf/10.1002/adfm.202212697>.
- [114] Senokos, E., Ou, Y., Torres, J., Sket, F., González, C., Marcilla, R., Vilatela, J., 2018. Energy storage in structural composites by introducing cnt fiber/polymer electrolyte interleaves. *Scientific Reports* 8. doi:[10.1038/s41598-018-21829-5](https://doi.org/10.1038/s41598-018-21829-5).
- [115] Senokos, E., Reguero, V., Cabana, L., Palma, J., Marcilla, R., Vilatela, J.J., 2017. Large-area, all-solid, and flexible electric double layer capacitors based on cnt fiber electrodes and polymer electrolytes. *Advanced Materials Technologies* 2, 1600290. URL: <https://onlinelibrary.wiley.com/doi/abs/10.1002/admt.201600290>, doi:<https://doi.org/10.1002/admt.201600290>, arXiv:<https://onlinelibrary.wiley.com/doi/pdf/10.1002/admt.201600290>.

- [116] Shalouf, S.M., Zhang, J., Wang, C.H., 2014. Effects of mechanical deformation on electric performance of rechargeable batteries embedded in load carrying composite structures. *Plastics, Rubber and Composites* 43, 98–104. URL: <https://doi.org/10.1179/1743289813Y.0000000064>, doi:10.1179/1743289813Y.0000000064, arXiv:<https://doi.org/10.1179/1743289813Y.0000000064>.
- [117] Shen, C., Xie, Y., Zhu, B., Sanghadasa, M., Tang, Y., Lin, L., 2017. Wearable woven supercapacitor fabrics with high energy density and load-bearing capability. *Scientific Reports* 7. doi:10.1038/s41598-017-14854-3.
- [118] Shirshova, N., Bismarck, A., Carreyette, S., Fontana, Q., Greenhalgh, E., Jacobsson, P., Johansson, P., Marczewski, M., Kalinka, G., Kucernak, A., Fridner, J., Shaffer, M., Steinke, J., Wienrich, M., 2013a. Structural supercapacitor electrolytes based on bicontinuous ionic liquid-epoxy resin systems. *J. Mater. Chem. A* 1, 15300–15309. doi:10.1039/C3TA13163G.
- [119] Shirshova, N., Qian, H., Shaffer, M.S., Steinke, J.H., Greenhalgh, E.S., Curtis, P.T., Kucernak, A., Bismarck, A., 2013b. Structural composite supercapacitors. *Composites Part A: Applied Science and Manufacturing* 46, 96–107. URL: <https://www.sciencedirect.com/science/article/pii/S1359835X12003247>, doi:<https://doi.org/10.1016/j.compositesa.2012.10.007>.
- [120] Sigma-Aldrich, a. Safety data sheet: 1-ethyl-3-methylimidazolium bis(trifluoromethylsulfonyl)imide URL: <https://www.sigmaaldrich.com/NL/en/sds/sial/11291>.
- [121] Sigma-Aldrich, b. Safety data sheet: 1-ethyl-3-methylimidazolium tetrafluoroborate URL: <https://www.sigmaaldrich.com/NL/en/sds/aldrich/711721>.
- [122] Sigma-Aldrich, c. Safety data sheet: Formaldehyde solution URL: <https://www.sigmaaldrich.com/NL/en/product/sial/15512>.
- [123] Sigma-Aldrich, d. Safety data sheet: Formaldehyde solution URL: <https://www.sigmaaldrich.com/NL/en/product/sial/307521>.
- [124] Sim, L., Majid, S., Arof, A., 2012. Ftir studies of pema/pvdf-hfp blend polymer electrolyte system incorporated with licf3so3 salt. *Vibrational Spectroscopy* 58, 57–66. URL: <https://www.sciencedirect.com/science/article/pii/S092420311100169X>, doi:<https://doi.org/10.1016/j.vibspec.2011.11.005>.
- [125] Smashicons, . Spatula free icon URL: https://www.flaticon.com/free-icon/spatula_3005165?term=spatula&related_id=3005165.
- [126] Steindl, M., . Aircraft fuselage section URL: <https://grabcad.com/library/aircraft-fuselage-section-1>.
- [127] Subhani, K., Jin, X., Mahon, P.J., Kin Tak Lau, A., Salim, N.V., 2021. Graphene aerogel modified carbon fiber reinforced composite structural supercapacitors. *Composites Communications* 24, 100663. URL: <https://www.sciencedirect.com/science/article/pii/S2452213921000395>, doi:<https://doi.org/10.1016/j.coco.2021.100663>.
- [128] Sánchez-Romate, X.F., Bosque, A.D., Artigas-Arnaldas, J., Muñoz, B.K., Sánchez, M., Ureña, A., 2021. A proof of concept of a structural supercapacitor made of graphene coated woven carbon fibers: Eis study and mechanical performance. *Electrochimica Acta* 370, 137746. URL: <https://www.sciencedirect.com/science/article/pii/S0013468621000359>, doi:<https://doi.org/10.1016/j.electacta.2021.137746>.
- [129] Technische-Universität-Dresden, . On the way to the new generation of 3d-printed, structural supercaps URL: https://tu-dresden.de/ing/maschinenwesen/ilk/das-institut/news/auf-dem-weg-zur-neuen-generation-3d-gedruckter-strukturtragender-supercaps?set_language=en.
- [130] Textreme, a. How to work with textreme URL: <https://www.textreme.com/>.

- [131] Textreme, b. The spread tow technology URL: <https://www.textreme.com/technology/what-is-spread-tow-technology/>.
- [132] Thomas, J., Qidwai, S., 2005. The design and application of multifunctional structure-battery materials systems. *Journal of Minerals, Metals and Materials Society* 57, 18–24. doi:10.1007/s11837-005-0228-5.
- [133] Thommes, M., Kaneko, K., Neimark, A.V., Olivier, J.P., Rodriguez-Reinoso, F., Rouquerol, J., Sing, K.S., 2015. Physisorption of gases, with special reference to the evaluation of surface area and pore size distribution (iupac technical report). *Pure and Applied Chemistry* 87, 1051–1069. URL: <https://doi.org/10.1515/pac-2014-1117>, doi:doi:10.1515/pac-2014-1117.
- [134] Tibor, . Eyes to hear with URL: <https://grabcad.com/library/eyes-to-hear-with>.
- [135] T.S, A.K., . Boston dynamics spot URL: <https://grabcad.com/library/boston-dynamics-spot-1>.
- [136] Tunalı, B., Kaya Kınaytürk, N., 2009. Ft-ir spectroscopic study of triethyl phosphate adsorption on fau type zeolite. *Asian Journal of Chemistry* 21, 4914–4918.
- [137] Valkova, M., Nguyen, S., Senokos, E., Razavi, S., Kucernak, A., Anthony, D., Shaffer, M., Greenhalgh, E., 2023. Current collector design strategies: The route to realising scale-up of structural power composites. *Composites Science and Technology* 236, 109978. URL: <https://www.sciencedirect.com/science/article/pii/S0266353823000714>, doi:<https://doi.org/10.1016/j.compscitech.2023.109978>.
- [138] Veloso, G.B.R., Andrade, R.S., Cicarelli, R.M.B., Iglesias, M., Chiari-Andréo, B.G., 2020. Ionic Liquids as “Green Solvents”: Are they Safe?. Springer International Publishing, Cham. pp. 1–25. URL: https://doi.org/10.1007/978-3-030-44995-7_1, doi:10.1007/978-3-030-44995-7_1.
- [139] Wang, Y., Qiao, X., Zhang, C., Zhou, X., 2019. Development of structural supercapacitors with epoxy based adhesive polymer electrolyte. *Journal of Energy Storage* 26, 100968. URL: <https://www.sciencedirect.com/science/article/pii/S2352152X19308862>, doi:<https://doi.org/10.1016/j.est.2019.100968>.
- [140] Wang, Y.J., Kim, D., 2007. Crystallinity, morphology, mechanical properties and conductivity study of in situ formed pvdf/licl₄/tio₂ nanocomposite polymer electrolytes. *Electrochimica Acta* 52, 3181–3189. URL: <https://www.sciencedirect.com/science/article/pii/S0013468606010759>, doi:<https://doi.org/10.1016/j.electacta.2006.09.070>.
- [141] Wehner, L.A., Mittal, N., Liu, T., Niederberger, M., 2021. Multifunctional batteries: Flexible, transient, and transparent. *ACS Central Science* 7, 231–244. URL: <https://doi.org/10.1021/acscentsci.0c01318>, doi:10.1021/acscentsci.0c01318, arXiv:<https://doi.org/10.1021/acscentsci.0c01318>. PMID: 33655063.
- [142] Wendong, Q., Dent, J., Arrighi, V., Cavalcanti, L., Shaffer, M., Shirshova, N., 2021. Biphasic epoxy-ionic liquid structural electrolytes: minimising feature size through cure cycle and multifunctional block-copolymer addition. *Multifunctional Materials* 4, 035003. doi:10.1088/2399-7532/ac1ea7.
- [143] Wong, D.H.C., Vitale, A., Devaux, D., Taylor, A., Pandya, A.A., Hallinan, D.T., Thelen, J.L., Mecham, S.J., Lux, S.F., Lapidés, A.M., Resnick, P.R., Meyer, T.J., Kosteckı, R.M., Balsara, N.P., DeSimone, J.M., 2015. Phase behavior and electrochemical characterization of blends of perfluoropolyether, poly(ethylene glycol), and a lithium salt. *Chemistry of Materials* 27, 597–603. URL: <https://doi.org/10.1021/cm504228a>, doi:10.1021/cm504228a, arXiv:<https://doi.org/10.1021/cm504228a>.
- [144] Works, J.G., . Josh gore works p1 tiny whoop carbon reinforced drone URL: <https://grabcad.com/library/josh-gore-works-p1-tiny-whoop-carbon-reinforced-drone-1>.

- [145] Wu, Y., Li, Y., Wang, Y., Liu, Q., Chen, Q., Chen, M., 2022. Advances and prospects of pvdf based polymer electrolytes. *Journal of Energy Chemistry* 64, 62–84. URL: <https://www.sciencedirect.com/science/article/pii/S2095495621002096>, doi:<https://doi.org/10.1016/j.jechem.2021.04.0076>.
- [146] Xu, J., Geng, Z., Johansen, M., Carlstedt, D., Duan, S., Thiringer, T., Liu, F., Asp, L., 2022. A multicell structural battery composite laminate. *EcoMat* 4. doi:[10.1002/eom2.12180](https://doi.org/10.1002/eom2.12180).
- [147] Xu, K., 2004. Nonaqueous liquid electrolytes for lithium-based rechargeable batteries. *Chemical reviews* 104, 4303–417. doi:[10.1002/chin.200450271](https://doi.org/10.1002/chin.200450271).
- [148] Xu, Y., Lu, W., Xu, G., Chou, T.W., 2021a. Structural supercapacitor composites: A review. *Composites Science and Technology* 204, 108636. URL: <https://www.sciencedirect.com/science/article/pii/S0266353820324301>, doi:<https://doi.org/10.1016/j.compscitech.2020.108636>.
- [149] Xu, Y., Pei, S., Yan, Y., Wang, L., Xu, G., Yarlagadda, S., Chou, T.W., 2021b. High-performance structural supercapacitors based on aligned discontinuous carbon fiber electrodes and solid polymer electrolytes. *ACS Applied Materials & Interfaces* 13, 11774–11782. URL: <https://doi.org/10.1021/acscami.0c19550>, doi:[10.1021/acscami.0c19550](https://doi.org/10.1021/acscami.0c19550), arXiv:<https://doi.org/10.1021/acscami.0c19550>. pMID: 33683859.
- [150] Yadav Shikha, Kamble, Z.B.B.K., 2022. Advances in multifunctional textile structural power composites: a review. *Journal of Materials Science* 57, 17105–17138. URL: <https://doi.org/10.1007/s10853-022-07713-8>, doi:[10.1007/s10853-022-07713-8](https://doi.org/10.1007/s10853-022-07713-8).
- [151] Yang, H., Wu, N., 2022. Ionic conductivity and ion transport mechanisms of solid-state lithium-ion battery electrolytes: A review. *Energy Science & Engineering* 10, 1643–1671. URL: <https://onlinelibrary.wiley.com/doi/abs/10.1002/ese3.1163>, doi:<https://doi.org/10.1002/ese3.1163>, arXiv:<https://onlinelibrary.wiley.com/doi/pdf/10.1002/ese3.1163>.
- [152] Yu A.a, Chabot V.a, Z.J., 2017. *Electrochemical supercapacitors for energy storage and delivery: Fundamentals and applications*. CRC Press. doi:<https://doi.org/10.1201/b14671>.
- [153] Zhang, S., Pan, N., 2015. Supercapacitors performance evaluation. *Advanced Energy Materials* 5, 1401401. URL: <https://onlinelibrary.wiley.com/doi/abs/10.1002/aenm.201401401>, doi:<https://doi.org/10.1002/aenm.201401401>, arXiv:<https://onlinelibrary.wiley.com/doi/pdf/10.1002/aenm.201401401>.
- [154] Zhou, H., Li, H., Li, L., Liu, T., Chen, G., Zhu, Y., Zhou, L., Huang, H., 2022. Structural composite energy storage devices — a review. *Materials Today Energy* 24, 100924. URL: <https://www.sciencedirect.com/science/article/pii/S2468606921002896>, doi:<https://doi.org/10.1016/j.mtener.2021.100924>.



Literature Supplementary Information

Electrode materials	Electrode BET surface area (m ² /g)
N-doped Zn–Cu selenide-MXene (<i>N@ZnCuSe₂ – MXene</i>) [26]	657.32
<i>ZnCuSe₂ – MXene (Ti₃C₂Tx)</i> [26]	583.98
P-doped Cu–Mn selenide nanowires (<i>P@Cu_{0.5}Mn_{0.5}Se₂</i>) [28]	524.617
<i>NiCo₂O₄</i> [107]	478.16
<i>Cu_{0.63}Co_{0.37}Se₂</i> nanowires [23]	195.65
ZnO nanorods [27]	139
CuO nanowires [24]	132.85
CAG/GNP5wt% (soak and press) [64]	223
Activated carbon slurry on CF [29]	162.77
CAG/MWCNT1wt% (soak-and-press) [6]	66.18
CAG/GNP3wt% (soak-and-press) [6]	63.95
CAG/PW-CSTF [7]	230
SWCNT (Supergrowth) infiltration [113]	196
Electrophoretic Deposition (EPD) [54]	193
CAG soak-and-press [100]	163.1
CAG infusion (152x102 mm ²) [100]	118
CAG infusion (220x170 mm ²) [100]	80.7
CAG (soak-and-press) [6]	54.61
CNT grafting [51]	45.8
CNT sizing [51]	33.4
KOH-activated carbon fabric [99]	23.3
GNP spray coating [6]	4.72
CO ₂ -activated [99]	1.1
Air-activated [99]	0.6
Pristine carbon fabric [99]	0.21

Table A.1: Brunauer-Emmett-Teller (BET) surface area of the electrodes.

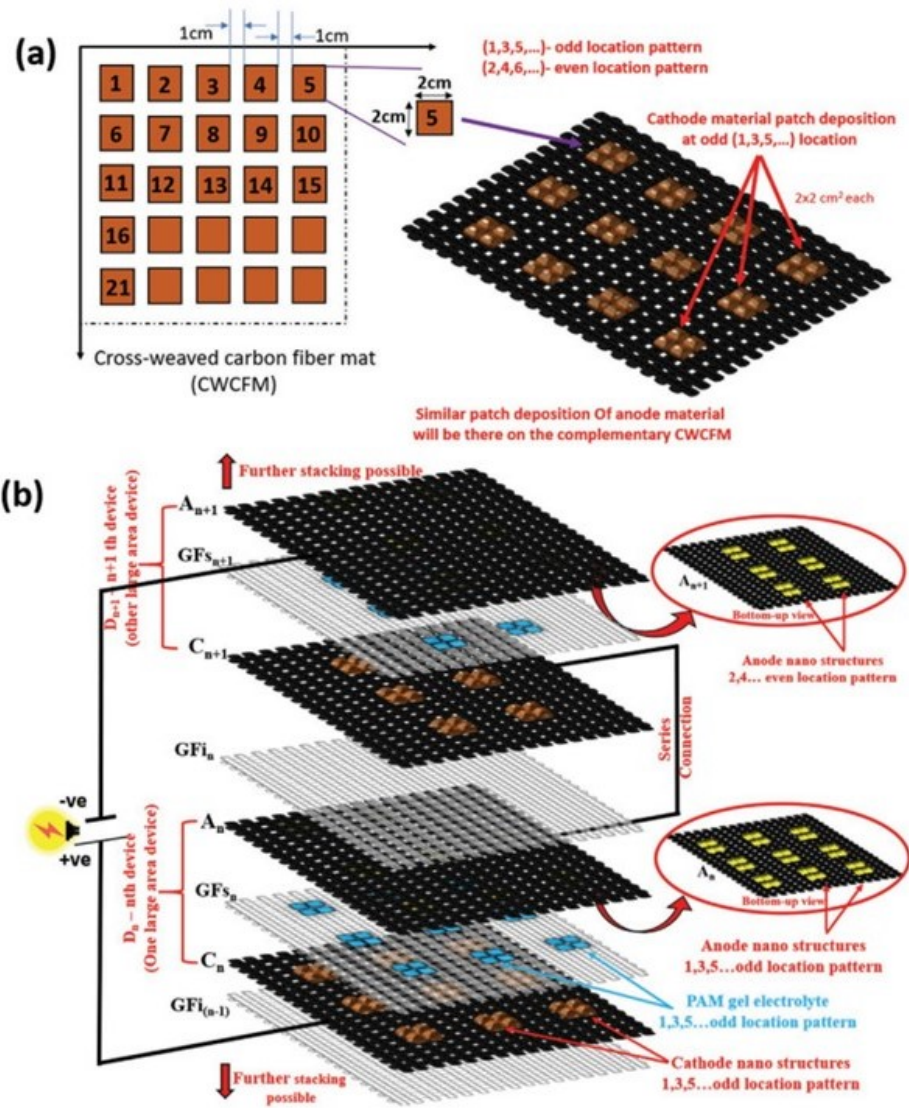


Figure A.1: Left: Parallel SSC design with interlaced current collectors pattern. Right: SSC design with the pattern of the locally coated material on carbon fabrics [91].

B

Carbon Aerogel Reinforced Carbon Fabric

The original design concept for a structural supercapacitor is shown in Figure B.1. The spacing of the plain weave carbon fibre spread tow (PW-CFST) is filled with a continuous carbon aerogel (CA)-graphene nanoplatelets (GNP) network. The electrode surface is deposited with carbon particles as GNP and activated charcoal. The two electrodes are separated with a gel polymer electrolyte and encapsulated with glass fabrics. In this section, the impregnation methods of resorcinol-formaldehyde solution in a carbon non-crimp fabric are presented. Carbonisation cannot be performed due to the lack of a nitrogen-filled box furnace.

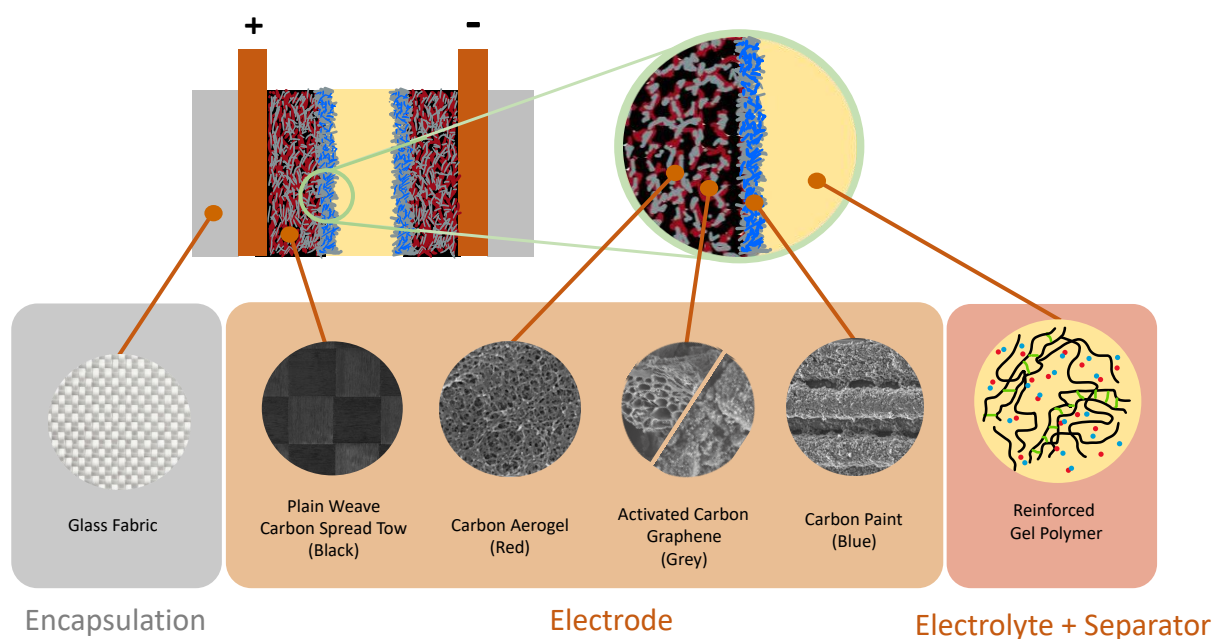


Figure B.1: Structural supercapacitor concept reinforced by carbon aerogel (CAG). CAG image: [88]. The dots in the gel polymer represents cations and anions. The black-coloured chains in the gel polymer represent polymer chains with a degree of cross-linking labelled in green.

B.0.1. Materials and Equipment

In this study, carbon non-crimp fabric ST 150 g/m² is used as the carbon fabric instead of the Textreme plain weave carbon fibre spread tow due to its unavailability during its designated experimental time frame. Formaldehyde solution (15512, 37% in aqueous solution), Resorcinol (307521), sodium carbonate (223484) and sodium hydroxide (221465) are provided by Sigma-Aldrich. Molar ratios of materials (R: resorcinol, F: formaldehyde, W: distilled water) are used to present the number of materials added to the solution.

B.0.2. Method 1: Glass Plate Pressing

The 50 mm by 50 mm carbon non-crimp fabric (NCF) is first heat treated at 450°C for 30 minutes. Molar ratios of $R/F = 0.5$, $R/Na_2CO_3 = 50$, and $R/W = 0.25$ are used to formulate the RF solution. Sodium carbonate (Na_2CO_3) is used as the catalyst. The solution is mixed for 1 hr at 400 rpm until it turns into a reddish colour. The solution is poured into large Petri dishes, and the NCF is soaked for 1 hour. Due to the hydrophobic nature of the NCF surface, the NCF cannot be fully soaked, which is flipped every 15 minutes.

Carbon non-crimp fabrics (NCF) wetted with the resorcinol-formaldehyde (RF) solution are pressed between two glass plates by vacuum bagging at a 200-millibar vacuum. The set was cured in the oven for 72 hrs at 90°C. The resorcinol and formaldehyde in the solution form a continuous network to become a gel. After curing, the yellowish solution becomes a dark reddish brittle solid.

The RF gel coating is not homogeneous. The red circle indicates the excess RF resin, which showed resin fracture. The blue circle is the desired RF gel-coated carbon fibre which showed a reddish colour and a homogeneous distribution. The reason for the non-homogeneous results is due to the wrinkle of the Kapton tape after heat treatment that holds the non-crimp fabrics (NCF) together. The non-crimp fabrics are scattered after heat treatment and cannot be processed as a fabric surface without the holding of the Kapton tape. The process is shown in [Figure B.2](#).

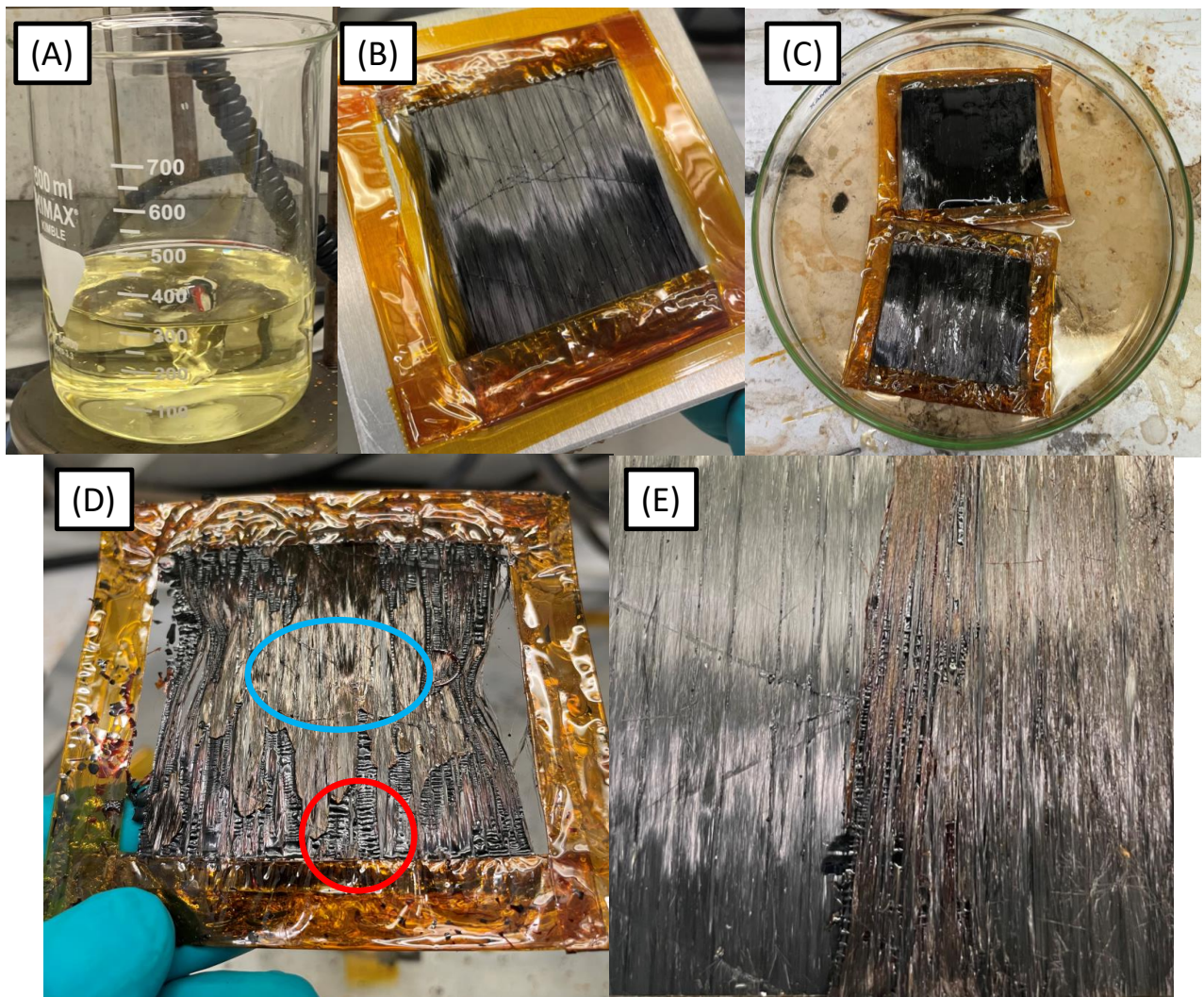


Figure B.2: (A) Resorcinol-formaldehyde (RF) solution. (B) Heat-treated carbon non-crimp (NCF) fabrics (C) Soaking NCF in the RF solution. (D) Glass plate-pressed RF gel-coated NCF. (E) NCF before (left) and after (right) RF gel coating.

B.0.3. Method 2: Vacuum-Assisted Resin Transfer Moulding

Molar ratios of $R/F = 0.5$, $R/Na_2CO_3 = 500$, and $R/W = 0.25$ are used to formulate the RF solution. The reason for decreasing the Na_2CO_3 catalyst amount is based on the excessive Na_2CO_3 shown after a $600^\circ C$ 30-minute carbonization without inert gas. The solution is mixed for 1 hr at 400 rpm until it turns into a reddish colour. A carbon non-crimp (NCF) fabric 150 mm by 120 mm is used for RF solution infusion.

Infusion is performed under the fumehood with a 300-millibar vacuum which takes the resin 9 seconds to travel from the inlet to the outlet. The infusion layup sequence from bottom to top is steel plate, NCF, release film, peel ply, flow mesh, and vacuum bag. The infused fabric is cured at room temperature for 24 hours and 72 hours at $80^\circ C$ with a 300-millibar vacuum. After RF solution infusion, the fabric showed no fibre distortion and could easily detach from the mould. The result showed a low content of RF gel coating on the fabrics in [Figure B.3 \(A\)](#).

To enhance the infusion process, the flow mesh was eliminated to allow for better fibre wetting. Additionally, the amount of catalyst was increased to $R/Na_2CO_3 = 300$. An infusion was carried out under an 800-millibar vacuum for 21 seconds. The infused fabric was subsequently cured at room temperature under a 600-millibar vacuum for 24 hours, followed by an additional 24 hours at $80^\circ C$ under the same vacuum.

It is discovered that the poor coating of the resorcinol-formaldehyde (RF) gel on the non-crimp fabric (NCF) shown in [Figure B.3](#) is due to the poor wettability of the distilled water shown in [Figure B.3 \(D\)](#). Water as a solvent needs to be replaced or mixed with another solvent which has a lower surface tension.

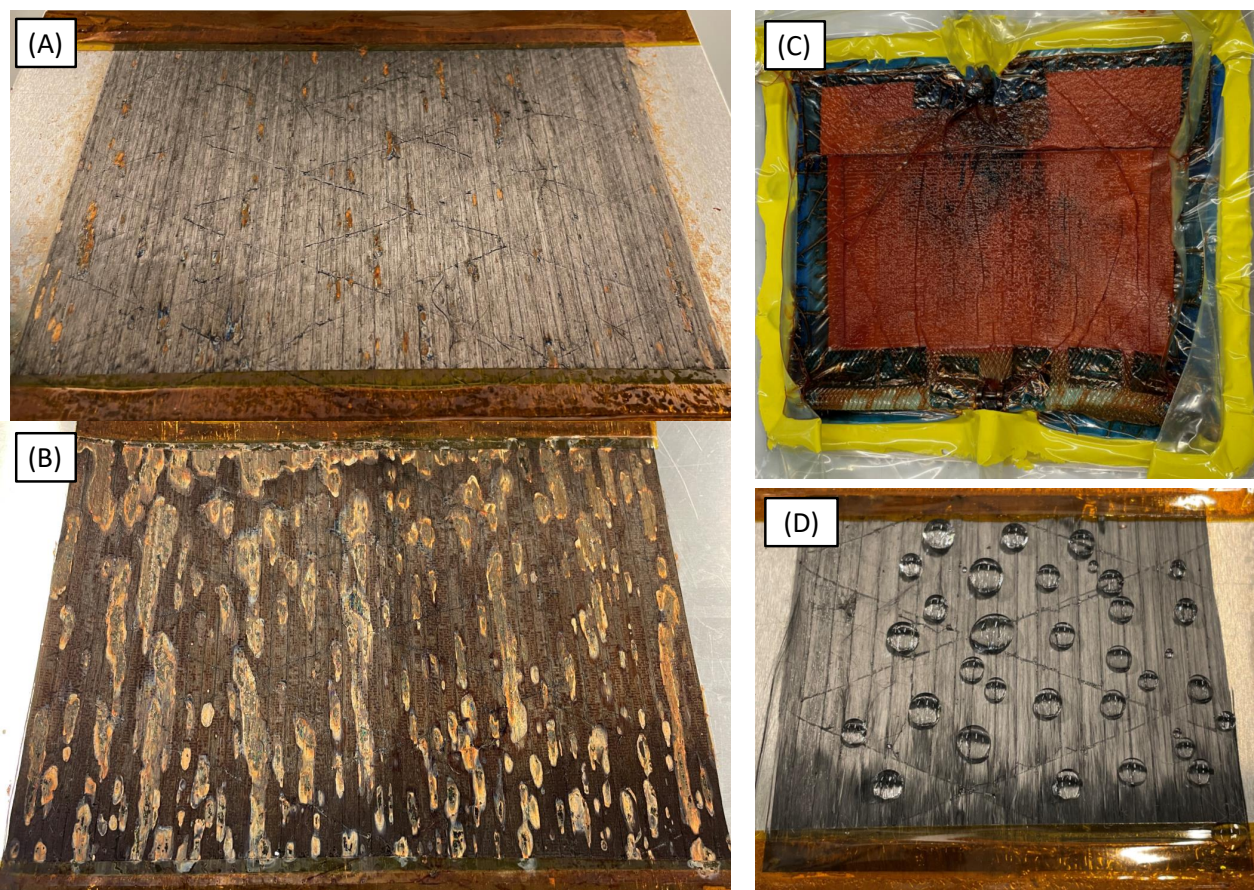


Figure B.3: (A) Resorcinol-formaldehyde (RF) infusion trial 1, 300-millibar vacuum infusion. (B) Resorcinol-formaldehyde (RF) infusion trial 2, 800-millibar vacuum infusion. (C) Trial 2 VARTM of the cured vacuum setup. (D) The hydrophobic surface of the non-crimp fabric.

B.0.4. Method 3: Glass Plate Pressing with Ethanol Solvent

Glass plate pressing without vacuum bagging pressure is used to coat resorcinol-formaldehyde (RF) gel on 150 mm by 120 mm non-crimp fabric (NCF). The glass plate pressing method is improved by attaching the Kapton tape only at the edge normal to the fibres. Molar ratios of $R/F = 0.5$, $R/N a_2 C O_3 = 300$, $R/W = 0.05$ and $R/\text{ethanol} = 0.2$ are used to mix the RF solution for 1 hour at 400 rpm. Ethanol is added to improve the wettability of the RF solution. Non-crimp fabric (NCF) has good wettability with the solution and is soaked in the resorcinol-formaldehyde (RF) solution for 1 hour. Curing is performed at 70°C for 72 hours. The result showed in Figure B.4 (A) has an improved distribution of RF gel on NCF due to the improved wettability. During the curing process, the release film wrinkled and caused a non-homogeneous RF gel distribution with resin-rich and dry spots. Carbonization was attempted using method 3, but it resulted in dispersed fibres shown in Figure B.4 (C) due to contamination and oxidation caused by the lack of an inert gas-filled furnace.

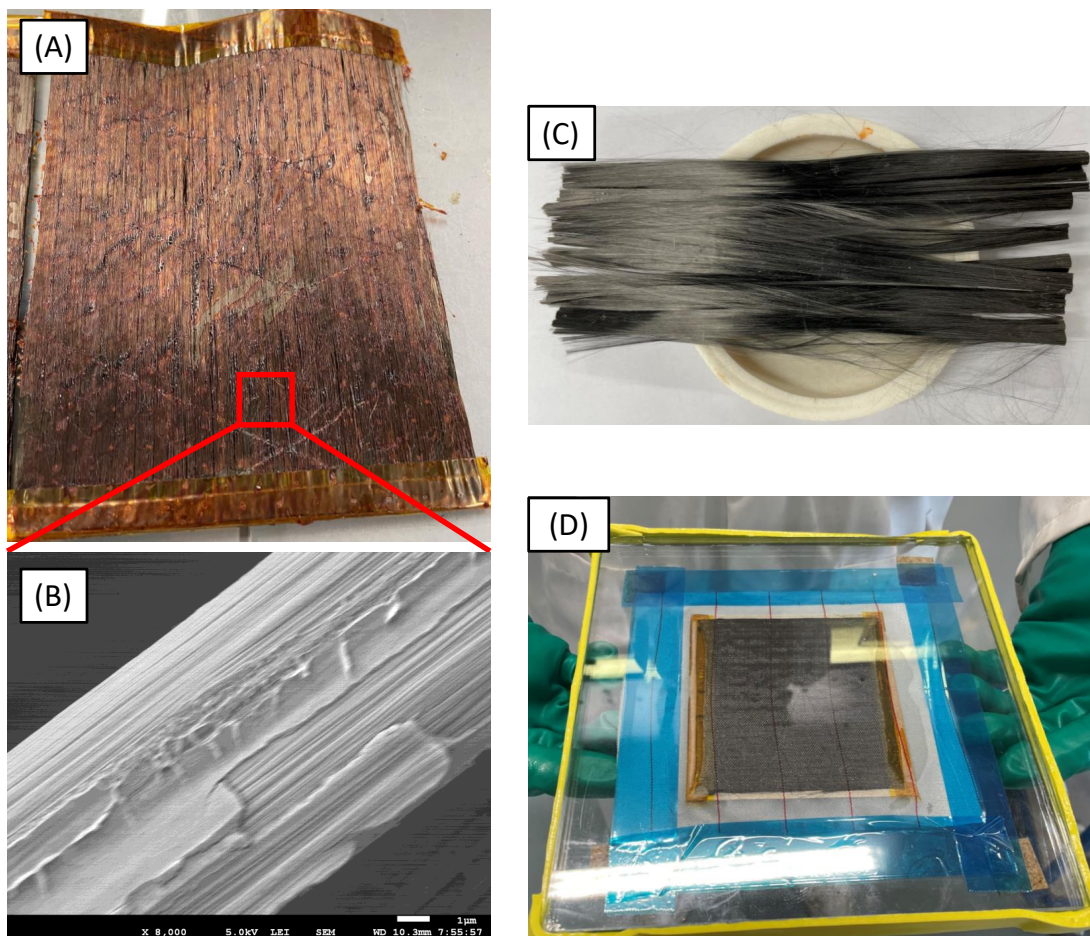


Figure B.4: (A) Non-crimp fabric coated with resorcinol-formaldehyde (RF) gel. (B) SEM image of a single fibre coated with the RF gel (C) Carbonization of the sample under a nitrogen vented furnace at 600°C for 30 minutes. (D) Glass plate clamping method.

B.0.5. Conclusions

The resorcinol-formaldehyde (RF) solution formulation in method 3 works well for producing an RF gel-coated non-crimp fabric. VARTM is preferred for scaling up when compared with glass plate pressing. VARTM using an 800 millibar vacuum infusion is suitable to avoid fabric distortion. Curing should be done first at room temperature for 24 hours and then at 70°C for 72 hours. This method has the benefit of solidifying the NCF at room temperature first, which prevents wrinkling of the peel ply and release film from affecting the homogeneity of the NCF surface. The curing temperature varies between research, while the curing time is widely reported to be 72 hours [7, 100].

A plain weave spread tow fabrics coated with carbon aerogel is successfully demonstrated by Asfaw et al. shown in Figure B.5 [7]. Molar ratios of $R/F = 0.5$, $R/KOH = 50$, and $R/W = 0.07$ are used to formulate the RF solution. A high surface area of $230 \text{ m}^2/\text{g}$ is obtained. Carbon aerogel proves to be a good candidate for structural supercapacitor electrodes [7, 50, 100]. However, the long curing duration, hazardous chemicals used during processing and the stiff RF gel-coated fabric that hinders flexibility are the challenges.

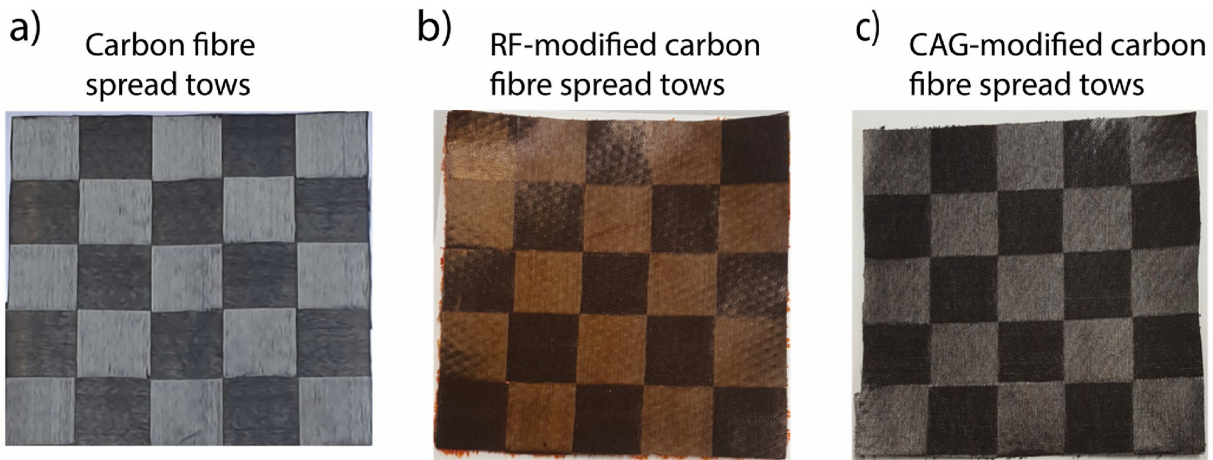


Figure B.5: (A) Spread tow fabrics coated with carbon aerogel [7].

C

Gantt Chart

Step	Task	Duration	Description	Mon	Tues	Wed	Thur	Fri	Mon
1	Cutting Carbon Fibre Spread Tow	Flexible	Done before heat treatment	█					
2	Carbon Fibre Spread tow Heat treatment	Flexible	Heat treating 24 electrode cells require 2 heat treatment repetitions	█					
3	Gel Polymer Electrolyte Solution Fabrication	16hr	Tues 11:30am - Wed 9:00am	█	█				
4	Gel Polymer Electrolyte Film Fabrication	24hr	Wed 11:00am - Thursday 11:00am		█	█			
5	Graphene Nanoplatelets Slurry Fabrication	1hr	Vortex mixing 10 mins			█			
6	Attach Copper Tape	2hr	Weight the taped electrode			█			
7	Electrode Fabrication	2hr	Weight slurry coated electrode				█		
8	Sandwiching Supercapacitor Cells	5hr	Assemble cells and prepare vaccum setup				█		
9	Low Vacuum Pressure Heating Treatment	24hr	850 millibar low vacuum				█	█	
10	Cell Storage in Parafilm	2hr	Right after the vaccum bag is opened						█

Figure C.1: Production Gantt chart for batch one.

Step	Task	Duration	Description	Mon	Tues	Wed	Thur	Fri
1	Cutting Carbon Fibre Spread Tow	Flexible	Done before heat treatment					
2	Carbon Fibre Spread tow Heat treatment	Flexible	Heat treating 24 electrode cells require 2 heat treatment repetitions.					
3	Gel Polymer Electrolyte Solution Fabrication	16hr	Tues 11:30am - Wed 9:00am					
4	Gel Polymer Electrolyte Film Fabrication	24hr	Wed 11:00am - Thursday 11:00am					
5	Carbon Slurry Fabrication	1hr	Vortex mixing 10 mins					
6	Electrode Fabrication	2hr	Weight slurry coated electrode					
7	Attach Copper Tape	2hr	Weight the taped electrode					
8	Sandwiching Supercapacitor Cells	5hr	Assemble cells and prepare vaccum setup					
9	Low Vacuum Pressure Heating Treatment	24hr	850 millibar low vacuum					
10	Attach Wires	1hr	Use copper tape to attaches wires					
11	Cell Storage in Parafilm	2hr	Right after the vaccum bag is opened					

Figure C.2: Production Gantt chart for batch two.

Step	Task	Duration	Description	Mon	Tues	Wed	Thur	Fri
1	Cutting Carbon Fibre Spread Tow	Flexible	Done before heat treatment					
2	Carbon Fibre Spread tow Heat treatment	Flexible	Heat treating 24 electrode cells require 2 heat treatment repetitions.					
3	Gel Polymer Electrolyte Solution Fabrication	16hr	Tues 11:30am - Wed 9:00am					
4	Gel Polymer Electrolyte Film Fabrication	24hr	Wed 11:00am - Thursday 11:00am					
5	Graphene Nanoplatelets Slurry Fabrication	1hr	Vortex mixing 10 mins					
6	Attach Copper Tape and Wires	2hr	Weight the taped electrode					
7	Electrode Fabrication	2hr	Weight slurry coated electrode					
8	Sandwiching Supercapacitor Cells	5hr	Assemble cells and prepare vaccum setup					
9	Low Vacuum Pressure Heating Treatment	24hr	850 millibar low vacuum					
10	Cell Storage in Parafilm	2hr	Right after the vaccum bag is opened					

Figure C.3: Production Gantt chart for batch three.

D

Measurements

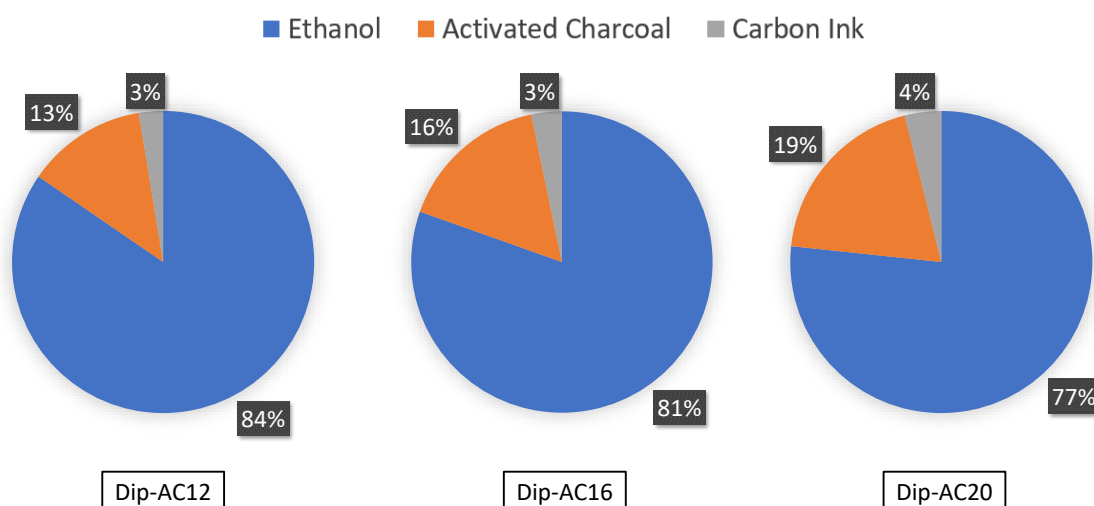


Figure D.1: The weight ratios of the three different slurries based on varying concentrations of activated charcoal.

	Sample Area (mm ²)	Electrode Weight (mg)	Slurry Weight (mg)	Capacitance (mF)
PW-CSTF	630	127.7	0	0.5
Carbon Paint	540	132.1	22.4	2.1
Dip-AC-12-1	690	173.6	34.7	58.5
Dip-AC-12-2	630	155.2	34.9	52.5
Dip-AC-12-3	600	173.8	45.9	160.1
Dip-AC-16-1	600	179.3	32.6	132.9
Dip-AC-16-2	680	192.8	47	121.5
Dip-AC-16-3	714	199.4	44.8	166.7
Dip-AC-20-1	665	201.8	51	149.3
Dip-AC-20-2	680	218.7	72.8	225.8
Dip-AC-20-3	700	215.4	100.1	225.6

Table D.1: Dip coating sample properties.

	Sample Area (mm ²)	Electrode Weight (mg)	Slurry Weight (mg)	Capacitance (mF)
b-AC200-1b(1)	580	130.9	13.7	111.7
b-AC200-2b(2)	600	151.4	29.2	127.7
b-AC200-3b(3)	504	152.8	38	89.8
b-AC200-4b(4)	690	205.3	82.6	176.7
b-AC200-5b(5)	644	208.3	98.4	152.4
b-AC300-1b(1)	600	140.5	27.4	164.7
b-AC300-2b(2)	600	166.6	39.2	173.8
b-AC300-3b(3)	630	189.6	66.7	137.6
b-AC300-4b(4)	588	191.8	82.6	167.5
b-AC300-5b(5)	525	208.4	114.5	100.3
b-AC400-1b(1)	528	117.8	15.5	124.9
b-AC400-2b(2)	572	143.2	40.4	174.7
b-AC400-3b(3)	528	166.3	77.4	131.3
b-AC400-4b(4)	588	221.5	106.3	148.3
b-AC400-5b(5)	588	255.1	147.9	153.5
b-AC500-1b(1)	609	148.1	23.5	199.7
b-AC500-2b(2)	682	197.5	62.1	215.4
b-AC500-3b(3)	577.5	193.2	99.8	136.7
b-AC500-4b(4)	585	244.7	137.6	134.5
b-AC500-5b(5)	550	236.2	156.1	74.7

Table D.2: Brush application of the activated charcoal (AC) sample properties.

	Sample Area (mm ²)	Electrode Weight (mg)	Slurry Weight (mg)	Capacitance (mF)
b-GNP200-1b(1)	745.5	158.5	11.4	248.4
b-GNP200-1b(2)	714	157.6	12.2	205.2
b-GNP200-2b(3)	580	152.9	29.1	428.5
b-GNP200-2b(4)	680	162.4	29.2	488.1
b-GNP300-1b(1)	567	127.1	14.6	319.3
b-GNP300-1b(2)	640	148.3	26.8	370.2
b-GNP300-2b(3)	638	161.1	36.9	742.8
b-GNP300-2b(4)	600	157.9	52.4	473.2
b-GNP400-1b(1)	609	142.8	18	340.3
b-GNP400-1b(2)	563.75	133.3	16.8	418.7
b-GNP400-2b(3)	649	165.8	41.9	597.5
b-GNP400-2b(4)	553.5	161.9	50.4	915.3
b-GNP500-1b(1)	580	143.7	17.4	467.7
b-GNP500-1b(2)	630	164.3	27.7	545.8
b-GNP500-2b(3)	609	213.2	101.1	939.6
b-GNP500-2b(4)	560	206.9	107.7	916.3

Table D.3: Brush application of the graphene nanoplatelets (GNP) sample properties.

	Sample Area (mm ²)	Electrode Weight (mg)	Slurry Weight (mg)	Capacitance (mF)
b-AC80-GNP320-b1(1)	530	132.8	15.3	357.9
b-AC80-GNP320-b1(2)	650	160.6	25.2	519.2
b-AC80-GNP320-b2(3)	551	173.9	43.8	470.9
b-AC80-GNP320-b2(4)	494	144.3	73.1	494.3
b-AC160-GNP240-b1(1)	540	135.5	24.7	306.3
b-AC160-GNP240-b1(2)	609.5	140.3	18.1	325.2
b-AC160-GNP240-b2(3)	551	169.4	38.2	478.6
b-AC160-GNP240-b2(4)	507	155.6	36.7	479.8
b-AC240-GNP160-b1(1)	569.75	142.2	22.3	317.2
b-AC240-GNP160-b1(2)	672	147.7	14.2	223.3
b-AC240-GNP160-b2(3)	609	171.3	40.2	387.4
b-AC240-GNP160-b2(4)	553.5	162.8	47.3	394.8
b-AC320-GNP80-b1(1)	525	124.6	16.2	197.6
b-AC320-GNP80-b1(2)	580.5	150	20.1	219.8
b-AC320-GNP80-b2(3)	560	168.1	36.6	229.5
b-AC320-GNP80-b2(4)	540	161.5	29.5	218.9

Table D.4: Brush application of the mixed activated charcoal-graphene nanoplatelets sample properties.

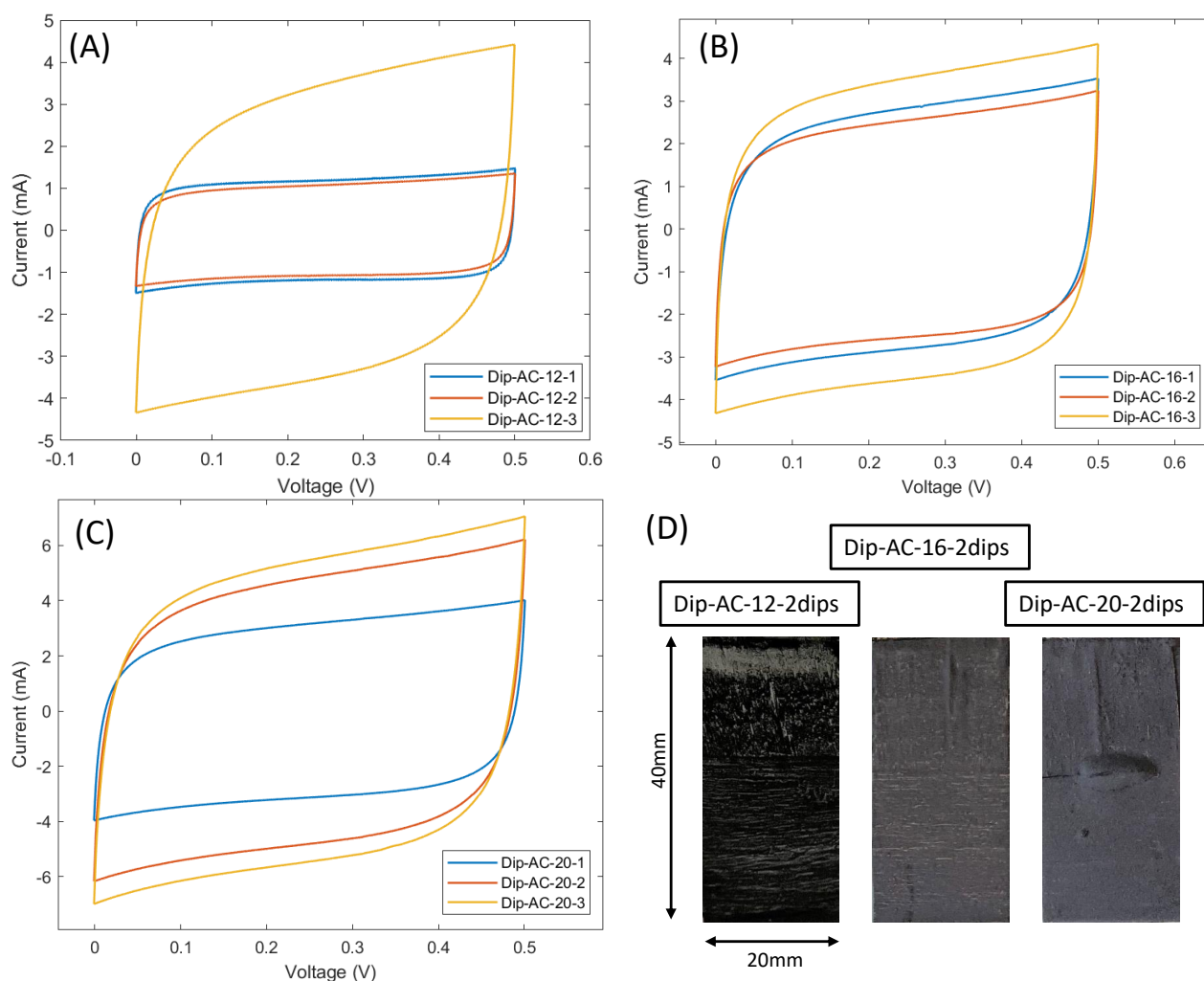


Figure D.2: CV plots of the dip-coated samples. (A) CV curve of the Dip-AC-12 slurry. (B) CV curve of the Dip-AC-16 slurry. (C) CV curve of the Dip-AC-20 slurry. The numbers 1 to 3 indicate the number of dips. (D) Surfaces of the dipping samples.

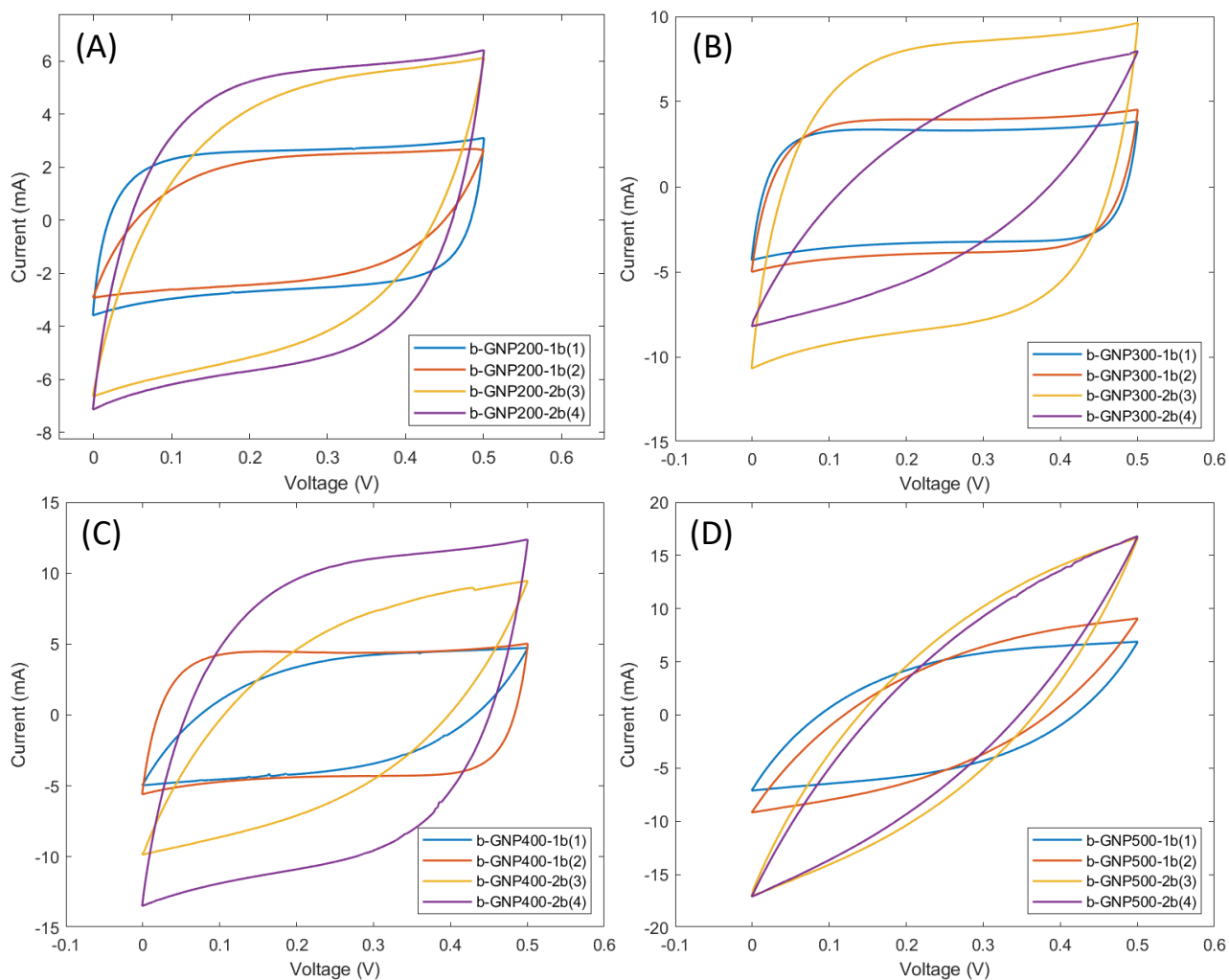


Figure D.3: CV plots of the electrode samples brush-coated with the GNP slurry. (A) CV curves of the b-GNP200 slurry. (B) CV curves of the b-GNP300 slurry. (C) CV curves of the b-GNP400 slurry. (D) CV curves of the b-GNP500 slurry.

Sample Code	Image.	Droplet	Left Angle (°)	Right Angle (°)	Mean Angle (°)
b-GNP300-1b(2)	img1	distilled water	123.01	123.19	123.1
b-GNP300-1b(2)	img2	distilled water	98.67	97.28	97.97
b-GNP300-1b(2)	img3	distilled water	116.52	114.53	115.53
b-GNP300-1b(2)	img4	distilled water	121.11	121.03	121.07
Mean					114.4175
b-AC300-1b	img1	distilled water	108.81	104.56	106.69
b-AC300-1b	img2	distilled water	99.37	98.06	98.71
b-AC300-1b	img3	distilled water	140.35	139.75	140.05
b-AC300-1b	img4	distilled water	105	107.12	106.06
Mean					112.8775

Table D.5: Brush application of the mixed activated charcoal-graphene nanoplatelets sample properties.

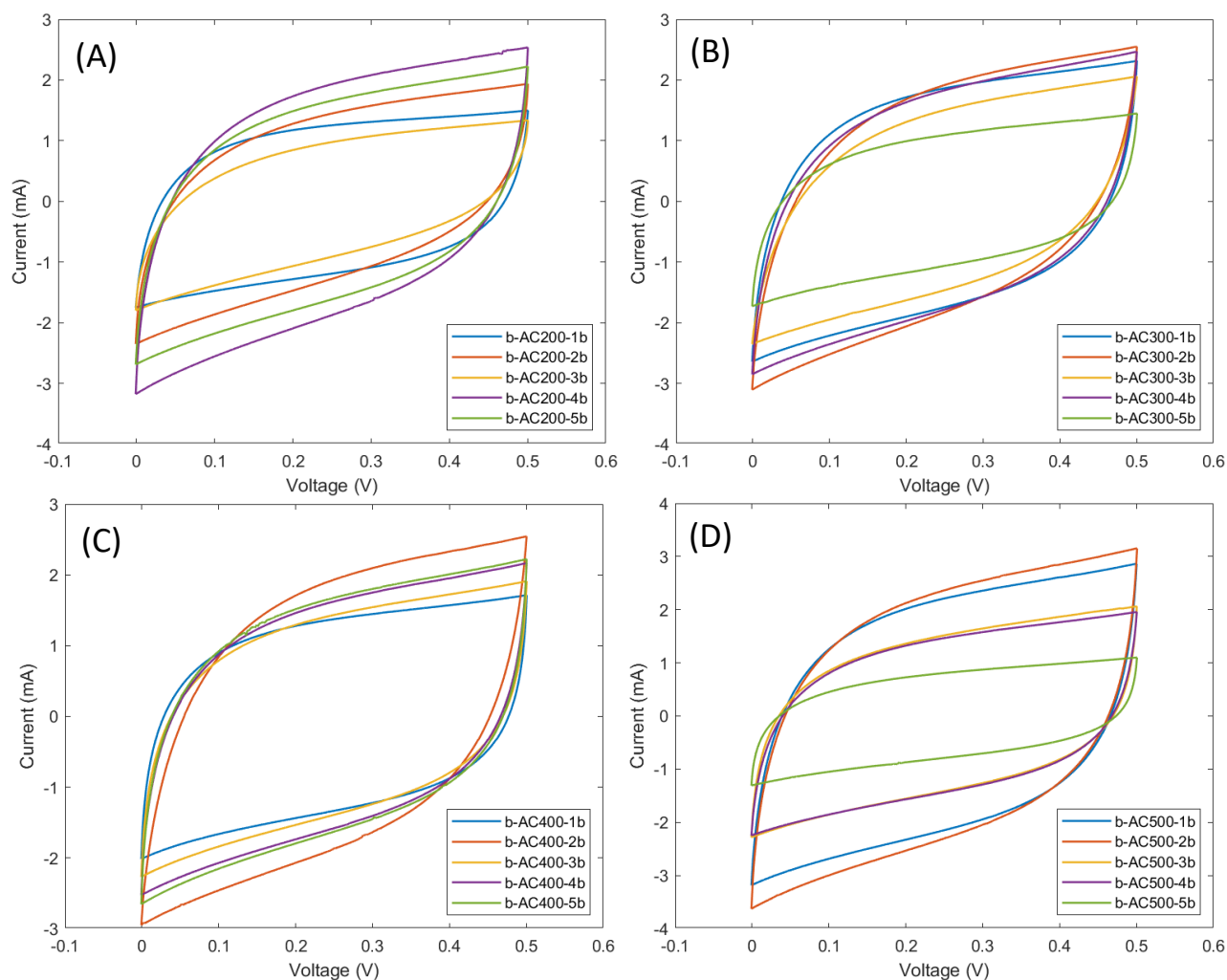


Figure D.4: CV plots of the electrode samples brush-coated with the AC slurry. (A) CV curves of the b-AC200 slurry. (B) CV curves of the b-AC300 slurry. (C) CV curves of the b-AC400 slurry. (D) CV curves of the b-AC500 slurry.

Materials' Weight in Grams			
Code name	TEP	PVDF-HFP	LiTFSI
LiTFSI-100%	10	2	2
LiTFSI-80%	10	2	1.6
LiTFSI-60%	10	2	1.2
LiTFSI-50%	10	2	1
LiTFSI-40%	10	2	0.8
LiTFSI-30%	10	2	0.6
LiTFSI-20%	10	2	0.4
LiTFSI-10%	10	2	0.2
LiTFSI- 0%	10	2	0

Table D.6: Formulation table of the gel polymer electrolyte for batch 1.

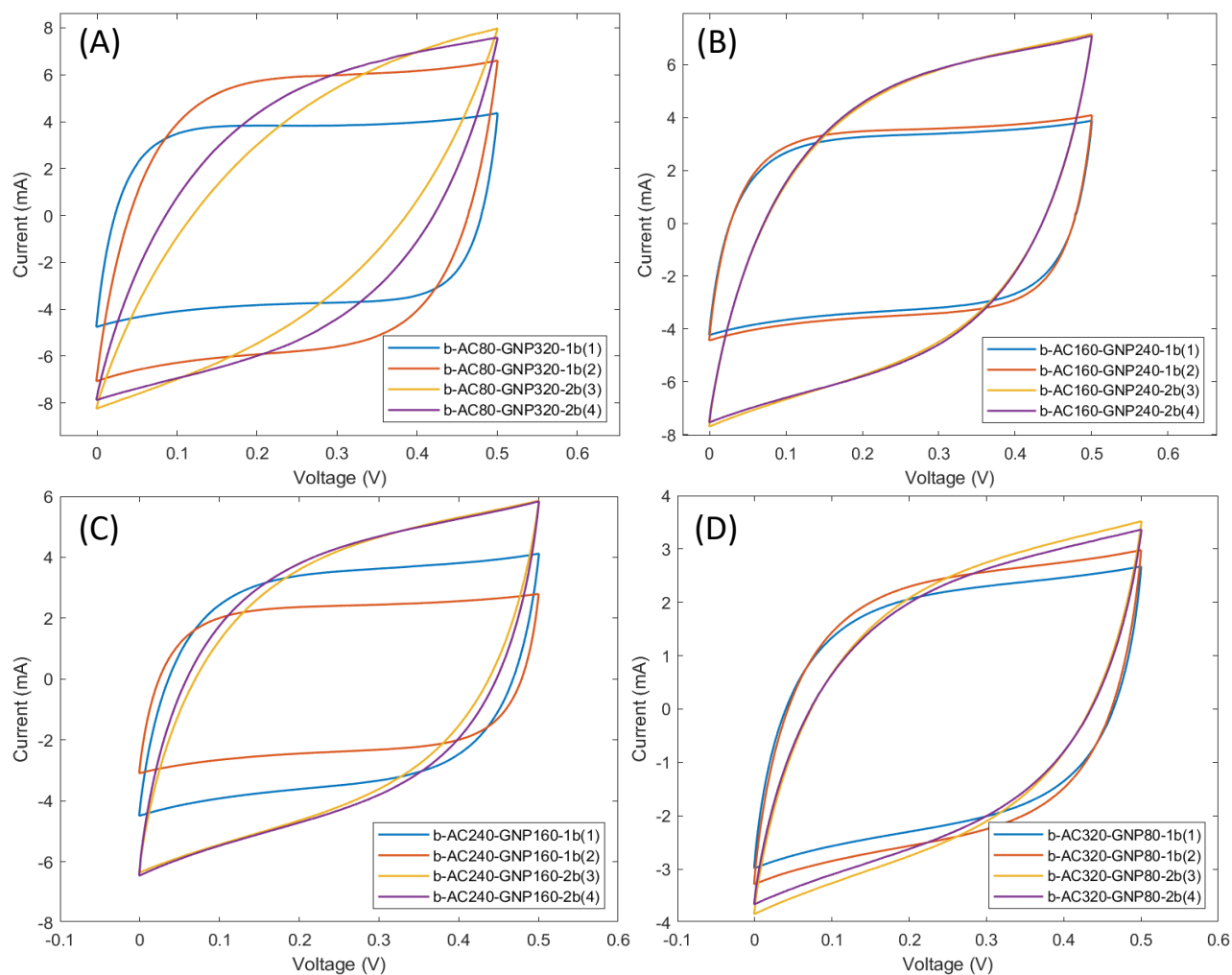


Figure D.5: CV plots of the electrode samples brush-coated with the GNP-AC mixed slurry. (A) Specific capacitance normalised by the electrode weight (PW-CSTF and slurry). (B) Specific capacitance normalised by the slurry weight. (C) Areal capacitance is normalised by the surface area of the PW-CSTF. (D) CV curves of the highest electrode-specific capacitance for each slurry formula. The numbers 1&2 were brushed once, while 3&4 were brushed twice.

	(mm)				
Sample Name	Thickness	Length	Width	Support Span	Length/Span Ratio
no-film-no-bag-1	1.364	81.272	63.846	58.000	1.401
no-film-no-bag-2	1.414	82.082	61.874	58.000	1.415
no-film-no-bag-3	1.358	81.368	62.780	58.000	1.403
no-film-no-bag-4	1.318	81.460	62.628	58.000	1.404
no-film-no-bag-5	1.392	81.596	62.340	58.000	1.407
no-film-with-bag-1	1.374	82.710	63.438	58.000	1.426
no-film-with-bag-2	1.376	82.650	62.146	60.000	1.378
no-film-with-bag-3	1.326	82.272	63.210	60.000	1.371
no-film-with-bag-4	1.352	82.758	62.892	60.000	1.379
no-film-with-bag-5	1.346	81.290	62.078	75.000	1.084

Table D.7: Dimensions of the mock-up samples with no PE film as the mock-up gel polymer electrolyte. Each dimension of the samples is measured five times at different locations.

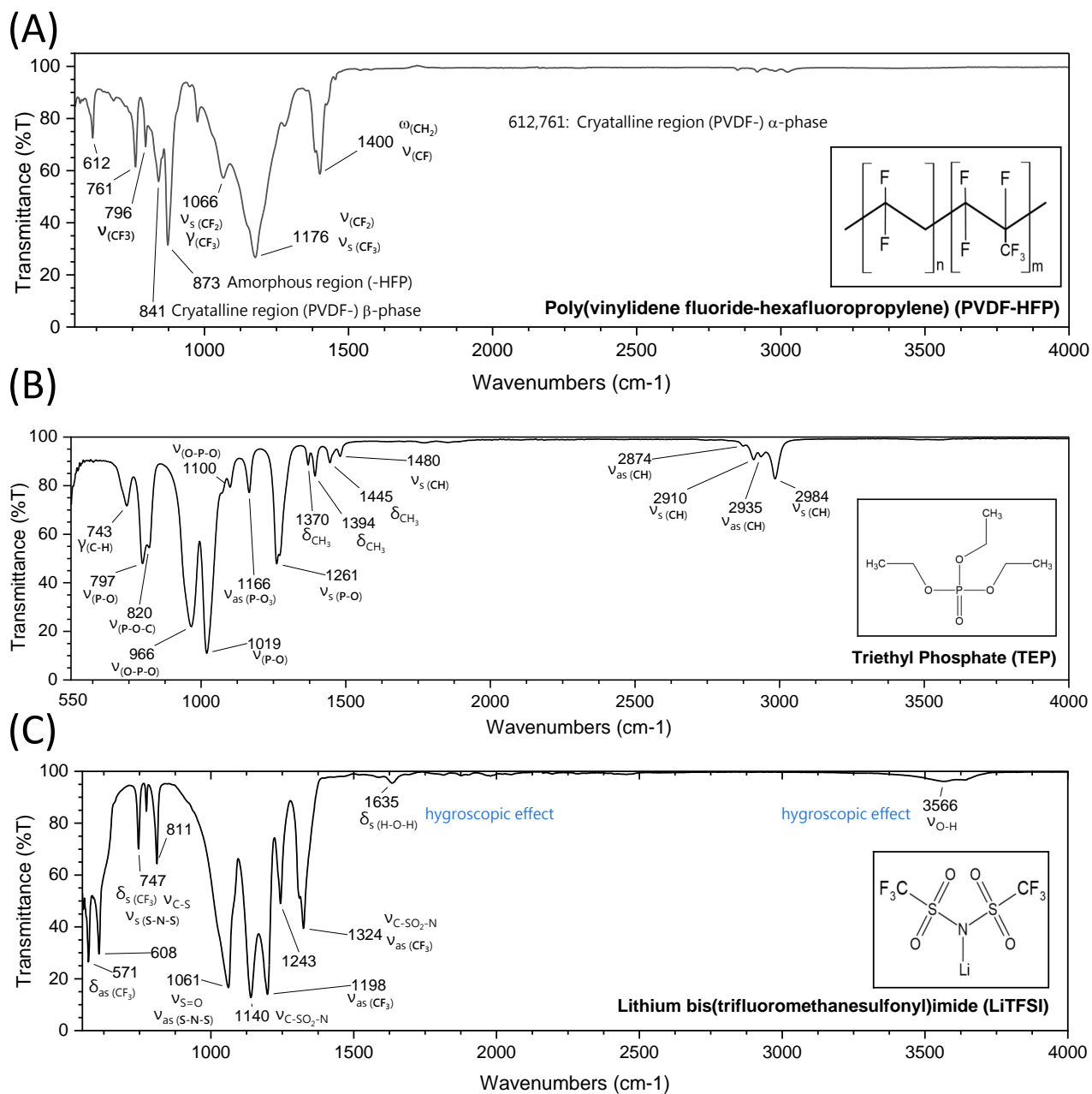


Figure D.6: The FTIR spectrum and the corresponding functional groups at the transmittance peaks of the (A) PVDF-HFP [52, 80, 96, 124] (B) TEP [36, 83, 136] and (C) LiTFSI [77, 102, 103, 143].

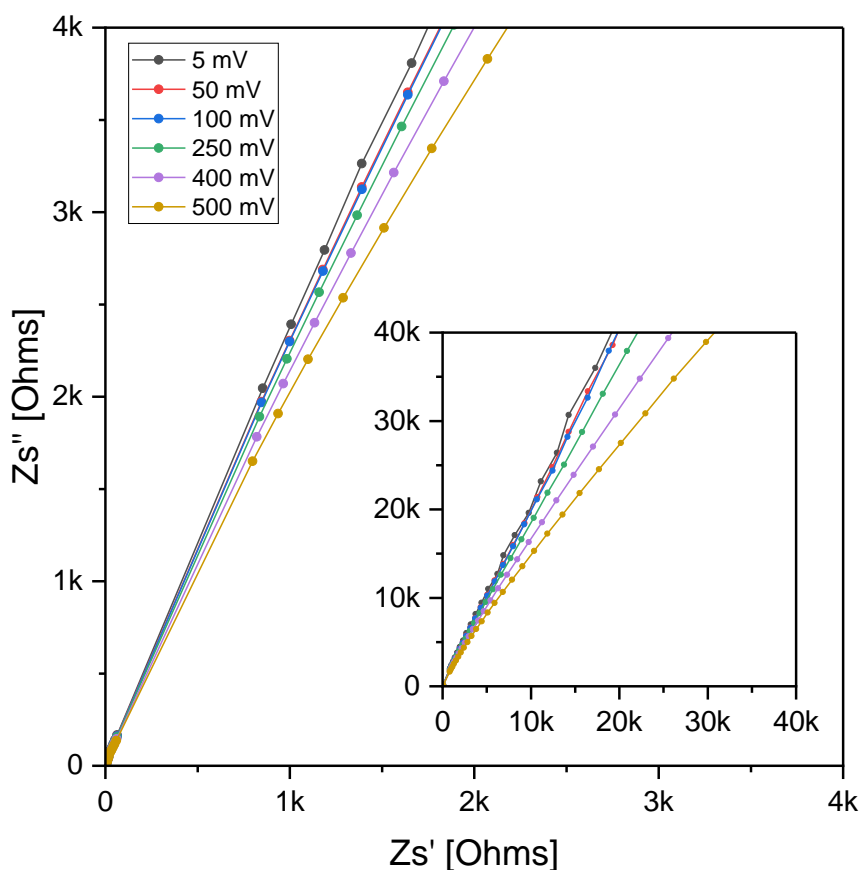


Figure D.7: The behaviour of the Nyquist plot of gel polymer electrolyte (GPE) LiTFSI-60% when the alternating potential V_{rms} is varied. The gel polymer electrolyte LiTFSI-60% is vacuum dried for 24 hours at 70°C. The electrochemical impedance spectroscopy was measured on the fifth day after the GPE was produced.

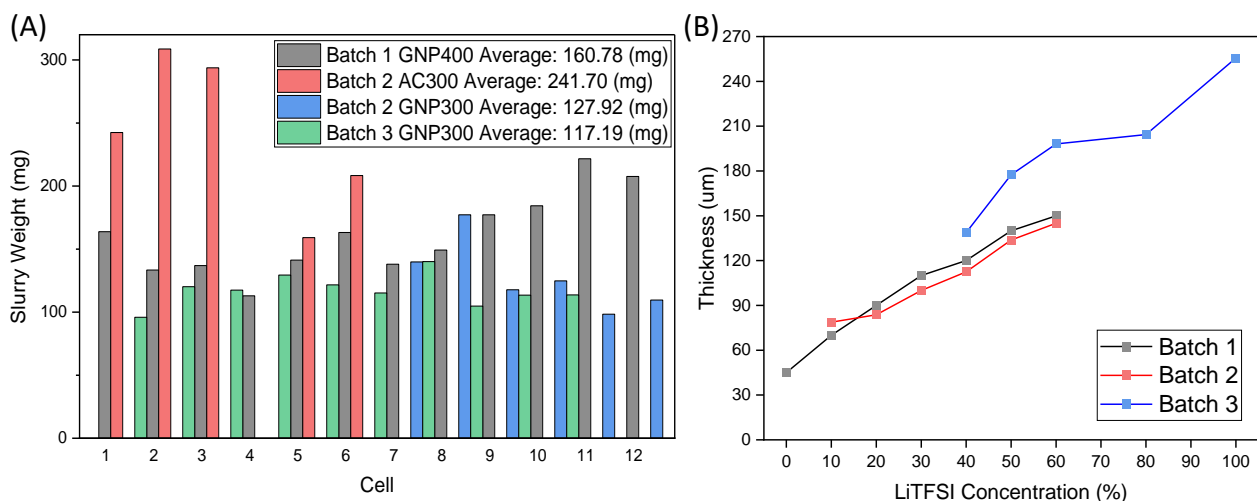


Figure D.8: (A) Slurry deposition weight using the brush application method for batch 1 to batch 3. (B) Relationship between gel polymer electrolyte thickness and LiTFSI concentrations. Batch 1 and 2 used a 600 μm solution casting gap while batch3 used a 800 μm gap.

(mm)					
Sample Name	Thickness	Length	Width	Support Span	Length/Span Ratio
with-film-no-bag-1	1.482	83.642	62.098	57.000	1.467
with-film-no-bag-2	1.452	83.346	62.554	57.000	1.462
with-film-no-bag-3	1.468	82.682	62.108	57.000	1.451
with-film-no-bag-4	1.440	82.428	63.074	57.000	1.446
with-film-no-bag-5	1.460	83.496	63.450	57.000	1.465
with-film-with-bag-1	1.470	82.954	62.520	57.000	1.455
with-film-with-bag-2	1.460	81.576	62.224	57.000	1.431
with-film-with-bag-3	1.480	85.276	62.796	57.000	1.496
with-film-with-bag-4	1.408	83.210	62.608	57.000	1.460
with-film-with-bag-5	1.452	82.978	62.710	57.000	1.456

Table D.8: Dimensions of the mock-up samples with PE film as the mock-up gel polymer electrolyte. Each dimension of the samples is measured five times at different locations.

(mm)					
Sample Name	Thickness	Length	Width	Support Span	Length/Span Ratio
b2-Cell1	1.420	80.896	62.872	57.000	1.419
b2-Cell2	1.420	80.330	63.688	57.000	1.409
b2-Cell3	1.500	80.402	63.184	57.000	1.411
b2-Cell4	1.570	80.988	63.712	57.000	1.421
b2-Cell5	1.580	80.578	63.218	57.000	1.414
b2-Cell6	1.630	80.606	62.996	57.000	1.414
b2-Cell7	1.740	82.562	65.310	57.000	1.448
b2-Cell8	1.610	84.144	64.546	57.000	1.476
b2-Cell9	1.620	83.386	63.932	57.000	1.463
b2-Cell10	1.690	84.324	63.618	57.000	1.479
b2-Cell11	1.630	84.576	65.798	57.000	1.484
b2-Cell12	1.420	83.618	65.832	57.000	1.467

Table D.9: Batch 2 full cell dimensions for the three-point flexural test. Each dimension of the samples is measured five times at different locations.

Sample Name	(mm)				
	Thickness	Length	Width	Support Span	Length/Span Ratio
b3-Cell1	1.95	83.98	68.79	57.00	1.47
b3-Cell2	2.02	83.91	67.67	57.00	1.47
b3-Cell3	2.05	84.25	68.62	57.00	1.48
b3-Cell4	2.13	81.63	68.66	57.00	1.43
b3-Cell5	2.27	84.66	68.26	57.00	1.49
b3-Cell6	2.13	83.37	67.55	57.00	1.46
b3-Cell7	2.12	84.20	68.06	57.00	1.48
b3-Cell8	2.16	88.97	69.58	57.00	1.56
b3-Cell9	2.16	84.21	66.85	57.00	1.48
b3-Cell10	1.95	83.22	68.96	57.00	1.46

Table D.10: Batch 3 full cell dimensions for the three-point flexural test. Each dimension of the samples is measured five times at different locations.

Sample Name	Flexural Chord Modulus of Elasticity (GPa)	Flexural Strength (MPa)
no-film-no-bag-1	10.97	302.28
no-film-no-bag-2	10.46	250.47
no-film-no-bag-3	11.49	299.40
no-film-no-bag-4	12.66	321.24
no-film-no-bag-5	10.86	303.03
Mean (STD)	11.29 (0.85)	295.28 (26.49)
no-film-with-bag-1	10.41	246.79
no-film-with-bag-2	11.93	260.67
no-film-with-bag-3	12.98	295.03
no-film-with-bag-4	12.72	305.81
no-film-with-bag-5	13.03	245.58
Mean (STD)	12.21 (1.1)	270.78 (27.96)

Table D.11: Mean values and standard deviation of the mock-up samples with no PE film as the gel polymer electrolyte mock-up.

Sample Name	Flexural Chord Modulus of Elasticity (GPa)	Flexural Strength (MPa)
with-film-no-bag-1	12.64	177.54
with-film-no-bag-2	11.79	162.51
with-film-no-bag-3	11.34	162.72
with-film-no-bag-4	12.09	167.69
with-film-no-bag-5	11.60	170.25
Mean (STD)	11.89 (0.5)	168.14 (6.21)
with-film-with-bag-1	12.05	160.76
with-film-with-bag-2	11.68	166.27
with-film-with-bag-3	11.74	149.09
with-film-with-bag-4	12.60	170.55
with-film-with-bag-5*	6.07*	140.45*
Mean (STD)	12.02 (0.42)	161.67 (9.29)

Table D.12: Mean values and standard deviation of the mock-up samples with a PE film as the gel polymer electrolyte mock-up.*The sample's data is excluded from the mean and STD calculation.

Cell Code	Batch 2		Batch 3	
	Flexural Chord Modulus (Gpa)	Flexural Strength (MPa)	Flexural Chord Modulus (Gpa)	Flexural Strength Up to 7mm deformation (MPa)
Cell1	20.48	219.36	3.50	71.09
Cell2	20.71	198.80	3.50	77.33
Cell3	17.00	243.11	2.63	48.77
Cell4	9.45	121.11	2.55	54.57
Cell5	10.21	154.76	2.26	52.27
Cell6	9.67	125.03	3.39	52.07
Cell7	7.22	145.79	3.22	46.51
Cell8	8.27	136.64	3.25	52.47
Cell9	5.87	166.37	3.17	58.67
Cell10	6.91	140.35	4.63	70.76
Cell11	7.01	154.99	–	–
Cell12	10.34	208.80	–	–

Table D.13: The flexural chord modulus and the flexural strength of batch 2 and batch 3 full cells. Batch 3 cells are tested to a maximum of 7 mm deformation.

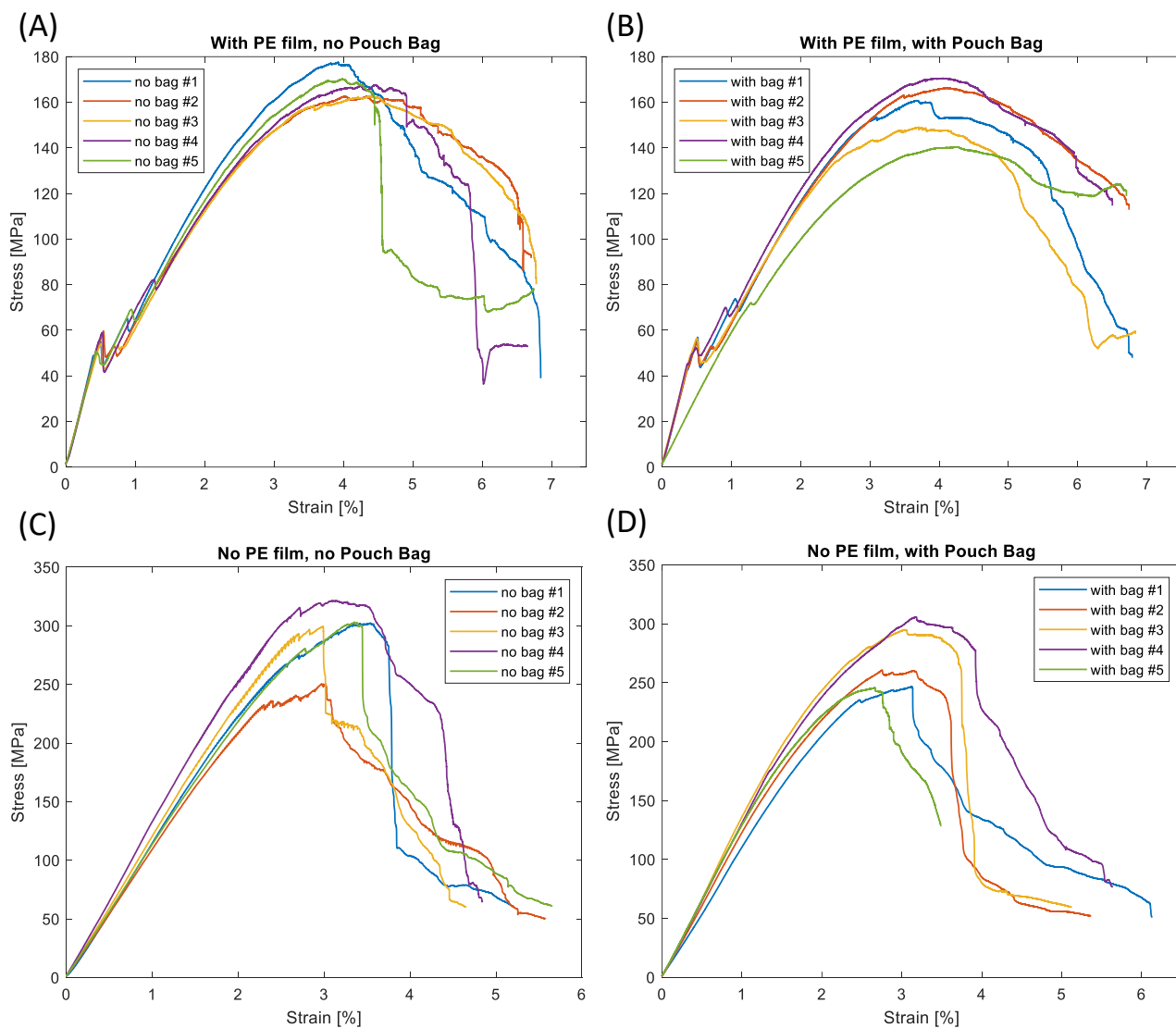


Figure D.9: Stress strain plots of the mock-up samples. (A) With a PE film as the gel polymer electrolyte (GPE) mock-up, without a pouch bag. (B) With a PE film as the gel polymer electrolyte (GPE) mock-up, with a pouch bag. (C) Without a PE film as the GPE mock-up, without a pouch bag. (D) Without a PE film as the GPE mock-up, with a pouch bag.